Alexandra Furtado Guerreiro

Master of Science

Comparison of the radiosensitisation ability of metal oxide nanoparticles using clinical megavoltage X-rays

Thesis submitted in partial fulfilment of the requirements for the degree of
Doctor of Philosophy in
Radiation Biology and Biophysics

Supervisor: Jon Golding, Senior Lecturer, Open University

Co-supervisors: Nigel Mason, Professor and Head of School, University of Kent

Maria Alice Santos Pereira, Assistant Professor, NOVA School of Sciences and Technology

Examination Committee:

Chairperson: Professor Paulo Manuel Assis Loureiro Limão-Vieira

Raporteurs: Professor Frederick Currell

Dr Octávia Gabriela da Silva Viegas Nené Monteiro Gil

Members: Professor Malgorzata Śmialek-Telega

Professor Pedro António de Brito Tavares

Professor Jon Golding

FACULDADE DE CIÊNCIAS E TECNOLOGIA
UNIVERSIDADE NOVA DE LISBOA

May, 2020

NOVA Lisbon University

Faculty of Science and Technology

Alexandra Furtado Guerreiro

Master of Science

Comparison of the radiosensitisation ability of metal oxide nanoparticles using clinical megavoltage X-rays

Thesis submitted in partial fulfilment of the requirements for the degree of
Doctor of Philosophy in
Radiation Biology and Biophysics

May, 2020

Comparison of the radiosensitisation ability of metal oxide nanoparticles using clinical megavoltage X-rays

To my mother, sister and niece

Acknowledgements

The work presented in this thesis was performed at Open University and at GenesisCare in Milton Keynes and I would like to thank everyone that contributed to make this work possible.

To my supervisor, Dr Jon Golding, I would like to thank his commitment in my work and for always being there when I needed. His guidance and assistance were crucial to make this thesis come true.

To Eleanor Crabb and Nicholas Chatterton I would like to thank for all their input and all the brain storm that helped developed this thesis.

To Genesis Care staff, such as Aquila Sharif and all the radiographers, I would like to thank all their availability and effort to assist me in this thesis and make it possible.

Also, I would like to thank Open University staff such as Dr Igor Kraev, Dr Radka Gromnicova, Brett Keith, George Bryant and Dr Matthew Kershaw for all their technical assistance.

I would like to thank professor Nigel Mason and Sir John Mason Academic Trust for the support provided for the development of this work. To professor Alice S. Pereira for all her support from Portugal.

Many thanks to Fundação para a Ciências e Tecnologia (FCT/MCTES), Radiation Biology and Biophysics Doctoral Training Programme (RaBBiT, PD/00193/2012); UID/Multi/04378/2013 (UCIBIO); UID/FIS/00068/2013 (CEFITEC); and grant number PD/ BD/114450/2016 for granting me this PhD fellowship.

I would like to thank all the friends I made at Open University and that made my journey much easier and happier. A special thanks to Marcelle Silva, Sonia Azeggagh, Edu Frias and Radka Gromnicova for all the shared moments and their amazing support as friends that I will keep for life.

Also, I would like to thank my friends Nidia Almeida and Fausto that I met in the beginning of this journey and that made my experience so much better and fun. I hope we share many other journeys together. To Dr Cristina Timóteo for the support and friendship provided whenever I needed.

I would like to thank my closest friends and family for their support and for being present in my life. Thank you, Alexandros Kostopoulos, for all the moments we shared, all your support, encouragement, and companionship. A special thanks to my mother, sister and father for believing in me, and being so patient and so supportive. Mum and sister there are no words to describe how important you are for me and I dedicate this thesis to you. Also, I want to welcome our new member of the family, my niece Alice, which although still very young I hope in the future she will be able to read this thesis and know that my life became a brighter place with her presence. Thank you so much!

Abstract

A wide range of nanoparticles (NPs), composed of different elements and their compounds, are being developed by several groups as possible radiosensitisers, with some already in clinical trials. However, no systematic experimental survey of the clinical X-ray radiosensitising potential of different element NPs has been made. In this thesis, a direct comparison is made through the irradiation-induced (10 Gy of 6 MeV X-ray photon) production of reactive oxygen species (ROS) such as hydroxyl radicals, superoxide anion radicals and singlet oxygen in aqueous solutions of the different metal oxide NPs. Also, cancer cell and DNA damage due to these NPs is studied under irradiation conditions.

The results of this thesis showed that without any X-rays, several NPs produced different radicals. Furthermore, NPs such as vanadium oxide (V_2O_5) produced a significant amount of radicals compared to water and to the other types of NPs when irradiated with 10 Gy of 6 MeV X-rays and NPs such as copper oxide (CuO) showed significant cell and DNA damage that is not related to the production of ROS.

Beyond identifying promising metal oxide NPs radiosensitisers, these results have shown evidence that the chemical and biological effects of these NPs are also present in the mode of action of these radiosensitisers challenging the pure physical radio-enhancement concept.

Keywords: metal oxide nanoparticles; clinical X-ray; ROS; hydroxyl and superoxide radical; singlet oxygen; radiosensitiser.

Resumo

Uma gama ampla de nanopartículas (NPs), compostas de diferentes elementos e dos seus compostos, encontram-se a ser desenvolvidas por diferentes grupos como possíveis radiossensibilizadores, onde algumas encontram-se em ensaios clínicos. No entanto, nenhum estudo sistemático comparativo do potencial de radiossensibilização por raios-X usados clinicamente dos diferentes elementos de NPs foi realizado. Nesta tese, a comparação directa é realizada através da indução de espécies reactivas de oxigénio (ROS), como os radicais hidroxilo e o anião superóxido, e o oxigénio singleto, por irradiação (10 Gy de 6 MeV de fotões raios-X) em soluções aquosas das NPs dos diferentes óxidos de metais. Para além disso, o dano causado a células cancerígenas e ao DNA devido à acção destas NPs é estudado nestas condições de irradiação.

Os resultados desta tese mostram que, sem a acção dos raios-X, diferentes NPs produziram diferentes radicais. Nanopartículas como o óxido de vanádio (V_2O_5) produziram uma quantidade significativa de radicais quando comparado à ausência de NPs e também quando comparado aos outros tipos de NPs quando estas foram irradiadas com 10 Gy de 6 MeV de fotões raios-X e NPs de óxido de cobre (CuO) mostraram um dano significativo celular e ao DNA que não se encontra relacionado com a produção de ROS.

Para além de identificarem NPs de óxidos de metais promissores à radiossensibilização, estes resultados mostraram evidência de que os efeitos químicos e biológicos destas NPs estão também presentes no seu modo de acção enquanto radiossensibilizadores, desafiando assim o conceito da acção puramente física da radiossensibilização.

Palavras-chave: nanopartículas de óxidos de metais; raios-X clínicos; espécies reactivas de oxigénio; radicais hidroxilo e o anião superóxido; oxigénio singleto; radiossensibilizador.

Table of Contents

List of Figures

List of Tables

List of Abbreviations and Symbols

3D-CRT: Three-Dimensional Conformal Radiation Therapy

7OH-CCA: 7-hydroxycoumarin-3-carboxylic acid

A549: Human Alveolar Basal Epithelial Adenocarcinoma cell line

AgNP: silver nanoparticles

Balb/c 3T3: Mouse Fibroblast cell line

BEAS-2B: Human bronchial epithelium non-cancerous cell line

Caco2: Human Epithelial Colorectal Adenocarcinoma cell line

CAT: Catalase

CCA: Coumarin-3-Carboxylic Acid

CIT: citrate

DEF: Dose Enhancement Factor

DHE: Dihydroethidium

DLS: Dynamic Light Scattering

DMEM: Dulbecco´s Modified Eagle Medium

DNA: Deoxyribonucleic Acid

DSBs: Double Strand Breaks

DU145: Human Prostate Adenocarcinoma cell line

e^-/h^+ : electron/hole

EPR: Enhanced Permeability Retention

FF: Flattening Filter

H_2O_2 : Hydrogen peroxide

HaCaT: Human Keratinocyte cell line

hMSCs: Human Mesenchymal Stem cells

$HO^\cdot$: Hydroxyl radical

HSC-3: Human Tongue Squamous carcinoma cell line

IMRT: Intensity-modulated Radiation Therapy

L132: Lung Epithelial carcinoma cell line

LINAC: Linear Accelerator

LNCaP: Human Prostate Adenocarcinoma cell line

MDA-MB-231: Human Breast carcinoma cell line

mMSCs: Mouse Mesenchymal Stem cells

NP: Nanoparticle

NPs: Nanoparticles

NSs: NanoSheets

$^1O_2$: Singlet oxygen

$O_2^{-\cdot}$: Superoxide

PAA: Polyacrylic Acid

PBS: Phosphate-Buffered Saline

PEG: Polyethylene Glycol

PEI: Polyethylenimine

PVA: Polyvinyl Alcohol

PVP: Polyvinyl-pyrrolidone

RAW 264.7: Mouse Myeloid cell line

rMSCs: Rat Mesenchymal Stem cells

ROS: Reactive Oxygen Species

RT: Radiotherapy

SABR: Stereotactic Ablative Radiotherapy

SEM: Standard Error of the Mean

SNB-19: Human Glioblastoma cell line

SOD: Superoxide Dismutase

SOSG: Singlet Oxygen Sensor Green

SPIONs: SuperParamagnetic Iron Oxide Nanoparticles

SSBs: Single Strand Breaks

TEM: Transmission Electron Microscopy

U87MG: Human Glioblastoma cell line

XRD: X-ray Diffraction

Z: Atomic number

1 – Introduction

One of the applications of radiation is to treat cancer, a disease that arises approximately in one among every three individuals. Cancer is a disease that consists of the abnormal growth of cells that do not follow the normal rules of cell division (Hejmadi, 2010).

The cancer treatment that uses radiation to kill cancer cells is called radiotherapy (RT). People have been using ionising radiation to treat cancer for more than 120 years (Nickoloff, 2015). The main goal of RT treatment is the irradiation of a target tumour volume while minimizing the amount of radiation absorbed in the healthy tissue.

In RT there are essentially two modes of treatment: internal radiation therapy and external beam radiation therapy. Internal RT uses radiation sources that are placed inside the body, such as implants (brachytherapy) or as injections, capsules or drinks (radioisotope therapy). External RT uses a machine that produces radiation and directs it into the body, to the tumour.

This project focuses on methods to selectively enhance external RT, which is the most common type of radiation therapy used for cancer treatment.

1.1 Radiotherapy

1.1.1 X-ray beam treatment

In the past 40 years, the combination of high-voltage linear accelerators able to reach deep tissues with computed tomography to allow 3D treatment planning in RT has gained widespread use and minimised exposure to normal tissues (Nickoloff, 2015).

X-rays are produced through the bombarding of a target with energetic electrons. These X-rays consist of bremsstrahlung photons, which result from electron-nucleus Coulomb interactions, and characteristic photons, which result from electron transitions between atomic shells. Different X-ray energies (wavelengths) can be produced. X-ray tubes produce X-rays in the range of kilovoltage energies, called superficial X-rays (50-150 kV) or orthovoltage X-rays (150-300 kV); while linear accelerators (LINACs) produce X-rays with megavoltage energies.

Kilovoltage X-ray beams do not penetrate the body very deeply and deposit most of the X-ray dose close to the surface of the patient and due to the attenuation and scattering of the beam the dose drops-off rapidly with depth. Nowadays, the primary therapeutic clinical use for kilovoltage X-rays is the treatment of skin cancers (Hill et al., 2014). Megavoltage X-rays are more penetrating and have largely replaced kilovoltage treatments. Due to its extensive use and due to its different applications, megavoltage X-rays is the beam energy used in this thesis.

Megavoltage X-rays are produced in a treatment machine called a linear accelerator (LINAC), represented in Figure 1.1. For this high-energy radiation to be produced, an electron beam is needed.

These electrons are produced by an electron gun and then accelerated through a waveguide that increases their energy from keV to MeV range (Podgorsak, 2005). When the electrons hit an X-ray target, X-rays are produced. The LINAC and the treatment couch rotate about a point called isocentre.

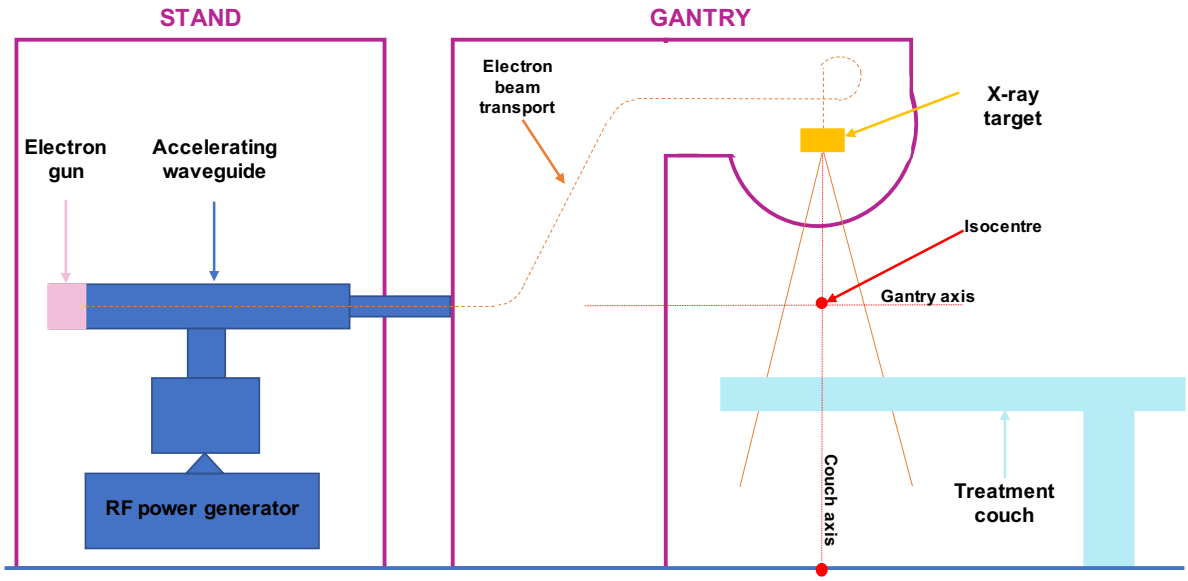

Figure 1.1: Design configuration for a medical LINAC.

1.1.2 Megavoltage X-ray physical properties

In a typical treatment, electrons are accelerated to an energy of 6 MV and hit a tungsten target to produce X-ray photons with an energy spectrum from 0 to a maximum value of 6 MV.

The absorption of X-ray energy per kilogram of matter, the so-called dose measured in units of gray (Gy), varies with depth through the patient. At the skin entry point the dose is D_s, as shown in Figure 1.2. Being at the surface an initial dose build-up occurs due to the contribution of secondary photoelectrons until it reaches a maximum value D_{max} at a depth of z_{max}. This maximum value is followed by an exponential decrease which follows the Beer-Lambert law until it reaches a value of D_{ex} which happens when radiation exits the patient's body.

Energy fluence decreases exponentially with the Lambert Beer's law:

$$\frac{\psi}{\psi_0} = e^{-\mu x}$$

where ψ is the energy fluence in MeV/cm^2 at a depth x in matter, ψ_0 is the primary beam fluence and μ is the linear attenuation coefficient in cm^{-1}.

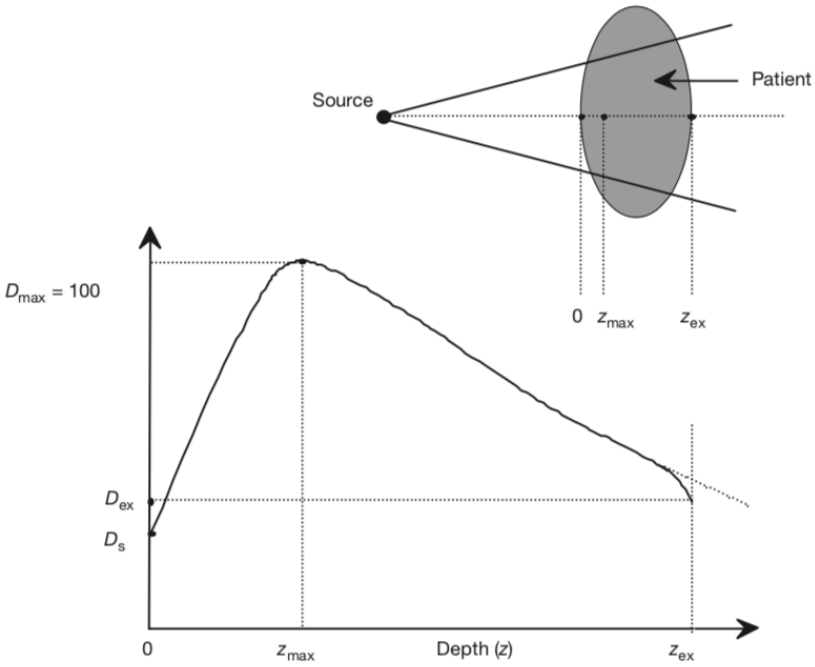

Figure 1.2: Typical dose distribution on the central axis of a megavoltage beam. D_S is a superficial dose, at z_{max} depth dose reach a maximum value D_{max}, D_{ex} is the dose delivered to the patient at the beam exit point z_{ex}: we can observe a small curve downwards due to missing scatter contribution at the exit point from point beyond the exit dose point (Podgorsak, 2005).

As shown in Figure 1.3, the build-up region increases with increasing photon energy. Also, surface dose, D_s, and dose maximum depth, z_{max}, depend mainly on the beam energy. For a 6 MV X-ray beam, the first 1.5 mm of tissue (the skin) receives ~15% of the maximum dose while for an 18 MV X-ray skin receives ~10% (Podgorsak, 2005).

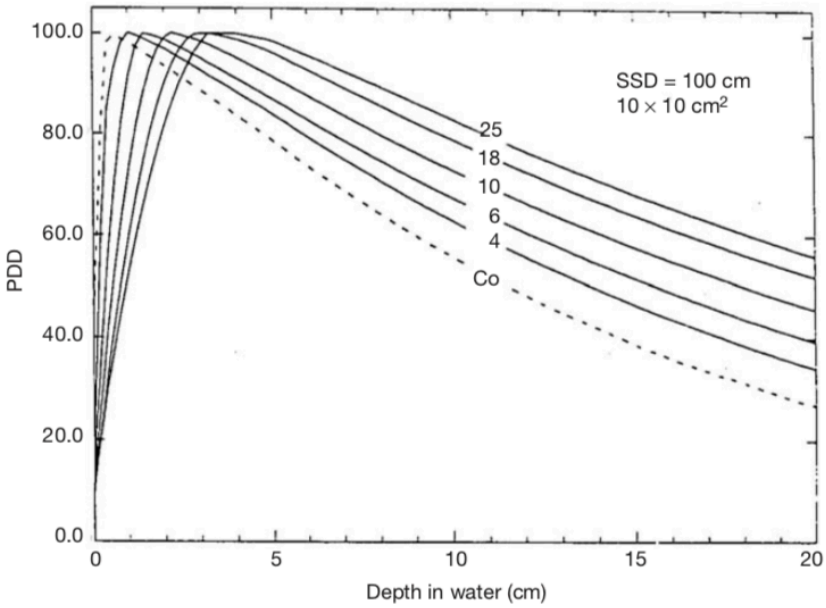

Figure 1.3: Percentage depth dose (PDD) curves for MV X-ray beams with energies from Co to 25 MV at a surface to source distance (SSD) of 100 cm for a 10×10 cm^2 field. The maximum dose is at 1.5 cm depth for 6 MV and at 5 cm depth for 25 MV (Podgorsak, 2005).

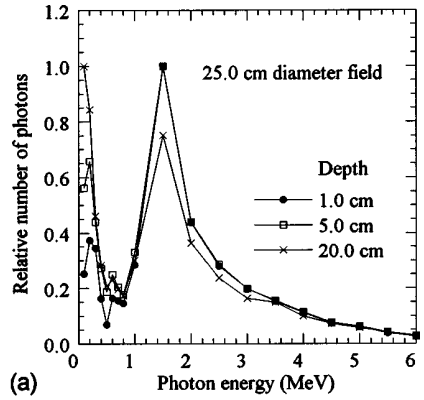

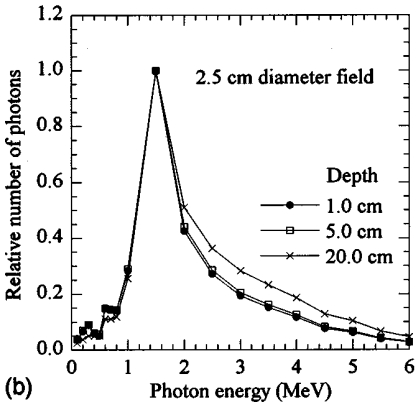

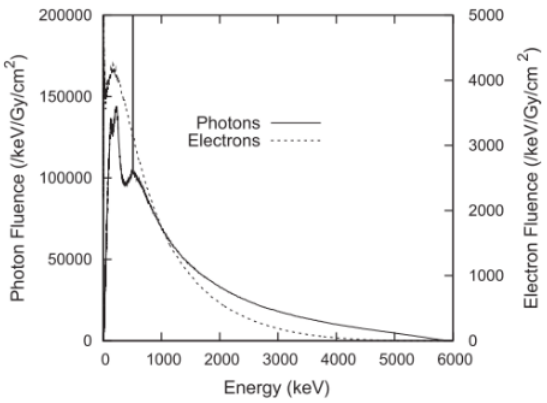

(c)

Figure 1.4: Energy spectra due to a 6 MeV LINAC beam at different depths of water. (a): 25.0 cm diameter field (J. L. Robar & Clark, 1999); (b): 2.5 cm diameter field (J. L. Robar & Clark, 1999); (c): simulation of a cylindrical water volume (10 cm long and 10 cm diameter) exposed to a 5 cm diameter beam, directed along the cylinder's central axis (McMahon et al., 2011).

A 6 MeV LINAC beam has contributions from lower photon energies, as it can be observed in Figure 1.4. These lower energies will be very useful for photocatalysis on metal oxide surfaces and DNA damage, as it will be explained later. From Figures 1.4 (a) and (b), one can see that depending on the

field size (25 cm vs 2.5 cm) the mean photon energy of 6 MeV X-ray beams varies. For large beams (25 cm) the mean photon energy decreases with depth up to 15 cm due to an increase of phantom scatter (J. L. Robar & Clark, 1999). Figure 1.4 (c), calculated at a depth of 5 cm shows the contribution of both low-energy photons and secondary electrons, significant to dose deposition.

1.1.3 Current methods of improving radiotherapy targeting

Photon (X-ray) RT, known as XRT, can be improved by techniques such as 3D conformation RT (3D-CRT) and intensity-modulated radiation therapy (IMRT). These techniques allow high doses to be shaped to tumours while minimizing doses to surrounding normal tissue (Thariat et al., 2013).

Due to the appearance of three-dimensional radiation treatment planning (3D-RTP) and computer-controlled radiation therapy (CCRT) delivery systems it was possible the implementation of three-dimensional conformal radiation therapy (Purdy, 2001). 3D-CRT technique conforms the radiation into the target volume with the goal of minimizing the amount of radiation that hits the surrounding normal tissue. The increased access of volumetric images of a patient's internal anatomy has led to the development of 3D-CRT techniques since it allowed the delineation of soft tissue anatomy (King et al., 2017).

A type of 3D-CRT technique is the IMRT was developed to improve RT both through increased tumour control probability and decreased normal tissue complication probability (Podgorsak, 2005). This technique uses multileaf collimators mounted inside the gantry that provide non-uniform radiation beam intensities. These collimators can move during the treatment, dynamically shaping the beams in order to match the shape of the target volume. It relies on inverse treatment planning, in which instead of changing the beams to achieve the dose limits required for each target and organ at risk the user gives the dose limits and the computer calculates the best shape of the beams, and on 3-D multimodality imaging to define the target volumes (Podgorsak, 2005). IMRT is capable of achieving a much higher degree of target conformity and/or normal tissue sparing than the other treatment techniques (Purdy, 2001). This higher degree of target conformity allows the delivery of higher radiation doses than other 3D-CRT techniques, meaning that the conventional 2 Gy radiation dose fractions can be increased. An example of a type of IMRT treatment which uses high radiation doses in a small number of treatment fractions is the Stereotactic ABlative RT (SABR) used to treat metastatic cancer which has spread to a limited number of sites, called oligometastatic disease (King et al., 2017).

Due to IMRT conformal dose distribution with narrower margins, microscopic tumour cells might end up out of the radiation field resulting in tumour reoccurrence. The sharp dose gradient in IMRT requires advanced imaging and accurate delineation of different structures, making it very sensitive to set-up uncertainties and organ motion (Rehman et al., 2018). The most important disadvantage associated with IMRT is the increase in total body irradiation. Although this technique saves organs at risk from receiving high radiation dose, at the same time it spreads out the delivered dose to the whole body

increasing total body exposure (Rehman et al., 2018). To achieve the prescribed dose, IMRT requires a significantly larger number of monitor units than other techniques which results in an increase of radiation scattered and radiation leakage that causes secondary malignancies (Purdy, 2008). Furthermore, this technique is time consuming and requires complex procedures such as its planning, delivery, and quality assurance. Despite all the efforts to improve radiation therapy, healthy tissue surrounding the tumour may still be exposed to levels of radiation that can cause both short and long-term side effects. For this reason, my thesis is focused on the use of radiosensitisers to better target the radiation dose to the tumour and help decrease the side effects of MV X-ray RT treatment.

1.2 Importance of Reactive Oxygen Species (ROS)

One of the main effects of ionising radiation in an aqueous environment, such as a cell, is the formation of highly reactive species that can damage cells. This section describes those reactive species, while the interaction of radiation with cells will be discussed in Section 1.3.

Reactive oxygen species (ROS) play a very important role in aerobic life. The damage that ROS produce to biological molecules, such as DNA, constitutes one of the most efficient pathways used in RT to kill cancer cells (Hosoya & Miyagawa, 2014).

Within the group of reactive chemical species two major types can be distinguished: radicals that have one or more unpaired electron(s) in their outer molecular orbitals; and non-radicals that do not contain unpaired electrons.

Non-radical species, although they do not contain unpaired electrons, are chemically reactive and can be easily converted into radical species.

Reactive oxygen species are partially reduced forms of molecular oxygen (O_2) and include hydroxyl radical ($HO^{\cdot}$), hydrogen peroxide (H_2O_2), superoxide anion (O_2^{-}), and ozone (O_3), as shown in Figure 1.5.

RADICALS	NON-RADICALS
Superoxide 	**Hydrogen Peroxide** 
Hydroxyl Radical 	**Ozone** 

Figure 1.5: Radicals and non-radicals from reactive oxygen species.

The radicals serve as the reactive intermediates for the inherent biological action of oxygen and can be found in high amounts in mitochondria, where the respiratory chain from this cell structure liberates electrons that may interact with molecular oxygen producing superoxide. This superoxide can in turn produce other ROS starting a chain reaction (Trachootham et al., 2009).

In aqueous solutions, superoxide exists in equilibrium with its conjugate acid, the perhydroxyl radical (HO_2) (Rose, 2012):

$$HO_2 \leftrightarrow H^+ + O_2^-$$

This means that, when talking about superoxide anion in water, both O_2^- and HO_2 are included since one does not exist without the other.

Under normal physiological conditions, ROS production can promote cell proliferation and differentiation (Boonstra & Post, 2004), but when the levels of these species become too high it starts to damage biological material, such as: nucleic acids, proteins and free amino acids, lipids and carbohydrates (Sies, 1985). For this reason, the maintenance of ROS homeostasis is crucial for normal cell function. Some ways in which cells detoxify ROS include superoxide dismutase (SOD) which converts superoxide to hydrogen peroxide and oxygen; catalase converts hydrogen peroxide into water and oxygen; glutathione peroxidase converts hydrogen peroxide into water or lipid peroxides into alcohols. The loss of these defence mechanisms provokes an abnormal ROS level leading to a condition known as oxidative stress (Toyokuni et al., 1995).

Diseases including cardiovascular disorders, diabetes, chronic inflammation, and cancer can be the product of perturbations in cellular redox homeostasis, since pathological conditions are a result of serious increase in ROS levels which can lead to an irreversible oxidative damage (Alimoradi et al., 2017).

1.3 Effects of radiation in cells

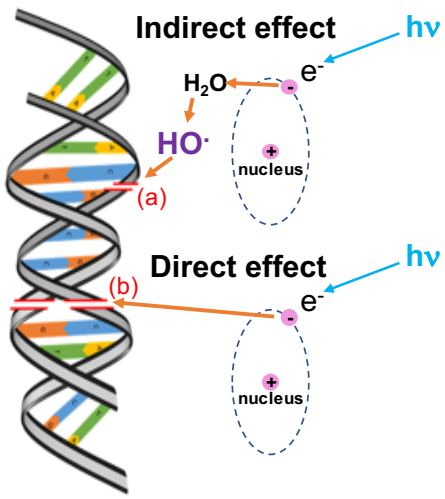

Figure 1.6: Direct and indirect actions of radiation in cell DNA; (a) – single strand break; (b) – double strand break.

There are two ways of radiation interacting with cells: directly or indirectly, as shown in Figure 1.6. It is estimated that around 40% of X-ray damage is direct and 60% indirect (Baskar et al., 2014).

Through the direct way, X-rays are absorbed in biological material interacting directly with critical targets in the cells (Hall et al., 2016). Biological damage can occur due to the ionized or excited atoms of the target. The most effective constituent is the cell DNA in the nucleus. In this case, the ability of the cell to reproduce and thus survive may be affected. The cell may be destroyed if the chromosomes do not replicate properly or the information carried by the DNA molecule undergoes significant alteration due to the interaction of the radiation with the atoms within the cell.

In the indirect way, the radiation damages the cell through the formation of free radical species, which occur due to the excitation and ionization of water molecules inside or in the vicinity of the cell.

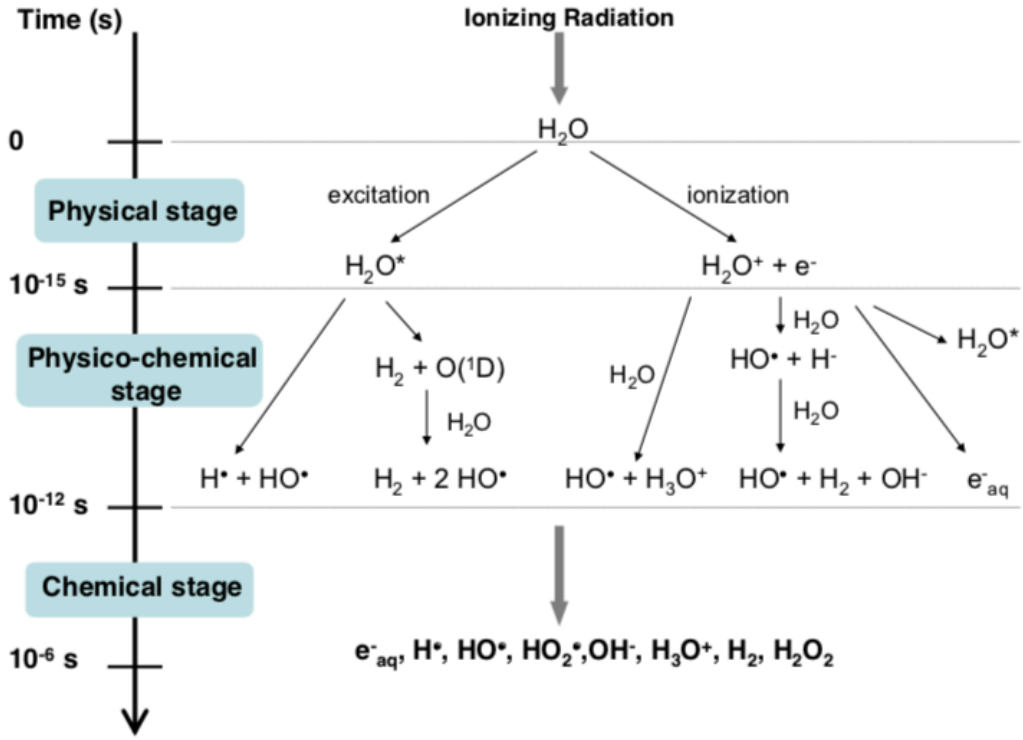

Figure 1.7: Main reactions occurring during the three stages of water radiolysis (Le Caër, 2011).

The interaction of a photon with a water molecule, known as water radiolysis, leads to the formation of radical and non-radical species such as shown in Figure 1.7. The photon can either excite a water molecule or ionize it producing a secondary electron (e^-). Both these interactions will lead to the formation of fragments such as hydrogens (H) or hydroxyls (HO). Furthermore, the produced fragments can recombine or interact with other fragments or ions to form either harmless compounds to the cells such as water (H_2O) or harmful species, such as radicals, that contribute to cell death. The species more relevant for the process of cell death are hydroxyl radicals ($OH^{\cdot}$), superoxide anion (O_2^-) and hydrogen peroxide (H_2O_2).

After the initial primary radical formation (i.e., chemical stage in Figure 1.7), both H and e^-_{aq} are converted to $OH^{\cdot}$ radicals by reaction with H_2O_2 (Bielski et al., 1985):

$$e^-_{aq} + H_2O_2 \rightarrow OH^{\cdot} + OH^-$$

$$H + H_2O_2 \rightarrow OH^{\cdot} + H_2O$$

The $OH^{\cdot}$ radicals then react with H_2O_2 to yield HO_2 :

$$OH^{\cdot} + H_2O_2 \rightarrow HO_2 + H_2O$$

There is a higher probability of the radiation to interact with the water within the cell than with the DNA inside the nucleus, which takes up only a small proportion of the cell. Most of the radiation damage caused within the cell is due to the indirect pathway since 70% of the cell constitutes of water (Desouky et al., 2015). This means that, since water makes up most of the cell's volume, the indirect path is the one that should be used and studied to improve RT treatment and is the focus of this thesis.

It is worth mentioning that low energy electrons (e^-), showed in Figure 1.7, are species that contribute very efficiently to the damage of the DNA molecule. They can either damage this molecule through the direct pathway or the indirect one through a number of mechanisms such as dissociative electron transfer from water-interface electron traps to DNA bases, quenching of dissociative electron attachment to DNA and quenching of dissociative electronically excited states of H_2O in contact with DNA (Alizadeh et al., 2013).

The direct and indirect action of radiation can also cause damage to cellular components other than DNA, such as protein, enzymes, organelles, membranes (Wang et al., 2018). The damage to one of these components can lead to cellular death.

Both direct and indirect radiation mechanisms can cause different types of damages to cell DNA, such as abasic sites, pyrimidine dimers, alkylation adducts, single strand breaks (SSBs) and double strand breaks (DSBs) (Dahlmann et at., 2009). Both SSBs and DSBs are shown in Figure 1.6. DSB is the most effective damage, since it leads to cell death if not repaired (Baskar et al., 2014). Due to mechanical stress or different types of chemical modification DNA structure may be broken in one strand of the double helix, leading to a SSB (Figure 1.6(a)) or broken in two strands of the double helix leading to a DSB (Figure 1.6(b)). It is very difficult to achieve DSB to DNA structure, but the most significant of the external agents that is able to achieve it is ionising radiation (Jeggo & Löbrich, 2007).

Reactive oxygen species primarily induce base damage and SSBs. DSBs arise indirectly from further action of trying to repair some lesions in the strand or can arise from two closely located SSBs (Jeggo & Löbrich, 2007).

DSBs can also occur during the normal life cycle of the cell, more specifically during DNA replication or in meiosis (Mladenov & Iliakis, 2011). Furthermore, within the cell, DSBs arise due to reactive oxygen species generated by normal respiratory metabolism (Featherstone & Jackson, 1999).

When oxygen is present a higher number of reactions will occur (Parveen, 2001) such as:

$$H^{\cdot} + O_2 \rightarrow HO_2^{\cdot} \rightarrow H_2O_2 + O_2 \qquad \text{reaction 1}$$

$$HO_2 + e^- \rightarrow HO_2^- + H^+ \rightarrow H_2O \qquad \text{reaction 2}$$

$$X^{\cdot} + O_2 \rightarrow XO_2^{\cdot} \rightarrow X + O_2^{\cdot} \qquad \text{reaction 3}$$

Reaction 3 refers to the interaction of oxygen with an organic molecule X, such as DNA, RNA, and proteins.

In an oxygenated environment, oxygen molecules can extract an electron from the radical anions turning them into radical cations that have a long life to cause DNA damage. On the other hand, in a hypoxic environment the electron from the radical anion tends to combine with the radical cation, with no damage to the DNA. In conclusion, the presence of oxygen increases the DNA damage produced by a given dose of radiation.

Cells sensitivity increase due to ionising radiation in normal oxygen environment compared to cells sensitivity in hypoxia conditions is called the oxygen effect, and although it has the ability of modifying the dose it is independent of the radiation dose. The ratio between the dose required to achieve a given cell survival in the absence of oxygen compared to the dose required for the same effect under normoxia conditions is called the oxygen enhancement ratio (OER), and its value varies between 2.5-3 for X-ray radiation (Nair et al., 2001).

For radiosensitisation to happen the lowest concentration of oxygen at which normoxia radiosensitisation occurs is as low as 0.25%, since at this concentration dose-response curve is shifted half-way towards the fully aerated condition (Kennedy et al, 1980).

1.4 Tumour environment

It is important to outline the characteristics of the tumour environment to find ways to make these cells weaker and more susceptible to radiation. Increased levels of ROS are a common feature in tumour environment since cancer cells have a higher metabolism and produce more ROS via mitochondrial respiration. Cancer cells adapt to this toxic environment and these adaptation mechanisms also contribute to tumour metastasis (Chen et al., 2007).

Although cancer cells have a higher capability of resisting to high levels of oxidative stress compared to normal cells, their maximum level is still limited. If cancer cells are exposed to agents that overcome that limit, they will die (Fruehauf & Meyskens, 2007).

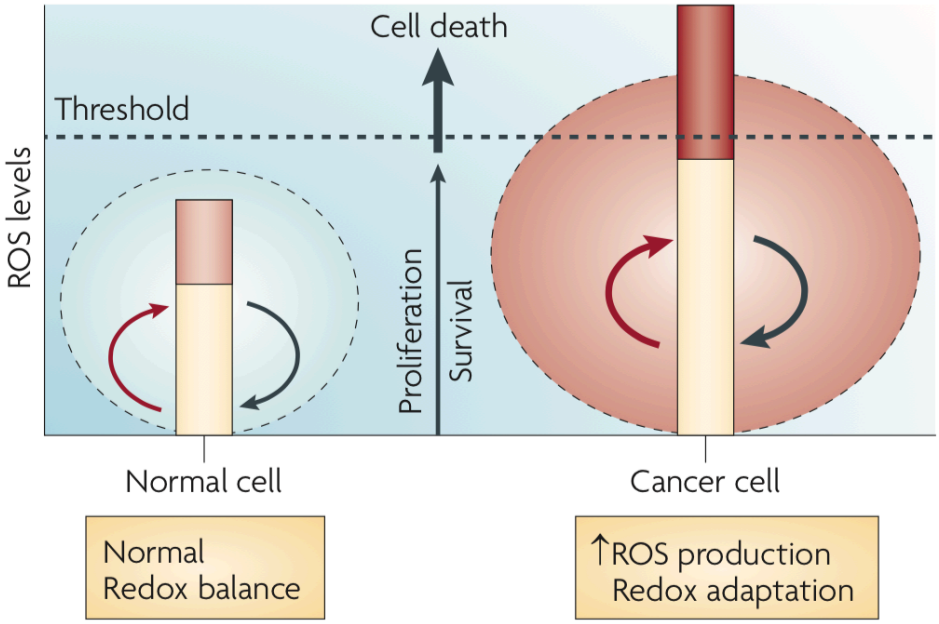

Figure 1.8: The biology of cancer redox (Trachootham et al., 2009).

Figure 1.8 presents a schematic of what happens in redox cancer cell biology. Redox homeostasis is maintained by normal cells through the balance between generation and elimination of ROS. Exogenous ROS stress can be fought through the reserve antioxidant capacity of normal cells, preventing the ROS level from reaching the cell-death threshold, showed by the horizontal dotted line in the figure. In cancer cells, ROS level is higher than in normal cells but still below the threshold, since these abnormal cells arise from a redox adaptation response that leads to an upregulation of antioxidant capacity and a shift of redox dynamics with high ROS generation and elimination. In this way, cancer cells are more dependent on the antioxidant system and more sensitive to further oxidative stress due to the proximity to the cell-death threshold. This redox characteristic of cancer cells constitutes a possibility for a therapeutic approach to defeat them, since a further increase in ROS production (red bar) will induce cell death (Trachootham et al., 2009).

Characteristics such as high metabolic rate, poor blood supply and a ‘leaky’ vascular system (Figure 1.9) lead to low oxygen regions, known as hypoxia regions. Different parts of tumour tissues present heterogeneous areas of oxygenation, where peripheral zones are higher in oxygen levels than the innermost ones (Alimoradi et al., 2017).

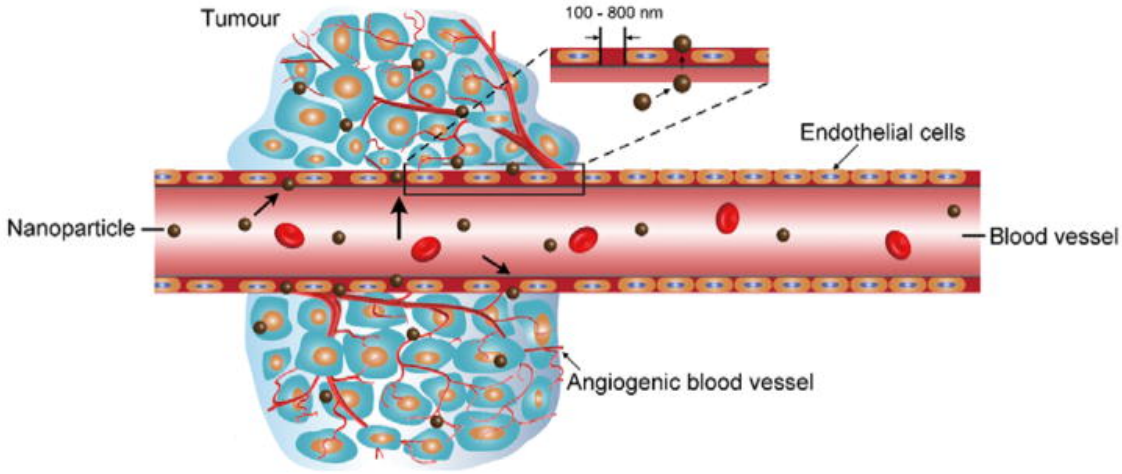

Figure 1.9: Schematic representation of tumour vasculature structure (Dai et al., 2017).

Hypoxia is a state of low oxygen levels that in tumours consists of 1-2% O_2 compared to the normal tissues (Muz et al., 2015). Tissue normoxia, also known as physoxia, is the oxygenation in healthy tissues that varies between the organs due to blood vessel network diversity and metabolic activity. Table 1.1 summarizes the oxygenation in different organs and their respective tumours. Normoxia conditions performed at the laboratory are far from the oxygen values found in healthy organs and its value in *in vitro* experiments is 20.9% O_2 (Muz et al., 2015).

Table 1.1: Comparison of the oxygenation in organ and respective tumours (Muz et al., 2015).

Tissue/Organ	Physoxia (median % O_2)	Cancer	Hypoxia (median % O_2)
Brain	4.6	Brain tumour	1.7
Breast	8.5	Breast cancer	1.5
Cervix (nullipara)	5.5	Cervical cancer	1.2
Kidney cortex	9.5	Renal cancer	1.3
Liver	4.0-7.3	Liver cancer	0.8
Lung	5.6	Non-small-cell lung cancer	2.2
Pancreas	7.5	Pancreatic tumour	0.3
Rectal mucosa	3.9	Rectal carcinoma	1.8

In these hypoxic regions cells lack molecular oxygen and other nutrients due to the unbalanced growth of the tumour cells and vascular components. Consequently, these cells do not have an adequate blood

supply. At distances more than about 150 μm from the capillary tissue, oxygen tension decreases rapidly with distance falling to a level where cell division cannot happen. Cells deprived of oxygen die, forming necrotic regions, while in the interface between the well-oxygenated and the necrotic regions viable hypoxic cells tend to occur (McKeown, 2014).

The lack of oxygen in the environment of cancer cells makes these cells more resistant to radiation damage than those in a normal oxygen environment. Due to the hypoxic environment of cancer cells, tumours are up to three times less susceptible to radiation damage than normal cells (Paterson, 1981). The reason for this is that oxygen is an important ingredient in the pathway of ROS production. This happened due to oxygen being a potent radiosensitiser in a way that it aids formation of DNA-damaging free radicals increasing the effectiveness of a given dose of radiation.

Cells use glycolysis and oxidative phosphorylation to make ATP for cellular energy. Although glycolysis is less efficient than oxidative phosphorylation, 2 ATP molecules vs 30 ATP molecules respectively, it is a faster process since production of lactate through glucose is 10 to 100 times faster than the complete oxidation of glucose in the mitochondria. Furthermore, using glycolysis to produce energy not only ensures ATP production but this process requires the pentose-phosphate pathway which additionally produces ribose sugars essential for nucleotides required for cell division. Also, this cycle produces a high amount of NADPH essential to produce fatty acids, cholesterol and regenerating gluthione antioxidants. On the whole, the amount of ATP synthesised over any given period of time is comparable between glycolysis and oxidative phosphorylation (Liberti & Locasale, 2016). Otto Warburg, in the 1920s, observed very high amounts of glucose being consumed in tumours compared to the surrounding tissue. This ‘Warburg effect’ describes the metabolism of a cancer cell to produce energy, from the predominantly oxidative phosphorylation to predominantly aerobic glycolysis. It is thought that one of the main reasons why cancer cells use this respiratory mechanism is that upregulated glycolysis constitutes a growth advantage which promotes proliferation and invasion (Gatenby & Gillies, 2004).

To overcome this limitation approaches such as hyperbaric oxygen, hypoxic cell radiosensitisers such as misonidazole and nitroimidazole, and hypoxic cytotoxins, such as tirapazamine were used without clinical success (Wardman, 2007). Hyperbaric oxygen is the oxygen released at pressures of 2-4 atmospheres to increase the oxygen in the plasma. This technique was supposed to allow the O_2 to diffuse further through tissue than normobaric oxygen breathing, since diffusion distance of oxygen through respiring tissue increases with the initial oxygen tension (Rockwell et al., 2009). Hyperbaric oxygenation demonstrates an overall positive effect on RT treatment but has not been adopted and remains to be validated as a standard treatment (Gérard et al., 2019).

More recently, hypoxia imaging during RT treatment became a technique of study. The level of oxygen present in tumour cells is cyclic, where cells that are hypoxic before RT treatment become oxygenated during or after the treatment. In this way, monitoring the oxygen level during the treatment may help if the RT fraction is given when tumour reoxygenation is expected to be at its maximum so as to optimize the oxygen enhancement ratio (Gérard et al., 2019).

Radio-enhancing NPs and new radiosensitising drugs may be delivered into the tumour to improve oxygenation. In the class of radiosensitising drugs are fluorochemicals able to dissolve considerable amounts of oxygen and deliver it through passive diffusion into the hypoxic regions (Gérard et al., 2019). Although both pre-clinical and clinical studies have shown that hypoxia can be reduced to improve the outcome of radiation therapy, hypoxic modification has still not been established as a standard treatment with RT (Horsman & Overgaard, 2016).

The need to predict and assess the patient's response to the RT treatment is of extreme importance since RT continues to be the most widely used treatment for cancer, even in conjunction with other types of cancer treatment such as surgery and chemotherapy (Jeggo & Löbrich, 2007). This would lead to an important step for the optimization of this cancer treatment.

RT can be optimized by either the use of radiosensitisers to kill the tumour cells or by radioprotectors to protect the normal tissues from radiation damage.

1.5 Radiosensitisers

The poor response of many tumours to radiation despite the improvement of techniques using conventional sources of radiation have led to the development of other approaches. Three main approaches were considered: hyperbaric oxygen, proton and neutron beams, and radiosensitisers (Paterson, 1981).

The use of hyperbaric oxygen, to increase oxygen tension during irradiation in tumour cells, has not shown an increase in tumour control rates (Henk, 1986). Radiosensitisers have become the most reliable approach since they are inexpensive and widely available and still have a whole potential to be explored.

Radiosensitisers make cancer cells more vulnerable to radiation therapy by enhancing the effect of ionising radiation within the cancer cells while leaving the healthy cells out of the target. The advantage of these materials is that since they passively or actively are conformed to the tumour site the effect of the enhanced radiation leads to an increased dose in the initial treatment within the cancer cells enabling the reduction of the number of treatments for the patient, while still achieving the initially prescribed dose.

The role of these materials can be viewed as the same as the oxygen, in the sense that they can act to restore, at least to some extent, the radiosensitivity of hypoxic tumour cells. In summary, radiosensitisers are oxygen substitutes that are capable of diffusing into hypoxic tumour cells and sensitise them via a similar mechanism to oxygen.

An important feature of radiosensitisers that relates to oxygen is that these compounds are not easily metabolised. In this way, during diffusion to tumour cells they can penetrate further into hypoxic regions (Parveen, 2001).

To define a compound as a radiosensitiser it is crucial to understand the interaction between the compound and the radiation of study. If the combination results in a biological response greater than what would be expected from the radiation by itself, than one can conclude that there is a synergistic effect behind it and the compound is classified as a radiosensitiser.

Radiosensitisers can perform through different mechanisms in order to apply their radiation-enhancing effects. Some of the possible mechanisms of radiosensitisation are (Gill & Vallis, 2019):

1. Inhibition of post-irradiation cellular repair processes: being DNA a critical target for ionising radiation the inhibition of its damage repair pathways will contribute to an increase in radiotoxicity;
2. Cell-cycle dysregulation: compounds that are able to arrest the cell-cycle at a specific phase can be considered radiosensitisers. For example, cells in late G1 or G2/M phases are more sensitive to the effects of radiation while cells in S phase are the most resistant;
3. Radiosensitivity enhancement in hypoxic cells: the radioresistance of hypoxic cells makes it difficult the generation of ROS by ionising radiation. Oxygen-mimetic sensitisers help the increase in ROS in these cells, enhancing the efficacy of the treatment;
4. Production of cytotoxic substances: Radiolysis of the sensitiser produces cytotoxic molecular fragments which in turn contribute to cell-death;
5. Generation of Auger electrons near DNA: Explained in the next section, high atomic number materials after radiation exposure produce Auger electrons due to inner-shell ionization. If the X-rays energy matches the K-shell energy of its electrons, these materials, when internalised by the tumour cells, will enhance the tumour-absorbed dose. This phenomenon may enhance the radiobiological effects of ionising radiation and potentially explains sensitisation by heavy-metal nanomaterials.

Table 1.2 summarises some examples of radiosensitiser for each of the mechanisms stated.

Table 1.2: Example of radiosensitiser for each radiosensitisation mechanism.

Radiosensitisation mechanism	Example of radiosensitiser	Function	Reference	Current status
1	PARP inhibitor olaparib and ATR inhibitor VX-970	Prevent SSB breaks repair and increase IR-damage DNA damage	Verhagen et al., 2015 Fokas et al., 2012	FDA approved Clinical trial – NCT03718091
2	LY2606368 and SRA737	Specific inhibitors of the checkpoint kinases	King et al., 2015 Sen et al., 2019	Clinical trial – NCT03414047 Clinical trial – NCT02797977
3	Nimorazole	Mimic the effect of oxygen in radiochemical process	Overgaard, 2007	Clinically used
4	DTP348	Hypoxia-selective cytotoxicity	Aspatwar et al., 2018	Clinical trial – NCT02216669

5	AGuIX and NBTXR3	Enhanced absorbed dose	Lux et al., 2018 Bonvalot et al., 2019	Clinical trial – NCT03818386 Clinical trial – NCT03589339

Physicochemical properties such as, for example, size, shape, coating, and functionalization, control their pharmacokinetics, bioavailability, biodistribution, as well as targeting and intracellular delivery. Tumour vasculature is more leaky than normal vasculature, allowing small particles and larger drugs to enter the tumour environment. Furthermore, the lymphatic drainage of tumour tissue is less efficient than in normal tissues, meaning that particles are not easily removed. Together, these two factors constitute the Enhanced Permeability and Retention (EPR) effect. Thus, specific tumour targeting can be achieved by passive targeting via the EPR effect, active targeting by using high-affinity targeting-molecules, and stimuli-responsive triggered release to endogenous or exogenous stimuli (Liu et al., 2018).

Studies have shown a general relationship between the efficiency of sensitisation and the electron affinity, i.e. oxidizing abilities for chemical radiosensitisers (Adams et al., 1971). Hypoxic cell radiosensitisation happens when one electron is transferred to the radiation-induced lesion, resulting in the fixation of the chemical damage. A lot of studies regarding chemical radiosensitisers have been done (Candelaria et al., 2006; Wardman, 2007) and are still being undertaken (Farhood et al., 2019; Wang et al., 2018).

This thesis is focussed on metal-based radiosensitisers with a diameter within the nanometer range (nanoparticles). When an incoming high-energy X-ray photon encounters heavy-metal atom, two important phenomena occur: ejection of photoelectrons and ejection of Auger electrons, as shown in Figure 1.10.

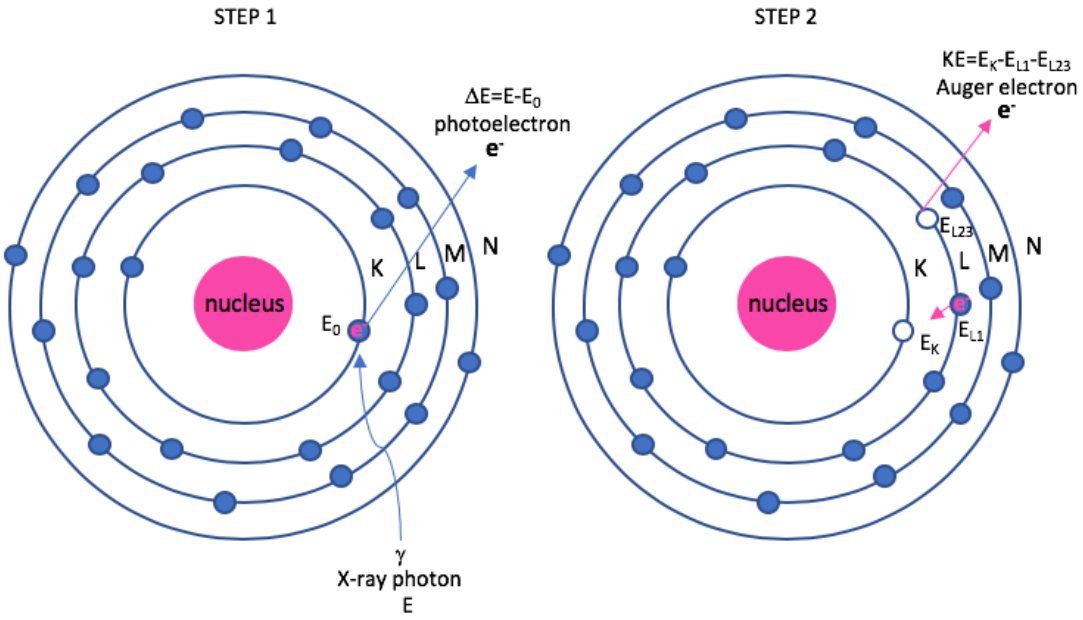

Figure 1.10: Photoelectron and Auger electron schematic in an atom. Step 1: emission of a photoelectron with a kinetic energy (ΔE) equal to the difference in energy between the incoming photon (E) and the binding energy of the electron in the K-shell (E_0); Step 2: emission of a Auger electron with a kinetic energy (KE) equal to the difference in energy between the binding energy of the electron in the K-shell (E_K) and the binding energies of the electrons in the L-shell (E_{L1} and E_{L23}).

In Figure 1.10, if a high energy X-ray photon has enough energy and it is absorbed by an atom in the surface of the metal-based NP, an innermost electron will be ejected. This phenomenon is the photoelectric effect and it results in the ejection of a photoelectron with a kinetic energy equal to the difference in energy between the incoming photon and the binding energy of the electron in the K-shell. An electron from a higher energy state, in this case, the L-shell, will then occupy the empty state in the K-shell. From this transition an X-ray is emitted and if absorbed by another electron in the L-shell, an Auger electron is ejected. In this example, this process is termed a KLL Auger transition. The kinetic energy of an Auger electron is equal to the energy difference of the singly ionized initial state and the doubly ionized final state. The resulting kinetic energy E_{KLL} is given by $E_{KL1L2,3} = E_K - E_{L1} - E_{L2,3} - \Phi$. The term Φ comes from the electron work function and from the equation it can be concluded that the kinetic energy of the Auger electron is independent of the type and energy of the primary beam.

The energy $E_K - E_{L1}$ can be then released as a radiative decay, with emission of an X-ray and in this case an electron vacancy in the K-shell is filled by an electron from the L-shell so the characteristic energy of the emitted photon is called the K-alpha (K_a) spectral line, or as a non-radiative decay, with emission of an Auger electron and the result depends on the relative probabilities of Auger emission and X-ray fluorescence, as shown in Figure 1.11.

As it can be seen from Figure 1.11, the Auger emission is greater for lighter elements, while for heavier elements X-ray yield becomes greater. The energies and relative intensities of Auger transitions show a systematic behaviour with increasing atomic number (Z). In heavier elements, which exhibit more

energy levels, more Auger transitions are possible.

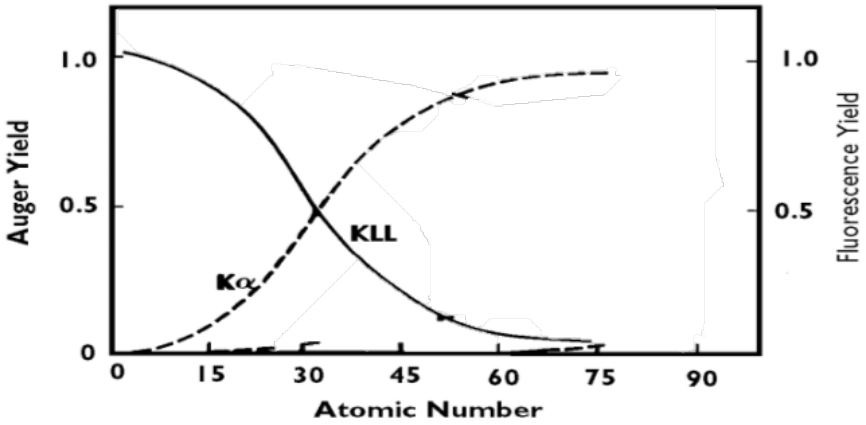

Figure 1.11: Relative probabilities of Auger emission and X-ray fluorescence. The solid lines show the Auger yield; the dashed lines show the fluorescence yield (results obtained from Reinhardt & Kern, 2008 and modified for the purpose of this thesis where irrelevant curves have been removed).

In terms of importance for the RT treatment, the fluorescent photons from X-ray fluorescence are able to travel longer ranges, up to centimetres, while Auger electrons travel much shorter distances, typically 10 nm (Hainfeld et al., 2008). This means that the former, depending on the tumour size, may not provide the desired localized tumour effect, but the latter, due to the fact that the electrons are weakly bound, they can be effective in producing very high local ionization density. For the Auger effect to be useful, the emitting atom should be close to the target molecule to damage the molecule, due to the short distance they are able to travel, although some Auger electrons can travel 50 nm in water.

In summary, photoelectrons are the result of the electrons emitted along the primary paths of the ionising radiation which induce inner shell ionization of the metal atoms, whether the Auger electrons result from the relaxation of the excited core of the metal atoms.

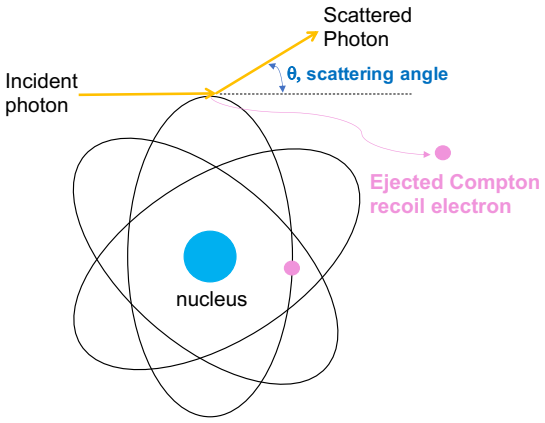

Figure 1.12: Schematic representation of Compton scattering.

Emission of Auger electrons and fluorescent photons can be caused by either photoelectric absorption or by Compton scattering. Basically, in photoelectric absorption the photon is absorbed by the photoelectron, while in Compton scattering the incident photon greatly exceeds the binding energy of the electron to the atom, so the photon does not disappear. Instead it is deflected through a scattering angle θ, as shown in Figure 1.12. Part of its energy is transferred to the recoil electron, thus the photon loses energy in the process. The energy transferred

does not depend on the density, atomic number, or any other property of the absorbed material (Cherry et al., 2004).

At a photon energy of about 100 keV or more the photon radiation beam attenuation in the target is mostly caused by Compton scattering and not by photoelectric absorption (Kljuev, 2001). The photoelectric effect varies approximately as $(Z/E)^3$, where Z is the atomic number of the target and E is the incident photon energy. For high-Z elements this effect dominates the interaction with matter at energies <0.5 MeV, while for energies >1 MeV pair production dominates (Hainfeld et al., 2008). In pair production electron-positron pairs are created if the incident photon energy exceeds twice the rest mass of the electron (2×0.511 = 1.022 MeV) and it depends on Z^2. All these physical interactions of radiation with metals made these materials a possible choice to improve the RT treatment.

Adding to the physical interactions, biocompatibility is a quality that needs to be studied since these metals will be introduced into the human body, specifically that they will need to be injected into the blood flow and reach the tumour site. Luckily, if these metals are produced in the nanometer range, it will allow them to accumulate into the cancer cells due to the leaky nature of the tumour vasculature and its lack of efficient lymphatic drainage as explained before in Figure 1.9. Relying on the EPR effect for NP delivery is a passive strategy while relying on the ligand-receptor binding is an active strategy. The later improves selective accumulation to targeted site and thus discriminates between the cancerous and healthy tissues (Attia et al., 2019).

For a metal-based NP the basic operation of the radiosensitisation process focuses on physical dose enhancement, chemical contribution and biological phase, as shown in Figure 1.13.

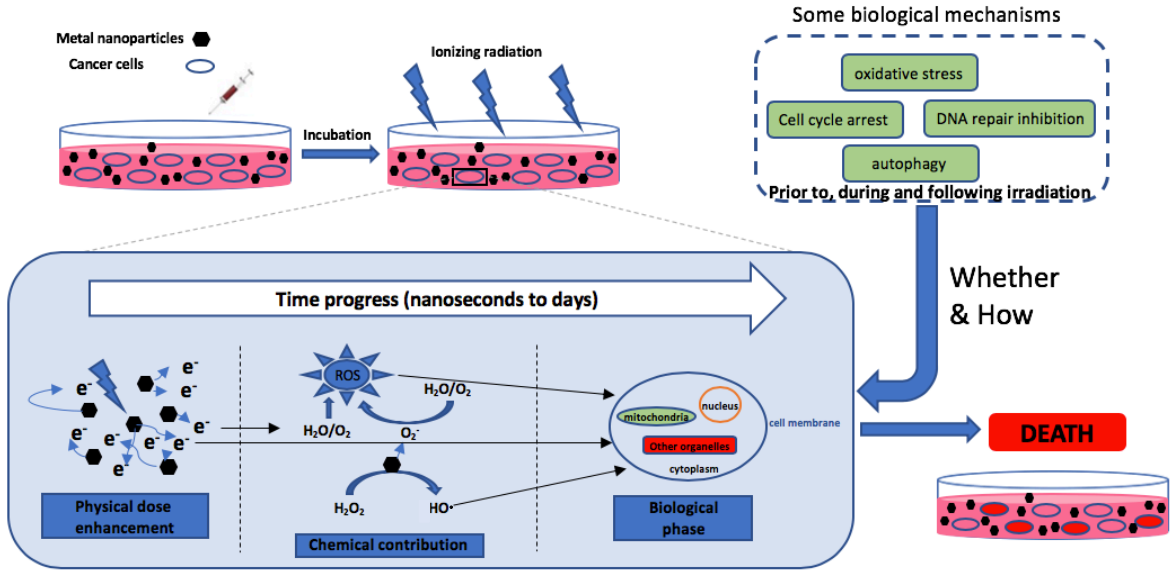

Figure 1.13: Schematic illustration of metal-based NPs radiosensitisation process (modified from Liu et al., 2018).

As illustrated in Figure 1.13, the common procedure for the study of metal-based NPs is to load them into the cells for a specific time and irradiate them (Upper-left). Biological mechanisms will happen

within the cells due to the radiation itself, the combined effect of radiation with the NP in study and also due to the NP itself (Upper-right). The basic operation of the radiosensitisation process will then lead to lethal cellular damage where the primary targets, depending on the cellular and subcellular distribution of the NPs, will include cell membrane, cytoplasm, nucleus, mitochondria, endoplasmic reticulum, and other organelles. In this way, the photoelectrons and Auger electrons produced from the combination of radiation with NPs will contribute to a dose enhancement due to the direct interaction of these species with the cells or due to the indirect interaction where these species will increase the amount of ROS damaging even more cells than the amount of ROS produced by radiation alone. Also, $HO^{\cdot}$ production occurs due to the catalytic-like mechanism/surface-catalyzed reaction present in metal-based NPs (Lower-left). These interactions produce cell damage that leads to cell death and can be probed by the number of cells that survived after a certain period of time. The combination of ionising radiation and metal-based NPs induces physical, chemical and biological mechanisms that contribute for the observed enhanced cell-killing effects (Lower-right) (Liu et al., 2018).

As mentioned before, the increase of ROS in cancer cell can exert the opposite of what it is expected from the RT treatment, such as the initiation and progression of cancer (Wu, 2006). On the other hand, increasing ROS levels can also be toxic to cancer cells which will make them more vulnerable to damage by further ROS attacks induced by external agents such as the ionising radiation used in RT (Trachootham et al., 2009).

This method is not straightforward due to the complexity of redox alterations in cancer cells. A lot of factors are involved in the redox regulation and stress response and they still need to be better understood. In this way, the simple addition of ROS may not lead to cancer cell apoptosis and the persistency of this approach may actually instead contribute to a community of cancer cells that developed an antioxidant capacity making them resistant to exogenous stress (Tiligada, 2006).

A lot of investigations have been made using radiosensitisers to cooperate with RT treatment, however, a diversity of challenges such as poor biocompatibility, lack of targeting specificity, and radiosensitisation with clinical energies, mostly MV energies, increase the need for new and optimal radiosensitisers.

1.6 Radioprotectors

Hypoxic cells may limit the response of tumours to conventional RT because of their inherent radioresistance (Kennedy et al, 1980). Although this fact constitutes one of the main limitations for this type of treatment it is not the only one.

Another main challenge of RT is the fact that tumours are located near normal tissues and organs at risk making the doses delivered to the target volumes limited. For this reason, agents that present radioprotective properties have been used to reduce normal tissue complication probability (Liu et al., 2018). These agents are called radioprotectors and have the opposite role of a radiosensitiser.

Figure 1.14 shows response curves for cancerous and normal tissues to RT. The use of radioprotection agents has the goal of increasing the separation between both curves by shifting normal tissue curve response to the right. In this way, a better control of the tumour with less damage to normal tissue is possible to be achieved. An ideal radioprotection agent is one that protects normal tissue while preserving anti-tumour effectiveness, and presents low or none toxicity (Grdina et al., 2002).

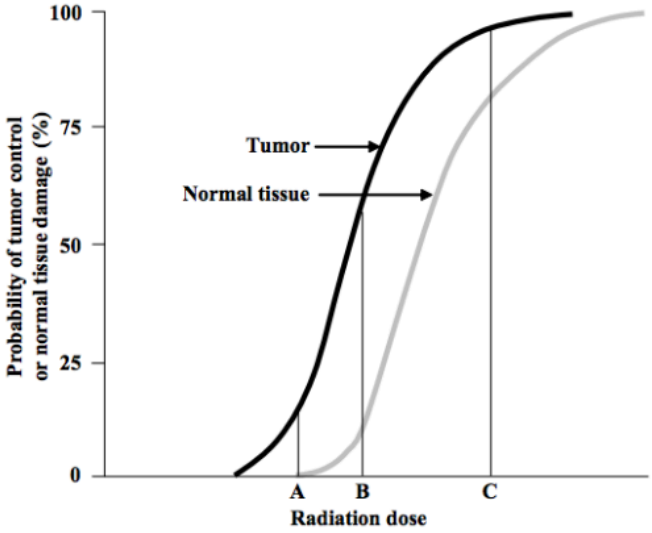

Figure 1.14: Probability of tumour control and normal tissue damage at varying radiation doses (Grdina et al., 2002).

Radioprotection can occur through different mechanisms such as suppressing the formation of reactive species, detoxification of radiation induced species, target stabilisation and enhancing the repair and recovery processes, and induction of hypoxia in the tissues (Kuntić et al., 2013).

One pathway for radioprotection is the removal of radiation-induced reactive free-radical species. Certain agents are oxidised by free radicals and form stable compounds incapable of reacting with other cellular components. Indirect damage from radiation is prevented by reducing the amount of radical species that cause damage to the normal cells. It has been demonstrated with polymers the repair through hydrogen donation. If a molecule R-H is exposed to radiation it is converted into a radical (Biaglow, 1981). Using a protective agent that can donate a hydrogen atom to this radical can restore this molecule back into its original state.

Sulfydryl compounds of the aminothiols form mixed disulfides with the sulfydryl compounds of cellular proteins and this is a mechanism proposed for aminothiols for radioprotection through this binding. If one of these disulfides is attacked by free radicals, one of the sulphur atoms is reduced and the other is oxidised. In the case of the sulphur atom of the protein being the one that is reduced, and the sulphur atom of the protective agent is oxidised, then the protein is not damaged. Therefore, the cellular proteins are protected in 50% of the cases (Varanda & Tavares, 1998).

Furthermore, radioprotectors might also prevent radiation damage by stabilising the target, such as DNA. Binding of aminothiols to DNA has been considered a potentially good pathway for radioprotection. Sulfhydryl compounds of the radioprotective aminothiols bind and stabilise those parts of DNA helix which are not covered by histones. This process reduces both primary and secondary damage, decreasing DNA replication rate so that repair processes can act before alterations are replicated (Brown, 1967).

Inducing hypoxia through oxidation of some thiols consumes enough oxygen to reduce its tension. In certain conditions, sulphydryl compounds (RSH) of the thiols may use consumption of oxygen as a mechanism for radioprotection. RSH compounds that can undergo an oxidation reaction with molecular oxygen can be good candidates for radioprotectors.

Some compounds, such as thiols, exert more than one radioprotective mechanism and depending on the irradiated system and on the specific radiation conditions they can be more or less important (Varanda & Tavares, 1998). For example, some thiols compounds exert radioprotective activity without altering oxygen tension on the tissues.

Studies of other different compounds besides thiols also have been done. Antioxidant enzymes and mimetics, like glutathione peroxidase, antioxidant nutrients, such as vitamins C and E, phytochemicals, such as herbal preparations, physiological and receptor mediated protectors, such as bioactive lipids, and nucleic acid derivatives and interactions, such as RNA preparations (Weiss & Landauer, 2009).

Apart from the group of antioxidant enzymes and mimetics, metals can be also considered radioprotectors. Different endogenous metals can alter cellular radiosensitivity in a pro-oxidant or antioxidant way. Mice injected, twenty-four hours prior to irradiation, with metals responsible for inducing metallothionein (MT), such as Cd (3 mg/kg), Mn (20 mg/kg) and Zn (10 mg/kg) showed protection against 6.3 Gy X-ray irradiation (Matsubara, 1988).

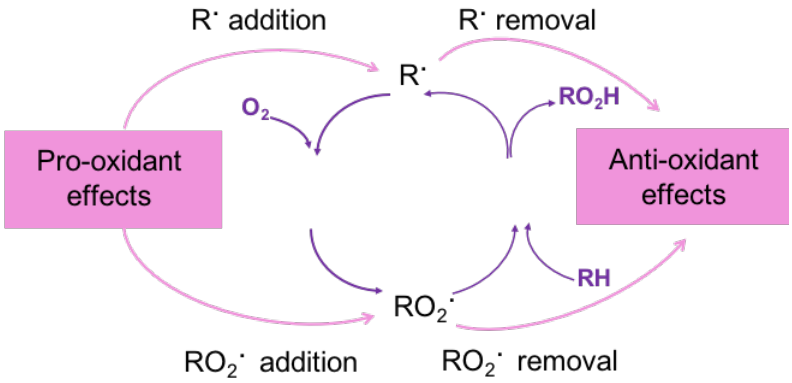

Figure 1.15: Chain reaction (modified from: Gilbert, 1963).

As shown in Figure 1.15, increasing the free-radical concentration is a pro-oxidant effect, and decreasing the free-radical concentration is an antioxidant effect. Cations can sometimes exert a pro-oxidant effect, enhancing free-radical production. For example, cations such as cobalt, manganese,

nickel and zinc increase the rate of oxidation of reduced glutathione exposed to high oxygen pressure (Gilbert et al., 1958). On the other hand, cobalt and manganese cations accelerate the decomposition of H_2O_2 and this removal can be considered an antioxidant action. Cobalt was tested in different biological systems such as peas, mice, bacteria and showed an antioxidant action against oxygen toxicity (Gilbert, 1963).

A more recent study showed a radioprotective effect of date syrup (Abou-Zeid et al., 2018). The authors pre-treated rats with date syrup by stomach intubation and then irradiated them with 6 Gy gamma-rays. They concluded that this substance was effective in reducing radiation-induced hepatotoxicity, oxidative stress, inflammatory response, and DNA damage. Due to these results, date syrup can be a potential supplement in the RT to protect normal cells from the toxic effects of radiation.

Amifostine was the only compound that has been officially approved for human use, but it still presents significant toxicity (Kuntić et al., 2013). Cerium oxide (CeO_2) NPs are a type of metal oxide NP that are known for its radioprotection effects. These NPs offer protection against radiation induced damage in different tissues due to its potential as a biological free radical scavenger or antioxidant (Baker, 2013).

Still a lot of investigation needs to be done to find a good radioprotector, but toxicity and inability to differentiate between normal and cancer cells are the main reasons for their failure in clinical applications. For this reason, a compound with the ability to protect only normal cells and to differentiate tumour cells is ideal for a radioprotector and so these compounds need to be modified by taking advantage of the difference in oxygen levels between normal cells and tumour cells as well as their associated biochemical characteristics (Nair et al., 2001).

1.7 Gold NPs as radiosensitisers

A study showed that 1.9 nm gold (Au) NPs, through intravenous injection, in combination with 250 kVp X-rays resulted in eradication of most tumours in mice, while the mice with no irradiation or gold only treatment died within 15 days, as it can be seen from Figure 1.16 (Hainfeld et al., 2004). This study introduced a new perspective to the use of metal NPs, especially gold.

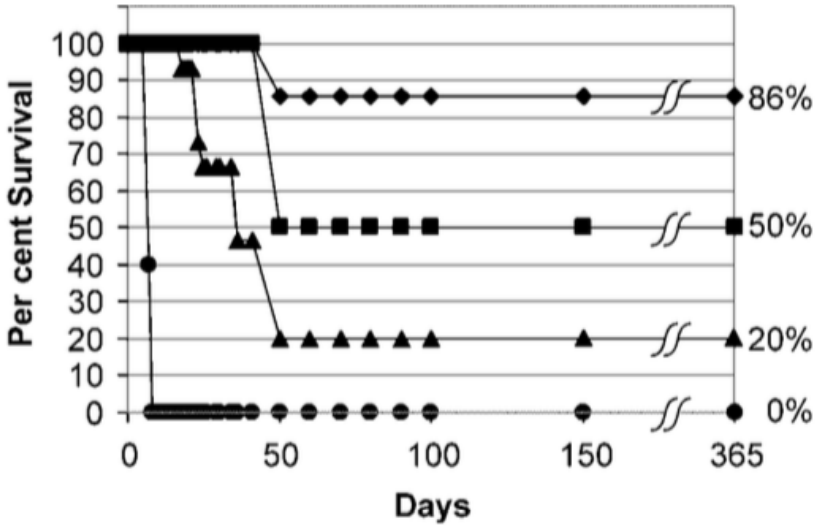

Figure 1.16: Plot of mice survival after various treatments of subcutaneous EMT-6 tumours; Circles: no treatment (n=17), and gold only (1.35 g Au/kg, no irradiation), indistinguishable from no treatment (n=4); triangles: irradiation only (26 Gy, 250 kVp), producing 20% long-term (> 1 year) survival (n=15); squares: irradiation after i.v. injection of 1.35 g Au/kg gold NPs, 50% long-term survival (n=4); diamonds: irradiation after 2.7g Au/kg injection producing 86% long-term survival (n=7) (Hainfeld et al., 2004).

Au NPs have the following advantages (Hainfeld et al., 2008):

- Biocompatibility;
- Absorbs energy 3 times more than iodine at 20 and 100 keV;
- Can be cleared from the blood slower than small molecules enhancing tumour delivery;
- Provide tumour specificity through EPR effect;
- Can be made over a wide range of sizes (1-1000 nm);
- Have different surface ligands, thiols (S-R) or phosphorous (P-R), allowing multifunctionality for optimal properties.

Surface characteristics and size are two very important features easy to modify in Au NPs that can have very important outcomes regarding toxicity and uptake. Using for example a sulphur-polyethylene glycol (PEG) as coating of Au NP can prevent reticuloendothelial system uptake and the overall size will also be a strong factor for blood retention time, as well as the surface coating.

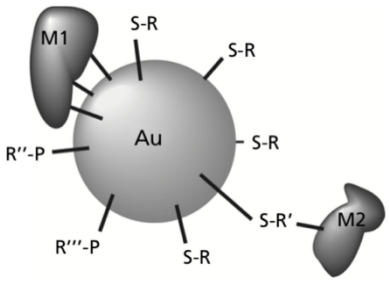

Figure 1.17: Diagram of a Au NP with ligands (Hainfeld et al., 2008); S-R and P-R represent sulphur (S) or phosphorus (P) atoms, respectively, attached to a functional group (R); M1 and M2 represent molecules attached by ionic and covalent interactions, respectively.

Surface atoms have a covalent-strength binding affinity with sulphur (S-R) or phosphorus (P-R) atoms, so various functional groups such as PEG, carboxyl or amino groups, thiol derivatized drugs, DNA, lipids, and carbohydrates are easily attached, as shown in Figure 1.17. Through covalent bounds with this functional groups, antibodies or peptides can be included on Au NP surface, as represented in the figure by M2. Another possibility is adsorbing

molecules directly, which may not contain free thiols or phosphorus atoms, but can adsorb onto gold surface by ionic or hydrophobic interactions at multiple sites, as shown in the figure by M1.

A very important characteristic to consider is the size of the NP which can have a major impact in its characteristics. The size of the NP will influence the number of ligand sites that are possible to have. For the same ligand smaller NPs will have a lower number of ligand sites than larger ones (Hainfeld et al., 2008). Furthermore, small particles are rapidly clear through kidneys, whereas larger ones will not go through kidney filtration.

Regarding the colour, it is the surface plasmon resonance (SPR) effect that gives the colour to gold particles at nanosizes. Depending on the metal, SPR bands will vary according to the spectral region. For example, gold, silver and copper NPs have strong SPR bands in the visible region, while other metals show broad and weak band in the UV region (Huang & El-Sayed, 2010).

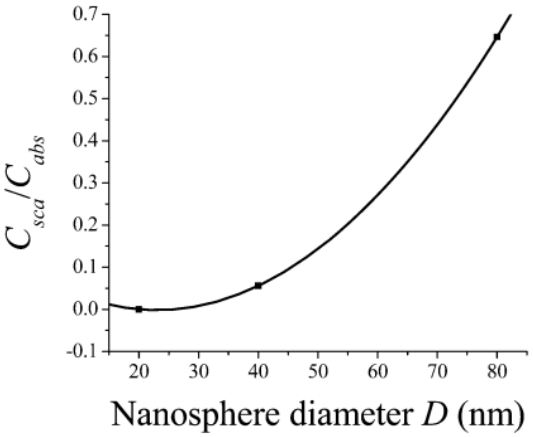

Figure 1.18: Ratio of scattering to absorption of NPs with nanosphere diameter (Jain et al., 2006).

Light absorption and scattering are strongly enhanced by SPR effect. As the nanosphere diameter increases, the relative contribution of scattering to the total extinction C_{sca}/C_{abs} increases, as seen from Figure 1.18. This feature can be useful for the choice of Au NPs for biomedical applications. While larger NPs will be more suitable for imaging due to their higher scattering efficiency, smaller ones would be more useful for photothermal therapy, since light is mainly absorbed by the particles and thus efficiently converted to heat for cell and tissue death (Huang & El-Sayed, 2010).

Chemisorption energies for oxygen are shown in Figure 1.19 for some transition metals (Bligaard et al., 2004). The more negative the oxygen chemisorption energy value, the easier the metal surface oxidation. Basically, gold is the only metal with an endothermic chemisorption energy meaning that this metal does not bind to oxygen at all, being inert in an oxygen atmosphere.

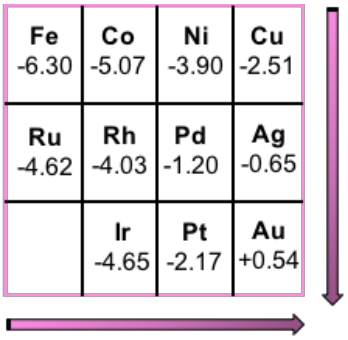

Figure 1.19: Dissociative chemisorption energies for oxygen on transition metal surfaces with respect to a molecule in vacuum (modified from Hvolbæk et al., 2007).

In this way, despite the fact of gold being chemically inert, when down to the nanoscale, Au NPs surface presents catalytic activity (Haruta et al., 1987). When adding these particles into RT treatment, not only the effect of the direct interaction with radiation will be present, where photoelectric, Compton and pair-production will play a role, but also the effect of ROS interaction with their catalytically active solid surface. The reacting molecules adsorb onto Au NPs surface, where they are fragmented, and new bonds are formed on the surface. The products can be released back into the liquid or gas phase. Using these materials results in a large contact area between the active material of the catalyst and the surrounding gas or liquid phase (Hvolbæk et al., 2007).

The relative effect of gold (Z=79) to soft tissue (Z=7.4) in the energy range above gold's K-edge, 80.75 keV, is $79^3/7.4^3=1217$, which is a very large contribution of this metal's photoelectric effect. Regarding pair production, the relative effect of gold to water is $79^2/7.4^2=114$. For gold, pair-production may have some contribution for photons produced by a 10 MeV LINAC, but photoelectric effect contribution in beams with those energies is lost (Hainfeld et al., 2008). From Figure 1.20, it can be seen that in the range of MeV energies used in current RT treatment the ratio of absorption between gold and water becomes theoretically negligible (Mesbahi, 2010).

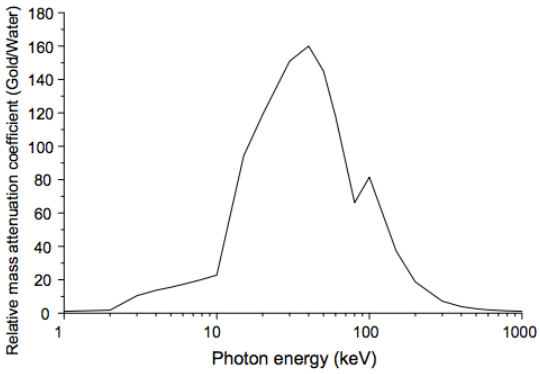

Figure 1.20: Variation of relative mass attenuation coefficient of gold to water with photon energy (Mesbahi, 2010).

Although in theory radiosensitisation of gold should be lost at megavoltage energies, some experimental studies showed that the photon interaction with matter produces Compton electrons with a spectrum of energy which have higher absorption coefficient with Au NPs compared to the surrounding biological medium (Mesbahi, 2010). For example, an improvement in dose enhancement for megavoltage X-rays was seen if the flattening filter (FF) was removed (Robar et al., 2002; Cho, 2005). A FF is a metal filter placed into the radiation beam to even out the dose across the irradiation area. However, it also removes the lower energy X-rays. The dose enhancement seen by Robar *et al.* makes sense, since the removal of the filter allows lower energies to pass and to contribute more for the photoelectric effect of the high-Z materials.

These controversial results led to further investigation. Through Monte Carlo simulations the dose enhancement due to the use of Au NPs for different radiation treatments with and without FF and different NP concentrations was quantified (Cho, 2005). The study showed that without the FF the dose enhancement factor (DEF), which represents the ratio of the dose deposited in tumour with NPs and

the dose deposited in the tumour without the NPs, for the maximum Au NP concentration used of 30 mg Au/g tissue using 6 MeV, was of 1.053, whereas with the FF the DEF was of 1.025.

Other studies showed enhancement for megavoltage X-rays. Using 50 nm Au NPs, it was showed in a cervical cancer cell line (HeLa) evidence of enhancement of radiation sensitisation at clinically relevant X-ray energies (6 MeV) with a radiation enhancement factor of 1.17, where the measured effect exceeded the theoretically predicted dose enhancement (Chithrani et al., 2010). For a human breast carcinoma cell line (MDA-MB-231), using 1.9 nm Au NPs and a concentration of 12 μM, it was observed with 6 and 15 MV photons a sensitizer enhancement ratio (SER) of 1.29 and 1.16, respectively (Jain et al., 2011). In addition, this study also showed that sensitization was cell specific, not occurring in human prostate adenocarcinoma cell line (DU145) or in lung epithelial carcinoma cell line (L132), for either keV or MeV energies despite Au NP uptake occurring in these cell lines.

These observations lead to different answers for the explanation of the radiosensitisation found for Au NPs since the theory due to the lack of contrast between tissue and gold predicts no radiation enhancement at MV energies. It was suggested through the use of the Local Effect Model (LEM) that Au NPs radiosensitisation is driven by dose inhomogeneities on the nanoscale rather than changes in dose over the entire cell (Stephen J. McMahon et al., 2011). This phenomenon may contribute to the similar radiosensitisation observed in megavoltage and kilovoltage experiments. The study showed high energy concentrations in the vicinity of the Au NPs due to the high production of low-energy secondary electron after gold ionisations, resulting in highly inhomogeneous dose distributions on the nanoscale, as shown in Figure 1.21. As in the kV range, MV energies can generate single ionisations in Au NPs that can deposit high doses in the surrounding water volume because of the cascade of low-energy secondary electrons generated after the ionising event in gold (Stephen J. McMahon et al., 2011).

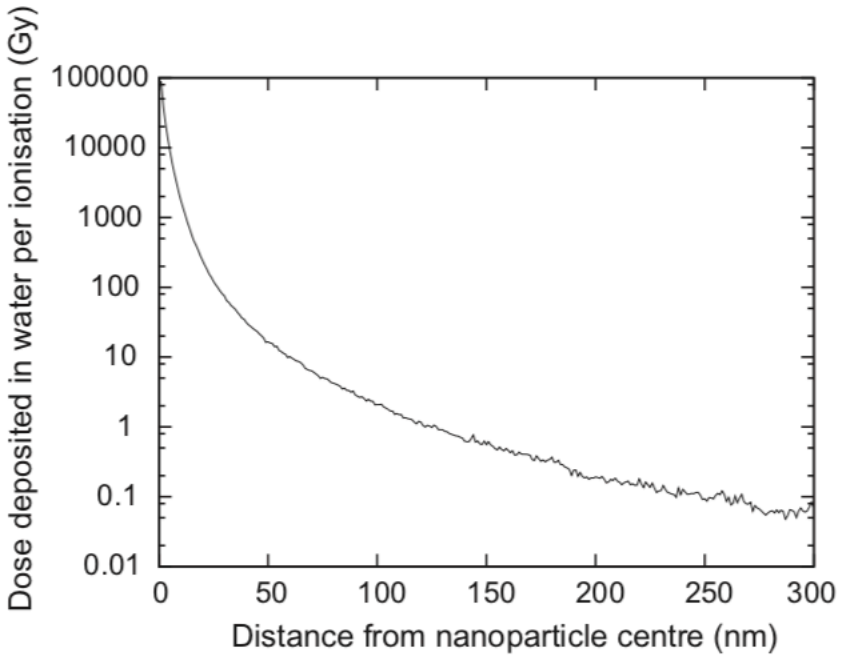

Figure 1.21: Average radial dose deposited following a single ionising event in a 2 nm Au NPs during a 6 MeV LINAC irradiation (Stephen J. McMahon et al., 2011).

As mentioned before, Au NPs at the nanoscale present catalytic activity. A study demonstrated that Au NPs showed intrinsic catalytic activity toward H_2O_2 decomposition and superoxide scavenging (He et al., 2013). It was observed that the generation of radical species such as hydroxyl radicals and oxygen was strongly dependent on the pH, where lower pH was needed for $HO^{\cdot}$ formation and higher pH for O_2 (He et al., 2013).

Metal NPs may be good candidates to improve RT treatment and so their study under hypoxic conditions is crucial since tumour cells live under these conditions. Investigation towards the understanding of Au NPs behaviour under hypoxic conditions showed that for MCF-7 and HeLa cells the highest uptake following prolonged exposure under 0.2% of oxygen was for NPs of 50 nm size (Neshatian et al., 2014). A concentration of 0.6 nmol of NPs was used and it was showed that NP uptake of the cells pre-exposed to hypoxia for 18 h was in average 1.5 times higher than the one of cells under normoxic conditions. The stability of the NP size was measured under normoxic and hypoxic conditions for 24 h and it was concluded that NPs are stable under both conditions.

Conflicting results regarding the performance of Au NPs under hypoxic conditions show that more research under cancer cells environmental conditions is needed. A study reported that actually the Au NP uptake was significantly lower under hypoxic than oxic conditions (Jain et al., 2014). In this case cell lines such as DU145, MDA-MB-231 and L132 cells were exposed to a concentration of 12 μM of 1.9 nm Au NPs. Both the DU145 and MDA-MB-231 cell lines showed that a higher reduction in cell growth induced by Au NPs in hypoxia than in normoxia, but for L132 cells the growth inhibitory effects were similar under both conditions. Regarding radiosensitisation using 160 kV X-rays, for MDA-MB-231 cells the SERs were similar at 21% and 1% oxygen concentration, 1.41 and 1.39, respectively, but was much lower at 1.1 for 0.1% oxygen. It was suggested that the lower radiosensitisation observed under hypoxia was due to the reduction in Au NPs cellular uptake. No significant radiosensitisation occurred in DU145 or L132 cells in 0.1% or 21% oxygen conditions.

Another important question is whether the localisation of the NPs should be within the cell to provoke its apoptosis. It is generally assumed that NPs have to be inside the cell nucleus, where the most important constituent is (the DNA) to destroy cancer cells. However, it was seen through experimental studies that Au NPs are mostly taken up into the cytoplasm of the cell and still show radiosensitisation effects (Chithrani et al., 2010). For example, mitochondrion can be a good target since is responsible for many important functional roles in the cell such as energy metabolism, apoptosis regulation, ROS production, and cell signalling. Through Monte Carlo simulations, a study showed that although Au NPs tend to be within the cytosol, physical dose enhancements are not restricted to the vicinity of the NPs and can extend to the nucleus and to the mitochondria, contributing in this way to NP dose enhancement effects observed experimentally (McNamara et al, 2016).

The mechanism, through which Au NPs increase cell killing and DNA damage with X-rays, is still unknown. Using 1.9 nm Au NPs at a concentration of 500 μg/ml, MDA-MB-231 cells were irradiated with 1.5 Gy X-rays of photon energies between 10 keV to 60 keV (McQuaid et al., 2016). The energy

range used in the study was justified by the fact that, although is much lower than the clinical energies use in RT treatments, a large proportion of X-rays produced by a LINAC are in the low keV energy range. For instance, 10% of a 6 MeV LINAC beam spectrum is made up of photons with energies less than 200 keV (please refer back to Fig. 1.4). The results suggest a different interaction between Au NPs and DNA molecules, due to the paradox of increased cell killing with little evidence of the increase in short term DNA damage. It was concluded that other mechanisms are responsible for cell death at lower X-ray energies, so photoelectrons can be playing a less effective role than it was thought. Furthermore, according to the prediction of LEM, Auger electrons are the predominant source of dose enhancement. Considering their short range, within several hundred nanometres from Au NP surface, and the localisation of the NPs within the cell but outside of the cell nucleus, nuclear DNA is consequently outside the range of the majority of these particles, which means that there must be a different target to provoke the cell damage observed with the use of Au NPs with radiation. Studies have been focusing on finding the target responsible for the radiosensitisation seen with Au NPs and the results suggest mitochondria as the main target (McMahon et al., 2017; Ghita et al., 2017).

More recently, a study aimed to identify other mechanisms than the physical assumptions alone for the radiosensitisation measured with Au NPs found a biological mechanism that might be behind this enhanced radiation-induced cell death (Taggart et al., 2016). Au NPs were found to inhibit the enzyme protein disulphide isomerase, an important enzyme for correct folding of proteins in the endoplasmic reticulum and for the formation of glutathione antioxidant. Inhibition of this enzyme can lead to cell stress and make cells more susceptible to radiation-induced ROS damage.

The controversial results concerning Au NP radiosensitisation can be originated from the differences in performed investigations in terms of key parameters including Au NP size, shape, and concentration, type of cell lines, and radiation source.

Although a promising candidate for the improvement of RT treatment there are still crucial unknown phenomena underlying Au NPs radiosensitisation due to the lack of agreement between theoretical and experimental evidence.

1.8 Metal oxides as radiosensitisers

Different types of metals have been considered to explore radiation dose enhancement in tumours. Theoretical research, using Interactive Data Language (IDL) program to solve the equation for DEF, was made exploring materials with atomic numbers ranging from 25 to 90 and showed, for 6 MV X-rays and a NP density of 5 mg/ml, a DEF range from 1.004 to 1.007 (Roeske et al., 2007).

Elements such as manganese, copper, iron and zinc have crucial roles as co-factors in various proteins and enzymes, such as catalase (CAT), superoxide dismutase (SOD), cerulo-plasmin and metallothionein (Weiss & Landauer, 2009). Although it is probable that antioxidant enzymes, such as glutathione peroxidase, manganese SOD (MnSOD), copper-zinc SOD, and CAT, are important in

providing protection from radiation exposure, the proper balance of the enzymes in specific cells and in the whole organism required for maximum radioprotection is not understood yet. For example, a large increase in Mn-SOD in some model systems may have a radiosensitising effect rather than a protective effect, probably related to the inability of the cell to cope with overproduction of hydrogen peroxide or hydroxyl radicals (Weiss & Landauer, 2006).

Not all the NPs used in this thesis have been considered for RT, although research has been made with some of them for the purpose of improving this type of cancer treatment:

Iron-based NPs: radiosensitisation of this metal NPs has been attributed to the production of ROS, owing to their surface-catalysed Haber-Weiss cycle and Fenton reaction, compensating in this way their low atomic number of 26 (Klein et al., 2012). Iron NP surfaces catalyse in aqueous solutions H_2O_2 through the Haber-Weiss cycle which starts via the superoxide-driven reduction of Fe^{3+} to Fe^{2+} and results into the formation of highly reactive $HO^{\cdot}$ (Voinov et al., 2011). A study showed superparamagnetic iron oxide NPs (SPIONs) radiosensitisation effect through their incubation in MCF-7 cells for 24 h at a concentration of 0.1 mg Fe/mL after irradiation with 120 kV X-rays at a dose of 3 Gy (Klein et al., 2012). Human Alveolar Basal Epithelial Adenocarcinoma cell line (A549) irradiated with 5 Gy and incubated for 24 h with uncoated Fe_3O_4 NP systems and a concentration of 500 μg/ml, showed a significant increase in ROS production when compared with radiation alone (Hauser et al, 2016).

The iron-catalysed Haber-Weiss reaction, which makes use of Fenton chemistry, is considered the main mechanism by which the highly reactive radical is generated in biological systems (Hauser et al, 2016):

$$\text{Fenton chemistry: } Fe^{2+} + H_2O_2 \rightarrow Fe^{3+} + HO^{-} + HO^{\cdot}$$

$$\text{Haber-Weiss reaction: } O_2^{-} + H_2O_2 \rightarrow O_2 + HO^{-} + HO^{\cdot}$$

Under normal conditions, only traces of iron exist in proteins such as transferrin or ferritin. Proteins take up Fe ions in a way that the circulating Fe ions bind to transferrin and accumulate in the cells in the form of ferritin. Iron absorption is controlled to prevent excess storage or oxidative attack. The uptake of iron NPs can increase the intracellular unbound iron, resulting in cell damage or death, especially when combined to additional therapies. Cell uptake of iron oxide NPs enhances ROS production through two different pathways: release of Fe ions into the cytosol where chelation by citrate (CIT) or adenosine phosphate takes place, resulting in the iron ions participating in the Haber-Weiss cycle; or the surface of the NP may act directly as a catalyst for the Haber-Weiss cycle and the Fenton reaction. Via these pathways formation of hydroxyl radical occurs (Hauser et al, 2016).

Only a few formulations of SPIONs have been approved for clinical uses due to insufficient tissue selectivity, low drug loading capacity, and lack of control over their biodistribution (Revia & Zhang, 2016).

Hafnium-based NPs: due to their high atomic number (Z=72) and chemical stability, a type of 50 nm-sized functionalised hafnium oxide NPs called NBTXR3, with a negative surface charge has been used

for clinical trials (Liu et al., 2018). For HT1080 fibrosarcoma cell line a DEF of 1.4 was achieved for 6 MV X-rays at 4 Gy and a concentration of 64 g/l of NBTXR3 NPs (Maggiorella et al., 2012). This type of HfO_2 NPs has been design for direct local intratumoural injection and to be activated by RT (Pottier et al., 2014). Research with NBTXR3 NPs showed that, for different human cancer cell lines and different X-ray energies, radioenhancement increased with both NP concentration and radiation dose (Marill et al., 2014).

Titanium-based NPs: this metal has shown application in photocatalytic chemistry. Its mechanism of action involves generating ROS upon photoexcitation by UV radiation (at energies less than 10 eV), but since UV radiation has limited tissue penetration these NPs are less effective for deep tissues (Kwatra et al, 2013). To make titanium NPs more susceptible to X-ray based stimulation, TiO_2 NPs are often combined with gadolinium or other rare earth metals (Kwatra et al, 2013).

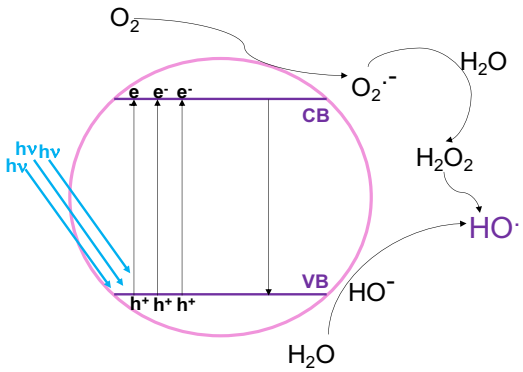

Figure 1.22: General mechanism of the photocatalysis. VB - valence band; CB – conduction band.

TiO_2 is the most-studied photocatalyst because of its ability to oxidize a large number of organic compounds into harmless compounds such as carbon dioxide and water using ultraviolet light, and potentially, visible-light (Fujishima & Zhang, 2006). Photocatalysts such as titanium rely on the electron (e^-) transition between the valence and conduction band, as shown in Figure 1.22. When an e^- makes a transition from the valence to the conduction band it leaves a hole (h^+) in the valence band. For TiO_2 NPs, both species, e^- and h^+, can then further generate free radicals at the NP surface, as shown in the following equations (Wong & Chu, 2003):

Equation 1: $TiO_2 + h\nu \rightarrow TiO_2 (e^- + h^+)$

Equation 2: $h^+ + OH^- \rightarrow HO\cdot$

Equation 3: $e^- + O_2 \rightarrow O_2^-$

The highly oxidizing positive hole has been considered to be the dominant oxidizing species contributing to the photocatalytic activity of TiO_2 (Wong & Chu, 2003). Photocatalytic activity of TiO_2 has been extensively studied (Nosaka et al., 2014).

TiO_2 is only toxic in the presence of UV radiation and so using HepG2 cells a study compared the cytotoxic and genotoxic potential of non-irradiated and UV pre-irradiated TiO_2 NPs for two sizes of particles <25 nm and >100 nm (Petković et al., 2011). This study showed that, independently of the particle size, UV radiation increases the cytotoxicity and the genotoxicity of anatase TiO_2 NPs, and in particular, oxidative DNA damage. The authors concluded that generation of ROS after irradiation was

the main mechanism responsible for the observed toxic effects, since UV radiation has enough energy to excite electrons from the valence band to conduction band (see Figure 1.22), resulting in the formation of highly reactive electron-hole pairs. In an aqueous environment, electrons reduce oxygen to give superoxide anion radicals, which can be dismutated to H_2O_2, while holes oxidize water to give hydroxyl radicals, as shown in Figure 1.22. Also, an interesting finding in this study was the fact of TiO_2 NPs to remain activated, i.e. in the excited stage, even after irradiation was discontinued, which can explain their higher toxic and genotoxic potential compared to the non-irradiated NPs.

For TiO_2 NPs coated with a dye it was found that visible-light activates the NPs leading to degradation of plasmid DNA *in vitro* (Blatnik et al., 2012). An *in vivo* study demonstrated the efficacy of TiO_2 NPs for RT when these particles are doped with rare earth elements after irradiation with 200 kV X-rays (Townley et al., 2012). Human glioblastoma cell lines, SNB-19 and U87MG, internalized with titanium oxide nanotubes (TiONts) showed no cytotoxicity and decreased DNA repair efficiency after irradiation as well as amplified G_2/M cell-cycle arrest (Mirjolet et al., 2013). In this study, cells were incubated with a concentration of 1 μg/ml of TiONts for 24 h and irradiated with 10 Gy by a linear photon accelerator (clinac600 Varian).

A study on titanium-based NPs to use them for deep-tumour treatments concluded that titanium peroxide NPs (TiOxNPs) could be used to optimize pancreatic cancer therapy. TiOxNPs were tested in a human pancreatic cancer model both, *in vitro* and *in vivo,* and the results showed a high ROS production upon 150 keV X-rays irradiation (Nakayama et al., 2016).

Zinc-based NPs: a semiconductor material with a broad range of applications with a very low risk to human health. A great advantage of this type of NPs is their ability to absorb a wide range of the visible spectrum due to its wide band gap energy. This results in fast recombination of photogenerated charges and thus leads to a low photocatalytic efficiency (Lee et al., 2016). ZnO NPs have the ability to respond to ionising radiation since they exhibit scintillation upon excitation with X-rays. The induced radioluminescence results from the excitation of fluorescent centers by energy conversion taking place in the semiconductor NP. Such as for TiO_2 NPs the production of ROS will follow Equations 1, 2 and 3 (Lee et al., 2016). ZnO NPs induce cell death through their ability to form ROS (Bogdan et al., 2017).

ZnO NPs were investigated and to ensure chemical stability of an atmospheric zinc oxide core, the particles were coated with a silica layer (Generalov et al., 2015). Two human prostate adenocarcinoma cell lines, LNCaP and DU145, were exposed to 200 kV X-ray radiation after incubation of ZnO/SiO_2 NPs. The results demonstrated a radiation enhancement due to the NPs with an enhancement ratio of 1.97 for LNCaP cells and one of 1.19 for DU145 cells. It was concluded that the radiosensitising effect of the NPs was due to the X-ray induced catalysis at the NP surface.

ZnO NPs with a diameter less than 100 nm are relatively biocompatible, can additionally be used for drug delivery, and show anticancer activity by inducing apoptosis and autophagy (Jiang et al., 2018). For example, regarding apoptosis, ZnO NPs promote cancer cell death due to the intracellular release of zinc ions. This leads to an increase in ROS induction and subsequent cell death mediated by the

ROS triggered mitochondrial pathway. This process happens because the mitochondrial electron transport chain is associated with intracellular ROS generation. Excessive ROS production damages the mitochondria resulting in the release of cytochrome C that triggers intrinsic apoptosis (Jiang et al., 2018).

Different approaches have been used with metal-based nanomaterials to avoid radioresistance induced by tumour hypoxia. One of the approaches is through the generation of O_2 *in situ*. Due to the overproduction of hydrogen peroxide within malignant tumours, the approach of O_2 generation *in situ* via catalysing intracellular H_2O_2 provides a new way to provide continuous O_2 release in tumour cells (Chenyang et al., 2019). Manganese dioxide (MnO_2) is an excellent catalyst for decomposing H_2O_2 into O_2 within the tumour environment (Zhu et al., 2016). MnO_2 in the form of nanosheets (NSs) has high surface-to-volume ratio, which allow easy contact between the reactant molecules and the active sites, thus providing enhanced catalytic activities (Wu et al., 2019). Fan et al., (2015) explored MnO_2 NSs that can be reduced to Mn^{2+} by acidic H_2O_2 in solid tumours, improving radiosensitisation under hypoxia conditions through ROS generation.

Another approach is the use of nano-radiosensitisers with diminished oxygen dependence for hypoxic-tumour RT. In this way, the possibility of a radiosensitiser that could generate ROS without the use of oxygen was studied. Semiconductors have the ability of generating holes that can decompose H_2O molecules during RT and generate $OH^{\cdot}$. Using the semiconducting abilities of ZnO NPs, research showed that was possible to generate abundant electron-hole pairs and create highly toxic hydroxyl radicals, enhancing the anti-tumour therapeutic efficacy (Zhang et al., 2015). Furthermore, adding to the decomposition of water by a semiconductor, another possibility is the decomposition of H_2O_2 to generate oxygen-independent ROS. More importantly, using H_2O_2 instead of H_2O molecules for ROS production provides a more efficient way of enhancing cell killing in tumours and reducing damage to the surrounding healthy tissues, since H_2O_2 is overexpressed within tumour cells relative to normal cells (Chenyang et al., 2019). This approach was introduced by the use of $Cu_2(OH)PO_4$ nanocrystals that can simultaneously respond to endogenous stimuli, such as H_2O_2 and exogenous stimuli, such as X-ray irradiation (Chenyang et al., 2019). Under X-ray irradiation, these nanocrystals decompose intracellular H_2O_2 into $OH^{\cdot}$ via a Fenton-like reaction. This research showed that Fenton-like reaction was selectively activated in tumour cells due to the high amount of hydrogen peroxide found in cancer cells, compared with normal cells, resulting in enhanced RT with tumour selectivity. Compared to Fe-based NPs Fenton reaction, results showed that the Fenton-like reaction of $Cu_2(OH)PO_4$ nanocrystals had a more effective activity in hydroxyl radical generation at pH 6.5 (Chenyang et al., 2019).

In summary, new metal elements are being developed and used for cancer treatment. Each of the metallic elements offers specific characteristics due to their intrinsic properties that can be used in combination with different strategies to optimise RT treatment.

1.9 Research aims

This thesis has the aim of exploring and comparing different types of metal oxides and analyse their behaviour with respect to the production of ROS, within water, plasmid-DNA, and cancer cells. This might bring a deeper knowledge regarding radiosensitisation of metal oxide NPs and also explore other candidates for application in the RT treatment.

Even more important is the consistency of the results. Different studies have shown results regarding different types of NPs, but they are inconsistent. This has to do with the fact that different authors use different cell lines, different NP sizes and different radiations, so a fair comparison between the NPs used in different studies is not possible. For this reason, an effort was made in this thesis to try to overcome this lack of consistency.

For this thesis, characteristics such as NP size and coating remained constrained as far as possible (keeping in mind that small variations are always present), the same cell line was used, the same radiation source and same measurement techniques and analysis were used. Each experiment was done at the same time with all the different types of NPs used in each part of the thesis.

There were seven research questions:

- What is the metal oxide NP with the highest radiosensitisation for clinical 6 MeV X-rays?
- Does this type of NP, although with a higher radiosensitisation, have a good cell uptake?
- How toxic is this type of NP to cancer cells without radiation?
- What types of ROS does each NP produce?
- What is the ability of these metal oxide NPs to cause damage to DNA?
- Is there any correlation between the types of ROS produced and the damage caused to cancer cells or DNA?
- Does coating the NPs bring any advantages to cell uptake or radiosensitisation?

All these questions were addressed during this thesis and organized in different chapters.

- Chapter 1: Introduction
- Chapter 2: Materials and Methods; all the conditions, techniques and equipment used are described in this chapter.
- Chapter 3: Comparison of the radiosensitising ability of Period 4 transition metal oxide NPs; this part studies the ability of the different metal oxide NPs to produce the ROS that is more important for cell damage, hydroxyl radical, and how the NPs interact with cancer cells. A coating was chosen to understand if its presence would bring any advantage to the uptake and radiosensitisation of the NPs.
- Chapter 4: Comparison of the radiosensitisation ability of 22 different element metal oxide NPs using 6 MeV clinical X-rays; here focus is given to the interaction of the metal oxide NPs with plasmid DNA. Also, the main types of ROS, such as hydroxyl radical, superoxide, and single oxygen, responsible for cancer cell killing in the interaction of NPs with radiation, are studied.

- Chapter 5: Conclusions; a general conclusion is given based on the different results, and also future lines of experiment that can be conducted are described to bring more knowledge into this field.

2 – Materials and methods

2.1 Metal oxide nanoparticle-based methods

2.1.1 Nanoparticle characteristics

Metals from period four of periodic table, as shown in Figure 2.1, such as manganese (Mn), copper (Cu), nickel (Ni), zinc (Zn), iron (Fe), chromium (Cr), cobalt (Co), vanadium (Vn) and scandium (Sc), were investigated in the form of NPs for the first part of this thesis and compared to hafnium (Hf). For the second part other types were added such as aluminium (Al) and silica (Si) from period 3, zirconium (Zr) and molybdenum (Mo) from period 5, and lanthanides such as neodymium (Nd), samarium (Sm), europium (Eu), gadolinium (Gd), terbium (Tb), dysprosium (Dy), and erbium (Er).

Nanoparticles purchased from Sigma-Aldrich: Al_2O_3 (544833, <50 nm, 99.8%), SiO_2 (637238, 10-20 nm, 99.5%), TiO_2 (718467, 21 nm, 99.5%), Fe_3O_4 (637106, 50-100 nm, 97%), NiO (637130, <50 nm, 99.8%), CuO (544868, <50 nm, 82.6%) and ZnO (721077, <100 nm).

Nanoparticles purchased from US Research Nanomaterials: Cr_2O_3 (US3060, 60 nm, >99%), MnO_2 (US3319NMP, 50 nm, 98%), CoO (US3051, 50 nm, 99.7%), ZrO_2 (US3600, 40 nm, >99%), MoO_3 (US3330, 13-80 nm, 99.94%), Nd_2O_3 (US3350, 30-45 nm, 99.9%), Sm_2O_3 (US3450, 15-45 nm, 99.95%), Eu_2O_3 (US3543, 10-100 nm, 99.99%), Gd_2O_3 (US3240, 10-100 nm, 99.9%), Tb_4O_7 (US3455, 10-100 nm, 99.99%), Dy_2O_3 (US3080, 30 nm, >99.9%), Er_2O_3 (US3140, 10-100 nm, 99.9%) and HfO_2 (US3245, 61-80 nm, 99.99%).

Nanoparticles purchased from American elements: Sc_2O_3 (SC-OX-02-NP, <80 nm, 99%).

Nanoparticles purchased from Nanoshel: V_2O_5 (NS6130-03-399, <80 nm, 99.9%).

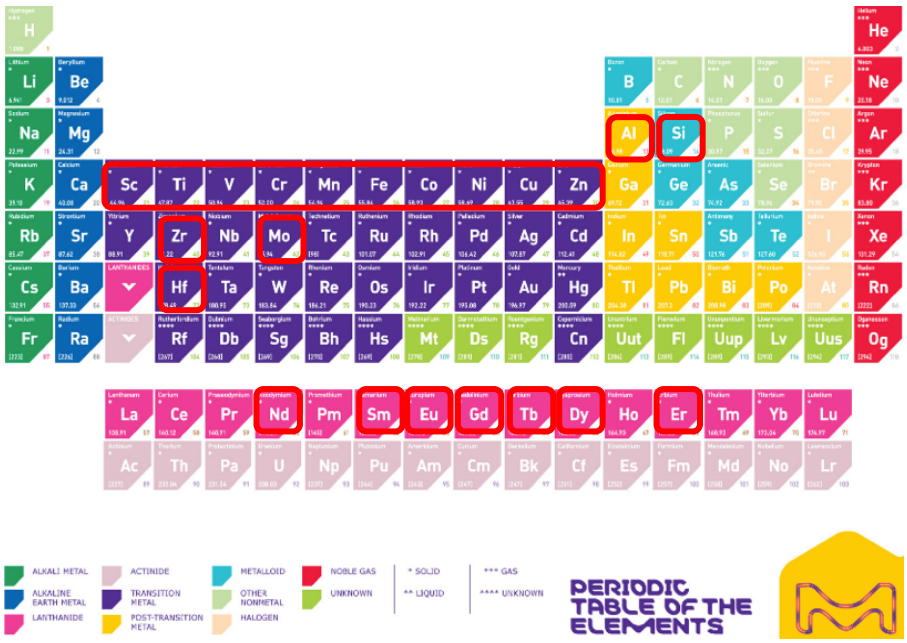

Figure 2.1: Periodic table with all the elements (outlined in red) chosen for this thesis (Sigma Aldrich).

2.1.2 Nanoparticle coating

Polyethylenimine (PEI) was used in this thesis with the aim of testing if the NP cellular uptake would increase in comparison to the non-coated counterparts.

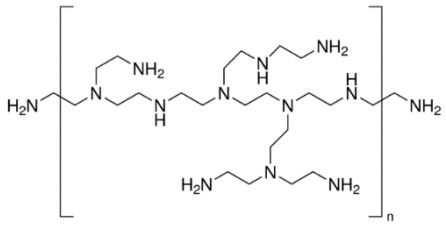

Figure 2.2: PEI branched structure (Sigma Aldrich).

A PEI solution in 50 wt. % in H_2O (482595) was purchased from Sigma Aldrich with a molecular weight of 1300 and a branched structure (as shown in Figure 2.2).

Samples were prepared using a PEI stock solution concentration of 1:100 in H_2O and a NP concentration of 1 mg/ml. A volume of 10 ml PEI stock solution was then added to 1 ml NP solution. This mixture was placed in an ultrasonic bath and sonicated for 1 h. After the sonication process was done, each solution was mixed in a vortex and then placed in a centrifuge at 2000x*g* for 10 min at 20 ℃. The supernatant was then discarded to remove the excess PEI and 10 ml of H_2O was added to the pellet. For a better cleaning, the sample was washed another two times with H_2O. To the final samples a volume of 2 ml of water was added and mixed in a vortex. Samples were placed in a beaker and dried at 50 ℃ for approximately 30 min. The dried samples were removed with a spatula and placed in cryogenic vials with a screw cap.

2.1.3 Nanoparticle physico-chemical characterization

2.1.3.1 Transmission Electron Microscopy (TEM)

NP size and shape was determined using TEM images. Solutions were prepared by mixing the NP powder in water and sonicating it for 1 h. A sample volume of 2 μl was dried on an electrostatically discharged carbon-coated grid. Each grid was placed in a JEM-1400 model (JEOL-USA) and different images were taken for each sample. Using ImageJ 1.49 software, NP diameters were calculated using 10 images of each TEM sample with 3000x magnification. Threshold approach was used by adjusting the images brightness to optimize the contrast with the background and then applying a threshold. ImageJ "Analyse particles" function was used, and the different steps were taken:

1. Image magnification scale was defined;
2. Pixel dimensions were then converted into nanometres;
3. Size dimensions were set between 1 nm and infinity;

A MACROS code was used to run the threshold approach through all the 10 images of each sample. Values of each sample were transferred into an excel spreadsheet and NP diameter was calculated using $d = 2 \times (\frac{\sqrt{A}}{\pi})$, where A is the measured area and d is the diameter. The excel "Data analysis" function was used, and a histogram was created for each type of NP.

2.1.3.2 Dynamic Light Scattering (DLS)/Zeta potential

The hydrodynamic diameter of 2.5 mM NPs in 3% PBS pH 7.4 was calculated with The Nano-flex II $180°$ DLS system using Flex 11.1.0.5 software (Microtrac). PEI coating in each sample was identified through zeta potential measurements. For this technique, a 5 mM NP sample of 10 ml in water was prepared and the potential was measured using Colloid Metrix Stabino II. Non-coated and PEI-coated samples potential was then compared to look for evidence of the PEI coating through the differences in the potential.

2.1.3.3 X-ray diffraction

Samples were analysed using a Siemens D5005 XRD with a long fine focus copper X-ray tube energised at 40 kV and 40 mA running conventional Bragg-Brentano geometry. Most runs were 0.5 s/step, with some at 8 s/step. Crystal phases were determined from XRD spectra using QualX2 software (Altomare et al., 2015) (version 2.24; Institute of Crystallography CNR, Bari, Italy) and PowCod database 1901.

2.2 Cell culture-based methods

2.2.1 Cell culture

The cell line used in this thesis was HSC-3 that is a human tongue squamous carcinoma cell line. This cell line was purchased from the American Type Culture Collection. HSC-3 cells were cultured in low glucose (1 g/L) DMEM (Gibco, 21885-108), supplemented with 10% FBS (Sigma-Aldrich, F9885) and 1% penicillin/streptomycin (ThermoFisher Scientific, 15140122) in a humidifier incubator at 37 ℃ with 5% CO_2. Cells were grown in T-75 culture flasks to about 80% confluency before passage.

2.2.2 Cytotoxicity of metal oxide nanoparticles

2.2.2.1 Clonogenic assay

The toxicity of metal oxide NPs and their effect on cell survival and proliferation was evaluated with a clonogenic assay on HSC-3 cell line. HSC-3 cells were seeded at 150 cells/well in a 24-well plate and allowed to adhere overnight. Next day, cells were exposed to 0, 1, 10, 30, and 100 μg/ml of each type of metal oxide NP for 24 h. After 24 h have passed the NP medium was removed and the wells were washed three times with DMEM media supplemented with 10% FBS and 1% penicillin/streptomycin. Cells were left to grow for 6 days to form colonies. After the end of the 6^{th} day, cells were briefly rinsed with water, stained, and fixed with 2% methylene blue in 50% ethanol solution for 4 h. The staining/fixation solution was removed, plates were rinsed with distilled water and dried. Colony counts were done by eye using a Zeiss AxioVert microscope and the IC25 values were estimated from logarithmic plots of NP concentration vs colony survival, normalized to the control. IC25 is the concentration at which the metal oxide NPs cause 25% cell colony reduction compared to the untreated controls.

2.2.3 Cellular uptake of metal oxide nanoparticles

2.2.3.1 Inductively coupled plasma mass spectrometer (ICP-MS)

Metal oxide NP cellular uptake was assessed by ICP-MS in the HSC-3 cell line. HSC-3 cells were seeded at 150 cells/well in 24-well plates and allowed to adhere overnight. Next day, cells were exposed to the IC25 concentration of each type of metal oxide NP for 24 h. After 24 h have passed the NP medium was removed and the wells were washed three times with DMEM media supplemented with 10% FBS and 1% penicillin/streptomycin. Cells were left to grow for six days to form colonies. After the

end of the 6th day, cells were briefly rinsed with water and dried. In order to measure the concentration of the NPs uptake by the cells, nitric acid was used to remove all the cells and the concentration of the remaining NPs were put into solution and measured by Agilent 7500 ICP-MS or Agilent 8800 triple quad ICP-MS. To convert the uptake in ppm into intracellular concentration in mg/ml it was assumed that 25,000 cells were loaded in each well for a total volume of 4 ml of HNO_3. Considering that each cell volume is equal to 2,000 microns cubed (Mitsui & Schneider, 1976) and that each NP is evenly dispersed in that volume, the intracellular concentration is equal to:

$$\text{intracellular c} = \frac{4}{0.00005} \times \text{ppb} = 80000 \times \text{ppb}$$

, where 0.00005 ml is the volume occupied by the 25,000 cells, since 25,000 cells = 50 million microns cubed = 0.00005 ml. Since 1 million ppb is equal to 1 mg/ml the intracellular concentration becomes:

$$\text{intracellular c} = \frac{80{,}000}{1{,}000{,}000} \times \text{ppb} = 0.08 \times \text{ppb}.$$

2.3 Reactive oxygen species (ROS) based methods

2.3.1 ROS probes

2.3.1.1 Hydroxyl radical probe

Coumarin-3-carboxylic acid (3-CCA) powder was purchased from Sigma Aldrich. A 5 mM stock was prepared in 6% PBS pH 7.4.

2.3.1.2 Hydrogen peroxide probe

Dihydrorhodamine 123 (DHR) solution was purchased from ThermoFisher Scientific. A 20 μM was prepared in 6% PBS pH7.4.

2.3.1.3 Singlet oxygen probe

Singlet oxygen sensor green (SOSG) was purchased from ThermoFisher. From a 5 mM methanolic

stock, a working solution of 1 μM was prepared in 6% PBS pH 7.4.

2.3.1.4 Superoxide anion probe

Dihydroethidium (DHE) was purchased from ThermoFisher. From a stock of 20 mM DHE in DMSO a working solution of 50 μM was prepared in 6% PBS pH 7.4.

2.3.2 ROS measurement

Experiments were run a minimum of three times independently and each time containing technical triplicates. Fifty microlitres of probe working solution was added to 50 μl of 5 mM NP in deionized water in black-walled 96-well plates (Cellstar, Greiner), producing a 2.5 mM NP working solution. After irradiation the fluorescence of each well was measured using a FLUOstar Optima plate reader (BMG Labtech), according to the type of probe: 3-CCA at Ex 390 nm/ Em 450 nm, DHR at Ex 485 nm/ Em 544 nm, SOSG at Ex 485 nm /Em 520 nm, and DHE at Ex 485 nm/ Em 590 nm (Zhao et al., 2003).

2.3.3 ROS calibration measurement

Each NP could potentially alter the fluorescence of the probe solution. Therefore, for each probe 50 μl serial dilutions of the fully oxidized fluorescence molecule in 6% PBS were mixed with 50 μl 5 mM NP solution and the fluorescence measured as already described.

For 3-CCA calibration was measured with 7-hydroxycoumarin-3-carboxylic acid (7OH-CCA, Sigma-Aldrich). For DHR calibration, rhodamine 123 (ThermoFisher Scientific) was used.

For SOSG calibration, 0.5 μM SOSG was reacted with 6% H_2O_2 and 2% NaClO. The reaction of H_2O_2 with NaClO generates singlet oxygen (To et al., 2014).

For DHE calibration, to generate DHE fluorescence products namely 2OH-E, 1.5 μM DHE was reacted with 0.5 mM xanthine in 0.9% NaCl and 10 mU/ml xanthine oxidase (Sigma-Aldrich). The stock of 2OH-E was generated by complete DHE oxidation for 6 h as previously described (Nazarewicz et al, 2013).

The molarity of each radical species is reported assuming an equimolar reaction between each probe and its cognate radical.

2.4 Plasmid DNA based methods

2.4.1 Plasmid DNA extraction

Plasmid pBR322 was extracted from bacteria using Qiagen plasmid midi kits and kept as a 50 ng/μl stock in 10 mM Tris-HCl, pH 8.5. Plasmid concentration was obtained from UV-vis measurements using NanoDrop One Spectrophotometer from ThermoFisher.

2.4.2 Plasmid DNA measurement

Ten microlitres of plasmid DNA were mixed with 10 μl of 5 mM NP solution in 96 well plates. Solutions were either left untreated or irradiated with 10 Gy of 6 MeV X-rays, as described below.

After irradiation, to assess the DNA irradiation damage a 50 well agarose gel electrophoresis was used. Five μl of each sample were mixed with 5 μl loading dye (Purple, New England Biolabs) and loaded onto 1% agarose electrophoresis gels containing 0.2 μg/ml ethidium bromide with a running buffer of Tris-Borate-EDTA with 0.2 μg/ml ethidium bromide. A 1 kb DNA ladder was also used (Quick-load Purple Plus, New England Biolabs).

Gels were run at 110 V for 1 h and then photographed using a G:Box Chemi XX6 gel documentation system (Syngene). DNA band intensities were quantified using the Gel Analysis feature of ImageJ software (version 1.52; NIH).

2.5 Hole quenching-based methods

2.5.1 Hole scavenger

2.5.1.1 Formic acid

A working concentration of 10 mM formic acid pH 3.5 was obtained from a 99.5% concentrated formic acid solution (Puangpetch et al., 2011; Tan et al., 2003).

2.5.2 Hole quenching measurement

Experiments were run a minimum of three times independently and each time containing technical triplicates. A working concentration of the hole scavenger was added to a 2.5 mM working concentration of NP solution and 50 μM working concentration of DHE with a total volume of 100 μl per well in black-walled 96-well plates (Cellstar, Greiner). After irradiation, the fluorescence of each well was measured using a FLUOstar Optima plate reader (BMG Labtech) and the DHE probe filters, Ex 485 nm/ Em 590 nm. For the formic acid pH 3.5 samples a pH 3.5 nitric acid solution was used as a reference to evaluate the effect of the pH in the formation of superoxide anions after irradiation. For this purpose, the formic acid experiment set-up and conditions were maintained where 10 mM of formic acid was replaced by 10 mM of pH 3.5 nitric acid.

2.6 Nanoparticle catalytic ability

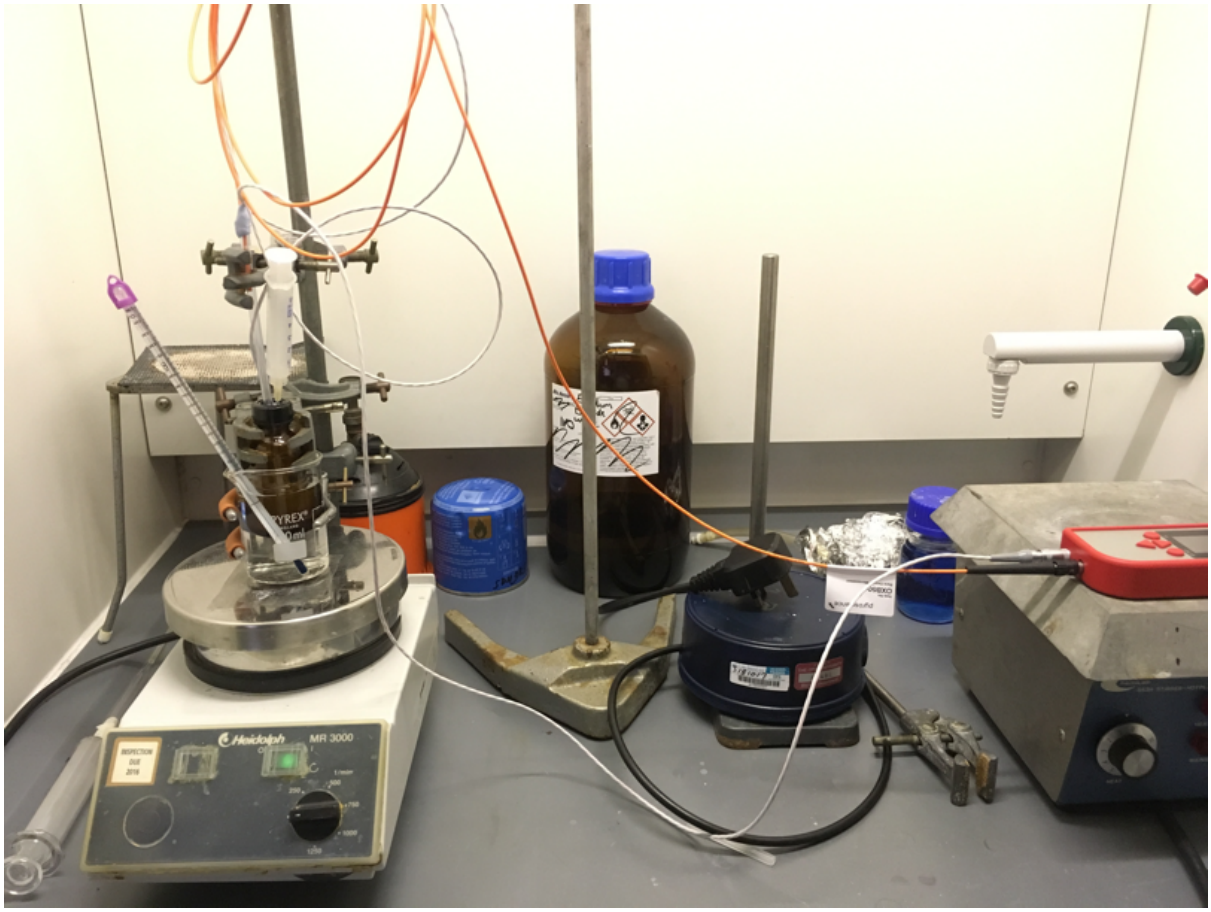

Figure 2.3: Nanoparticle catalytic ability measurement set-up.

Five ml of aqueous 5 mM NP solution was added to a 30 ml amber screw-cap PTFE/silicone septum bottle. The bottle was nearly fully immersed in a beaker of 100 ml in water at room temperature (20 ℃) with constant magnetic stirring of the NP solution, as shown in Figure 2.3.

An oxygen microsensor probe (OXB50, Pyro Science) was put into a plastic protection and sealed. The probe+plastic protection was inserted into a hole that was made into the amber cap and positioned around 2 cm above the liquid surface.

After stirring for 5 minutes, an aqueous solution of 6 ml 12% H_2O_2 was injected into a 6 ml 5 mM NP solution using a fine needle syringe.

Percentage oxygen concentration was measured in the gas phase at one second intervals for 10 min using a FireStingGO2 oxygen meter.

2.7 Hypoxia

To mimic a cancer cell hypoxic environment all plates were sealed in a plastic bag containing only 0.3% oxygen. For this purpose, an O_2/Ar cylinder was used to add the gas (O_2/Ar) into the plastic bag to remove as much oxygen as possible. For each bag, the gas was left for 30 seconds and this procedure was repeated three times. Before closing the bag, gas was added for another 60 seconds.

For the cancer cell experiments, before insertion of the gas, the cell medium was replaced by Gibco™ CO_2 Independent Medium purchased from Fisher Scientific and CO_2 from the incubator was removed. After irradiation, cell medium was again replaced by DMEM and CO_2 in the incubator changed to 5%.

2.8 X-ray irradiation

Plates were sandwiched between 10 cm solid water shielding (Gammex) with a 0.5 cm bolus on the bottom and 2 cm bolus with 5 cm solid water shielding on top. This set-up was chosen using a treatment plan based on CT scans of the plates to simulate the location of a deep tumour, preventing in this way backscatter build-up (Figure 2.4). Plates were irradiated with 10 Gy of 6 MeV X-rays at a dose rate of 5 Gy/min in a 25×25 cm^2 radiation field using a clinical linear accelerator (Versa HD, Elekta) at GenesisCare, Milton Keynes.

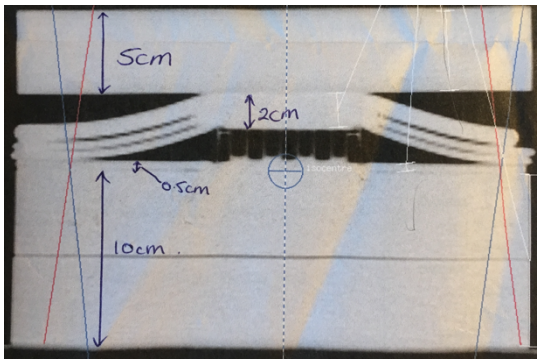

Figure 2.4: Plate set-up for irradiation at GenesisCare Milton Keynes Elekta LINAC using 6 MeV and 10 Gy.

2.9 Statistical analysis

Data were analysed using GraphPad 6.0 Prism software. All the experiments were performed in triplicate and on three independent times, so all values were normalized to their control, n=3.

The data of ROS and clonogenic assay where both non-irradiated and irradiated results are shown was analysed using a two-way ANOVA with Tukey's post-hoc test and α=0.05.

In the data of ROS and clonogenic assay for ratio and quenching results a one-way ANOVA with Dunnett's post-hoc test and α=0.05 was used.

The significance is always compared to the respective control. Asterisks indicate significant differences of *P<0.05, **P<0.01, ***P<0.001, ****P<0.0001. Mean ± SEM was plotted on all graphs.

3 Comparison of the radiosensitising ability of Period 4 transition metal oxide nanoparticles

3.1 Introduction

Different types of NPs have been a target of study in order to enhance RT treatment. One of the major issues with this field of research is the lack of comparable results due to the existence of different experimental variables and the assumption that NP radiosensitisation is primarily due to photoelectric electrons without much consideration for the role of surface catalysis. For example, within gold NPs, different results are shown regarding the gold radiosensitising ability due to the differences in size, cell line, beam type used (Rosa et al., 2017). For this reason, this thesis is focused on a systematic survey of the radiosensitising potential of different metallic NPs.

In this way, metal oxide NPs from period four of the periodic table, and hafnium oxide NPs for comparison, were chosen for this research, where size, cell line and beam type were maintained constant through the experimental procedure. Thus, the following metal oxide NPs were studied: Sc_2O_3, TiO_2, V_2O_5, CrO_2, MnO_2, Fe_2O_3, CoO, NiO, CuO, ZnO and HfO_2 as a heavy element positive control.

For clonogenic assays with cancer cells, the coating was one of the variables of concern in this study. Coating metal oxide NPs with organic molecules that are recognised and biocompatible may improve their cell uptake. Also, when injected into the bloodstream, it is important that the NPs present a high retention time before being taken up by macrophages. Coating of the NPs can overcome these limitations.

The coating of NPs with hydrophilic, neutral polymers can increase their stability in the blood circulatory system. The coating attaches to the surface of the NP either by adsorption, hydrophobic or electrostatic interactions, or by grafting via covalent bonds (Storm et al., 1995).

The enhanced stability in the blood through these polymer-coated NPs is due to their ability to prevent the adsorption of various blood components onto their surface. The coating confers “invisibility” to the NPs, which in turn reduces the uptake by liver and spleen macrophages and, thus, extends blood circulation times (Storm et al., 1995). Different types of coating can be used to achieve different properties such as stability, biocompatibility, or active targeting, where the NPs are modified with a specific active molecule that binds to the desired target cells or tissues.

One of the purposes of the coating in this thesis was to improve cellular uptake. Different polymer coatings have been used to modify NPs and improve their biocompatibility such as thiol-terminated methoxypoly, e.g. ethylene glycol (Liao & Hafner, 2005) and PEG that due to its amphiphilic characteristic provides good solubility to the NP, in both polar and non-polar solvents, which in turn is responsible for the high biocompatibility and good affinity for cell membranes (Choi et al., 2003).

The surface of NPs has also been modified with polyethylenimine (PEI) to increase cellular binding and uptake and prevent their aggregation under physiological conditions (Pissuwan et al., 2011). A study comparing the cellular uptake in human-derived retinal pigment epithelial (ARPE-19) cells between 80 nm silver NPs (AgNP) with four different coatings such as branched PEI, CIT, polyvinyl-pyrrolidone (PVP) and PEG showed that AgNP-PEI were positively charged and entered the cells at a higher rate

than the negatively charged or neutral particles. Furthermore, AgNP-PEI were toxic to the cells at lower doses than the other coatings and both AgNP-PEI and AgNP-CIT had a greater intracellular accumulation compared to AgNP-PEG and AgNP-PVP. This investigation concluded that positively charged AgNP-PEI increased cellular uptake, the particles agglomerated in the peri-nuclear region and presented increased mitochondrial toxicity (Zucker et al., 2019).

Although PEI can induce cell death and inhibition of cell differentiation, the use PEI with lower molecular weight, around 2 kDa, has shown to improve biocompatibility (Barrow et al., 2015). Furthermore, this type of PEI was reacted with a hydrophobic alkyl chain, which allowed for stabilisation of clusters of pre-formed hydrophobic SPIONs in water. This is represented by the mode of assembly shown in Table 3.1 for PEI. It was shown that for mouse mesenchymal stem cells (mMSCs) the uptake for the alkyl group on PEI polymer coated SPION was 7 pg[Fe] per cell at highest dose and incubation time, e.g. 7 mg/ml Fe for 24 h (Liu et al., 2011). Other different polymer coatings have been tried in iron oxide NPs, as shown in Table 3.1.

In *in vitro* studies, cellular growth media contains serum proteins, essential amino acids, vitamins, electrolytes, and other chemicals, such as antibiotics, and trace metals, that in contact with NPs can alter their physico-chemical properties, such as surface charge, size and aggregation state, and surface chemistry (Alkilany & Murphy, 2010). In cell growth media, NPs adopt the physico-chemical properties of the adsorbed protein shell, called “protein corona”, meaning that the surface chemistry of the NPs it is not the same as the original (Cedervall et al., 2007). Coatings such as PEG are often used to prevent the protein corona (Oh et al., 2018). For *in vivo* studies, the injection of the NPs into the blood stream may also modify the surface of NP and aggregation state due to their interaction with the proteins and electrolytes present in the blood (Alkilany & Murphy, 2010). Functionalized gold nanorods with PEG were used successfully to increase the circulation time of the injected NPs within the body (Eghtedari et al, 2009). The reticuloendothelial system of the body filters the injected NPs based on their size and surface characteristics limiting circulation time, which means NPs do not remain long enough in the blood stream to find their target. A recent study showed that an important parameter to be considered in the clearance of NPs is the density of the coating (Bertrand et al., 2017). In this research a PEG density threshold was identified below which blood clearance is fast.

Table 3.1: Important information of strategies used for designing polymer coated IONPs for optimized stem cell uptake (Barrow et al., 2015). The stem cell lines used are rat mesenchymal stem cells (rMSCs), mouse mesenchymal stem cells (mMSCs), human mesenchymal stem cells (hMSCs) and the different types of polymers include PEG, poly-$_L$-lysine (PLL), PEI and poly(N,N-dimethylacrylamide) (PDMAAm).

Polymer	Mode of assembly	Stem cell line used	Exposure concentration (μg[Fe] per ml)	Reported uptake (nearest pg[Fe] per cell)
Chitosan		hMSCs	50	18
Carboxym ethyl chitosan		hMSCs	50	27
Dextran		mMSCs	50	4
Pullulan		rMSCs	100	65
PEG	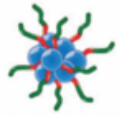	hMSCs	50	1 with NH2 only 2 with hyaluronic acid
PLL		hMSCs	20	65
PEI	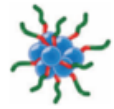	mMSCs	7	7
PDMAAm		rMSCs hMSCs	15 μg/ml (γ-Fe2O3)	23 37

Surface charge is another factor that affects NPs internalization into the cells. Uptake of magnetic NPs by breast and prostate cell lines was evaluated using silica-coated magnetic iron oxide maghemite (γ-Fe_2O_3) functionalized with either amino and carboxyl groups providing positive and negative surface charges, respectively (Kralj et al., 2012). From the results it was concluded that positively charged NPs presented a higher uptake rate into the cells than the negatively charged NPs for different cell lines. Since outer cell membrane is, in general, negatively charged it will attract the positively charged NPs and not the negatively charged ones (Kralj et al., 2012).

Research performed on polyvinyl alcohol (PVA), PEI and dextran coated IONPs, with different surface charges, demonstrated that the type and surface charge of polymer coated IONPs play an important role in protein adsorption, which can affect both colloidal stability and toxicity. In one study, the different polymer coatings, PVA, vinyl alcohol/vinyl amine copolymer (A-PVA) and PEI, were compared in order

to understand their influence on colloidal stability, cytotoxicity and cellular uptake in different cell media using SPIONs and HeLa cell line (Petri-Fink et al., 2008). Regarding the colloidal stability, all polymer coated SPIONs were stable in water and PBS but the stabilities were different in DMEM or Roswell Park Memorial Institute (RPMI) media. This data showed that the choice of medium influences the uptake of these particles by HeLa cells. Another study compared SPIONs coated with two different polymers, PVA and dextran (Sakulkhu, Mahmoudi, et al., 2014). Obtaining different surface charges, positive, neutral, and negative, the effect of the surface charge and surface polymer material on protein adsorption was investigated. PVA-coated SPIONs with negative and neutral charge adsorbed more serum proteins than the dextran-coated SPIONs, which resulted in a higher blood circulation time for PVA-coated NPs compared to the dextran-coated ones. The same group (Sakulkhu, Maurizi, et al., 2014) performed a study using PVA-coated SPIONs comparing the different surface charges, positive, neutral and negative, investigating the protein corona *in vivo*. Rat serum was extracted after interaction of NPs with the rat's physiological system, leading to more realistic results and better understanding and prediction of the destiny of NPs *in vivo*. Particles were left for 15 min in blood circulation in living rats and their protein corona showed differences due to their surface charge. Neutral particles showed the highest number of different proteins both *in vitro* and *in vivo*, positively charged particles showed the lowest number of different proteins *in vivo* and particles negatively charged showed the lowest number of different proteins *in vitro*.

Conformation, charge distribution and also the hydrophilicity/hydrophobicity of the adsorbed proteins could all affect the zeta potential measurement (Barrow et al., 2015). Protein adsorption is one of the important driving forces in the selection of a NP target destination, which will further affect cells, tissues and finally the body system. Proteins such as albumin, fibrinogen, IgG, complement C3, apolipoprotein A-I and apolipoprotein E19–22 bind to NPs of polymeric or inorganic nature (Sakulkhu et al., 2015).

Surface charge effects of IONPs in protein adsorption and cell uptake were investigated comparing a negatively charged coating such as polyacrylic acid (PAA) with a positively charged coating such as PEI. The hydrodynamic diameter was the same for both particles, 30 nm, and after 24 h of incubation large NP-protein bioconjugates with hydrodynamic sizes of around 1500 nm for PAA-coated NPs and around 3000 nm for PEI-coated NPs were observed. Although both NPs present a similar negative zeta potential within cell culture, the results showed that PEI-coated NPs were incorporated in much larger amounts than the PAA-coated NPs. Quantitative analysis showed that SHSY5Y cells can incorporate 100% of the added PEI-coated NPs up to 100 pg/cell, whereas for PAA-coated NPs the uptake was less than 50% (Calatayud et al., 2014).

3.2 Experimental design

3.2.1 Choice of nanoparticle size, shape and concentration

In this part of the work, the effects, such as toxicity, uptake and radiosensitisation, of different metal oxide NPs on human cancer cells was studied.

The NP diameter was aimed to be around 50 nm, since this size is optimal for cellular uptake (Chithrani et al., 2010). The NPs were collected based on their size, with no control of their shape, meaning the NPs used are mostly amorphous. Ideally, NPs should have a spherical shape. To increase cellular uptake, it was shown that for 50 nm gold NPs, the spherical shaped ones showed the highest cellular response when compared to gold nanospikes and gold nanorods, after a 24 h cell incubation (Ma et al., 2017).

To explore the interaction of the NPs with radiation without cells, the concentration chosen was 2.5 mM. This was a concentration high enough to give consistently detectable ROS species. In cell experiments, NPs could be administered at either equimolar or equitoxic doses. Both methods have their respective merits, but equimolar loading of NPs was chosen at a concentration designed to reduce clonogenic cell survival by 25% of control values (IC25).

3.2.2 Choice of nanoparticle coating

In the Introduction in Chapter 1, various types of NP coating were discussed. Here, the rationale for choosing PEI coating for the experiments in this thesis is explained. A study by Du and collaborators (Du et al., 2016) showed that iron oxide NPs coated with low-molecular weight PEI, 2000 Da, can be used as drug delivery carriers and cell tracking probes. Furthermore, a layer by layer technique was used to coat gold nanorods with PEI and the results demonstrated an increase in cellular uptake (Takahashi et al., 2008). To try to improve NP uptake and toxicity, in this thesis the chosen coating was PEI with a low-molecular weight of 1300 Da. Furthermore, the low-molecular weight was used to have a thin organic coating that would allow water to get to the NP surface. It has been shown that a thick coating lowers radiosensitisation efficiency (Gilles et al., 2014). This study used gold NPs functionalised with PEG or human serum albumin and the results showed that NP functionalisation significantly decreases hydroxyl radical production, so the authors suggested the use of a thin coating to avoid this problem. Another study using PEG-amine coating AuNPs showed that the use of these coating produced less hydroxyl radicals when irradiated with 10 Gy of 6 MeV X-rays compared to the CIT-capped AuNPs (Grellet et al., 2017).

PEI is a polymer with repeating unit that consists of an amine group and two carbon aliphatic CH_2CH_2 spacer with the chemical formula $(C_2H_5N)_n$. Polyethylenimines can be linear or branched, where the former consists of secondary amine groups and the latter can contain primary, secondary and tertiary amino groups, as shown in Figure 3.1.

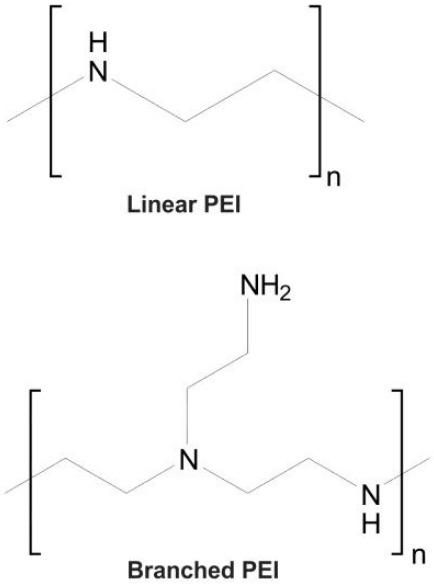

Figure 3.1: PEI structures (Omidi & Kafil, 2011).

Due to the favourable outcome that the branched PEI form showed in cell transfection it has become the most common form used for gene delivery (Godbey, Wu, & Mikos, 1999).

The change in the surface charge or zeta potential due to PEI coating has been examined and it was found that when branched PEI forms a complex with DNA, the complex presents a zeta potential of 31.5 mV, while PEI alone showed a zeta potential of 37 mV in solution (Godbey, Wu, Hirasaki, et al., 1999). Furthermore, in the same study, centrifugation of PEI/DNA complexes resulted in a decrease of zeta potential to 29.2 mV.

A characteristic that was seen to affect transfection efficiency and cell toxicity was the ratio between the PEI nitrogens to DNA phosphates. Reducing the charge ratio to 1:2 of the complexes reduced the amount of cell death associated with transfection (Godbey, Wu, & Mikos, 1999).

3.2.3 Choice of cell line

Since the aim was to find a type of NP that could improve the RT treatment, investigation of the NP effects in human cancer cells is very important.

NPs can be administered by different routes, such as subcutaneous, intravenous, intraocular and intramuscular (Oberdörster et al., 2005). In this sense, target organ, as liver, kidney, nervous system, or endothelial cells, should be reflected in the choice of the cell line to be used, in the evaluation of the cytotoxic potential of the NP.

Due to the amount of the different types of NPs studied in this thesis only one type of cell line was tested. In the Methods section, it was explained that HSC-3 oral squamous carcinoma cells were used. Here, the reasons behind this choice are clarified. HSC-3 cell line was chosen due to its proliferation ability and its round-shaped colony formation which facilitate the separation between colonies for colony counting. Also, although it is a cell type with oral squamous tissue origin, it presents a high degree of local invasiveness and a high rate of metastasis to cervical lymph nodes (Kinouchi et al., 2018). Studies have shown the ability of human oral squamous cell carcinoma cell lines to promote the growth and metastasis of solid tumours, known as angiogenesis (Michi et al., 2000). This ability makes this cell line appropriate for studies that aim at the understanding of the effects of NPs with 6 MeV X-ray energies.

3.2.4 Choice of irradiation parameters and radical probes

A 6 MeV X-ray beam, the most clinically-relevant megavoltage radiation (Stephen J. McMahon et al., 2016), was used, with a dose of 10 Gy, chosen based on the highest signal given by a 3-CCA testing at different Gy doses.

NP radiosensitising capacity was based on the amount of hydroxyl radicals they would generate when interacting with ionising radiation. The protocol chosen to measure the main radical type responsible for cancer cells death was the coumarin assay that was adapted to NP suspension (Sicard-Roselli et al., 2014). This technique was used due to its compatibility with NPs, experiment set-up, and sensitivity, down to 30 nM $HO^{\cdot}$ (Louit et al., 2009). The major known fluorescent product of hydroxylation of coumarin is 7-hydroxycoumarin (7-OHC). 3-CCA was chosen instead of coumarin, since the hydrogen in C3 with the carboxylic group eliminates hydroxylation in this position increasing, in this way, the fluorescence of 7-hydroxylated coumarin derivatives by twofold (Manevich et al., 1997).

Hydrogen peroxide is an important intermediate species during production of the radicals species involved in the process of cancer cell death. This assay was included with the aim of measuring the amount of H_2O_2 produced in water by megavoltage irradiation. It has been proposed that hydrogen peroxide produced by UV irradiation may be a precursor to hydroxyl radicals in the presence of metal oxide NPs (Miguel & Patrício, 2013). The fluorescent-responsive dye used to probe the amount of H_2O_2 was dihydrorhodamine (DHR). This non-fluorescent probe is oxidized in the presence of H_2O_2 and converted into a fluorescent product called rhodamine 123 (Henderson & Chappell, 1993).

To exclude any interference caused by the presence of NPs during the measurement a quenching assay was used for all radical probes. Studies showed that a direct comparison between the signal intensity attributed to 7-OH-CCA in water and the one in a gold NP suspension is not possible since the presence of NPs alters the mechanism, and hence regioselectivity, for $HO^{\cdot}$ yield of formation (Sicard-Roselli et al., 2014). The same happens to different metal oxide NP solutions. This quenching assay was designed with the aim to exclude the fluorescent background due to NP interference, since the experimental set-up used in this thesis was not suitable for the application of other techniques. Other

techniques included addition of NaCl solution to induce NP aggregation and therefore, its precipitation. This technique was tested for gold NPs and it was showed that due to the very large reduction of the surface area of gold, quenching was no longer seen in the aggregated state (Sicard-Roselli et al., 2014). However, salt precipitation may not work for all types of NPs. Furthermore, Sicard-Roselli *et al* showed that 1 nM of 32.5 nm diameter gold NPs do not induce any modification in the fluorescence intensity for incubation times shorter than 30 s. The present study used 22 different types of metal oxide NPs of around 50 nm diameter, where the NP incubation time exceeded 30 s since the irradiation set-up was at least 15 min away from the incubation set-up. In this sense, a simpler and adequate assay was used, assuming that NP fluorescence interference is constant after 30 min of incubation time, and consequently NP fluorescence interference can be excluded.

3.3 Results

3.3.1 Physico-chemical characterization of NPs

3.3.1.1 Transmission electron microscopy (TEM) and histogram size

In Table 3.2, TEM images and respective size distribution for each NP is presented. Size histograms showed consistency with TEM images of 3000x magnification. For structural observation reasons, an image at 150000x magnification is shown for each type of NP, not being representative of the average size.

Table 3.2: TEM images at 3000x and 150000x magnification, and the size distribution for all NPs, non-coated and PEI-coated ones. ImageJ was used to determine the diameter of each NP through the TEM images of 3000x magnification.

NPs	TEM image 3000x	TEM image 150000x	Size distribution (x axis: NP diameter in nm) (y axis: counts)
Sc	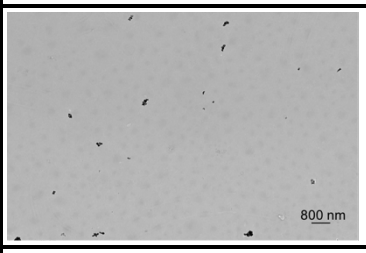	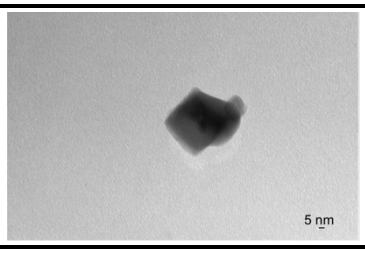	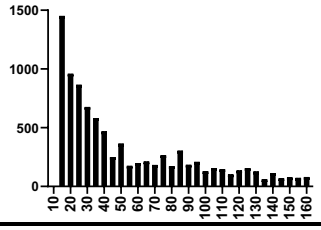
ScPEI	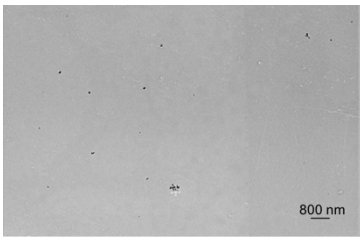	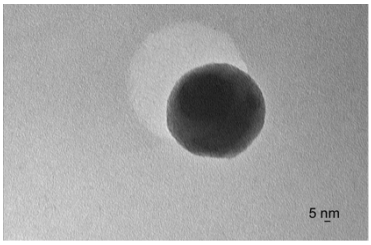	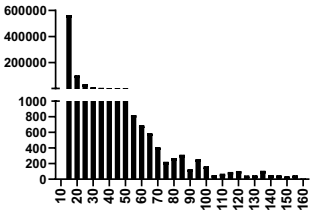
Ti	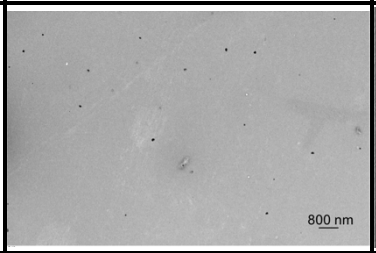	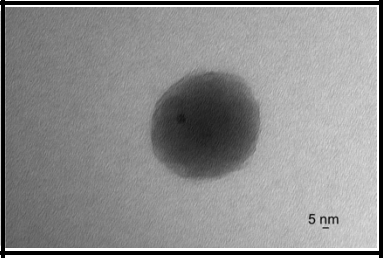	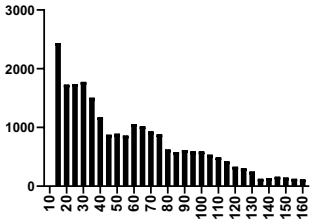
TiPEI	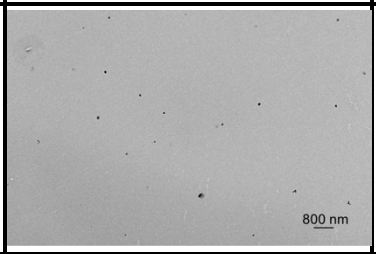	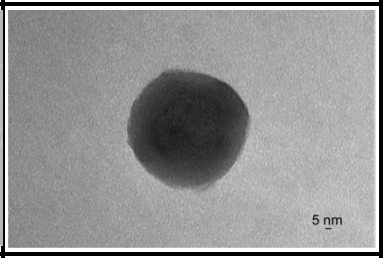	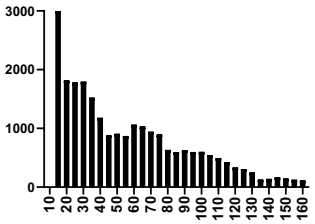
V	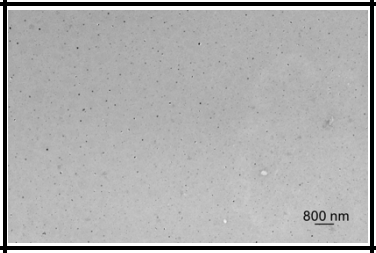	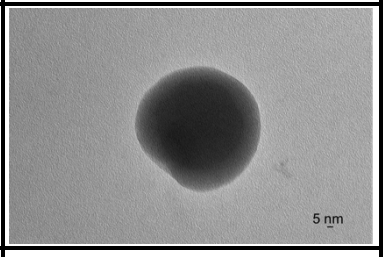	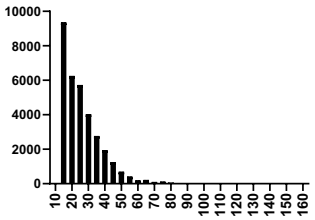
VPEI	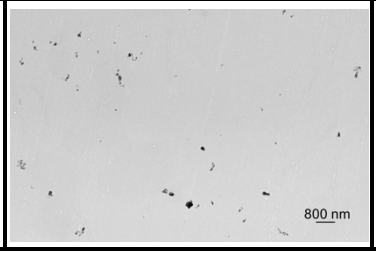	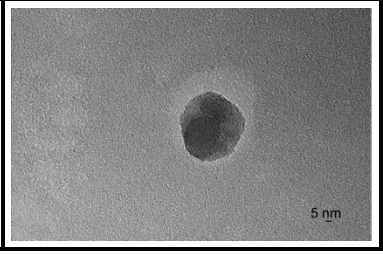	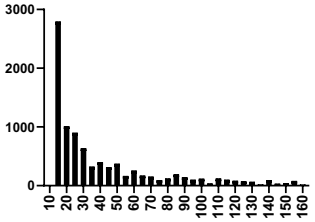

Cr	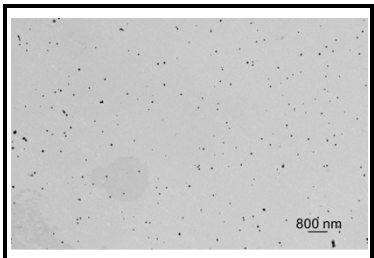	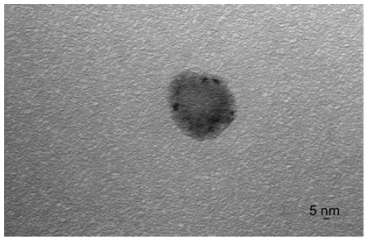	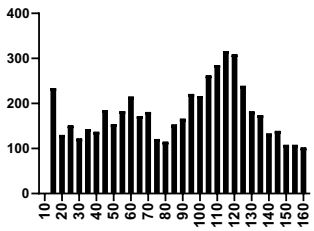
CrPEI	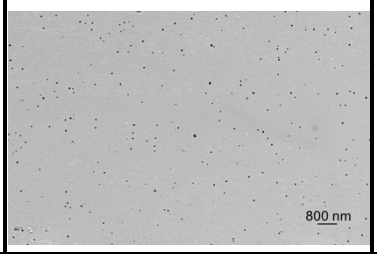	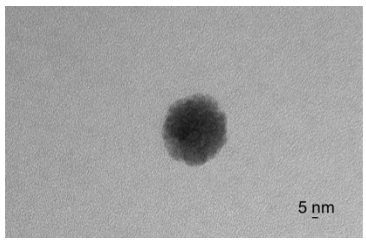	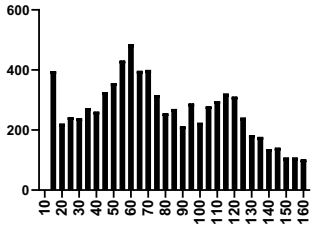
Mn	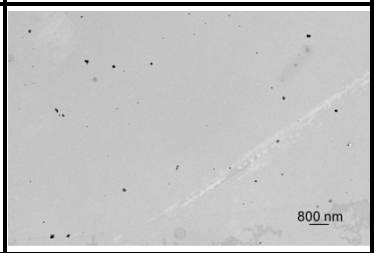	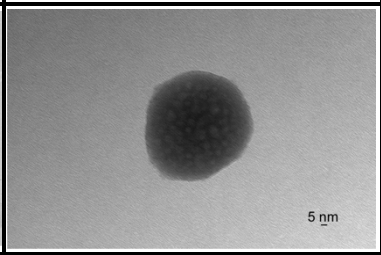	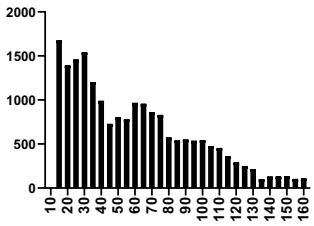
MnPEI	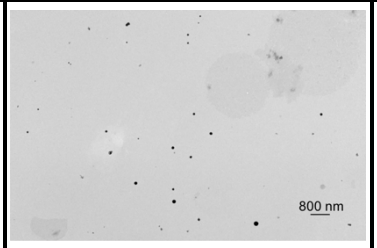	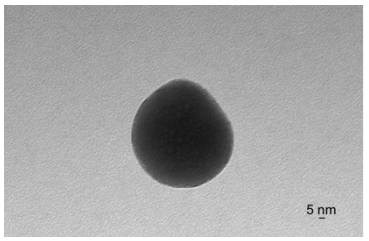	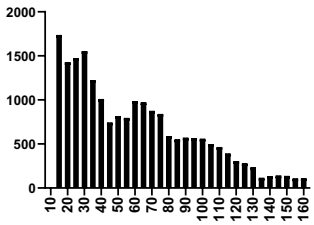
Fe	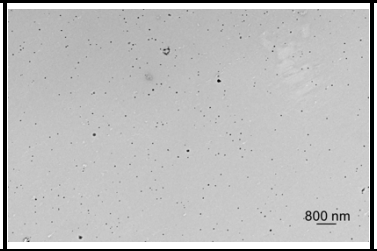	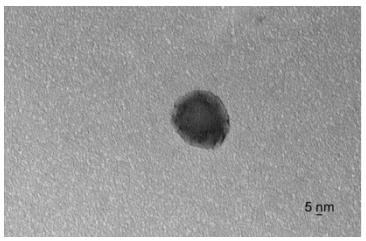	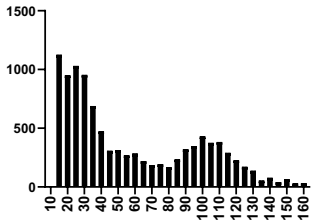
FePEI	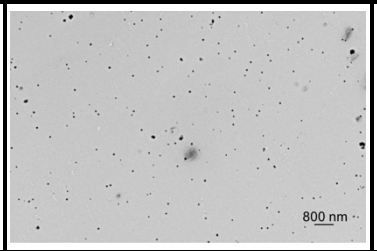	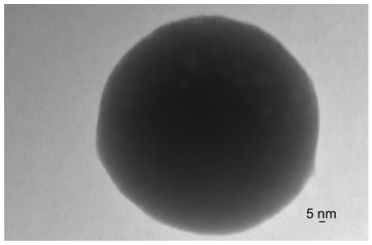	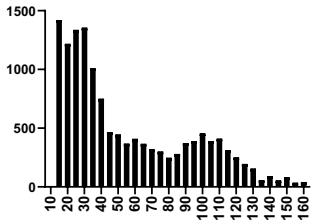
Co	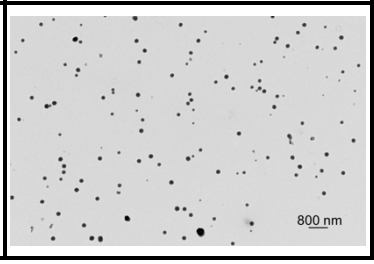	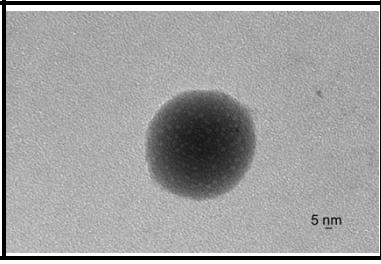	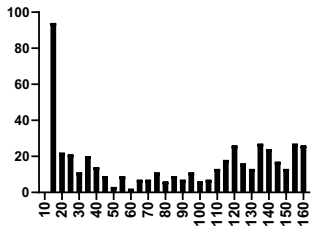

CoPEI	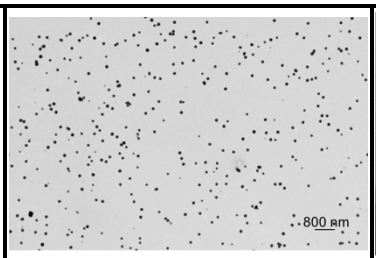	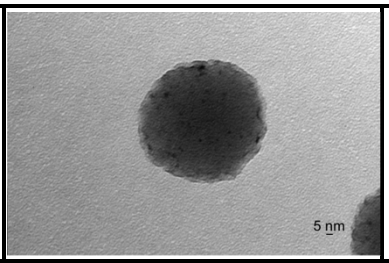	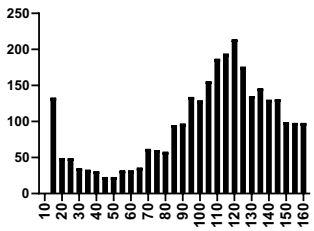
Ni	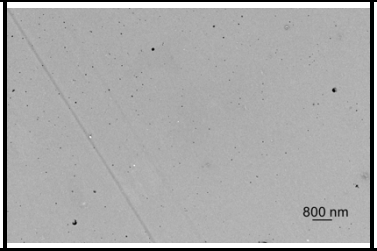	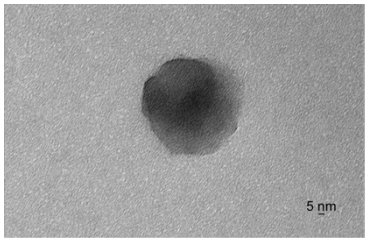	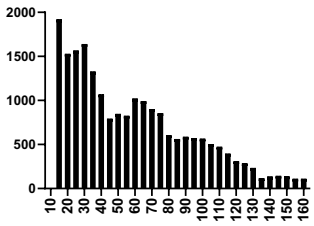
NiPEI	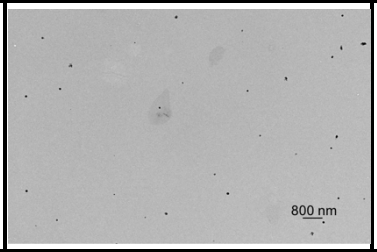	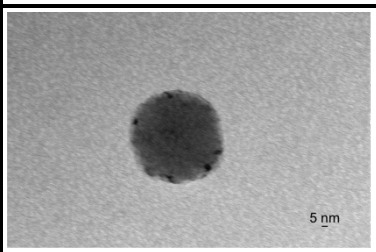	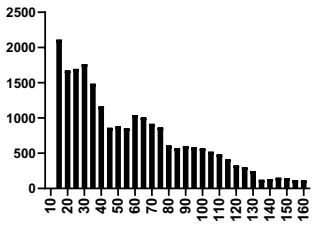
Cu	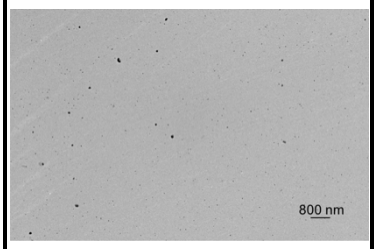	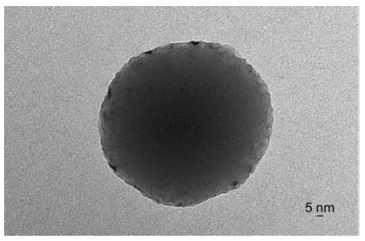	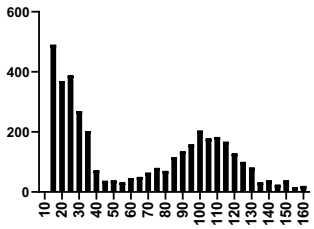
CuPEI	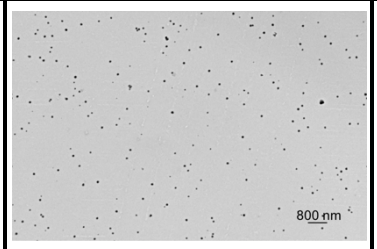	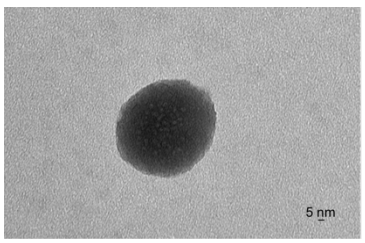	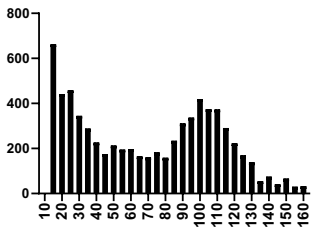
Zn	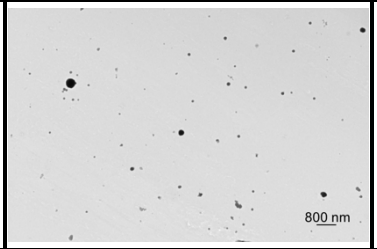	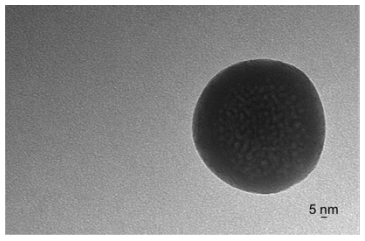	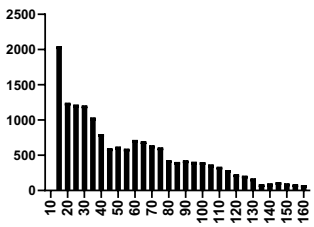
ZnPEI	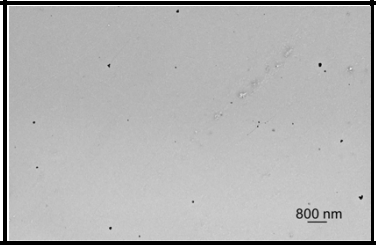	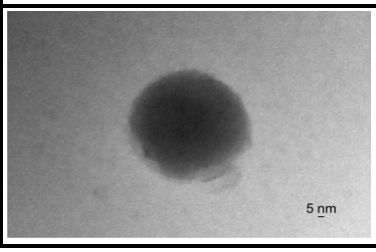	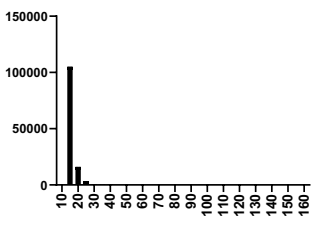

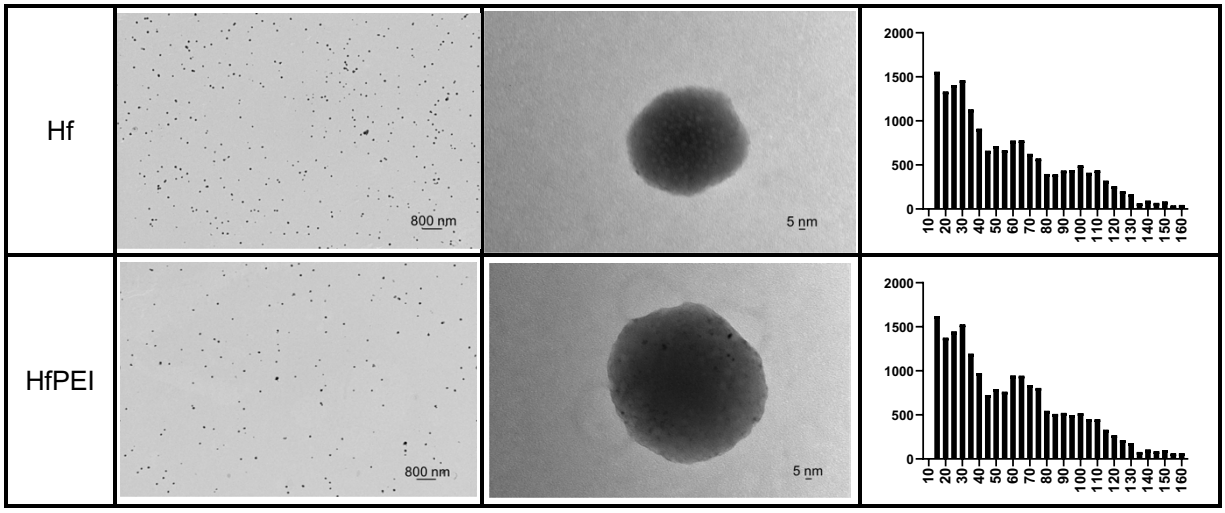

The histograms of Sc and ScPEI NPs are very different. TEM analysis demonstrated inconsistent results. In some cases, such as Sc, Cr, and Zn NPs, PEI incubation decreased the average NP size. In other cases, such as V, Co, and Cu, PEI incubation increased the average NP size. In the cases, such as Ti, Mn, Fe, Ni, and Hf, PEI incubation gave no obvious change in NP size. Various explanations are possible: either the coating process did not work (no size change); resulted in a selective loss of smaller particles during washing (larger particles left); or caused the breakdown of larger particles to smaller ones, or there was a selective loss of larger particles (smaller particles left).

3.3.1.2 Analysis of zeta potentials of NPs

Change in the zeta potential indicates the existence of PEI coating. As explained above, section 3.2.2, change in zeta potential indicates the presence of PEI/NP complexes. It is expected that, due to PEI positive charge, NPs with PEI coating present a more positive zeta potential.

Table 3.3 presents the zeta potential for each NP, where in each plot both PEI-coated and non-coated ones are compared. Colloidal dispersions with a zeta potential between ±10 to ±30 have incipient stability such as the case of V, Mn, NiPEI, CuPEI, Zn, ZnPEI, Hf and HfPEI NPs. A zeta potential between ±30 to ±40 means moderate stability, which is the case of Sc, ScPEI, TiPEI, VPEI, Cr, CrPEI NP solutions and the remaining NP solutions, such as Ti, MnPEI, Fe, FePEI, Co, CoPEI, Ni and Cu have a good stability, since their zeta potential has a value between ±40 to ±60. Fe, Sc, Ni, Cu, Zn, Cr, Co, and Ti NPs showed a more positive zeta potential due to PEI coating. On the other hand, PEI complexes with V, Mn, and Hf NPs showed a more negative zeta potential.

Table 3.4 summarises the TEM and zeta potential data. In general, a higher diameter corresponds to a more negative zeta potential, between coated and non-coated NP pairs. There are exceptions to the correlation found within TEM diameter and the zeta potential data. In the case of Co and CoPEI and Cu and CuPEI NPs pairs, a higher diameter corresponds to a less negative zeta potential.

Table 3.3: Zeta potential for each NP. In each plot, both coated and non-coated NPs are presented.

NP	Zeta potential	NP	Zeta potential
Sc	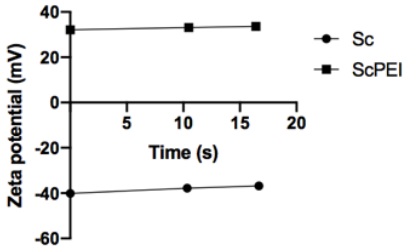	Fe	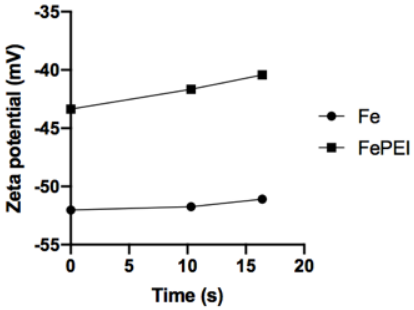
Ti	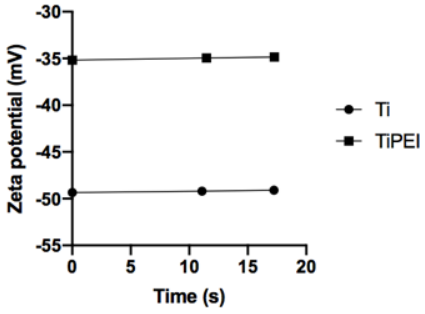	Co	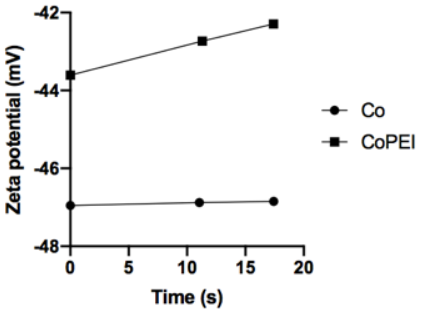
V	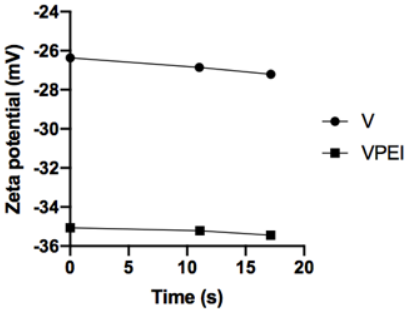	Ni	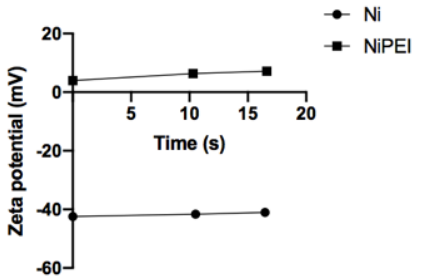

Cr	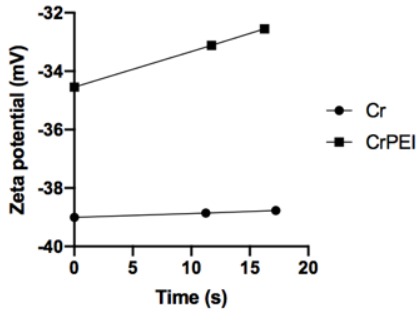 Zeta potential (mV) -32 -34 -36 -38 -40 0 5 10 15 20 Time (s) Cr CrPEI	Cu	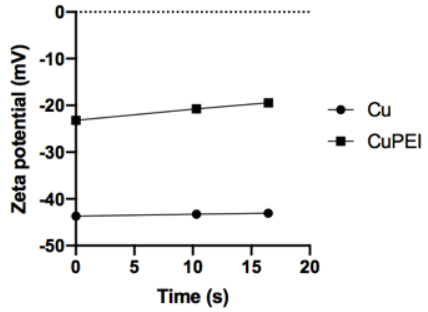 Zeta potential (mV) 0 -10 -20 -30 -40 -50 0 5 10 15 20 Time (s) Cu CuPEI
Mn	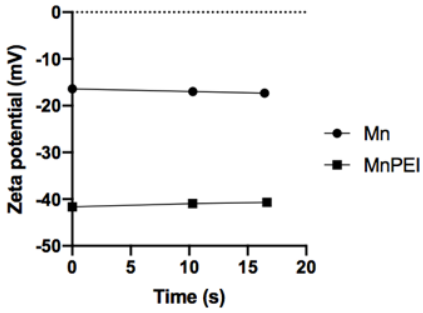 Zeta potential (mV) 0 -10 -20 -30 -40 -50 0 5 10 15 20 Time (s) Mn MnPEI	Zn	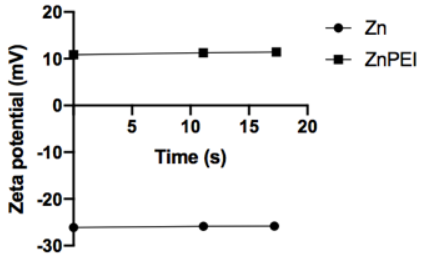 Zeta potential (mV) 20 10 0 -10 -20 -30 5 10 15 20 Time (s) Zn ZnPEI
Hf	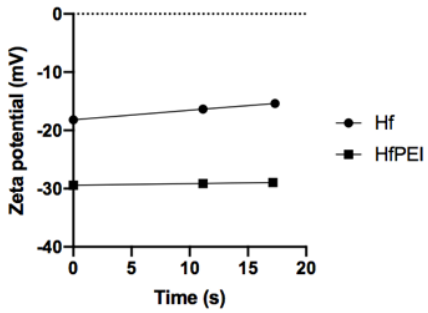 Zeta potential (mV) 0 -10 -20 -30 -40 0 5 10 15 20 Time (s) Hf HfPEI		

Table 3.4: Mean diameters from TEM analysis and mean zeta potential data for each type of NP.

NP type	Mean TEM diameter (nm)	Mean Zeta potential (mV)
Sc	53	-38.23
ScPEI	17	32.97
Ti	57	-49.21
TiPEI	56	-34.99
V	27	-26.81
VPEI	42	-35.24
Cr	88	-38.88
CrPEI	78	-33.40
Mn	59	-16.90
MnPEI	59	-41.09
Fe	58	-51.62
FePEI	55	-41.81
Co	83	-46.89
CoPEI	104	-42.88
Ni	59	-41.68
NiPEI	58	5.84
Cu	65	-43.34
CuPEI	70	-21.12
Zn	56	-25.91
ZnPEI	16	11.20
Hf	56	-16.63
HfPEI	58	-29.16

3.3.2 Catalytic ability

Metal oxide NPs are known for their catalytic ability (Ray & Pal, 2017). To probe the catalytic ability of the different types of NP studied in this thesis, the rate at which each NP decomposed H_2O_2 and generated O_2 was evaluated (Figure 3.2).

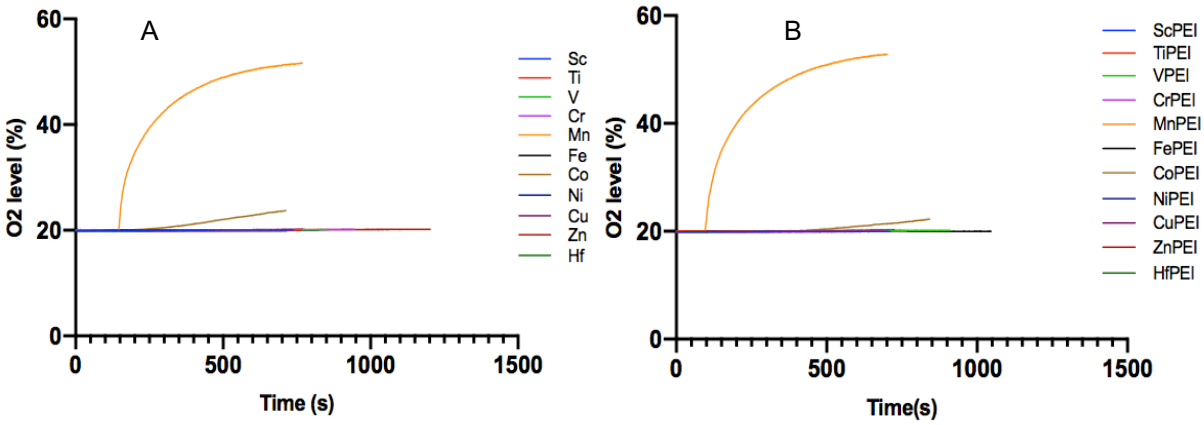

Figure 3.2: Catalytic activity of non-coated (A) and PEI-coated (B) NPs.

The results of the catalytic activity assays for non-coated NPs showed that manganese NP was the most efficient metal oxide NP, capable of decomposing H_2O_2 into O_2. PEI-coated NPs showed similar results to the non-coated NPs.

3.3.3 ROS production

3.3.3.1 ROS probe fluorescence quenching

An important phenomenon that needs to be considered when studying NPs interaction with radiation is the quenching of the fluorescent chemical compound in solution. When the direct measure used is the amount of ROS produced in the sample after irradiation, the presence of NP at the time of the measurement may compromise the real results. This is because NPs surface may interact with the produced ROS before interaction with the probe.

To quantify the effect that each type of NP has on the different probes used to measure the different ROS, quenching results were obtained. The interaction of each type of NP with the fluorescent versions of the probes used, namely 7OH-3-CCA and rhodamine 123, was measured. All results were normalized to the control. In Table 3.5, the quenching results related to 7OH-3-CCA are presented.

Table 3.5: 7OH-3-CCA quenching results for each NP. Each plot compares the coated and non-coated pair of each NP.

NP	CCA quenching	NP	CCA quenching
Sc	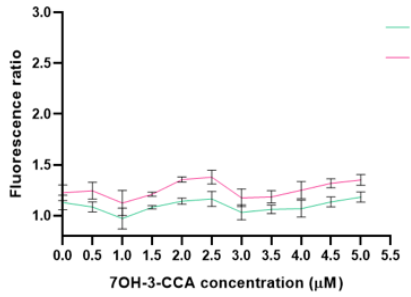	Fe	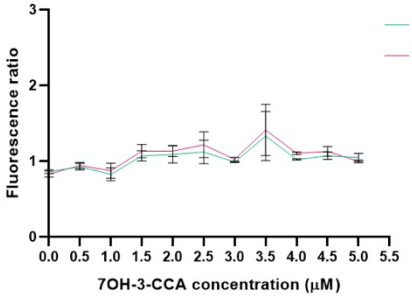
Ti	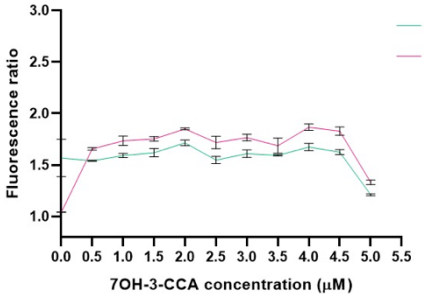	Co	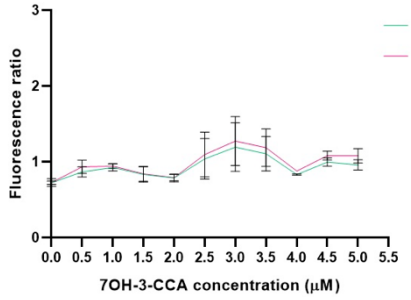
V	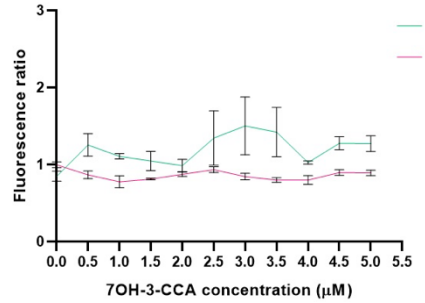	Ni	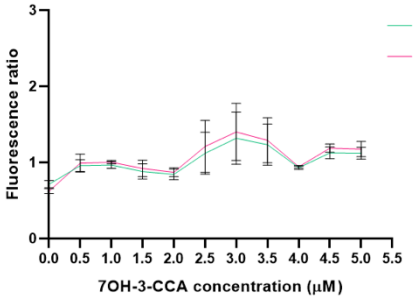
Cr	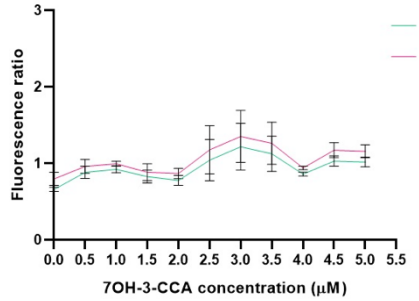	Cu	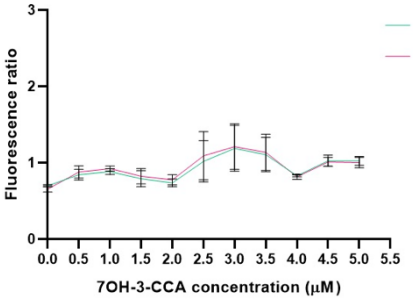

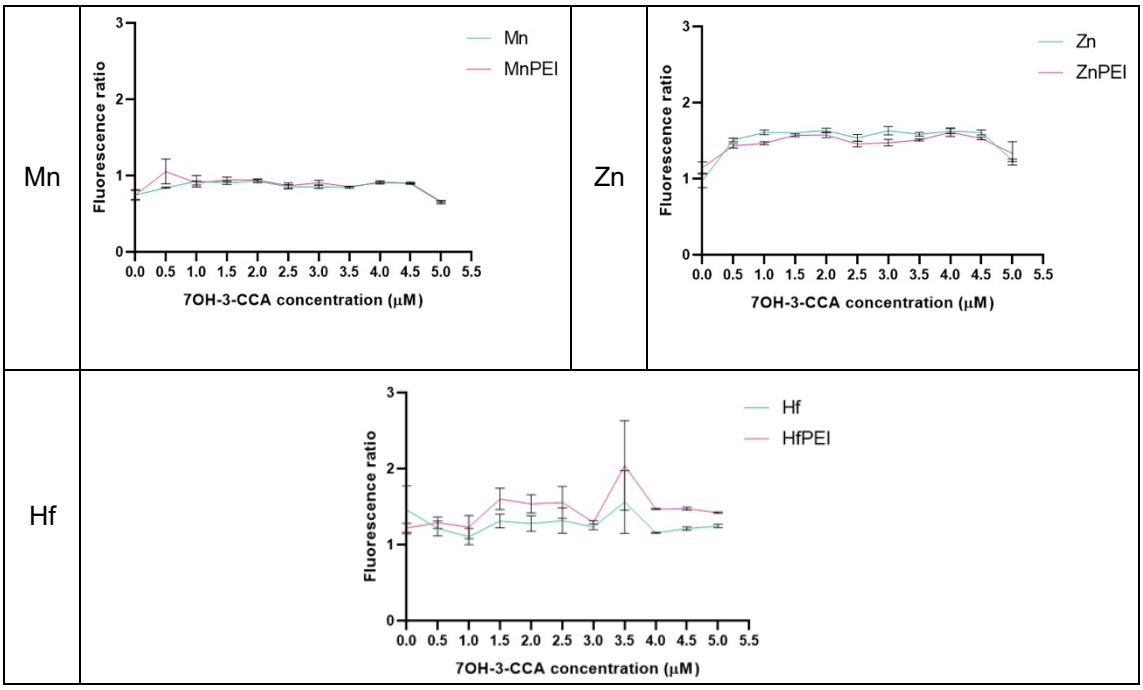

Table 3.6: 7OH-3-CCA quenching significant results correlation table for each NP. Significance was calculated between each NP and the control and between the coated and non-coated pairs using two-way ANOVA and Tukey's post-hoc test with α=0.05. The X symbol indicates no significance.

	control	Sc	ScPEI
Sc	****		****
ScPEI	****	****	

	control	Ti	TiPEI
Ti	****		X
TiPEI	****	X	

	control	V	VPEI
V	**		****
VPEI	****	****	

	control	Cr	CrPEI
Cr	X		****
CrPEI	X	****	

	control	Mn	MnPEI
Mn	****		X
MnPEI	****	X	

	control	Fe	FePEI
Fe	X		**
FePEI	X	**	

	control	Co	CoPEI
Co	X		****
CoPEI	X	****	

	control	Ni	NiPEI
Ni	X		**
NiPEI	X	**	

	control	Cu	CuPEI
Cu	X		X
CuPEI	X	X	

	control	Zn	ZnPEI
Zn	****		X
ZnPEI	****	X	

	control	Hf	HfPEI
Hf	****		***
HfPEI	****	***	

7OH-3-CCA quenching significant results are shown in Table 3.6. The NPs that did not show significance between the coated and non-coated ones were Ti, Mn, Cu and Zn NPs and comparing with control, Cr, Fe, Co, Ni and Cu NPs did not show significant differences, for both coated and non-coated pairs.

Table 3.7 shows Rhodamine 123 quenching results and Table 3.8 shows its significant results. The only NP that did not show significance between the coated and non-coated ones was Mn, for both coated and non-coated NPs, and comparing with control, Zn, Co, MnPEI, and Cr NPs did not show significant results.

Table 3.7: Rhodamine 123 quenching results for each NP. Each plot compares the coated and non-coated pair of each NP.

NP	DHR quenching	NP	DHR quenching
Sc	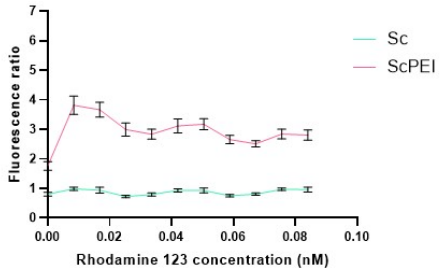	Fe	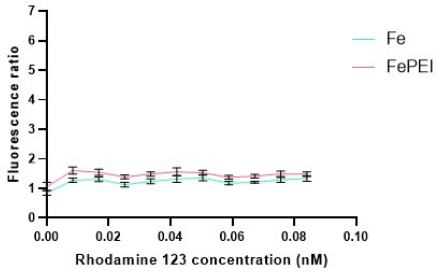
Co	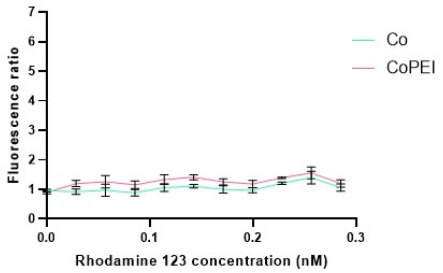	V	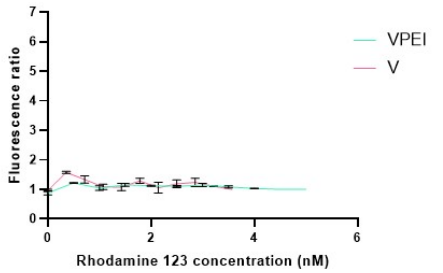
Ni	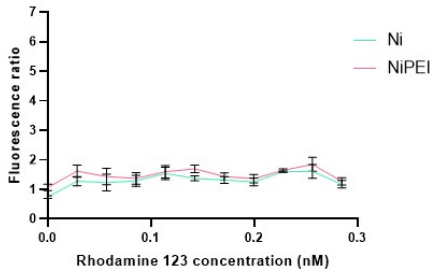	Cr	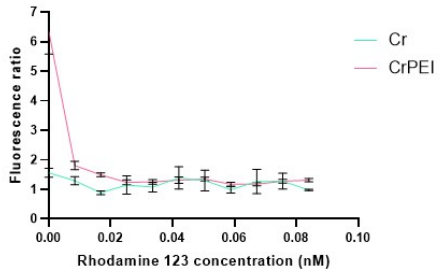
Cu	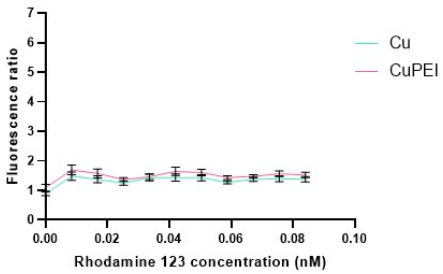	Mn	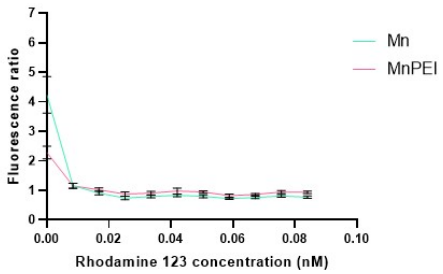
Zn	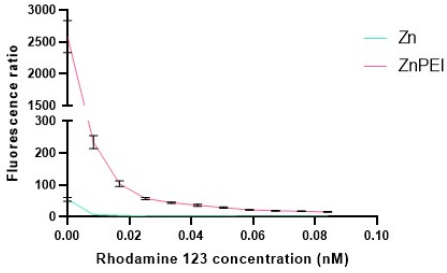	Hf	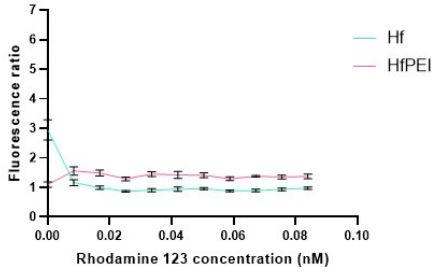

Table 3.8: Rhodamine 123 quenching significant results correlation table for each NP. Significance was calculated between each NP and the control and between the coated and non-coated pairs using two-way ANOVA and Tukey's post-hoc test with α=0.05. The X means no significance.

	control	Sc	ScPEI
Sc	*		****
ScPEI	****	****	

	control	Co	CoPEI
Co	X		****
CoPEI	****	****	

	control	V	VPEI
V	****		**
VPEI	*	**	

	control	Ni	NiPEI
Ni	****		*
NiPEI	****	*	

	control	Cr	CrPEI
Cr	X		****
CrPEI	****	****	

	control	Cu	CuPEI
Cu	****		***
CuPEI	****	***	

	control	Mn	MnPEI
Mn	*		X
MnPEI	X	X	

	control	Zn	ZnPEI
Zn	X		****
ZnPEI	****	****	

	control	Fe	FePEI
Fe	****		****
FePEI	****	****	

	control	Hf	HfPEI
Hf	**		****
HfPEI	****	****	

3.3.3.2 Testing coumarin-3-carboxylic acid (3-CCA) for best dose

To define the dose for all irradiation experiments and study the linearity of the 3-CCA signal, the probe 3-CCA acid was tested for different values of dose such as, 0, 2, 6, 8 and 10 Gy, and different concentrations, as shown in Figure 3.3.

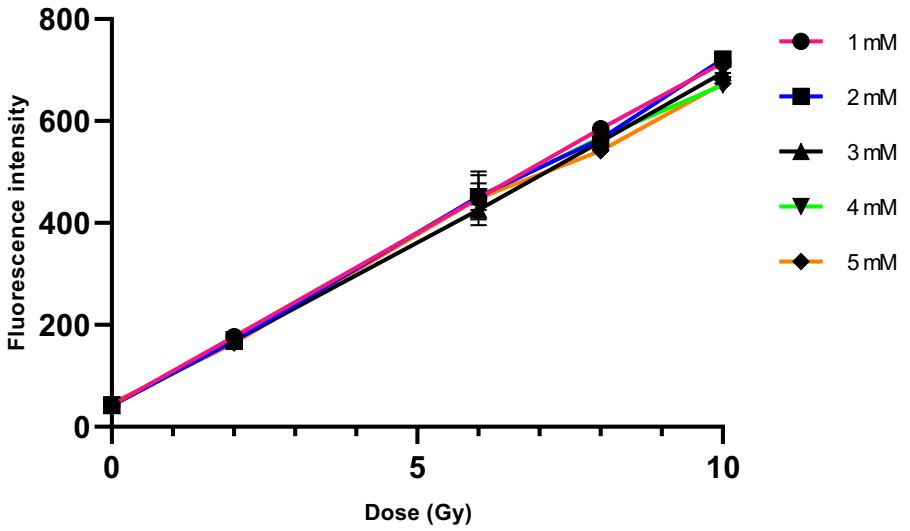

Figure 3.3: 3-CCA signal for different doses at different concentrations.

As it can be seen from the results on Figure 3.3, the highest fluorescence signal was achieved for a 10 Gy dose and there was no evidence of a deviation from linearity (R^2=0.98), so this value was chosen for the remaining of the irradiation experiments.

3.3.3.3 Evaluation of hydroxyl radicals in normoxia and hypoxia conditions

To evaluate the amount of hydroxyl radicals produced by each type of NP under normoxia and hypoxia conditions 3-CCA was the molecule used. Figure 3.4 shows the HO· production for each NP under both conditions.

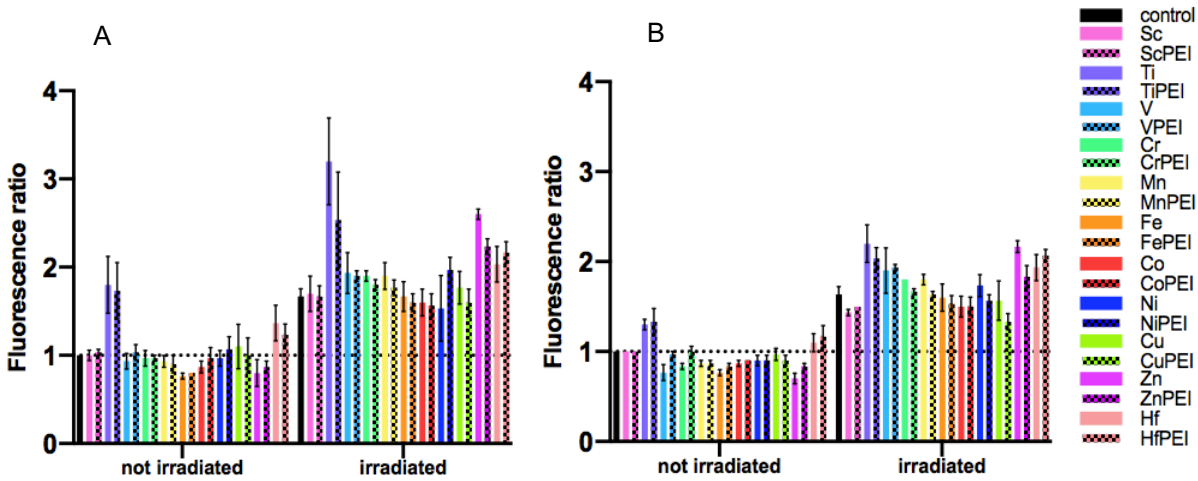

Figure 3.4: HO• production for each type of NP in both conditions. A - is related to normoxia conditions; B - is related to hypoxia conditions. The values were normalized to the non-irradiated control.

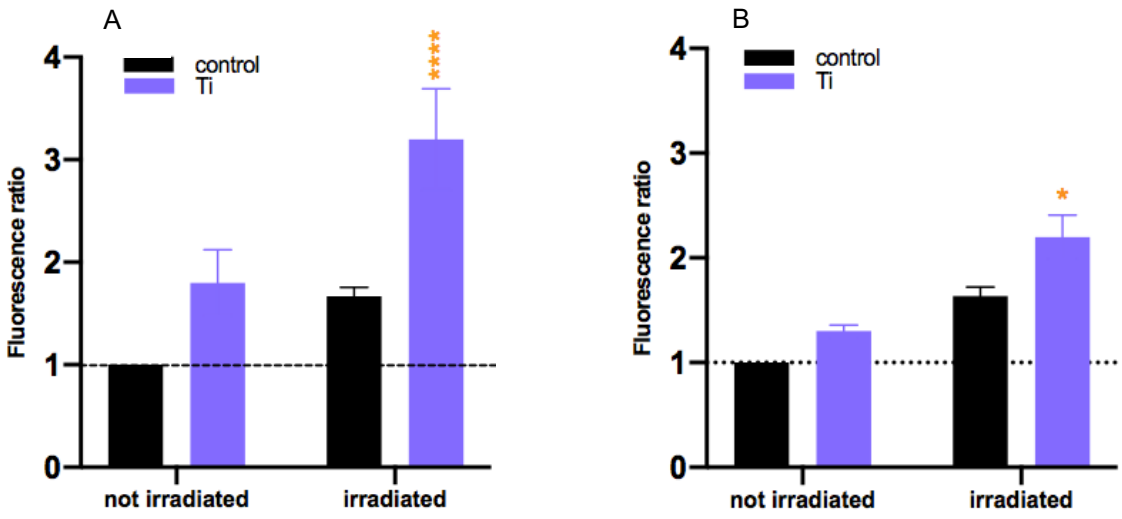

Figure 3.5: Significance results for $HO^{\bullet}$ using Prism Graphpad with two-way ANOVA and Tukey's post-hoc test with α=0.05, for hydroxyl radical production in normoxia (A) and hypoxia (B) conditions. The significance results showed are between the NP and the respective control (irradiated control vs irradiated Ti NP).

Results in Figure 3.5 do not consider the not irradiated data, so they do not show the actual $HO^{\cdot}$ production. On the other hand, these results are shown to outline the behaviour of certain NPs without radiation. As it can be seen, Ti NPs produce hydroxyl radicals without the presence of radiation.

Representation of the ratio between the irradiated and non-irradiated 3-CCA data is shown in Figure 3.6.

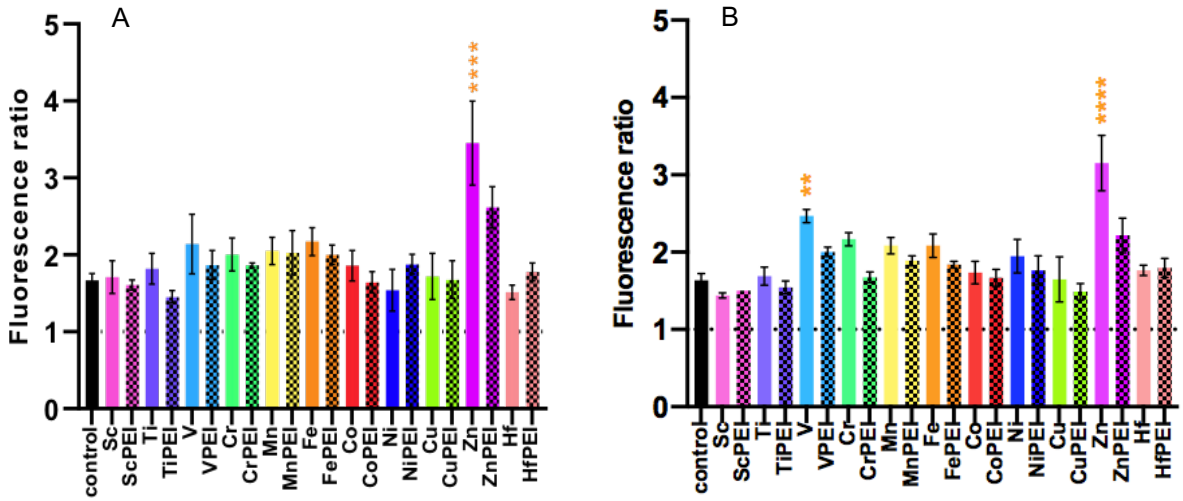

Figure 3.6: $HO^{\bullet}$ production for each type of NP in both conditions after taking the ratio between the irradiated and non-irradiated values. A - is related to normoxia conditions; B - related to hypoxia conditions. Significance was calculated between each NP and the control using one-way ANOVA and Dunnett's post-hoc test with α=0.05.

From the ratio results one can see that Zn NPs showed high significance in both conditions, normoxia and hypoxia. Also, V NPs showed significance in hypoxia conditions although not as high as Zn ones.

3.3.3.4 Evaluation of hydrogen peroxide in normoxia conditions

To evaluate the amount of hydrogen peroxide produced by each type of NP under normoxia condition DHR was the molecule used. Results are presented in Figures 3.7 and 3.8.

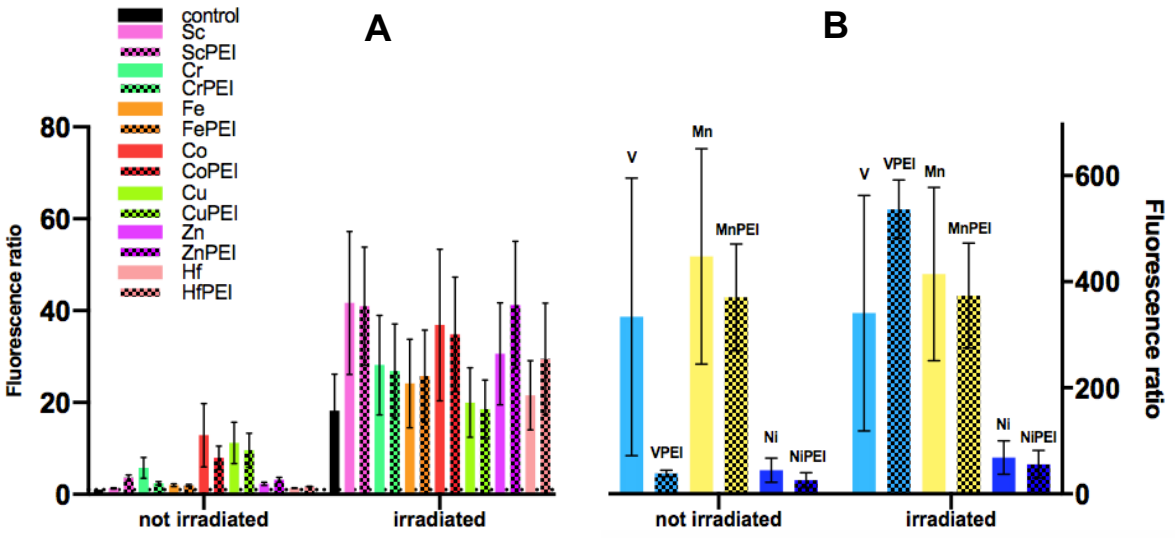

Figure 3.7: H_2O_2 production for each type of NP in normoxia conditions. **A** and **B** are from the same experiment (same control), but due to scale effects NPs were divided into two different plots. The values were normalized to the non-irradiated control.

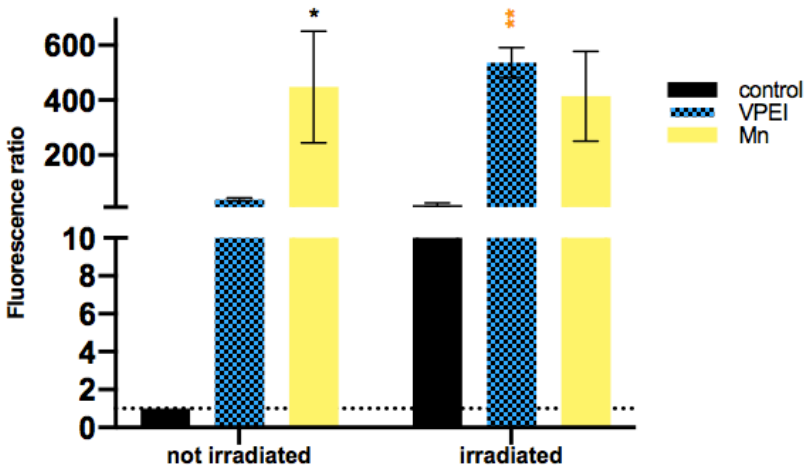

Figure 3.8: Significance results for H_2O_2 using Prism Graphpad with two-way ANOVA and Tukey's post-hoc test with α=0.05, for hydrogen peroxide production for each type of NP in normoxia conditions. The significance results showed are between the NP and the respective control (not irradiated control vs not irradiated Mn; irradiated control vs irradiated VPEI).

Once again, data in Figure 3.8 cannot be used to conclude about the actual H_2O_2 yield since they do not consider the not irradiated values. This data is important to show that Mn NPs show high hydrogen peroxide production without radiation. Other NPs, such as, MnPEI, V, VPEI, Ni and NiPEI also showed a high H_2O_2 yield without the presence of radiation, although not significant.

Representation of the ratio between the irradiated and non-irradiated DHR data is shown in Figure 3.9.

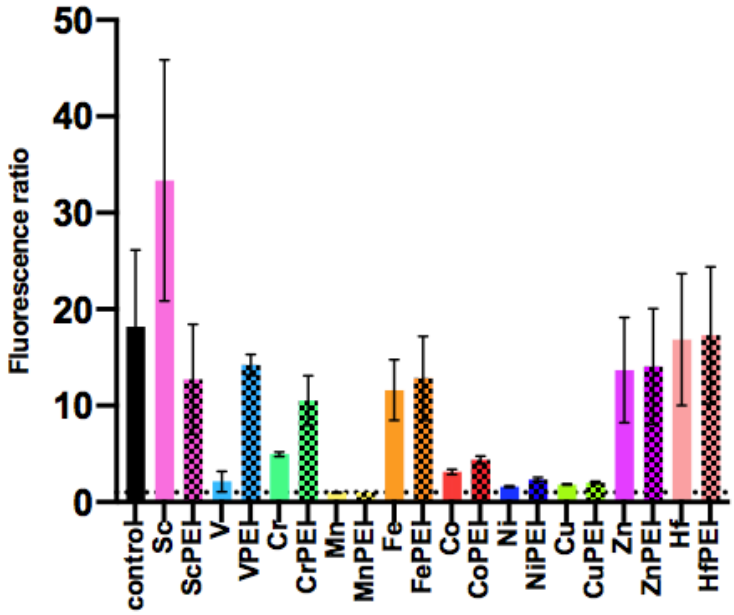

Figure 3.9: H_2O_2 production for each type of NP in normoxia conditions after taking the ratio between the irradiated and non-irradiated values. Significance was calculated using a one-way ANOVA with Dunnett's post-hoc test and α=0.05 and is related to the control sample.

For hydrogen peroxide the results showed no significance in the data. Error bars were high which did not allow a precise measurement for hydrogen peroxide production, but overall, it is possible to observe that Sc NPs may produce the highest amount of hydrogen peroxide when compared to the control.

3.3.3.5 Quenching results effect on radiosensitisation

Quenching effects were considered for both 3-CCA and DHR probes as shown in Figures 3.10 and 3.11, respectively.

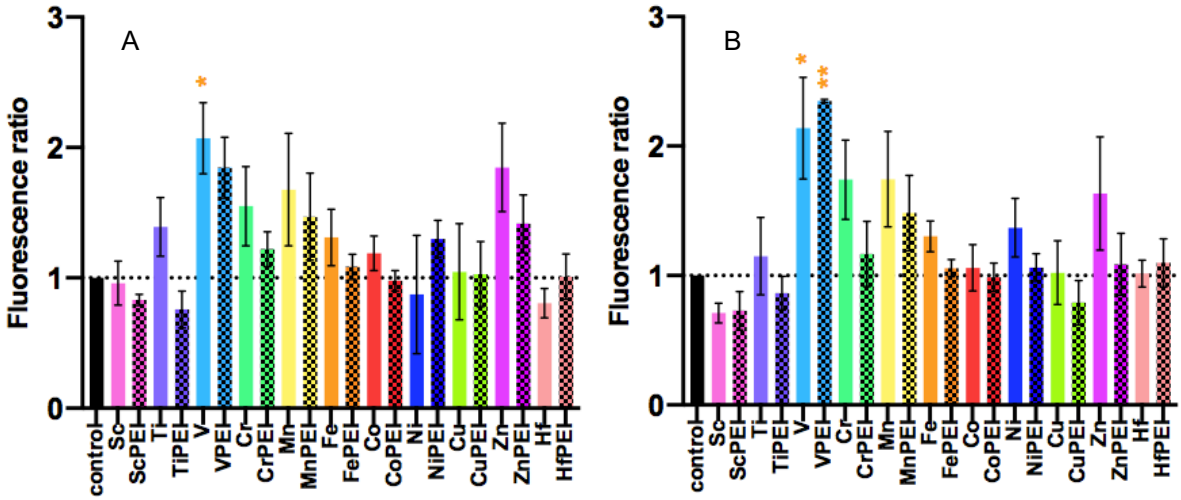

Figure 3.10: HO• production for each type of NP in both conditions considering quenching results. A – normoxia; B – hypoxia conditions. Non-irradiated data was subtracted to the irradiated data, normalized to the control, and divided by the averaged of the quenching results for each NP. The significant results between each NP and the control were calculated using a one-way ANOVA with Dunnett's post-hoc test and α=0.05.

For 3-CCA probe, the inclusion of the quenching measurements leads to a different interpretation of the results. The hydroxyl radical production, as shown in Figure 3.10, the results showed significance for vanadium NPs, meaning that these NPs under both conditions produce the highest amount of hydroxyl radical when irradiated with 6 MeV X-rays. For hypoxia conditions, the coated version of vanadium NPs also showed significant results. Furthermore, although without any significance, it is possible to see that Cr, Mn and Zn NPs may produce a fluorescence signal that is 1.5 times higher than the amount produced without the presence of these NPs.

For hydrogen peroxide production, under normoxia conditions, after taking into account the quenching results the results remain very similar. Figure 3.11 shows that VPEI NPs lead to a significant increase on the fluorescence signal.

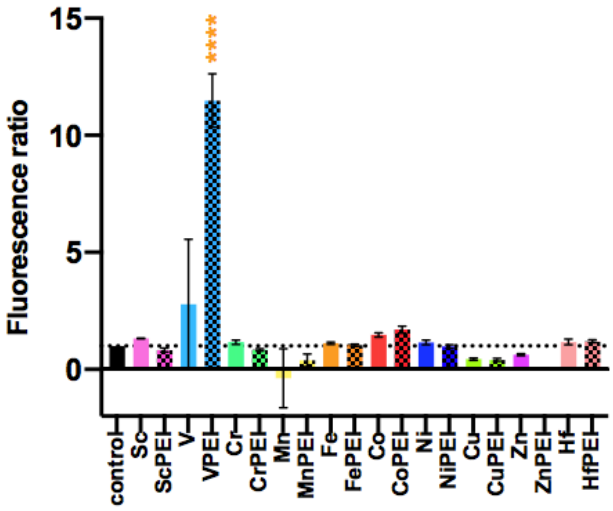

Figure 3.11: H_2O_2 production for each type of NP in normoxia conditions considering quenching results. Non-irradiated data was subtracted to the irradiated data, normalized to the control, and divided by the averaged of the quenching results for each NP. The significant results between each NP and the control were calculated using a one-way ANOVA with Dunnett's post-hoc test and α=0.05.

3.3.3.6 Spearman correlation results for fluorescence data

A Spearman correlation analysis was conducted among $HO^{\cdot}$ and H_2O_2 and the correlation coefficients (r_S) were calculated. Cohen´s standard was used to evaluate the strength of the relationships, where coefficients between 0.10 and 0.29 represent a small effect size, coefficients between 0.30 and 0.49 represent a moderate effect size, and coefficients above 0.50 indicate a large effect size (Cohen, 1988). This correlation requires that the relationship between each pair of variables does not change direction. This means that if the points on the scatterplot between any pair of variables appear to shift from a positive to negative or negative to positive relationship, the assumption is violated. Figure 3.12 presents the scatterplots of the correlations that take into account all the non-coated NPs studied. A regression line has been added to assist the interpretation.

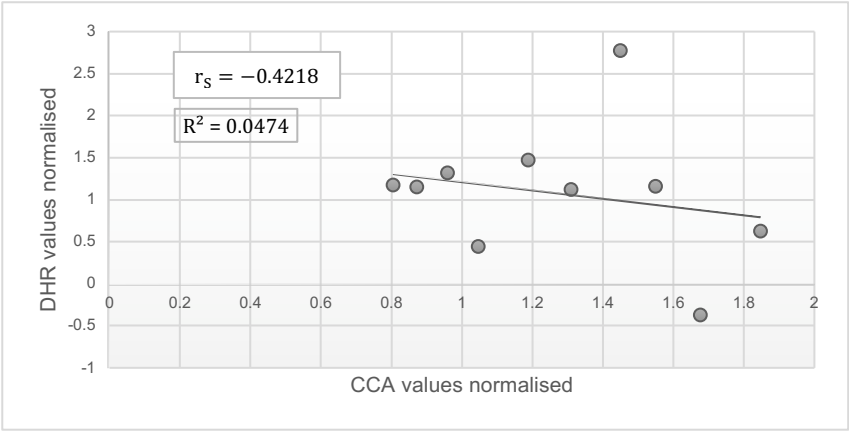

Figure 3.12: DHR vs CCA results scatterplots between each variable for all the NPs with the regression line. R^2 and r_S values were added.

A negative correlation was observed between $HO^{\cdot}$ (CCA) and H_2O_2 (DHR) values (r_S = -0.4218) as shown in Figure 3.12, although the results were not significant with $p > 0.05$. The correlation coefficient between H_2O_2 and $HO^{\cdot}$ was -0.4218, indicating a moderate effect size. This correlation indicates that as $HO^{\cdot}$ increases, H_2O_2 tends to decrease.

3.3.4 Nanoparticle cytotoxicity results

3.3.4.1 Clonogenic assay

The toxicity of each NP was assessed through a clonogenic assay, as shown in Table 3.9. In this experiment, six different concentrations, from 0 to 100 μg/ml, were used in HSC-3 cells.

Table 3.9: Cell toxicity for each type of NP. Each plot compares the toxicity between the coated and non-coated version of each NP. The values were normalized to the control.

NP	Cell toxicity	NP	Cell toxicity
Sc	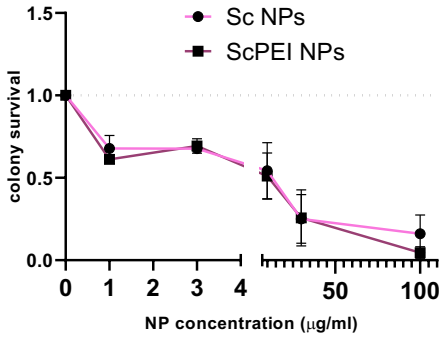	Fe	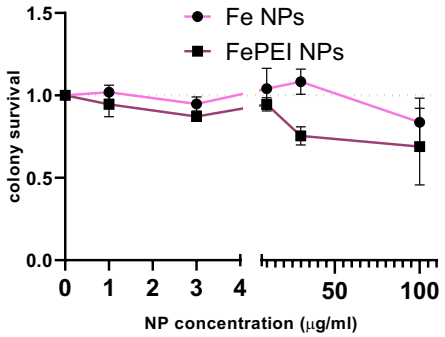
Ti	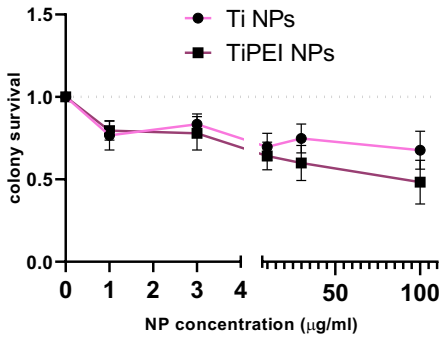	Co	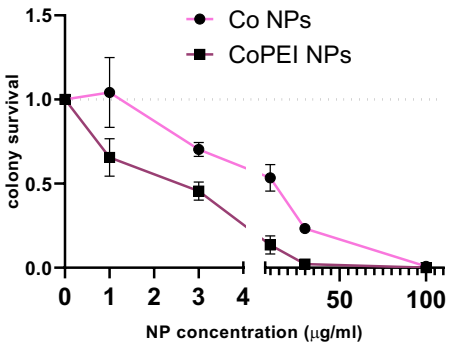
V	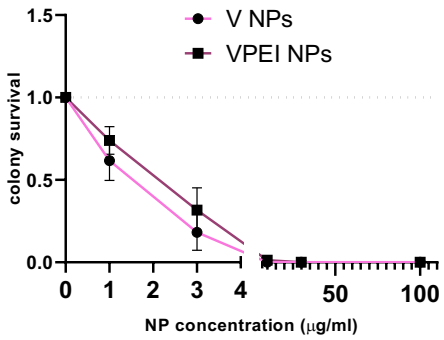	Ni	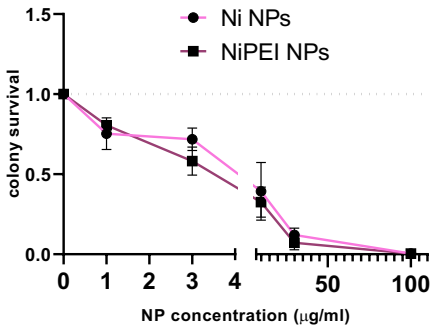
Cr	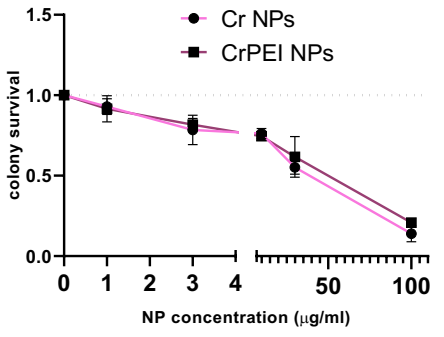	Cu	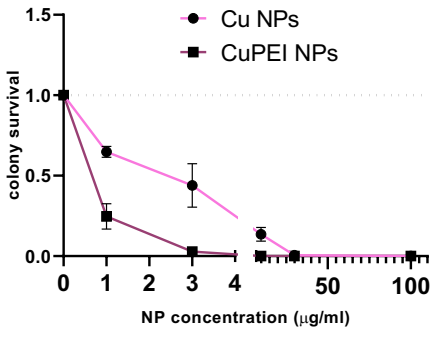

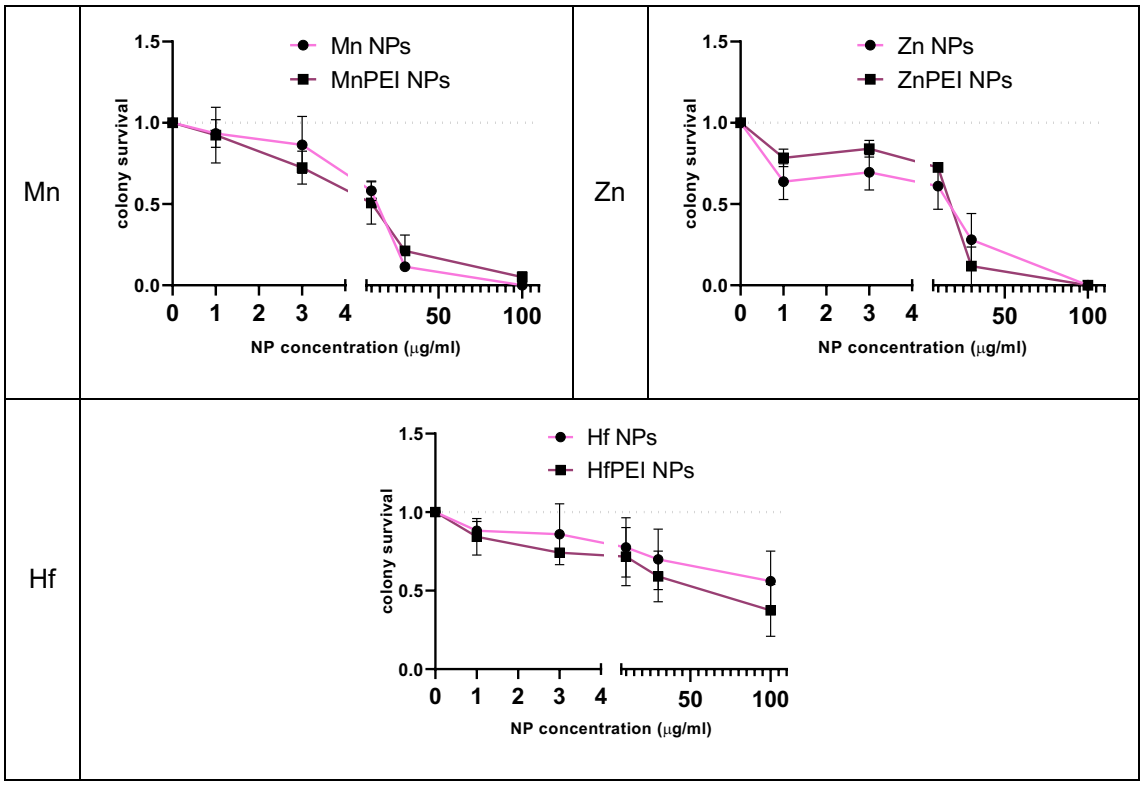

V and Cu NPs presented high toxicity towards HSC-3 cells, with less than 50% of survival at a concentration of 3 μg/ml. Titanium, iron and hafnium NPs were less toxic even at the maximum concentration of 100 μg/ml. Except for vanadium and zinc NPs, it can be seen from the results that PEI coating contributed to reduce the metal oxide NPs toxicity in most of the NPs. For Cr, Ni and V NPs the toxicity is very similar between the coated and non-coated NPs, while for Cu and Co NPs toxicity results are quite different between the coated and non-coated pairs.

3.3.4.2 Inductively coupled plasma mass spectrometry (ICP-MS)

The effect of the NPs in cancer cells is affected by the cellular uptake. To deepen the knowledge of the contribution of the NPs for cancer cell death in RT treatment, cell uptake for each NP was studied through ICP-MS, a technique that measures the concentration of the metals that constitute each NP within or at the surface of cells. Results are shown in Figures 3.13 and 3.14. Table 3.10 shows the initial loading metal concentration which takes into account only the concentration of the metal and not the one from the metal oxide.

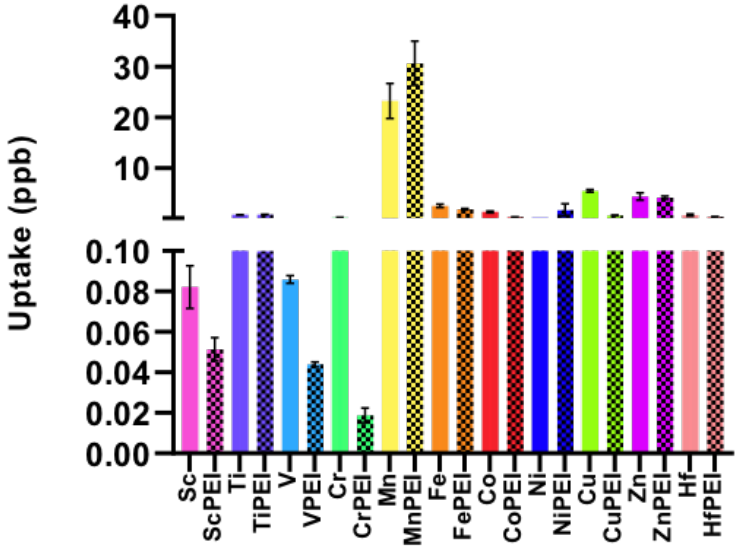

Figure 3.13: ICP-MS uptake results for each type of NP.

Table 3.10: Loading metal concentration for each type of NP.

Type of nanoparticle	Loading metal (mg/ml)
Sc	0.40
ScPEI	0.40
Ti	3.33
TiPEI	2.67
V	0.12
VPEI	0.29
Cr	6.00
CrPEI	6.00
Mn	1.67
MnPEI	2.10
Fe	64.29
FePEI	42.86
Co	1.50
CoPEI	0.50
Ni	1.00
NiPEI	1.00
Cu	0.25
CuPEI	0.06
Zn	6.00
ZnPEI	3.00
Hf	18.33
HfPEI	6.67

From the uptake results shown in Figure 3.13, it is possible to conclude that Mn and MnPEI NPs are the ones with the highest uptake. Fe and FePEI NPs have the highest loading concentration, as shown in Table 3.10, although their uptake was very similar to NPs such as Co, CoPEI, Ni, NiPEI, Cu, CuPEI,

Cr, Ti, TiPEI, Hf, HfPEI, Zn and ZnPEI. All these NPs had similar uptake values, independently of loading concentrations. Cu NPs, both coated and non-coated, are worth mentioning, since they have one of the lowest loading metal concentration, but a quite high uptake compared to the other types of NPs.

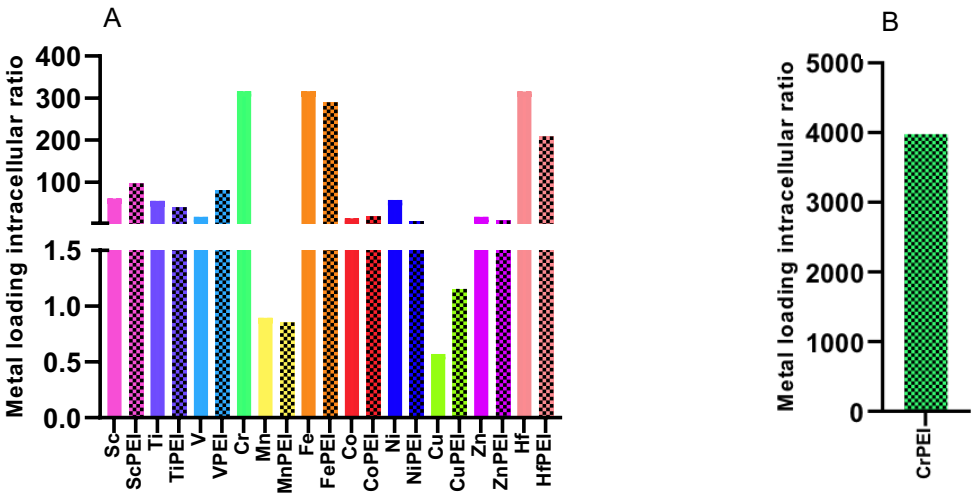

Figure 3.14: ICP-MS metal loading intracellular ratio results for each type of NP. **A** and **B** are from the same experiment (same control), but due to scale effects NPs were divided into two different plots.

The ICP-MS plot in Figure 3.14 represents the metal loading intracellular ratio for each NP. The higher this ratio, higher the number of NPs left outside the cell compared to the number inside of the cell. As shown in Figure 3.14, CrPEI NP is the one that exhibits the highest ratio. It can be concluded that this type of PEI-coated NP does not diffuse across the cell membrane. Other types of NPs that had a low intracellular intake and can be outlined are Cr, Hf, PEI-coated Hf, Fe, and PEI-coated Fe, although with a much lower value when compared to CrPEI. On the other hand, NPs such as Mn, MnPEI, Cu and CuPEI showed a low ratio, meaning that these NPs have a high uptake in HSC-3 cells.

3.3.4.3 Irradiation of cancer cells in normoxia and hypoxia

To understand how these metal oxide NPs would improve the RT treatment, HSC-3 cells were used. The interaction between the NPs, cells and radiation was studied using a clonogenic assay where the number of viable cell colonies was counted. The cell irradiation results for both normoxia and hypoxia conditions are shown in Figure 3.15.

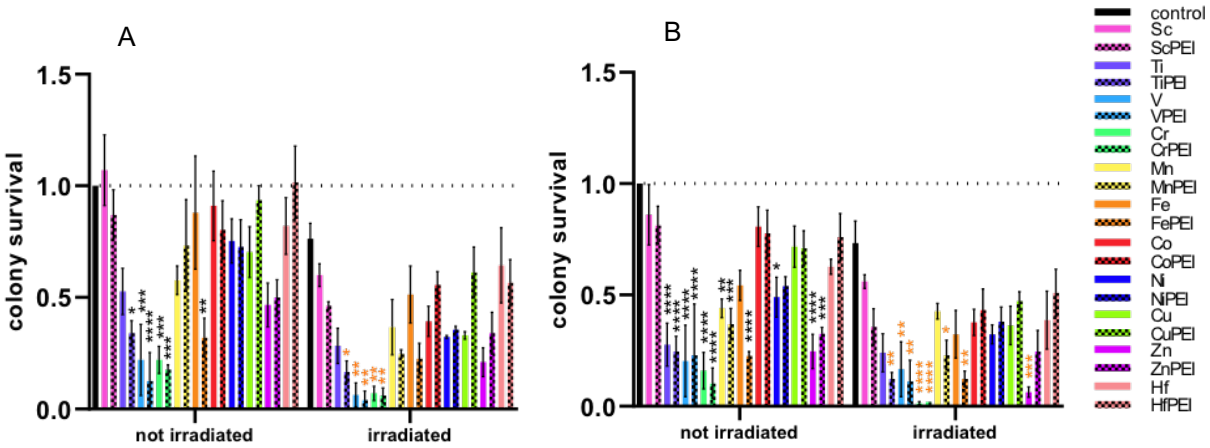

Figure 3.15: HSC-3 cell clonogenic assay for each type of NP in both conditions. A – normoxia; B – hypoxia conditions. Significance was calculated using two-way ANOVA with Tukey's post-hoc test and α=0.05. Significant differences are compared to the respective control (black asterisks are relative to the not irradiated control and orange asterisks are relative to the irradiated control).

In both normoxia and hypoxia conditions, radiation lowered the survival rate (Figure 3.15). In normoxia conditions, TiPEI, V, VPEI, Cr and CrPEI NPs showed the highest effect (Figure 3.15A). Moreover, although not significant, all NPs presented an effect due to radiation under these conditions demonstrating their radiosensitising effect.

For hypoxia conditions, in Figure 3.15B, TiPEI, V, VPEI, Cr, CrPEI, MnPEI, FePEI and Zn NPs showed the highest effect in these cells. Overall, all NPs showed a decrease in cell survival when irradiated.

The results for the ratio between the irradiated and non-irradiated values are presented in Figure 3.16.

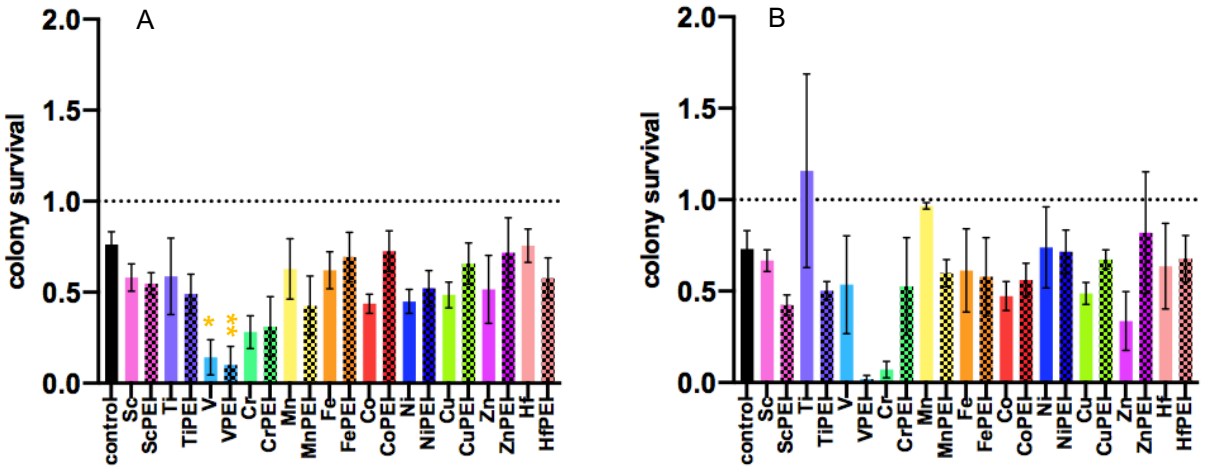

Figure 3.16: HSC-3 cell clonogenic assay for each type of NP in both conditions after taking the ratio between the irradiated and non-irradiated values. A – refers to normoxia; B – refers to hypoxia conditions. Significance was calculated using one-way ANOVA with Dunnett's post-hoc test and α=0.05. Significant differences are compared to the respective control.

Only normoxia conditions showed significant results for V and VPEI NPs. Also, in these conditions and without significance, Cr and CrPEI showed a low number of cell survival. In hypoxia conditions, results did not showed significance although VPEI, Cr and Zn NPs had the lowest value of cell survival.

3.3.4.4 Spearman correlation results for clonogenic data

A Spearman correlation analysis was conducted among cell irradiation and ICP-MS data and the correlation coefficients (r_S) were calculated. Once again, Cohen´s standard was used to evaluate the strength of the relationships. Figure 3.17 presents the scatterplots of the correlations that take into account all the non-coated and coated NPs studied for both normoxia and hypoxia conditions. A regression line has been added to assist the interpretation.

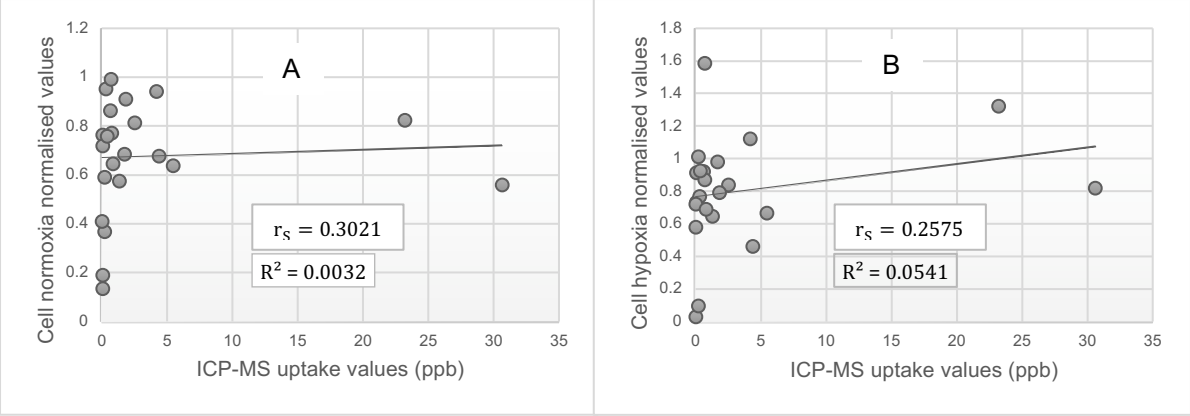

Figure 3.17: Cell irradiation vs ICP-MS results scatterplots between each variable for all the NPs with the regression line. R^2, and r_S values added. A- for normoxia; B – for hypoxia.

A positive correlation was observed for both conditions between cell irradiation and ICP-MS values, as shown in Figure 3.17, although the results were not significant with $p > 0.05$. The correlation coefficients between cell irradiation and ICP-MS were 0.3021 and 0.2575 for normoxia and hypoxia conditions, respectively. These results show a small effect size in normoxia conditions and a moderate effect size in the case of hypoxia conditions. This correlation indicates that as the uptake increases, cell survival tends to increase.

3.3.5 Spearman correlation results between fluorescence and clonogenic data

A Spearman correlation analysis was conducted among fluorescence and clonogenic data and the correlation coefficients (r_S) were calculated. Cohen´s standard was used to evaluate the strength of the relationships. Clonogenic data was corrected for the uptake values obtained from the ICP-MS results before the analysis.

Figures 3.18 and 3.19 present the scatterplots of the correlations that take into account all the non-coated and coated NPs studied. A regression line has been added to assist the interpretation.

Figure 3.18 shows the scatterplots between CCA fluorescence data and cell irradiation data for both normoxia (Figure 3.18A) and hypoxia (Figure 3.18B) conditions. A negative correlation was observed between $HO^{\cdot}$ (CCA) and cell irradiation values with r_S = -0.4082 and r_S = -0.3484 for both normoxia and hypoxia, respectively, although the results were not significant with $p > 0.05$. The correlation coefficients were between 0.3 and 0.49, which according to Cohen's standard indicates a moderate effect size for both conditions. This correlation indicates that as $HO^{\cdot}$ increases, cell survival tends to decrease.

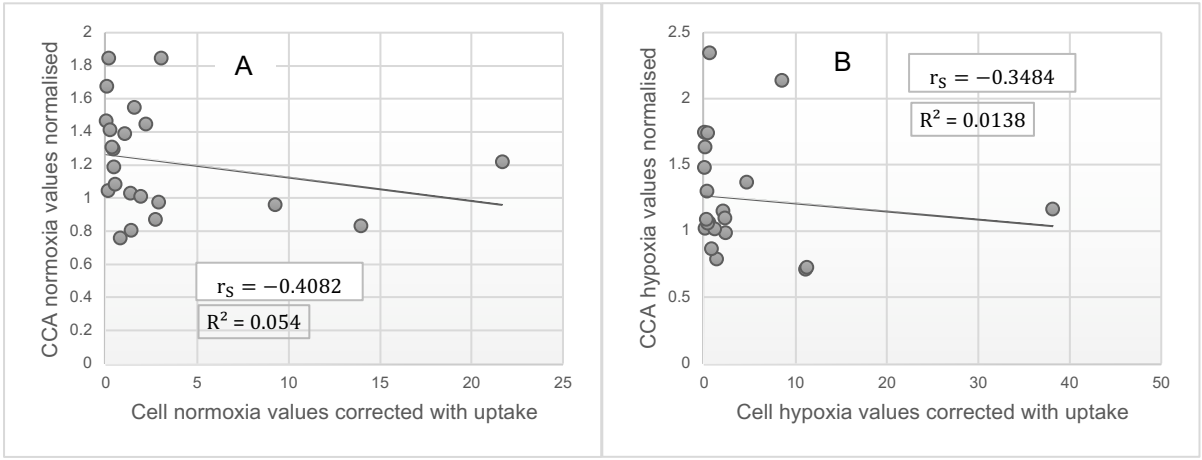

Figure 3.18: CCA vs cell irradiation results scatterplots between each variable for all the NPs with the regression line. R^2, and r_S values added. A- for normoxia; B- for hypoxia.

Figure 3.19 shows the scatterplots between DHR fluorescence data and cell irradiation data for normoxia conditions. A positive correlation was observed between H_2O_2 (DHR) and cell irradiation values with r_S = 0.6075. The correlation coefficient was higher than 0.5, which according to Cohen's standard indicates a large effect size. This correlation indicates that as H_2O_2 increases, cell survival tends to increase.

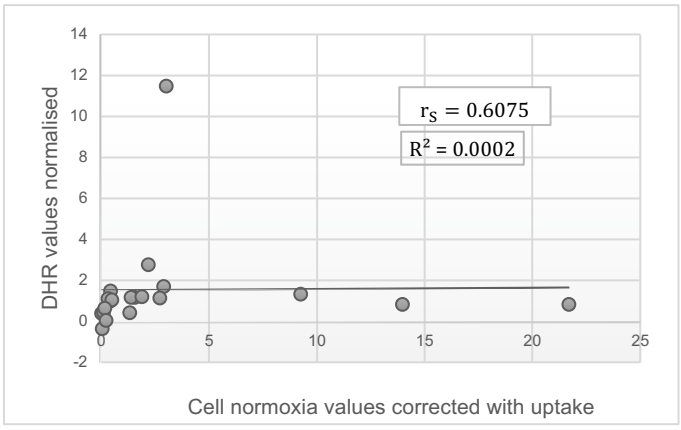

Figure 3.19: DHR vs cell irradiation results scatterplots between each variable for all the NPs with the regression line. R^2, and r_S values added.

3.4 Discussion

In this part of the thesis different types of NPs of metal oxides that are known for their catalytic ability, such as Mn and Cu (Haruta et al., 1987) or Fe known for its surface-catalysed Haber-Weiss cycle and Fenton reactions (Klein et al., 2012), were studied aiming the understanding of their interaction with cancer cells.

It is known from previous studies (Alkilany & Murphy, 2010) that coating with an organic molecule may sometimes help in their uptake by cells. This reason together with the low molecular weight of the PEI molecule, to decrease the interference with the radiosensitisation ability of the NPs, made this molecule the coating of choice for the NPs. To assess the presence of the PEI molecule at the NP surface zeta potential technique was used and the results showed a change in the charge between the coated NPs and their respective non-coated pair. Furthermore, the effect of PEI coating on the radiosensitising capacity of NPs was evaluated and the results showed that the coating overall did not had a great impact on this property. These conclusions are based on the fact that PEI molecule has bound to all the NPs equally, but on the basis of TEM and zeta potential results we are not confident that the coating happened equally for all NPs. Based on the ICP-MS results from Figures 3.12 and 3.13, one can conclude that the PEI coating did not improve cellular uptake.

Experiments were performed to assess the intrinsic ROS production and cellular radiosensitising ability of each NP and NP-PEI. These experiments are important to understand how any improvements in intrinsic ROS production are translated to the cancer cell environment.

In Table 3.11 a summary of the results regarding each NP.

Table 3.11: Summary of the results for each type of NP, where HO• and H_2O_2 production data include the quenching data. Highlighted in red boxes are the NPs with the most promising results in relation to all the parameters studied.

NP	HO • normoxia	HO • hypoxia	H_2O_2	IC50 toxicity (µg/ml)	ICP-MS (ppb)	Clonogenic normoxia	Clonogenic hypoxia
control	1.00	1.00	1.00			0.76	0.73
Sc	0.96	0.71	1.32	13.30	0.08	0.58	0.67
ScPEI	0.83	0.73	0.83	10.40	0.05	0.55	0.42
Ti	1.39	1.15	N/A	N/A	0.75	0.59	1.16
TiPEI	0.75	0.86	N/A	86.70	0.83	0.49	0.50
V	2.07	2.14	2.78	1.60	0.09	0.14	0.53
VPEI	1.84	2.35	11.49	2.20	0.04	0.10	0.02
Cr	1.55	1.74	1.16	39.60	0.24	0.28	0.07
CrPEI	1.22	1.17	0.84	50.50	0.02	0.31	0.53
Mn	1.68	1.74	-0.37	13.70	23.22	0.63	0.97
MnPEI	1.47	1.48	0.38	10.30	30.64	0.43	0.60
Fe	1.31	1.30	1.12	N/A	2.54	0.62	0.61
FePEI	1.09	1.06	1.04	N/A	1.85	0.69	0.58
Co	1.19	1.06	1.47	11.70	1.32	0.44	0.47
CoPEI	0.98	0.99	1.70	2.50	0.33	0.73	0.56
Ni	0.87	1.37	1.15	8.30	0.22	0.45	0.74
NiPEI	1.30	1.06	0.98	5.30	1.72	0.52	0.72
Cu	1.05	1.02	0.44	2.50	5.48	0.49	0.49
CuPEI	1.03	0.79	0.41	0.70	0.65	0.66	0.67
Zn	1.85	1.63	0.62	16.70	4.39	0.52	0.34
ZnPEI	1.42	1.09	-0.17	17.60	4.19	0.72	0.82
Hf	0.81	1.02	1.17	N/A	0.73	0.76	0.64
HfPEI	1.01	1.10	1.20	58.50	0.40	0.58	0.68

For the ROS evaluation experiment, both hydroxyl radicals and hydrogen peroxide were studied. Results showed that the NP with the highest hydroxyl radical production is the vanadium one. Also, although without significance, results suggested that the metal oxide NPs that might achieve the highest HO• production under normoxia conditions are VPEI, Cr, Mn and Zn. On the other hand, with significant results, V and VPEI are the NPs that produce more HO• under hypoxia conditions. NPs such as Cr, Mn and Zn also showed a high HO• production but not significant. Furthermore, regarding hydrogen peroxide, the highest H_2O_2 yield under normoxia conditions was PEI-coated vanadium NP.

To measure NP radiosensitising ability within cancer cells and radiation two experiments were performed, cytotoxicity and ICP-MS. The former is related to the harm these NPs can bring to the cancer cells (non-irradiated) and the latest is related to the uptake of each NP, which can both compromise the results when exposed to radiation. For example, if a particular NP has the capability of increasing HO• production when irradiated, but its uptake is very low, the hydroxyl radicals produced will not have a high impact in cancer cell death as expected, since they are not being produced inside the cell. Furthermore, toxicity is an important measurement for understanding if cancer cells are viable due to the combined effect of the NP with the radiation or because of the NP only. Toxicity results showed that vanadium and copper are the metallic-oxides NPs that present more toxicity towards HSC-3 cells and ICP-MS results demonstrated a very low uptake towards PEI-coated Cr NPs. NPs such as Cr, Hf, PEI-

coated Hf, Fe, and PEI-coated Fe also demonstrated a compromised uptake, although much less significant than CrPEI.

Table 3.12 summarises the toxicity results found in this thesis and the results from previous toxicity studies.

Table 3.12: Summary of toxicity results for each type of NP. N/A means that the NP did not presented a toxicity at IC50. Size and type of metal oxide used is also showed.

NP	IC50 toxicity (μg/ml) size (nm)/type	Chusuei2013 size (nm)/type	Zhang2012 size (nm)/type	Horie2012 size (nm)/type	Ivask2015 size (nm)/type
Sc	13.30 43/Sc_2O_3	-------	-------	-------	-------
Ti	N/A 57/TiO_2	N/A 46/TiO_2	N/A 12.6/TiO_2	>1 mg/ml 7/TiO_2	N/A 14.2/TiO_2
V	1.60 27/V_2O_5	-------	-------	-------	-------
Cr	39.60 88/CrO_2	N/A 63/Cr_2O_3	N/A 193/Cr_2O_3	-------	-------
Mn	13.70 59/MnO_2	35 82/Mn_2O_3	~20 51.5/Mn_2O_3	-------	70-200 14.9/Mn_3O_4
Fe	N/A 58/Fe_2O_3	N/A 48/Fe_2O_3	N/A 12.0/Fe_3O_4 N/A 12.3/Fe_2O_3	>1 mg/ml 39/Fe_2O_3	N/A 8.9/Fe_3O_4
Co	11.70 83/CoO	-------	N/A 10/Co_3O_4 50 71.8/CoO	>1 mg/ml 22/CoO	~150 9.2/Co_3O_4
Ni	8.30 59/NiO	75 16/NiO	N/A 140.6/Ni_2O_3 N/A 13.1/NiO	>1 mg/ml 20/NiO-B	-------
Cu	2.50 65/CuO	~3 47/CuO	~25 12.8/CuO	<0.1 mg/ml 48/CuO	~17 11.9/CuO
Zn	16.70 56/ZnO	~18 27/ZnO	~8 22.6/ZnO	<0.1 mg/ml 21/ZnO	10-30 19.7/ZnO
Hf	N/A 56/HfO_2	-------	N/A 28.4/HfO_2	-------	-------

Chusuei *et al* focused on the fourth period metal oxide NPs such as TiO_2, Cr_2O_3, Mn_2O_3, Fe_2O_3, NiO, CuO and ZnO and found that the cytotoxicity of fourth period metal oxide NPs increased with the atomic number of the transition metal oxide and it was not cell-type specific (Chusuei et al., 2013). They proposed that toxicity falls into three categories: the first, where Ti, Cr and Fe have zero to minimal toxicity; the second, where Mn and Ni have around 40% cell viability; and the third, where Cu and Zn present less than 20% cell viability. They used both human bronchial epithelium non-cancerous cell line (BEAS-2B) and A549 and the results were the same for both cell lines. In the results of this thesis, the trend with the atomic number was not seen although NPs such as Cu, Zn, Ti and Fe had similar toxicity results. NPs such as Cr and Mn showed differences in toxicity and it might have been due to the type of metal oxide used, CrO_2 vs Cr_2O_3 and MnO_2 vs Mn_2O_3. For Ni NPs although the same type of metal oxide was used in both studies the difference in toxicity might have been due to the NP size used, 59 vs 16 nm.

Furthermore, another research on 24 types of metal oxide NPs such as CO_3O_4, Cr_2O_3, Ni_2O_3, CuO, Mn_2O_3, CoO, ZnO, Al_2O_3, CeO_3, Fe_2O_3, Fe_3O_4, Gd_2O_3, HfO_2, In_2O_3, NiO, SiO_3, SnO_2, TiO_2, WO_3, Y_2O_3, Yb_2O_3, ZrO_2, La_2O_3, Sb_2O_3, using single-parameter assays in BEAS-2B as well as mouse myeloid (RAW 264.7) cell lines showed that for an exposure period of 24 h and a dose range between 400 ng/ml to 200 μg/ml seven NPs significantly decreased cell viability (Zhang et al, 2012). These seven NPs included CuO, Mn_2O_3, CoO, and ZnO with a marked declined in cell viability while CO_3O_4, Cr_2O_3, and Ni_2O_3 had lesser but still significant effects. The rest of the metals analysed had no significant effects. NP sizes were in the range 10-100 nm except for Cr_2O_3 and Ni_2O_3 that were much larger, 193 nm and 140 nm, respectively. For the cell line used in this thesis our results regarding Ti, Mn, Fe and Hf NPs were similar to the ones from Zhang et *al*.. In the case of Cr NPs, the difference on the toxicity results might be due to the difference in the metal oxide used, while for Ni, Cu and Zn NPs the difference in toxicity can be explained by the difference in size. The result regarding Co NPs cannot be explained due to differences in size or metal oxide used since they are very similar, so the type of cell line used also play an important role on the toxicity results obtained.

Horie et al. (2012) concluded that the most important cytotoxic factor of metal oxide NPs was metal ion release. This group used human keratinocyte cell line (HaCaT) and A549, and 24 kinds of industrial metal oxide NPs such as ZnO, CuO, NiO, Sb_2O_3, CoO, MoO_3, Y_2O_3, MgO, Gd_2O_3, SnO_2, WO_3, ZrO_2, Fe_2O_3, TiO_2, CeO_2, Al_2O_3, Bi_2O_3, La_2O_3, In_2O_3/SnO_2 (ITO), and cobalt blue pigments with different sizes. For the cell viability assay they used MTT assay with 24 h exposure to the NPs where ZnO, ZnO-SiO_2 coated and CuO NPs induced severe cell death at concentrations of 0.1 and 1.0 mg/mL in both HaCaT and A549 cells. Also, NiO green NPs induced severe cell death at concentration of 0.1 mg/mL. The cell viabilities of NiO black, Sb_2O_3, CoO and MoO_3 exposed cells were approximately 50% at concentration of 1.0 mg/mL. The cell viabilities of Y_2O_3 and MgO exposed cells were approximately 60%. The other types of metal oxides nanoparticles showed a very small effect on cell viability with a value of 80% or more. Particularly, there was no significant decrease of cell viability in Fe_2O_3, TiO_2, Al_2O_3 and cobalt blue exposed cells. Moreover, ZnO, CuO, NiO, MgO, and WO_3 showed a large amount of metal ion release in the culture medium, and TiO_2, SnO_2, and CeO_2 NPs showed strong protein adsorption ability.

In our results, ZnO, CuO and NiO NPs presented 100% cell death at 0.1 mg/mL and, Fe_2O_3 and TiO_2 did not presented any significant decrease in cell viability, similar to the results found by this group. The results in this thesis showed that CoO NPs decreased by 100% cell viability at 0.1 mg/mL, which does not match the 50% value found by this group at a much higher concentration of 1.0 mg/mL. This difference might be due to differences in the cell line used, NP size (22 nm vs 83 nm), or type of assay (MTT vs clonogenic).

For three different cell lines such as, A549, human epithelial colorectal adenocarcinoma cell line (Caco2) and mouse fibroblast cell line (Balb/c 3T3), exposure for 24 h to suspensions of 3-100 μg/ml metal oxide NPs was conducted and cellular viability was evaluated using Neutral Red Uptake (NRU) assay (Ivask et al., 2015). Toxicity results were very similar among the three cell lines, where Al_2O_3, Fe_3O_4, MgO, SiO_2, TiO_2, WO_3 were not toxic for concentrations below 100 μg/ml and for the remaining NPs the IC50 values were 16.4 μg/ml for CuO, 22.4 μg/ml for ZnO, 57.3 μg/ml for Sb_2O_3, 132.3 μg/ml for Mn_3O_4 and 129 μg/ml for Co_3O_4. In this study, toxicity from CuO, ZnO and Sb_2O_3 was attributed to the release of metal ions by these NPs, and toxicity from Mn_3O_4 and Co_3O_4 attributed to the ROS-inducing ability of these NPs (Ivask et al., 2015). From the catalytic ability results found in this thesis (Figure 3.4), Mn and Co NPs showed the highest value in oxygen levels which is consistent with the conclusion made by this group regarding the ROS-inducing ability of these NPs. Similarities with our results include the toxicity found for Fe_2O_3, TiO_2 and ZnO (22.4 μg/ml vs 16 μg/ml). IC50 values for our NPs were 2.4 μg/ml for CuO, 14 μg/ml for MnO_2 and 13 μg/ml for CoO. The latter results differ significantly from the ones found by this research group and these might be due to differences regarding the cell line used, NP size (11.9 nm CuO vs 65 nm CuO; 14.9 nm Mn_3O_4 vs 59 nm MnO_2; 9.2 nm Co_3O_4 vs 83 nm CoO) and type of assay (NRU vs clonogenic).

NP radiosensitisation ability within cancer cells is a phenomenon that is affected not only by the physical characteristics of the NPs but also their interaction with cancer cells. For both normoxia and hypoxia conditions experiments were conducted in this thesis where the interaction between NPs, cancer cells and radiation were assessed. For HSC-3 cells, in normoxia conditions, the NPs that had the highest effect in cell viability were V and VPEI with significant results. Cr and CrPEI NPs also showed an effect in cell death for normoxia conditions although not significant. For hypoxia conditions VPEI, Cr and Zn NPs showed the highest effect, although these results are not significant due to the high error bars present in the experiment.

Taking the results of ROS evaluation and comparing them with the HSC-3 cells clonogenic experiment a possible conclusion for the low cell survival due to V, VPEI, Cr, CrPEI and Zn NPs is the fact that these metal oxide NPs produce more hydroxyl radicals when exposed to radiation, that will in turn lead to cancer cell death. The NPs that showed the highest production in ROS, both $HO^{\cdot}$ and H_2O_2, were V and VPEI and both present significant effects also in the clonogenic experiments. Interestingly, PEI-coated vanadium NPs seem to contribute more for either hydroxyl radicals and cell death under hypoxia conditions, as can be seen from the fact that VPEI NPs appear with a higher significance for hydroxyl radical production under hypoxia conditions, but not under normoxia conditions. Even for cell death VPEI NP has a higher contribution than its non-coated counterpart, and a possible reason might be due

to the fact of this metal oxide NP produces hydrogen peroxide in a much higher amount than non-coated vanadium.

Zinc NPs contributed more to cell death than the coated ones and a possible explanation would be due to their size, although Zn NPs have a much higher diameter than its coated version (56 nm vs 16 nm). Moreover, ICP-MS results for both Zn and ZnPEI NPs are very similar so both these NPs have a very similar uptake by HSC-3 cells which is not very obvious due to the large difference between the coated and non-coated particles, in terms of size and zeta potential, as shown in Table 3.4. It is intriguing though that only Zn appear to contribute to cell death in hypoxia conditions and not its coated-form, which would be more likely to enter cells due to its positive zeta potential and its smaller diameter (Kralj et al., 2012). Depending on the pH, zinc oxide NPs can have either a positively charged surface (pH<9) or a negatively charged surface (pH>9). In the former, the chemisorbed protons (H^+) from the aqueous medium move out from the surface and the oxygen atoms become partially bound forming ZnO^-, while in the latter, H^+ from the medium are transferred to the particle surface forming $ZnOH_2^+$ (Degen & Kosec, 2000). Since for ZnO NPs the isoelectric point is around 9-10 (Degen & Kosec, 2000) they will present a positive surface charge under physiological conditions. Cancer cells normally present a negative surface due to the high concentration of anionic phospholipids on their outer membrane and large membrane potentials. Due to this surface charge difference between ZnO NPs and cancer cells the cellular uptake is promoted by electrostatic interactions (Rasmussen et al., 2010). Our results showed a negative zeta potential value for non-coated Zn NPs and positive zeta potential value for PEI-coated Zn NPs leading to the conclusion that non-coated Zn NPs uptake would be very low. ICP-MS results showed a similar uptake from both Zn and ZnPEI NPs. One possibility could be the fact that Zn NPs in the cell media turned out to have a positive surface charge which was not measured under the zeta potential measurement conditions. This would explain why a negatively charged NP would have a high uptake under cell environment. Furthermore, in terms of size, a study showed that as zinc oxide NP size decreases, ROS production increases (Hanley et al., 2009). Zn PEI-coated NPs were found to have a diameter of 16 nm compared to 56 nm of Zn NPs, so one would expect a higher ROS production from Zn PEI-coated NPs, which is not shown by the ROS evaluation results found in this thesis. Depicting Zn PEI-coated NPs as a 16 nm zinc oxide solid material with PEI molecules attached to the surface, as shown in Figure 3.20A, and the non-coated Zn NPs as a 56 nm diameter element with an average of four 16 nm zinc NPs aggregated (Figure 3.20B), we would expect approximately 4 times the contribution of ROS per NP. In this case, it would explain the contribution showed by Zn NPs in hydroxyl radical production in both normoxia and hypoxia, besides its contribution in cell death under hypoxia conditions. Another possible explanation can be the fact that the coating reduces the catalytic ability of zinc NPs to produce hydroxyl radicals which would, again, explain the results showed by the hydroxyl radical production in both conditions. In fact, it is believed that ZnO NPs cytotoxicity mechanisms, although not completely

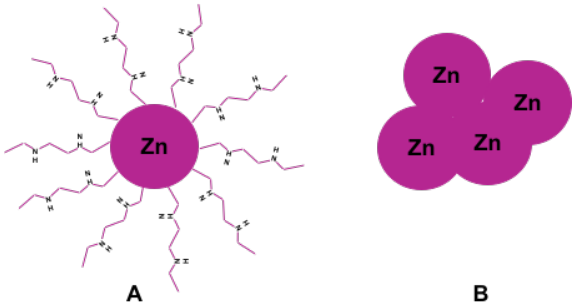

Figure 3.20: ZnPEI and Zn NPs illustration; A - 16 nm ZnPEI NPs; B - 56 nm Zn NPs.

understood, are due to ROS generation (Rasmussen et al., 2010). ROS oxidative stress has been described as a three-tier model, where Tier 1 is characterized by anti-oxidant defence, where there is an increase in antioxidant enzymes in order to restore cellular redox homeostasis, Tier 2 is characterized by an inflammation due to an increase in potent pro-inflammatory cytokines and chemokines and finally Tier 3 characterized by cytotoxicity which involves mitochondrial perturbation that leads to cell death by apoptosis or necrosis (Nel et al., 2006). These three tiers have been observed in ZnO NPs in immortalized phagocytic or bronchial epithelial cells leading to damage of lipids, proteins and DNA, and death by either necrosis or apoptosis (Rasmussen et al., 2010).

In general, it would be expected, due to the important role of oxygen in ROS production, that under hypoxia conditions ROS levels would be much lower than under normoxia conditions. The results on this thesis do not follow this behaviour. Instead, several reports indicate that the production of ROS actually increases in response to hypoxia (Hermes-Lima et al., 2015). Furthermore, there might exist a relation between the presence of the PEI coating and the production of hydrogen peroxide, which in turn is very useful under hypoxia conditions, since even with VPEI NPs presenting a lower uptake than V NPs they presented a higher toxicity to cancer cells. One of the major differences is the high hydrogen peroxide production seen by VPEI NPs. PEI exhibits weak-base buffering properties since it can take up H^+ ions (Curtis et al., 2016). These ions might contribute to the generation of $HO\cdot$ through the reaction of O_2^{2-} with e^- and $2H^+$ which will in turn generate H_2O_2 which then reacting with Cl^- will form HOCl and reacting with NO_2^- will form $NO_2\cdot$ leaving $HO\cdot$ as the remaining product (Mitra et al., 2019). The presence of metal oxides will generate O_2 through the Haber-Weiss reaction ($O_2^- + H_2O_2 \rightarrow O_2 + OH^- + OH\cdot$) and also H_2O_2 will be decomposed through the catalytic ability of these metal oxide NPs contributing even more for the production of hydroxyl radicals. Maybe the presence of O_2 for the formation of ROS is fundamental due to the reaction with $2H^+$ but in the presence of PEI the uptake of H^+ might increase radical formation through other mechanisms. Moreover, in general, PEI-coated NPs showed a lower hydroxyl radical production in both conditions. PEI-coated may not favor the production of this radical since it blocks the contact of the metal oxide surface with water molecules, not allowing the catalytic reaction to take place.

Manganese NPs showed some contributions in hydroxyl radical production in both conditions although not significant. Catalytic ability of manganese is very high as showed by the results in Figure 3.2. Some studies showed the intracellular oxidative stress and apoptosis in alveolar epithelial cells (AEC) induced by Mn_3O_4 NPs (VanWinkle et al., 2009; Frick et al., 2011). Oxidative stress induced by manganese is due to the following reactions (Aust et al., 1985):

$$Mn^{2+} + O_2 \rightarrow Mn^{3+} + O_2^-$$

$$2\ O_2^- + 2H^+ \rightarrow H_2O_2 + O_2 \text{ (superoxide dismutase)}$$

H_2O_2 products can then take two different routes (Frick et al., 2011):

$$2GSH + H_2O_2 \rightarrow GSSG + 2H_2O \text{ (catalyzed by glutathione peroxidase)}$$

or

$$Mn^{2+} + H_2O_2 \rightarrow Mn^{3+} + OH^- + OH^{\cdot}$$ (Fenton or Haber-Weiss reactions)

NP cytotoxicity results did not show any contribution from manganese NPs, only on hydroxyl radical production.

Cr NPs showed contribution in both hydroxyl radicals and cytotoxicity experiments. Studies on cell lines have shown their ability to produce ROS species inside cells. For example, a study on A549 and HaCaT cells showed an increase in intracellular reactive oxygen species level decreasing cell viability after exposure to 60 nm Cr_2O_3 NPs (Horie et al., 2011). Another study performed in A549 cells using 30 nm Cr_2O_3 NPs also showed increase intracellular ROS level indicating that oxidative stress might be the primary mechanism for its toxicity (Senapati et al., 2015). These observations agree with our results that showed the ROS generation capability of chromium NPs in producing hydroxyl radicals leading to cell death. Moreover, Cr NPs were more toxic to cells than CrPEI ones, which is in accordance with the ICP-MS results, that showed a much higher uptake from Cr NPs than for the coated ones.

Another potential toxicity mechanism can be through cell exterior damage even when the uptake is low (VanWinkle et al., 2009). Transition metal ions can transfer electrons to O_2 leading to H_2O_2 generation in the extracellular compartment. The H_2O_2 produced can induce damage on the cell exterior. This might be the reason why although CrPEI NPs presented very low uptake and most of the NPs were outside the cells it still presented relevant results for cell death under hypoxia conditions.

Overall, all the NPs that had a relevant effect on HSC-3 cells viability had a negative zeta potential, which is not in accordance with the results showed by some studies, where NPs with positive zeta potential have a better cell uptake (Kralj et al., 2012). A possible reason for this discrepancy is the fact that zeta potential measurements were made in PBS, pH 7.4 and NPs under cell medium will present a different surface charge due to the protein corona, as in the case of Zn NPs (Rasmussen et al., 2010).

In general, the NPs that showed the most significant results in ROS production and cell death are vanadium, both the coated and non-coated.

Vanadium like other transition metals, e.g. Fe, Cu, Cr and Si, produces ROS through Haber-Weiss and Fenton-type reactions (Manke et al., 2013). Vanadium NPs toxicity depends on the cell line used as showed by a study made for 2 different sizes of vanadium NPs, 20 nm and 100 nm, using 5 different cell lines (Ivanković et al., 2006). For 30 nm VO_2 NPs interaction with A549 and BEAS-2B cells, a similar sensitivity to V NPs was found for both cell lines and it was also found that enhanced reactive oxygen species generation and suppressed reduced glutathione were the major mechanisms of VO_2 NPs cytotoxicity (Xi et al., 2019). A study on thickness-tunable VO_2-modified quartz surface using human cholangiocarcinoma cells suggested that the released of vanadium ions can disrupt the mitochondrial electron transport chain and therefore elevate the intracellular ROS level of tumour cells, thereby leading to the dysfunction of the mitochondria through collapse of mitochondria membrane potential, inducing cancer cells apoptosis (Li et al., 2019).

Table 3.13 shows the most promising metal oxide NPs and their respective induced damage for a better picture of all the results found.

Table 3.13: Summary of the metal oxide NPs and their respective induced damage. Legend for the results without cells: change from control (= 1): + = 1.3-1.49; ++ = 1.5-1.69; +++ = 1.7-1.89; ++++ = 1.9-2.09; * = 2.10-10.0; ** = 10.1-18.0; *** = 18.1-26.0; **** = 26.1-50.0; 🌀 = 300.0-500.0. Legend for toxicity (IC50) results: ++++ = 0.0-3.0 μg/ml; +++ = 3.1-10.0 μg/ml; ++ = 10.1-17.0 μg/ml; + = 17.1-24.0 μg/ml; - = 24.1-31.0 μg/ml; -- = 31.1-38.0 μg/ml; --- = 38.1-45.0 μg/ml; ---- = 45.1-52.0 μg/ml; ----- = 52.1-90 μg/ml; 🌀 = > 90.1 μg/ml. Legend for cell radiosensitisation results: change from control: + = 0.26-0.35; ++ = 0.36-0.45; +++ = 0.46-0.55; ++++ = 0.56-0.65; +++++ = 0.66-0.75; - = -0.26-(-0.35); -- = -0.36-(-0.45).

	Without radiation NORMOXIA			With radiation NORMOXIA			Without radiation HYPOXIA	With radiation HYPOXIA	
NP	$HO^{\cdot}$	H_2O_2	HSC-3 cell toxicity	$HO^{\cdot}$	H_2O_2	HSC-3 cell radiosensitisation	$HO^{\cdot}$	$HO^{\cdot}$	HSC-3 cell radiosensitisation
Sc		+	++		+				
ScPEI		*	++						+
Ti	+++		🌀	+			+		--
TiPEI	+++		-----			+	+		
V		🌀	++++	++++	*	++++		*	
VPEI		****	++++	+++	**	+++++		*	+++++
Cr		*	---	++		+++		+++	+++++
CrPEI		*	----			++			
Mn		🌀	++	++				+++	
MnPEI		🌀	++	+		+		+	
Fe		++++	🌀						
FePEI		++++	🌀						
Co		**	++		+	+			+
CoPEI		*	++++		+++				
Ni		****	+++			+		+	
NiPEI		****	+++						
Cu		**	++++			+			
CuPEI		*	++++						
Zn		*	++	++++				++	++
ZnPEI		*	+	+					
Hf	+	+	🌀						
HfPEI		+++	-----						

It is possible to find some correlations from NPs of the same group of periodic table, such as the ability to generate hydroxyl radicals without radiation and cell toxicity, from both Ti and Hf NPs. For these NPs, both non-coated and coated NPs presented very similar results regarding cell toxicity. These NPs belong to the group 4 of the periodic table.

In general as hydroxyl radical increases, hydrogen peroxide tends to decrease (Figure 3.12). Metal oxide NPs are known for their ability to produce $HO^{\cdot}$ from H_2O_2 reaction with O_2^{-} through the Haber-Weiss reaction (Hauser et al, 2016):

$$\text{Haber-Weiss reaction: } O_2^{-} + H_2O_2 \rightarrow O_2 + HO^{-} + HO^{\cdot}$$

, meaning that as hydroxyl radical increases, hydrogen peroxide decreases, which is in agreement with the Spearman correlation results (Figure 3.12).

The ICP-MS correlation with cell irradiation results (Figure 3.17) showed that when uptake increases, cell survival tens to increase, which should not be the case. Increasing uptake of the NPs by the cells, will lead to a higher number of cells death, since more NPs will bring more harm to the intracellular

components, increasing the chances of the cell to lose its ability to reproduce when irradiated. This is a correlation with a small size effect (r_S=0.3), so this result would need more representative data for better conclusions regarding this relationship. There is always a possibility of some NPs help the cell removing the radicals formed during irradiation.

The result from the correlation between CCA and cell irradiation data was expected (Figure 3.18), since a higher increase in the number of $HO^{\cdot}$ is expected to reduce cell survival, as shown by the moderate size effect found through the Spearman correlation (r_S=-0.4). $HO^{\cdot}$ is considered one of the main species responsible for cancer cell death during irradiation, so an increase in the number of these species will lead to a higher number of cancer cells death, decreasing in this way their survival.

The result from DHR and cell irradiation correlation showed that as H_2O_2 increases, cell survival tends to increase (Figure 3.19), with a large size effect from Spearman correlation (r_S=0.6). This result might have two completely opposite conclusions. One could be the fact that, an increase in H_2O_2 formation means that $HO^{\cdot}$ is not being formed, since, from the Haber-Weiss reaction, H_2O_2 should decrease to form $HO^{\cdot}$. If a lot of H_2O_2 is being formed and not reacting with O_2^- to form $HO^{\cdot}$, then cell survival should increase, since $HO^{\cdot}$ is the main species responsible for cancer cell death during irradiation. If this is the case, our results are in conformation with what is expected to be the mechanism responsible for cancer cell death during RT. The other conclusion could be that the high number of H_2O_2 species present would lead to a higher number of $HO^{\cdot}$ species, which in turn would lead to a higher number of cancer cells death, decreasing cell survival. From this point of view, our results would not be in agreement with the responsible mechanism that occurs during RT. There is the possibility that the probes, used to measure both H_2O_2 and $HO^{\cdot}$, interfere with the main mechanism, changing the course of the reaction.

4 A comparison of the radiosensitisation ability of 22 different element metal oxide nanoparticles using clinical megavoltage X-rays – Published Paper

4.1 Introduction

This chapter is made of a paper I published with my supervisor, Dr Jon Golding. Here I tested a much wider range of elements for the NPs, including rare-earth metals. In this work, I was more interested in comparing the different types of NPs and their interaction with DNA, so experimental work with cells was not performed.

To try to understand more about radiosensitisation and the different types of ROS generated during the course of RT, here the approach was focused on studying not only hydroxyl radicals, but also superoxide and singlet oxygen and try to understand if there was any correlation between the different ROS produced and the type of NP.

While in the previous chapter there was a concern regarding the coating due to the fact that interaction with cells was one of the main studies and also an attempt to try to see a correlation between the formation of hydroxyl radicals and the hydrogen peroxide, here not only the number of elements was extended but also the type of ROS, and the main study was interaction with DNA. Furthermore, since some of the metals involved in this work are known for their catalytic ability, there was also an interest in studying how the formation of electron-hole pairs might be involved in the ROS production.

Following presentation of my paper, I made a discussion where I correlate the different type of ROS produced to try to understand if there is a major mechanism connecting hydroxyl radicals, superoxide, and singlet oxygen.

4.2 Paper

A comparison of the radiosensitisation ability of 22 different element metal oxide nanoparticles using clinical megavoltage X-rays.

Alexandra Guerreiro[1,2], Nicholas Chatterton[2], Eleanor M. Crabb[2], Jon P. Golding[2*].

[1] Faculty of Science and Technology. New University of Lisbon, Portugal.

[2] School of Life, Health and Chemical Sciences. The Open University, Milton Keynes, UK.

*Corresponding author: Jon.golding@open.ac.uk. Tel: 01908 653748

Abstract

Background: A wide range of nanoparticles (NPs), composed of different elements and their compounds, are being developed by several groups as possible radiosensitisers, with some already in

clinical trials. However, no systematic experimental survey of the clinical X-ray radiosensitising potential of different element nanoparticles has been made.

Here we directly compare the irradiation-induced (10 Gy of 6 MV X-rays) production of hydroxyl radicals, superoxide anion radicals and singlet oxygen in aqueous solutions of the following metal oxide nanoparticles: Al_2O_3, SiO_2, Sc_2O_3, TiO_2, V_2O_5, Cr_2O_3, MnO_2, Fe_3O_4, CoO, NiO, CuO, ZnO, ZrO_2, MoO_3, Nd_2O_3, Sm_2O_3, Eu_2O_3, Gd_2O_3, Tb_4O_7, Dy_2O_3, Er_2O_3 and HfO_2.

We also examine DNA damage due to these NPs in unirradiated and irradiated conditions.

Results: Without any X-rays, several NPs produced more radicals than water alone. Thus, V_2O_5 NPs produced around 5-times more hydroxyl radicals and superoxide radicals. MnO_2 NPs produced around 10-times more superoxide anions and Tb_4O_7 produced around 3-times more singlet oxygen. Lanthanides produces fewer hydroxyl radicals than water.

Following irradiation, V_2O_5 NPs produced nearly 10-times more hydroxyl radicals than water.

Changes in radical concentrations were determined by subtracting unirradiated values from irradiated values. These were then compared with irradiation-induced changes in water only.

Irradiation-specific increases in hydroxyl radical were seen with most NPs, but these were only significantly above the values of water for V_2O_5, while the Lanthanides showed irradiation-specific decreases in hydroxyl radical, compared to water.

Only TiO_2 showed a trend of irradiation-specific increase in superoxides, while V_2O_5, MnO_2, CoO, CuO, MoO_3 and Tb_4O_7 all demonstrated significant irradiation-specific decreases in superoxide, compared to water.

No irradiation-specific increases in singlet oxygen were seen, but V_2O_5, NiO, CuO, MoO_3 and the Lanthanides demonstrated irradiation-specific decreases in singlet oxygen, compared to water.

MoO_3 and CuO produced DNA damage in the absence of radiation, while the highest irradiation-specific DNA damage was observed with CuO. In contrast, MnO_2, Fe_3O_4 and CoO were slightly protective against irradiation-induced DNA damage.

Conclusions: Beyond identifying promising metal oxide NP radiosensitisers and radioprotectors, our broad comparisons reveal unexpected differences that suggest the surface chemistry of NP radiosensitisers is an important criterion for their success.

Keywords: Radiosensitiser, X-ray, megavoltage, metal oxide, nanoparticle, survey, radicals, DNA damage.

4.2.1 Background

Water radiolysis by ionising radiation results in the formation of several species, mainly: e^-_{aq}, $^{\cdot}OH$, $^{\cdot}H$, H_3O^+, OH^-, $^{\cdot}O_2H$, H_2O_2 and H_2. These products react with one another to form secondary species such as O_2, $^{\cdot}O_2^-$ and $^{\cdot}O_3$, with many additional short-lived intermediates (reviewed in Le Caë, 2011). Water radiolysis products range from highly oxidizing (e.g. $^{\cdot}OH$, H_2O_2 and O_2) to highly reducing (e.g. $^{\cdot}H$, $^{\cdot}e_{aq}^-$ and $^{\cdot}O_2^-$). These reactive species damage biological molecules and contribute around 60% of the biological damage due to X-ray radiotherapy (Saenko et al., 2013; D. Zhang et al., 2016; Jayakumar et al., 2014 and reviewed in Baskar et al., 2014). Although each clinical X-ray irradiation session only lasts for a few minutes, the radical-mediated damage can induce prolonged metabolic oxidative stress that continues to damage cells long after irradiation (Azzam et al., 2012).

Theoretical studies (McMahon et al., 2016; Hwang et al., 2017; Haume et al., 2016; Roeske et al., 2007) and experimental studies (Retif et al., 2015; Y. Liu et al., 2018) have demonstrated that X-ray-induced radical formation can be greatly increased in the vicinity of nanoparticles of high atomic number (*Z*) elements, their oxides or sulphides (e.g. Ag: (P. Liu et al., 2016); Gd: (Luchette et al., 2014; Lux et al., 2018); Hf: (Marill, Anesary, Zhang, Vivet, Borghi, et al., 2014); Pt: (Muhammad et al., 2018); Au: (Haume et al., 2016; Rahman et al., 2014); Bi: (Algethami, 2015; Sahu & Cates, 2017), which have large X-ray absorption cross sections and produce a shower of secondary electrons when irradiated. For this reason, high atomic number nanoparticles have been the focus of nanoparticle radiosensitiser research, some of which are being clinically evaluated (Y. Liu et al., 2018), such as the Gd NP, AGuIX (Lux et al., 2018) and the Hf NP, NBTXR3 (Marill, Anesary, Zhang, Vivet, Barendsen, et al., 2014), both of which are currently in Phase II clinical trials (NCT03818386 and NCT03589339).

However, NPs of many lower atomic number element oxides have been shown to be effective radiosensitisers, such as: Al (Roth et al., 2011), Si (Gara et al., 2012; Generalov et al., 2015; N. Zhao et al., 2016), Ca (Chu et al., 2013), Ti (Morrison et al., 2017), Fe (Khoei et al., 2014), Cu (Y. W. Jiang et al., 2019), Zn (Generalov et al., 2015), Zr (Carrasco-Flores & LaVerne, 2007). This suggests that other, physico-chemical and chemical processes, likely involving the nanoparticle surface, contribute to the overall pool of X-ray-induced radicals.

What is missing, however, are systematic experimental comparisons of these different element NPs as radiosensitisers. Most *in vitro* studies have been limited to comparing small ranges of elements, or more often to different compounds or surface functionalisation of a single element NP. Experimental differences, such as X-ray energy and dose, and concentration of nanoparticles further impede comparisons (Hwang et al., 2017; Rahman et al., 2014; Retif et al., 2015). Recent proposals have been made to standardise these parameters (Retif et al., 2015; Schuemann et al., 2018), but it will take time for these to become routinely adopted.

Only two studies have been published using a broad range of NPs, both with gamma radiation. Petrik *et al* (2001) compared hydrogen production from adsorbed water on a wide range of 28 different element metal oxide powders (Petrik et al., 2001). Chelnokov *et al* (2014) compared solvated electron production from 6 different element NPs (Chelnokov et al., 2014).

Because of the difficulties in comparing radiosensitisers across studies, we have performed a survey of a broad range of 22 different metal oxide NPs, to examine their intrinsic ability to generate reactive oxygen species and damage plasmid DNA under control and irradiated conditions using clinically relevant megavoltage X-rays (10 Gy of 6 MV X-rays).

Metal oxides, rather than pure metals, were chosen because nearly all of the transition metal elements we use are unstable in water and react to become oxides. We find that some metal oxides increased radiation-induced radical formation (V_2O_5, for hydroxyl radicals; TiO_2 for superoxides) while others were radioprotective. For instance, the Lanthanide oxides produced far fewer hydroxyl radicals than irradiated water only. Irradiation-induced DNA damage was greatest with CuO NPs.

4.2.2 Results

4.2.2.1 NP characterisation.

Transmission electron microscopy (TEM) and dynamic light scattering (DLS) were used to measure respectively the core and hydrodynamic size distributions of the NPs (Table 4.1; Supp Figures 1 and 2). By TEM, the most frequent diameter (mode) of each NP lay in a narrow range between 13 - 26 nm. Hydrodynamic diameter was generally similar or larger than the corresponding TEM value, suggesting some aggregation in solution.

Table 4.1: NP diameters measured by TEM and DLS. Integer values ±SD.

NP	TEM Mean dia (nm) ±SD	TEM Mode dia (nm)	DLS Median dia (nm) ±SD	DLS Poly-Dispersity	Supplier Quoted TEM dia (nm)
Al_2O_3	49±38	14	781±432	0.21	<50
SiO_2	46±45	13	424±364	0.25	10-20
Sc_2O_3	50±34	13	430±78	0.04	<80
TiO_2	61±43	14	439±315	0.17	21
V_2O_5	47±36	13	717±401	0.39	<80
Cr_2O_3	56±51	13	99±55	0.16	60
MnO_2	64±55	14	25±6	0.57	50
Fe_3O_4	49±40	15	805±336	0.14	50-100
CoO	46±39	14	71±15	0.47	50
NiO	58±44	19	375±283	0.23	<50
CuO	40±29	16	132±59	0.23	<50

ZnO	44±30	13	353±238	0.27	<100
ZrO_2	50±32	26	155±31	0.59	40
MoO_3	30±21	13	203±47	0.06	13-80
Nd_2O_3	64±51	15	227±131	0.53	30-45
Sm_2O_3	40±44	13	41±31	0.69	15-45
Eu_2O_3	69±56	13	8±2	0.54	10-100
Gd_2O_3	26±37	13	67±24	1.00	10-100
Tb_4O_7	107±108	13	1073±340	0.10	10-100
Dy_2O_3	42±30	14	938±301	0.18	30
Er_2O_3	64±67	13	333±41	0.01	10-100
HfO_2	105±84	18	74±13	0.69	61-80

X-ray diffraction (XRD) confirmed the crystal phase identity of all NPs, except Eu_2O_3 and Gd_2O_3 for which there was no close match in our database (Supp Figure 3).

4.2.2.2 Radical formation

Three fluorogenic probes were used to detect different types of radical: coumarin-3-carboxylic acid (CCA) detects hydroxyl radical, DHE detects superoxide and singlet oxygen sensor green (SOSG) detects singlet oxygen. Tables of raw fluorescence data, fluorescence-to-molarity calibration curves and corrected molarity data for 2.5 mM NPs with different concentrations of oxidised probes are presented in Supp File 1, while the corrected molarity data are also presented graphically in Figures 4.1 to 4.3.

For the hydroxyl radical probe CCA, the graph (Figure 4.1A) is dominated by V_2O_5, which shows high hydroxyl probe fluorescence, even without irradiation.

After subtracting the non-irradiated control values for each sample ('real' values, Figure 4.1B), V_2O_5 still demonstrates the largest irradiation-induced increase in hydroxyl radicals. Most of the other NPs show modest irradiation-induced increases in hydroxyl radicals, similar to water. However, the Lanthanides: Nd_2O_3, Sm_2O_3, Eu_2O_3, Gd_2O_3, Tb_4O_7, Dy_2O_3 and Er_2O_3 do not show any hydroxyl radical formation even following irradiation, suggesting this group of NPs participate in reactions that destroy hydroxyl radicals or inhibit their formation, resulting in no net increase in hydroxyl radicals.

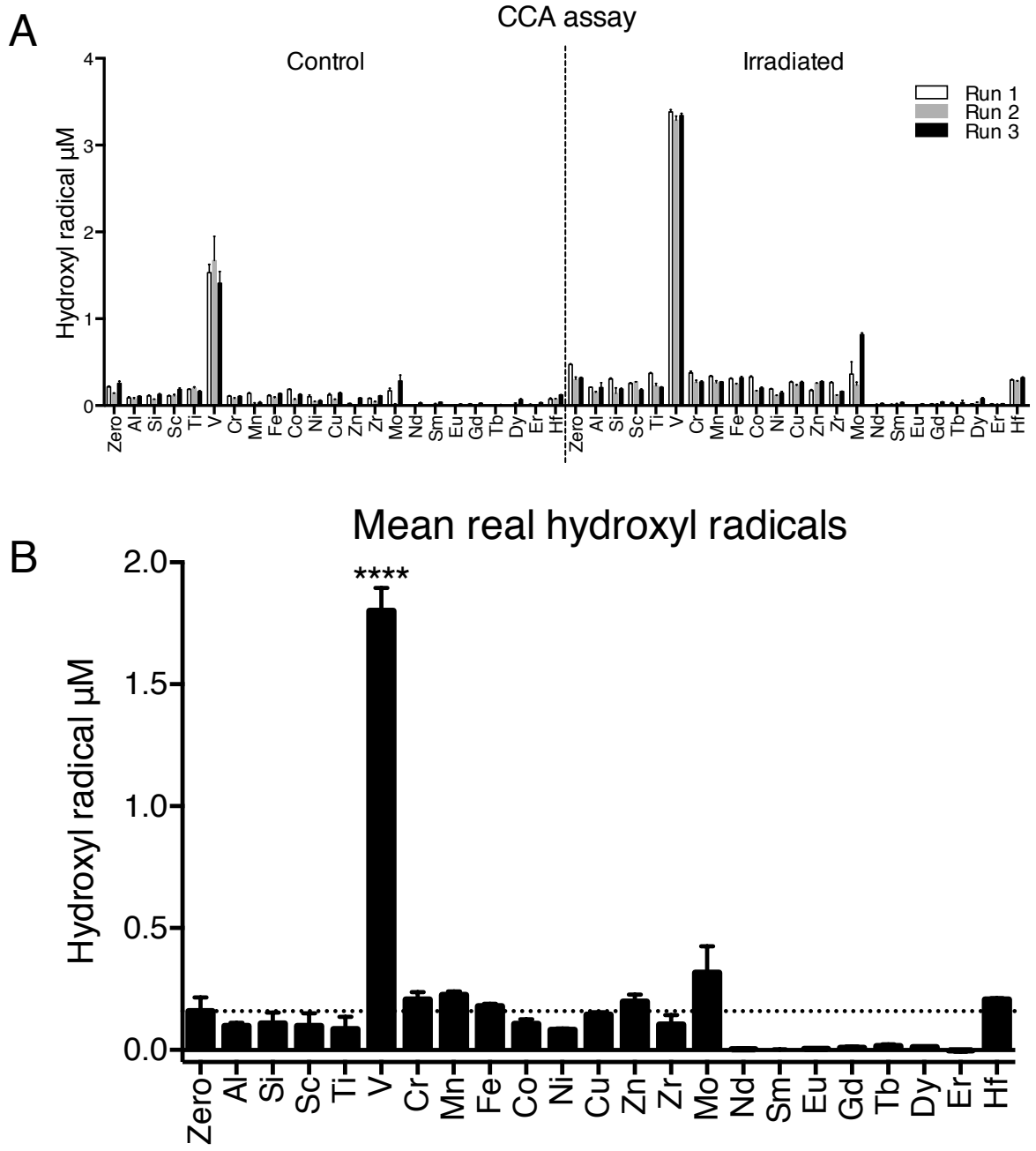

Figure 4.1: Hydroxyl radical production. A) Hydroxyl radical concentrations for unirradiated control (left side) and 10 Gy irradiated (right side) NPs. Data are shown for 3 independent experiments (run 1, run 2, run 3). B) Data from panel (A) replotted as 'real' values (10 Gy irradiated value minus 0 Gy control) ±SEM. Dotted line shows the irradiation-induced increase due to water only. **** denotes P<0.0001 significant difference, compared to no NP (zero).

For the superoxide anion probe DHE, the highest values are for MnO_2, and V_2O_5, both of which show high superoxide probe fluorescence even in the absence of irradiation. (Figure 4.2A).

After subtracting the non-irradiated control values for each sample (Figure 4.2B), most NPs show similar irradiation-induced superoxide values to water only. One possible exception is TiO_2, which appears to show a slightly higher irradiation-induced production of superoxides than water. More significantly,

although V_2O_5, MnO_2, CoO, CuO and Tb_4O_7 show greater superoxide generation overall (Figure 4.2A); after subtracting the non-irradiated value they show less irradiation-induced superoxide than water (Figure 4.2B), suggesting that irradiation makes less difference for these NPs as they are already actively generating these radicals, or that possibly these NPs might participate in reactions that destroy superoxides or inhibit their formation. MoO_3 shows considerably lower superoxide radical formation than water after irradiation, also suggesting that it inhibits superoxide formation and/or destroys already produced superoxide radicals.

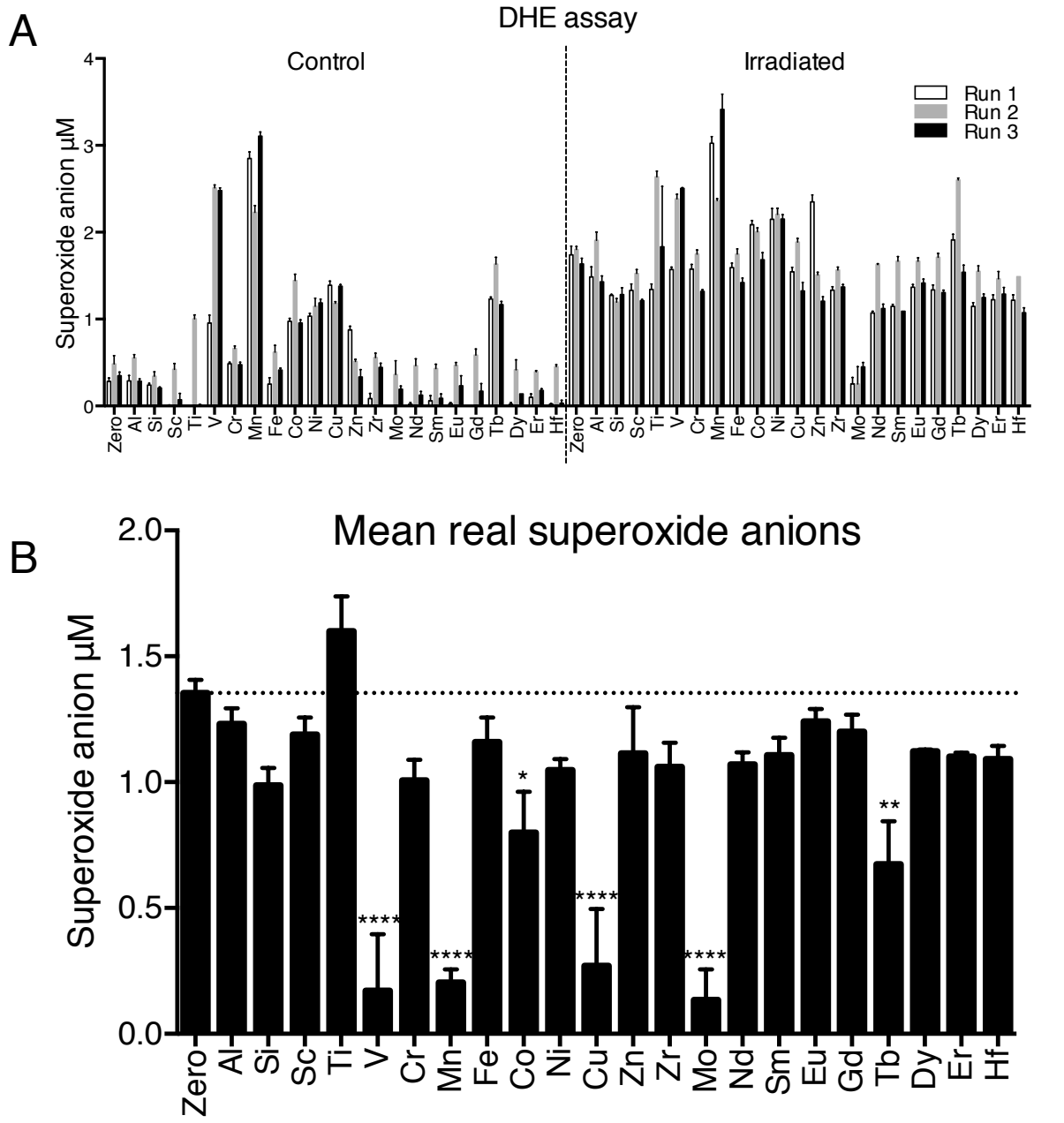

Figure 4.2: Superoxide anion radical production. A) Superoxide radical concentrations for unirradiated control (left side) and 10 Gy irradiated (right side) NPs. Data are shown for 3 independent experiments (run 1, run 2, run 3). B) Data from panel (A) replotted as 'real' values (10 Gy irradiated value minus 0 Gy control) ±SEM. Dotted line shows the irradiation-induced increase due to water only. ****, ** and * denote respectively P<0.0001, P<0.01 and P<0.05 significant differences, compared to no NP (zero).

For the singlet oxygen probe SOSG, the graph is dominated by Tb_4O_7, which shows high probe fluorescence in the absence and presence of irradiation (Figure 4.3A). There is also suggestion that MoO_3 again shows lower radical production than water with or without irradiation.

After subtracting the non-irradiated control values for each sample (Figure 4.3B), nearly half of the NPs show similar irradiation-induced singlet oxygen values to water-only: Al_2O_3, SiO_2, Sc_2O_3, TiO_2, Cr_2O_3, Fe_3O_4, CoO, ZrO_2 and HfO_2. The remaining NPs all show a tendency for less irradiation-induced singlet oxygen production than water; significantly lower in the cases of MoO_3 and V_2O_5 in particular, as well as for NiO, CuO, Nd_2O_3, Eu_2O_3, Gd_2O_3, and Dy_2O_3. Tb_4O_7 shows less irradiation-induced singlet oxygen production than water, although its absolute value is higher than water as it is so active on its own.

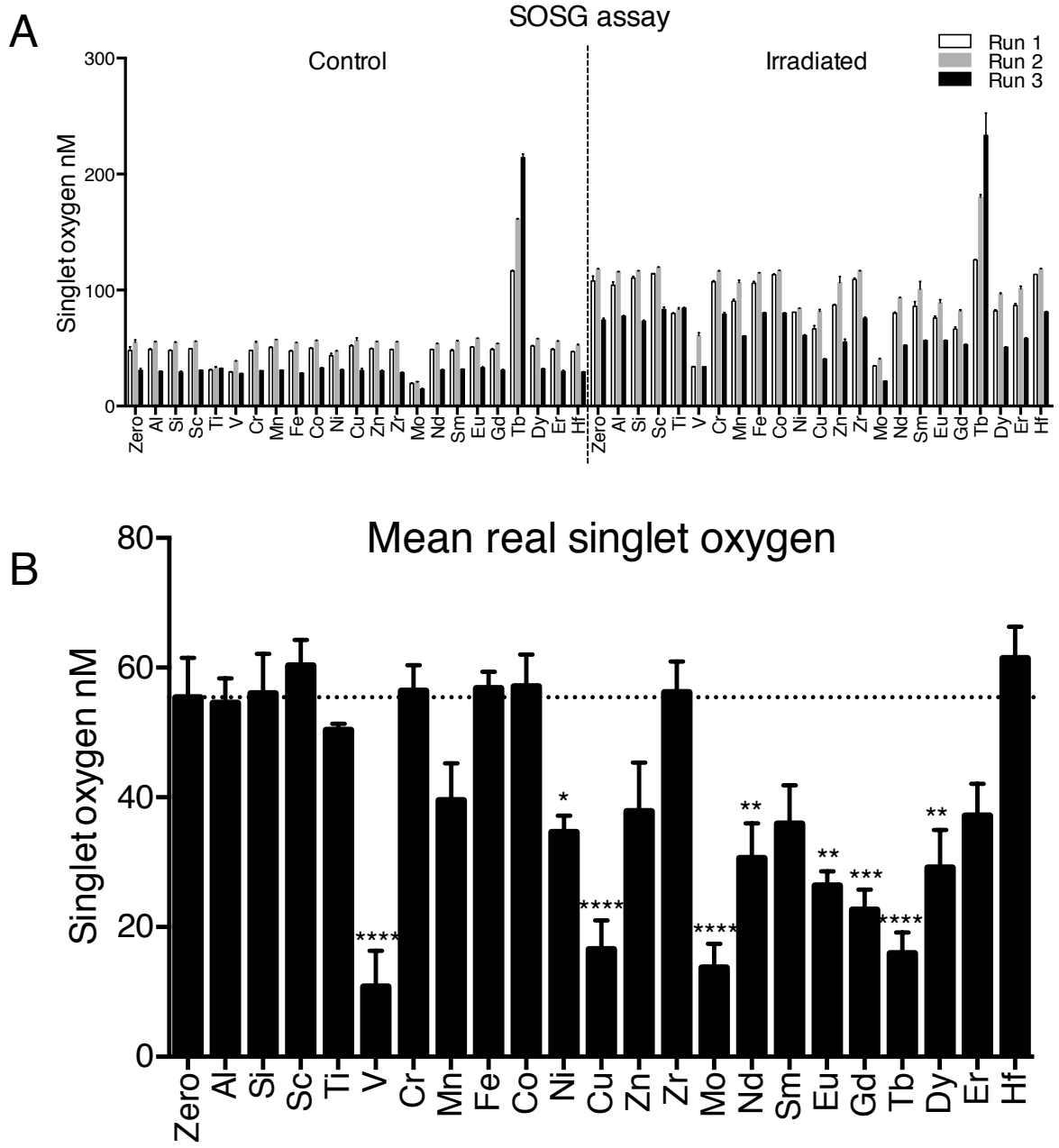

Figure 4.3: Singlet oxygen production. A) Singlet oxygen concentrations for unirradiated control (left side) and 10 Gy irradiated (right side) NPs. Data are shown for 3 independent experiments (run 1, run 2, run 3). B) Data from panel (A) replotted as 'real' values (10 Gy irradiated value minus 0 Gy control) ±SEM. Dotted line shows the irradiation-induced increase due to water only. ****, ***, ** and * denote respectively P<0.0001, P<0.001, P<0.01 and P<0.05 significant differences, compared to no NP (zero).

To help summarise the reactive oxygen species (ROS) data, the radiation-induced increase in each ROS is presented as a stacked bar chart (Figure 4.4A). Because many of the metal oxide NPs contain very different atomic proportions of their metal element (e.g. CuO NPs are 50% Cu, while MoO_3 NPs are 25% Mo) we have replotted these data to normalise ROS values by stoichiometry to the metal proportion of each NP (Figure 4.4B).

It is clear that superoxide is the main ROS produced by most irradiated NPs. The two exceptions are V_2O_5 and MoO_3, where hydroxyl radicals are the majority ROS. For each NP, singlet oxygen makes a very minor contribution.

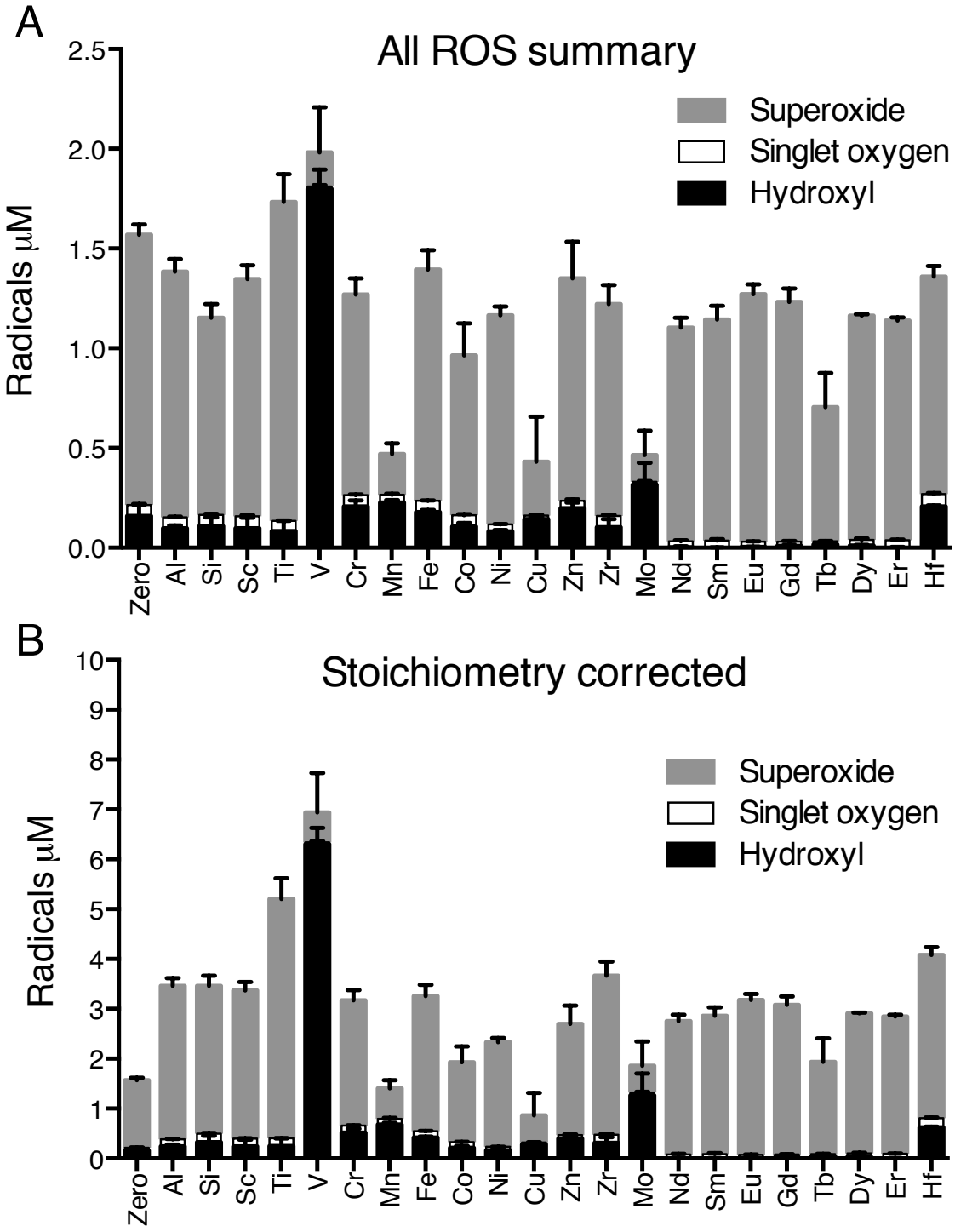

Figure 4.4: A) Stacked bar chart summarising the irradiation-induced ('real') change in overall radical production for each NP. B) Data from panel A replotted to normalise the proportion of metallic element atoms, based on each NP chemical formula. Values for water (zero) left unaltered. All values ±SEM.

4.2.2.3 Hole scavenger

High energy X-rays eject electrons from nanoparticles, leaving behind reactive holes with picosecond lifetimes that, unless already at the NP surface, are unlikely to take part in any reactions (Drescher et al., 2002). However, ejected electrons undergo subsequent collisions, sequentially lowering their energies to low eV levels (Stephen J. McMahon et al., 2011) where electron-hole (e^-/h^+) pairs can be formed in the metal oxides (Rodnyi, 1997). If these migrate to the NP surface before recombining, they can participate in reactions with surface-adsorbed oxygen to generate superoxides from electrons and hydroxyl radicals from holes (Le Caër, 2011; Sahu & Cates, 2017).

To assess the possible role of X-ray-induced e^-/h^+ pairs in superoxide formation by NPs, we repeated the superoxide assay in the presence of the hole scavenger 10 mM formic acid (Puangpetch et al., 2011; Tan et al., 2003), or a pH-matched 10 mM nitric acid control. If e^-/h^+ pairs are important players in our experiments, then we expect the hole scavenger to increase the lifetime of the electrons, thus promoting superoxide formation at the NP surface.

Considering the non-irradiated control values, some differences between nitric acid and formic acid conditions are observed for CuO and Tb_4O_7, with CuO showing higher superoxides in formic acid and Tb_4O_7 showing less superoxide in formic acid. Similar results were observed for these metal oxides with irradiation. After irradiation, MnO_2 also shows less superoxide formation in formic acid compared to in nitric acid. It is not clear why superoxide formation is lower in formic acid for these metal oxides.

After subtraction of the non-irradiated results, only Fe_3O_4, CoO, NiO and ZnO demonstrated irradiation-dependent increases in superoxide radical generation in the presence of formic acid, compared with nitric acid (Figure 4.5B).

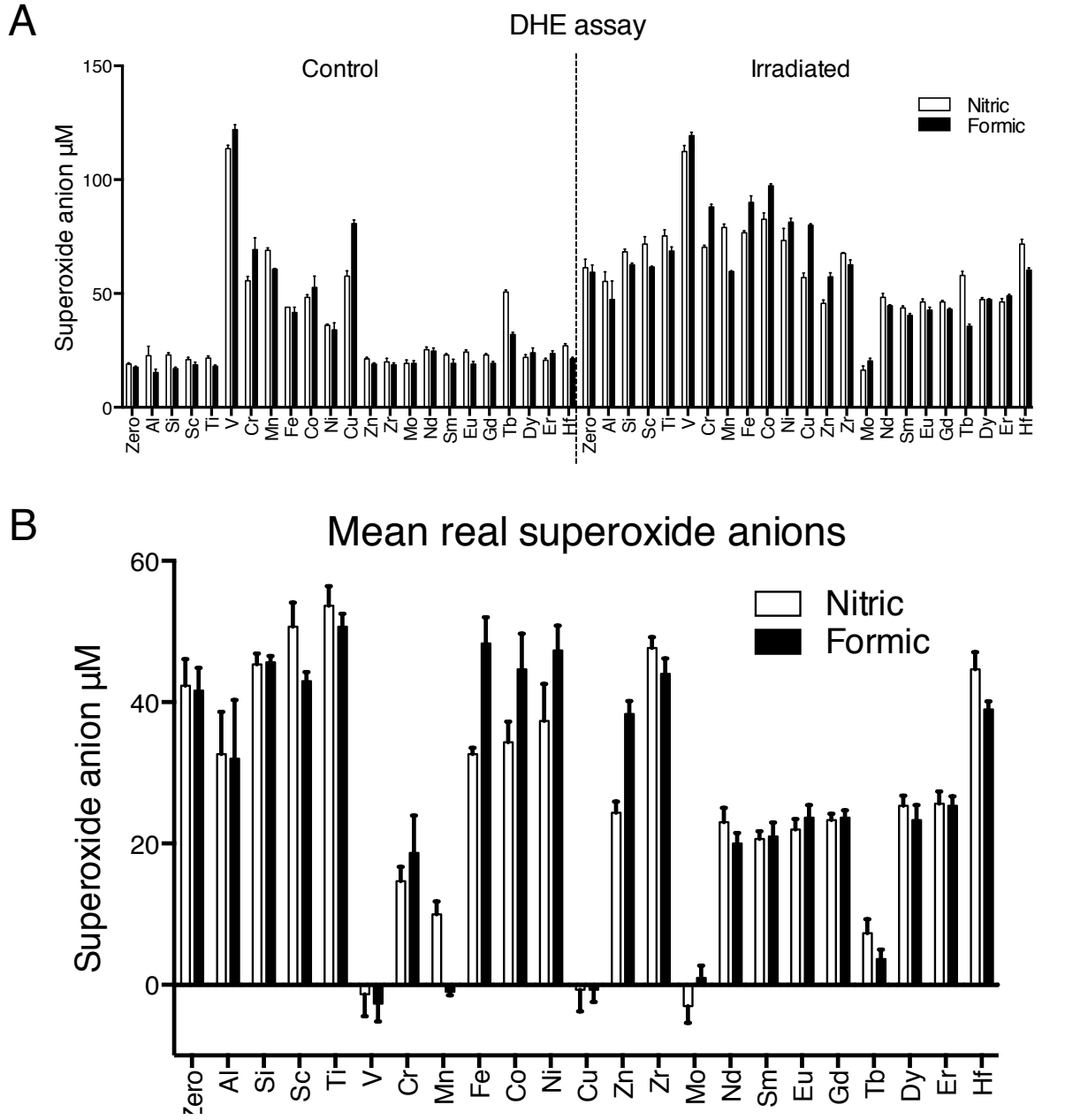

Figure 4.5: A) Superoxide formation in the presence of pH 3.5 10 mM nitric acid or pH 3.5 10 mM formic acid hole scavenger. Left side shows unirradiated controls and right side shows 10 Gy irradiated. N=3 and all values ±SEM. B) Data from panel (A) replotted as 'real' values (10 Gy irradiated value minus 0 Gy control) ±SEM.

4.2.2.4 DNA damage assay

Plasmid DNA normally exists as a tightly-wound supercoil. Single strand breaks allow the supercoil to relax to an open circle which demonstrates slower migration on an electrophoretic gel. We therefore quantified DNA damage in the presence of NPs by measuring the proportion of relaxed circular DNA (Figure 4.6).

In the absence of irradiation, MoO_3 and CuO caused the greatest damage to DNA. These NPs also demonstrated the greatest DNA damage following irradiation (Figure 4.6A-C).

When the DNA damage due to non-irradiated controls was subtracted from each irradiated value, it became clear that most NPs produced only slightly more irradiation-specific DNA damage than water (Figure 4.6D). Only CuO performed significantly better than water in terms of irradiation-specific DNA damage (Figure 4.6D).

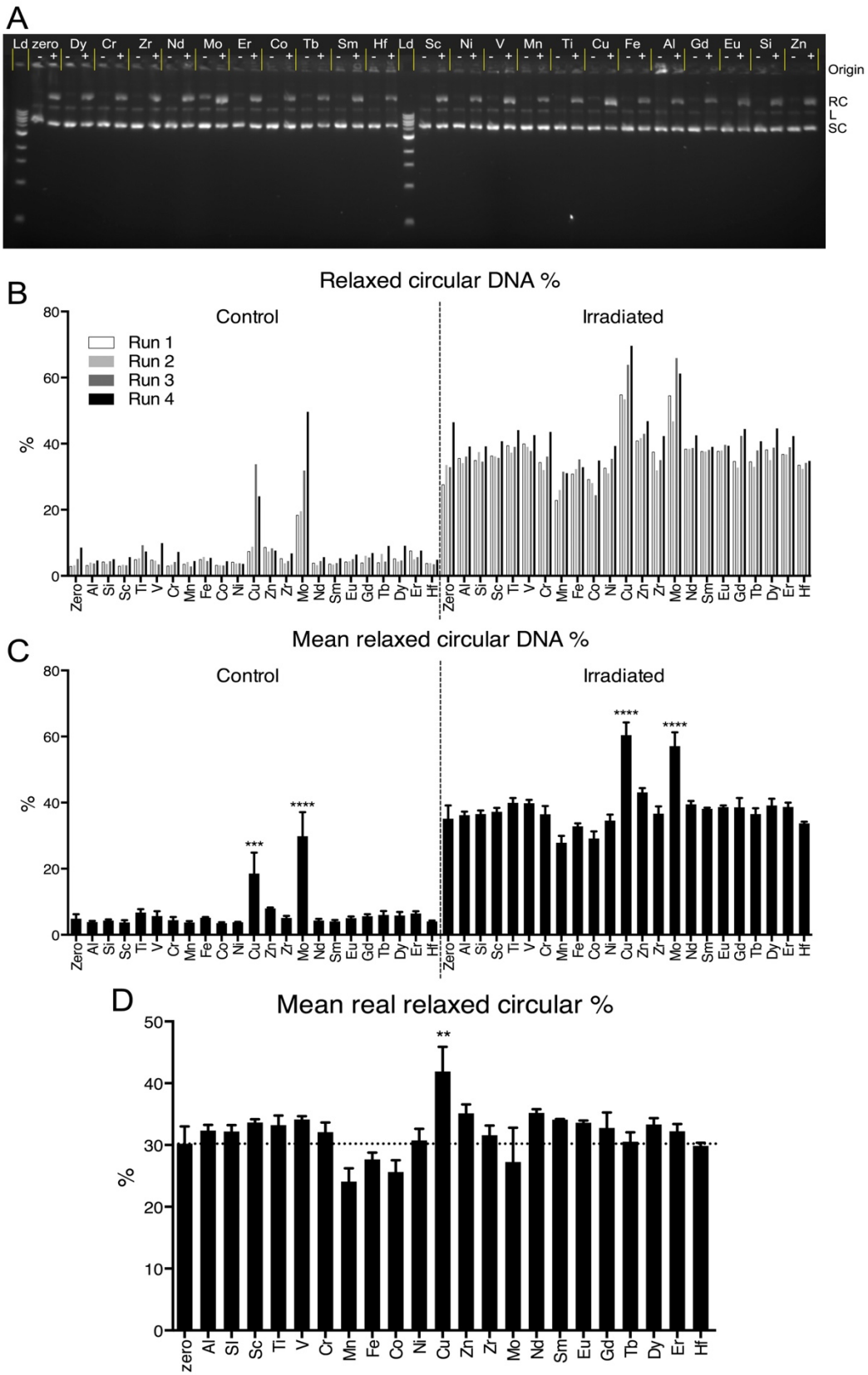
A
Ld zero Dy Cr Zr Nd Mo Er Co Tb Sm Hf Ld Sc Ni V Mn Ti Cu Fe Al Gd Eu Si Zn
Origin
RC
L
SC
B
Relaxed circular DNA %
Control
Irradiated
Run 1
Run 2
Run 3
Run 4
%
C
Mean relaxed circular DNA %
Control
Irradiated
***
****
****
%
D
Mean real relaxed circular %
**
%
zero Al Si Sc Ti V Cr Mn Fe Co Ni Cu Zn Zr Mo Nd Sm Eu Gd Tb Dy Er Hf

Figure 4.6: DNA damage assays based on the appearance of the relaxed circular form of plasmid DNA. A) Agarose gel from one experiment showing paired non-irradiated (-) and 10 Gy irradiated (+) samples. Bands corresponding to undamaged (supercoiled, SC), single strand break (relaxed circular, RC) and double strand break (linear, L) plasmid DNA are marked. Ld is 1 kb DNA ladder. Note that this gel is not loaded in atomic number order. B) Percentage relaxed circular DNA from each experiment. C) Average values from (B) ±SEM. D) Data from panel (C) replotted as 'real' values (10 Gy irradiated value minus 0 Gy control) ±SEM. Dotted line shows the irradiation-induced increase due to water only. ****, *** and ** denote respectively $P<0.0001$, $P<0.001$ and $P<0.01$ significant differences, compared to the respective no NP (zero) control.

4.2.3 Discussion

The ability of nanoparticles to act as X-ray radiosensitisers has generally been viewed as a physical process, due to the increased absorption of X-rays, followed by ejection of secondary electrons (photoelectric effect) and fluorescence photons that then interact with water or biomolecules to produce radiolysis products, which include damaging radicals (Kuncic & Lacombe, 2018). For this reason, the emphasis of NP radiosensitiser research has been on high atomic number elements, due to their expected greater interaction cross section with X-ray photons.

A theoretical study by McMahon *et al*, (2016), based on physical processes, computed the energy deposition within 1 μm around a series of X-ray irradiated pure element 20 nm NPs in water (Z=14, Si to Z=80, Hg). When all energy outputs are added together (Auger electrons, photoelectrons, Compton electrons, fluorescence, electron impact) the total energy deposition from 6 MV X-rays was relatively flat across all the elements studied (Fig. 3C,D in McMahon et al., 2016), implying that the choice of element makes little difference to the amount of ROS produced at these energies.

However, experimental data from Sicard-Roselli *et al* (2014) and Gilles *et al* (2018) demonstrated that many more hydroxyl radicals (Gilles et al., 2018; Sicard-Roselli et al., 2014) and solvated electrons (Gilles et al., 2018) are produced from X-ray irradiated Au NPs than can be explained purely by physical processes, such as the photoelectric effect. They proposed that additional radicals are produced via reactions of secondary electrons with interfacial water molecules, that become stretched due to their adsorption to the Au NP and therefore require much less energy for H-OH bond radiolysis than bulk water (255 kJ/mol instead of 460 kJ/mol) (R. Liu, 2013). This water distorting effect is not restricted to Au NPs: water molecules form similar structured layers up to 2 nm thick around any NP (Zobel, 2016; Zobel et al., 2015) and this is where most radiolytic reactions are expected to occur.

Moreover, nanoparticles will inevitably come into contact with excited water (H_2O^*) and ionised water (H_2O^+, e^-_{aq}), formed during the first 10^{-15} seconds of irradiation, plus the physico-chemical reaction products of these species, produced during the subsequent 10^{-12} seconds, such as $^{\cdot}OH$, $^{\cdot}H$, H_3O^+ and OH^-; and downstream products such as H_2O_2 (reviewed in Le Caër, 2011). Because of their high surface area and specific surface chemistries, nanoparticles could catalyse many more reactions from these intermediates and thereby increase the overall concentration of radicals.

This mismatch between theory and experimental observations for Au NPs prompted us to consider if a broad range of metal oxide NPs, well known for their catalytic properties, but hitherto not considered as

radiosensitisers because of their low atomic number, might be good radiosensitisers. We therefore experimentally compared the radical forming ability and DNA damage of 22 different metal oxides using clinically relevant 6 MV energy X-rays.

Two previous studies have compared the behaviour of several metal oxides under gamma irradiation. Chelnokov *et al* (2014) measured yields of solvated electrons, relative to water, following radiolysis of concentrated metal oxide NP aqueous solutions in low oxygen conditions. Six of those NPs are in common with our study: Al_2O_3, SiO_2, ZnO, Nd_2O_3, Sm_2O_3, and Er_2O_3 (Chelnokov et al., 2014). At the lowest NP concentrations tested (600 mM) Chelnokov found modest increases in solvated electrons for Sm_2O_3 (1.2 fold) and Er_2O_3 (1.4 fold), but no change for the other NPs tested. In normoxia, solvated electrons react with dissolved oxygen to give superoxide radicals, but we found no significant increases in superoxide for Sm_2O_3, and Er_2O_3. However, because Chelnokov's experiments were performed under argon, they are not directly comparable with ours.

Petrik *et al* (2001) examined hydrogen production from a thin layer of adsorbed water on 28 different metal oxides during high dose gamma irradiation (0.1 – 1.5 M Gy), only 14 of which are in common with our study and are compared here. Hydrogen is mostly produced during water radiolysis from reactions of solvated electrons with water; but can be produced via reactions involving hydrogen radicals that generate hydroxyl radicals as a by-product ($H_2O^* \rightarrow {}^{\cdot}OH + {}^{\cdot}H$, then ${}^{\cdot}H + {}^{\cdot}H \rightarrow H_2$). Thus, a tentative link could be made between hydrogen production in that study and our measurements of hydroxyl radicals. Petrik *et al* found an increased hydrogen yield relative to water with: ZrO_2, Nd_2O_3, Sm_2O_3, Eu_2O_3, Gd_2O_3, Er_2O_3 and HfO_2. Oxides that decreased hydrogen production relative to water were: MnO_2 and CuO. The other oxides Petrik *et al* tested (Al_2O_3, SiO_2, TiO_2, Cr_2O_3, NiO and ZnO) showed no difference in hydrogen production.

We find no significant irradiation-induced changes in hydroxyl radicals for any of these metal oxides. Indeed, our trend of decreased hydroxyl radicals for the Lanthanides is opposite to the increased hydrogen production data of Petrik *et al*.

Therefore, either the hydrogen radical-mediated pathway is such a minor player in the overall reactions that it is easily swamped by independent reactions and/or there are fundamental differences in the experimental designs. To address the second point, the most obvious difference is that Petrik *et al* exposed metal oxides to water vapour, to form a thin adsorbed layer, whereas we irradiate NPs in solution. Our protocol therefore allows two additional sets of reactions to occur. Firstly, energetic secondary electrons ejected from NPs can travel further in bulk water and participate in more reactions than is possible in a thin adsorbed layer of water. Secondly, NPs can migrate through bulk water, coming into contact with radiolytically-produced hydrogen peroxide and metastable radiolysis species, which they catalytically convert into various radicals (Le Caër, 2011; Lousada et al., 2013).

Moreover, for some of these catalytic reactions, the NP surface is not necessarily required. Metal ions released from NPs, such as V^{3+}, readily participate in Fenton-like catalytic reactions with hydrogen peroxide to generate hydroxyl radicals and hydroperoxide radicals (G. Du & Espenson, 2005).

Electron donation to singlet oxygen can generate superoxide anions (Saito et al., 1983) and, perhaps because of this, we find a partial correlation in our data between radiation-induced superoxide and singlet oxygen levels. Thus, the lowest levels of superoxide and singlet oxygen compared to non-irradiated values are seen with: V_2O_5, CuO, MoO_3, Tb_4O_7. Although MnO_2 does not fit this pattern, being very low with superoxide, but only slightly lowered with singlet oxygen. However, no strong correlation exists between high levels of superoxide and singlet oxygen.

Although superoxides can produce hydroxyl radicals via Fenton-like electron reduction of hydrogen peroxide (Richmond et al., 1981), our data show no consistent correlation between radiation-induced superoxide and hydroxyl radical levels.

Regarding the correlation of ROS levels to DNA damage, we summarise our data in Table 4.2.

Our data suggest that TiO_2 and V_2O_5 NPs are worth further investigation, because of consistent increases in both ROS and DNA damage. However, various surprises should also be explored. Notably, Sc_2O_3, ZnO, Nd_2O_3, Sm_2O_3, Eu_2O_3, Dy_2O_3 and especially CuO, produced more irradiation-induced DNA damage than expected from their total irradiation-induced ROS output.

Table 4.2: Summary table of total irradiation-induced: ROS, DNA damage and e-/h+ pair formation. Ranked from high to low ROS and for similar levels of damage, ranked in element order. Change from control: +/- = 10-25%; ++/-- = 25-50%; +++/--- = >50%.

NP	ROS	DNA damage	e^-/h^+ pair
V_2O_5	++	+	
TiO_2	+	+	
Al_2O_3	-		
Sc_2O_3	-	+	
Cr_2O_3	-		
Fe_3O_4	-		++
ZnO	-	+	++
ZrO_2	-		
Eu_2O_3	-	+	
Gd_2O_3	-		
HfO_2	-		
SiO_2	--		

CoO	--	-	++
NiO	--		++
Nd_2O_3	--	+	
Sm_2O_3	--	+	
Dy_2O_3	--	+	
Er_2O_3	--		
MnO_2	---	-	
CuO	---	++	
MoO_3	---		
Tb_4O_7	---		

CuO NPs cause DNA damage *in vivo* (Atha et al., 2012). Specifically, copper ions form adducts with DNA that cause structural distortions (Abdelhamid et al., 2018) and potentiate ROS-mediated damage (Cervantes-Cervantes et al., 2005). CuO is therefore likely to potentiate irradiation-induced DNA damage, without itself producing ROS and this could explain the mismatch between our DNA damage and ROS data for CuO.

The extent of NP-DNA interaction is likely to be an important variable for all the other NPs studied, since the radiation dose deposited near the NP increases exponentially as the NP surface is approached. Thus, in the interaction of 2 nm AuNPs with 6 MV X-rays, the dose can be enhanced several thousand-fold within 10 nm of the Au surface (McMahon et al., 2011). It is therefore likely that the binding of NPs to DNA, especially if these interactions physically destabilise DNA, will result in much greater irradiation damage. Conversely, NPs that do not make close contact with DNA will likely result in less DNA damage than predicted from their ROS output.

Of course, many of the NPs we have tested are far too toxic in their current formulation to be considered for direct translation to preclinical studies. NPs can be toxic via multiple parallel mechanisms (reviewed in (Sukhanova et al., 2018; Huang et al., 2017). These include: physical damage to membranes and organelles, disruption of membrane channels and biochemical reactions (Taggart et al., 2016), activation of death pathways (Tzelepi et al., 2019) and generation of ROS stress (Manke et al., 2013). In addition to their toxicity, many rare earth metal oxides also present fire and explosion hazards (Rim et al., 2013).

Of the two NPs we have identified as good radiosensitisers (V_2O_5 and TiO_2), only TiO_2 is of sufficiently low toxicity to consider following up. Indeed, some advances have already been made using

radiosensitisers based on TiO_2 NPs (Nakayama et al., 2016; Morrison et al., 2017; Townley, Rapa, et al., 2012).

We consider that the future of NP radiosensitisers most probably lies in the combination of high *Z* elements with catalytic oxides: using the photoelectric effect of high *Z* elements to feed secondary electrons into the catalyst. These composite NPs could be made as complex oxides, as has been done with Bi_2WO_6 (Sahu & Cates, 2017); aggregate mixtures, or core-shell arrangements. For instance, improved radiosensitisation has been reported using lanthanide-doped TiO_2 (Townley, Rapa, et al., 2012) and ZnO NPs (Ghaemi et al., 2016), ZnO-SiO_2 nanocomposites (Generalov et al., 2015) and Au-Bi_2S_3 heterostructures (X. Wang et al., 2019).

As with all catalysts, it will be important to consider ways to prevent 'fouling' of the catalytic surface by ligands or serum proteins *in vitro*, since we and others have previously shown that the presence of a ligand shell on AuNPs greatly decreases irradiation-induced ROS production (Gilles et al., 2014; Grellet et al., 2017).

4.2.4 Conclusions

We find large variations in the formation of three types of radical species in solutions of metal oxide NPs. In general, the largest irradiation-induced increases are seen for superoxides, where TiO_2 produces an additional 1.6 μM superoxide upon irradiation. This being some 0.2 μM more than water only. A more impressive increase is seen for hydroxyl radicals using V_2O_5, demonstrating an additional 1.8 μM hydroxyl radicals upon irradiation; 1.6 μM more than water only. However, bulk radical formation *per se* does not predict the extent of radiation-induced DNA damage in the presence of these NPs. Thus, although TiO_2 and V_2O_5 both produce more irradiation-induced DNA damage than water, CuO produces nearly 8% more DNA damage even though it shows one of the lowest irradiation-induced increases in radicals. Therefore, other factors that probably involve intimate DNA-NP interactions, such as DNA destabilisation and highly-localised increases in radical concentration near the NP surface, likely predominate.

In summary, when considering NP radiosensitisers, it is perhaps worth remembering the old phrase 'don't judge a book by its cover'. Theoretical predictions of energy output and biological damage are currently based on physical principles and need to be expanded to take account of subsequent chemical reactions on and near the NP surface.

Also, the purely catalytic nature of many NPs, within a 'sea' of radiolytic reactants needs to be considered in order to obtain a fuller picture of the intrinsic radiosensitising ability of a NP. These physical/chemical considerations then need to be put into a biological context. How well are they taken up by cells and is there any selectivity towards cancer cells? Once the NPs are in a biological medium of proteins and sugars, does this alter their ability to produce ROS and damage cancer cells? We know that our results pose more questions than they answer, but if this leads to a deeper understanding of

radiosensitisation theory and allows for rational choices of the best nanoparticle materials, then this is ultimately a good thing.

4.2.5 Methods

4.2.5.1 Nanoparticles

The following nanoparticles were obtained from US Research Nanomaterials: Cr_2O_3 (US3060, 60 nm, >99%), MnO_2 (US3319NMP, 50 nm, 98%), CoO (US3051, 50 nm, 99.7%), ZrO_2 (US3600, 40 nm, >99%), MoO_3 (US3330, 13-80 nm, 99.94%), Nd_2O_3 (US3350, 30-45 nm, 99.9%), Sm_2O_3 (US3450, 15-45 nm, 99.95%), Eu_2O_3 (US3543, 10-100 nm, 99.99%), Gd_2O_3 (US3240, 10-100 nm, 99.9%), Tb_4O_7 (US3455, 10-100 nm, 99.99%), Dy_2O_3 (US3080, 30 nm, >99.9%), Er_2O_3 (US3140, 10-100 nm, 99.9%) and HfO_2 (US3245, 61-80 nm, 99.99%).

The following nanoparticles were obtained from Sigma-Aldrich: Al_2O_3 (544833, <50 nm, 99.8%), SiO_2 (637238, 10-20 nm, 99.5%), TiO_2 (718467, 21 nm, 99.5%), Fe_3O_4 (637106, 50-100 nm, 97%), NiO (637130, <50 nm, 99.8%), CuO (544868, <50 nm, 82.6%) and ZnO (721077, <100 nm).

Sc_2O_3 was obtained from American Elements (SC-OX-02-NP, <80 nm, 99%).

V_2O_5 was obtained from Nanoshel (NS6130-03-399, <80 nm, 99.9%).

4.2.5.2 TEM

Samples were prepared by drop-coating films of the NP solutions on electrostatically discharged carbon-coated copper TEM grids and visualized on a JEM-1400 model EM instrument (JEOL, USA) operated at an accelerating voltage of 80 kV and x 30,000 magnification. Size histograms were measured from 20 TEM images per nanoparticle type at x3000 magnification using the Analyze Particles feature of ImageJ software (version 1.52; NIH) and are reported as the mean and median values.

4.2.5.3 DLS

The hydrodynamic diameter of 2.5 mM NPs in 3% PBS pH 7.4 were measured using a Nanotrac Flex particle size analyser, with Flex 11.1.0.5 software (Microtrac).

4.2.5.4 XRD

Samples were analysed using a Siemens D5005 XRD with a long fine focus copper X-ray tube energised at 40 kV and 40 mA, running conventional Bragg-Brentano geometry. Most runs were 0.5 s/step, with some at 8 s/step. Crystal phases were determined from XRD spectra using QualX2 software (Altomare et al., 2015) (version 2.24; Institute of Crystallography CNR, Bari, Italy) and PowCod database 1901.

4.2.5.5 Hydroxyl radical probe

5 mM stock of coumarin-3-carboxylic acid (CCA) powder (Sigma Aldrich) was prepared in 6% PBS pH 7.4.

4.2.5.6 Singlet oxygen probe

Singlet oxygen sensor green (SOSG) was purchased from ThermoFisher. From a 5mM methanolic stock, a working solution of 1 μM was prepared in 6% PBS pH 7.4.

4.2.5.7 Superoxide anion probe

Dihydroethidium (DHE) was purchased from ThermoFisher. From a stock of 20 mM DHE in DMSO a working solution of 50 μM was prepared in 6% PBS pH 7.4.

4.2.5.8 Radical measurement

Experiments were run a minimum of three times independently and each time containing technical triplicates. Fifty microlitres of probe working solution was added to 50 μl of 5 mM NP in deionized water in black-walled 96-well plates (Cellstar, Greiner), producing a 2.5 mM NP working solution. After irradiation, the fluorescence of each well was measured using a FLUOstar Optima plate reader (BMG Labtech), according to the type of probe: CCA at Ex 390 nm/ Em 450 nm, SOSG at Ex 485 nm /Em 520 nm, and DHE at Ex 485 nm/ Em 590 nm (H. Zhao et al., 2003).

4.2.5.9 Radical probe calibration curves

Each NP could potentially alter the fluorescence of the probe solution. Therefore, for each probe, 50 μl serial dilutions of the fully oxidized fluorescence molecule in 6% PBS were mixed with 50 μl 5 mM NP solution and the fluorescence measured as already described.

For CCA calibration, 7-hydroxycoumarin-3-carboxylic acid (7OH-CCA, Sigma-Aldrich) was used. For SOSG calibration, 0.5 μM SOSG was reacted with 6% H_2O_2 and 2% NaOCl. For DHE calibration, 1.5 μM DHE was reacted with 0.5 mM xanthine in 0.9% NaCl and 10 mU/ml xanthine oxidase (Sigma-Aldrich). We report the molarity of each radical species, assuming an equimolar reaction between each probe and its cognate radical.

4.2.5.10 Hole quenching

Fifty microlitres of 5 mM NP solutions were mixed with 50 μl of 50 μM DHE in either 10 mM formic acid pH 3.5 as a hole scavenger (Puangpetch et al., 2011; Tan et al., 2003) or 10 mM nitric acid pH 3.5 as a control.

Samples were irradiated in 96-well plates, as described and fluorescence measured at Ex 485 nm/ Em 590 nm, as described.

4.2.5.11 Plasmid DNA damage assay

Plasmid pBR322 was extracted from bacteria using Qiagen plasmid midi kits and kept as a 50 ng/μl stock in 10 mM Tris-HCl, pH 8.5. Ten microlitres of plasmid DNA were mixed with 10 μl of 5 mM NP solution in 96-well plates. Solutions were either left untreated or irradiated with 10 Gy of 6 MV X-rays, as described below. Five microlitres of each sample were mixed with 5 μl loading dye (Purple, New England Biolabs) and loaded onto 1% agarose electrophoresis gels containing 0.2 μg/ml ethidium bromide with a running buffer of Tris-Borate-EDTA with 0.2 μg/ml ethidium bromide. A 1 kb DNA ladder was also used (Quick-load Purple Plus, New England Biolabs). Gels were run at 110 V for 1 h and then photographed using a G:Box Chemi XX6 gel documentation system (Syngene), ensuring that no image pixels were saturated. DNA band intensities were quantified using the Gel Analysis feature of ImageJ software (version 1.52; NIH).

4.2.5.12 X-ray irradiation

Plates were sandwiched between two blocks of 10 cm solid water shielding (Gammex) to simulate the location of a deep tumour and X-rays were deposited within the liquid in each well by beam shaping, using a treatment plan based on CT scans of the plates. Plates were irradiated with 10 Gy of 6 MV X-rays at a dose rate of 5 Gy/min using a clinical linear accelerator (Versa HD, Elekta) at GenesisCare, Milton Keynes. The radiation field was 25 x 25 cm and previous calculations with a similar linear accelerator machine have shown that this field size, with 10 cm depth of water and 6 MV photons will produce a broad polychromatic energy spectrum from 0 – 6 MV, with the majority of the photon energies below 1 MeV (Konefał et al., 2015).

4.2.5.13 Statistical analysis

Data from three independent experiments were compared to the no NP control using one-way ANOVA with Dunnett's multiple comparisons (GraphPad Prism v6 software).

Declarations

Ethics approval and consent to participate: Not applicable.

Consent for publication: Not applicable.

Availability of data and materials: The datasets for the ROS assays are included in the supplementary information file. All other datasets are available from the corresponding author on reasonable request.

Competing interests: The authors declare that they have no competing interests.

Funding: This work was funded by grants from the Sir John Mason Academic Trust and Santander Bank. Alexandra Guerreiro is a PhD candidate in the New University of Lisbon RaBBiT doctoral training program and her stipend was provided by Fundação para a Ciências e Tecnologia (FCT/MCTES), Radiation Biology and Biophysics Doctoral Training Programme (RaBBiT, PD/00193/2012); UID/Multi/04378/2013 (UCIBIO); UID/FIS/00068/2013 (CEFITEC); and grant number PD/BD/114450/2016 to Alexandra Guerreiro. None of the funding bodies played any role in the study design, data collection and analysis, or writing of the manuscript.

Authors' contributions: AG performed all of the experiments and contributed to study design and data analysis. JG was the primary supervisor and designed the study and data analysis. NC and EC were members of the supervision team and contributed to study design and data analysis. All authors read and approved the final manuscript.

Acknowledgements: We thank the radiographers at Genesis Care, Milton Keynes for help with irradiations.

We also thank colleagues at the Open University for technical assistance: Dr Igor Kraev for help with TEM, George Bryant for help with DLS and Dr Matthew Kershaw for help with XRD. Additional thanks

to Open University undergraduate students Heather Walsh and Heather Allderidge for pilot work developing radical assays with TiO_2 nanoparticles.

Supplementary Figures

NPs	TEM image low magnification	TEM image high magnification	Size distribution (x axis: NP diameter in nm) (y axis: counts)
Al	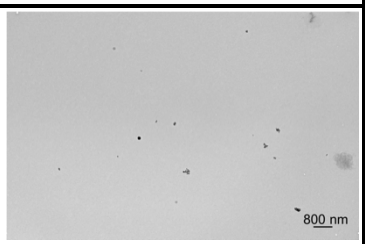	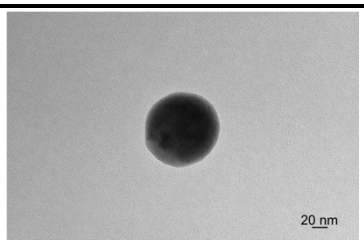	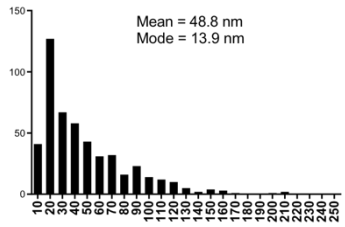
Si	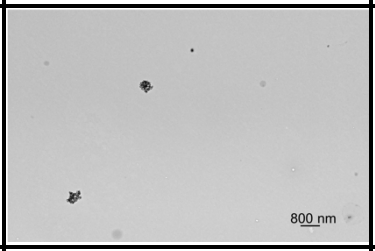	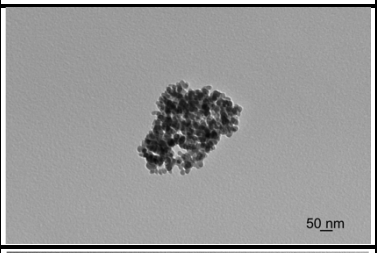	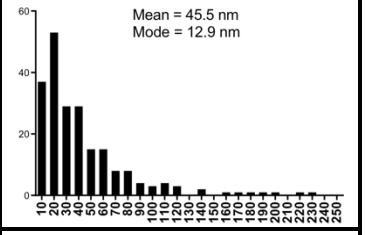
Sc	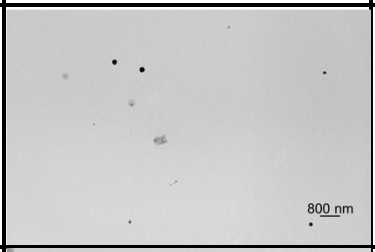	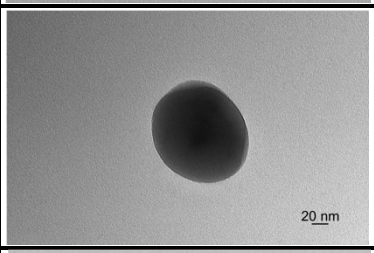	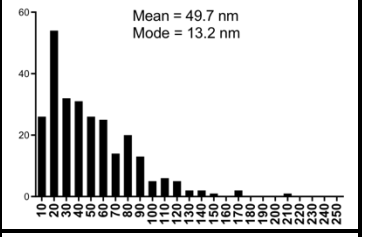
Ti	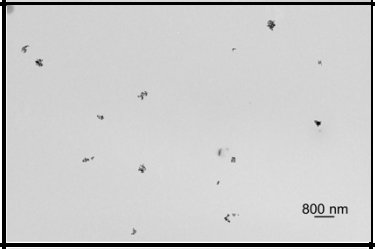	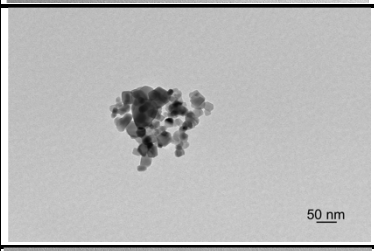	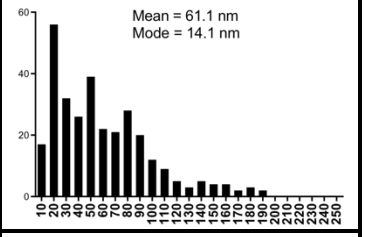
V	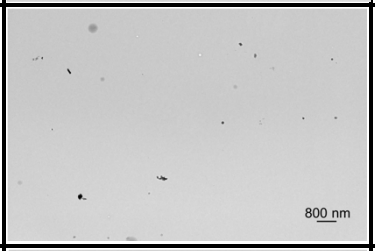	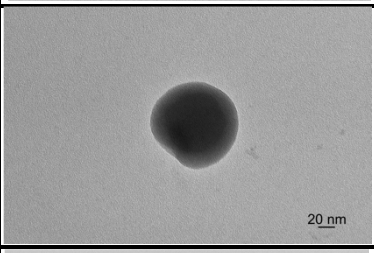	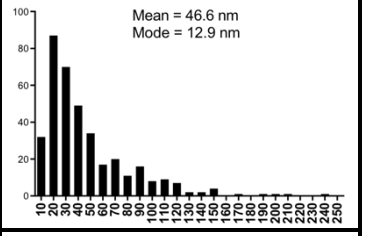
Cr	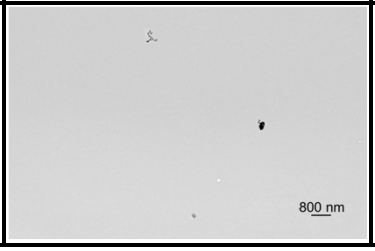	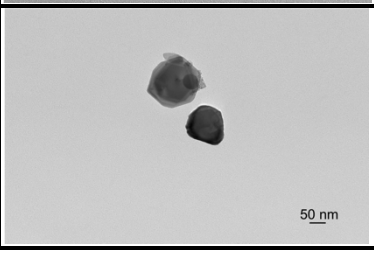	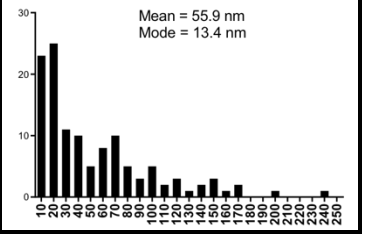

Mn	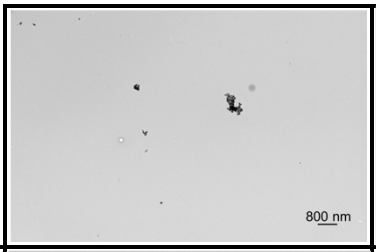	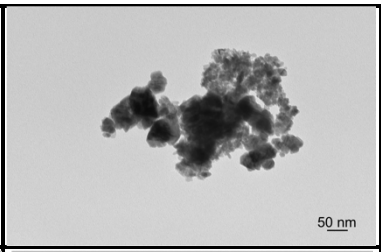	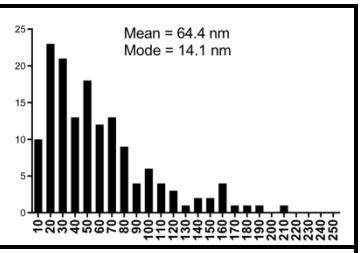
Fe	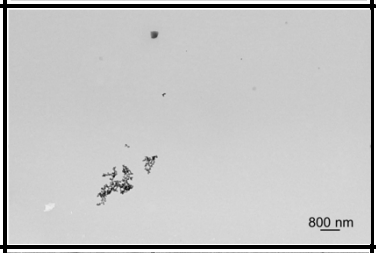	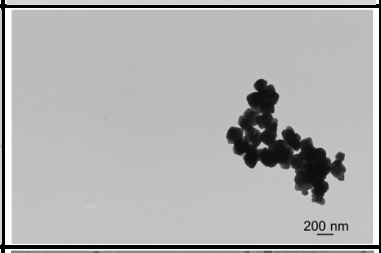	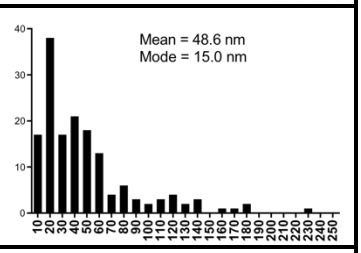
Co	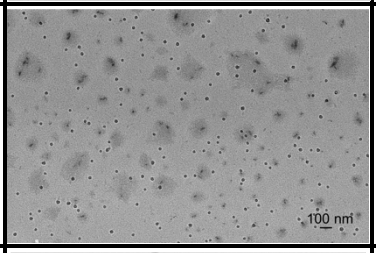	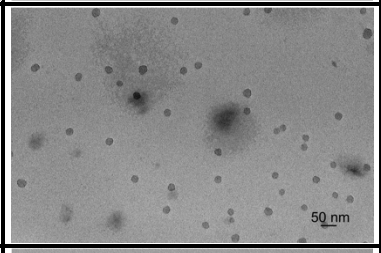	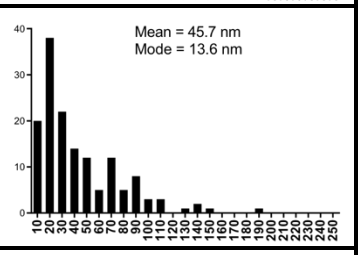
Ni	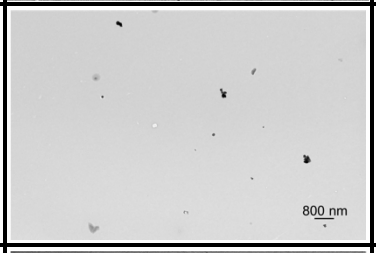	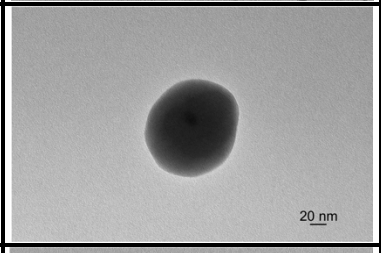	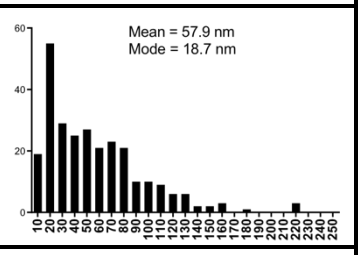
Cu	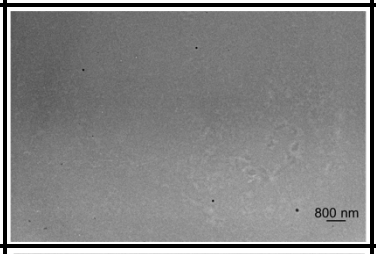	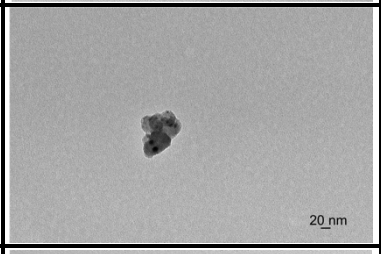	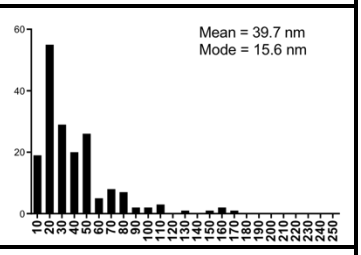
Zn	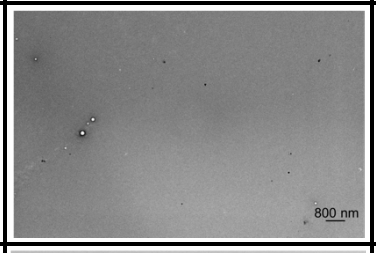	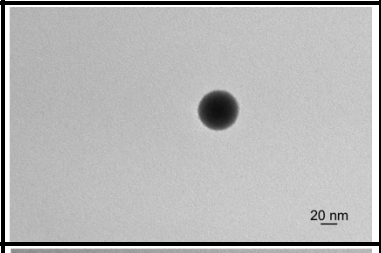	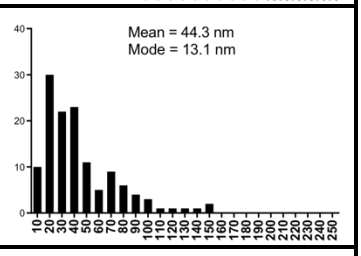
Zr	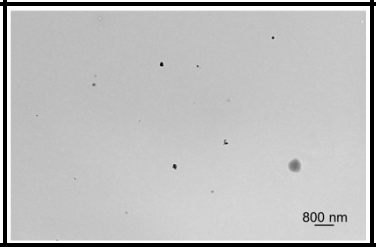	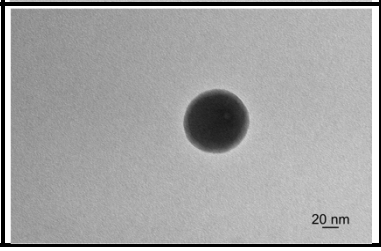	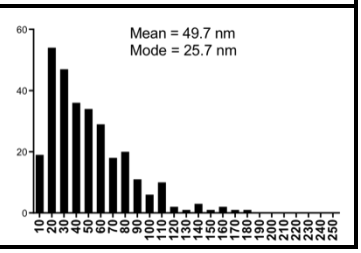

Mo	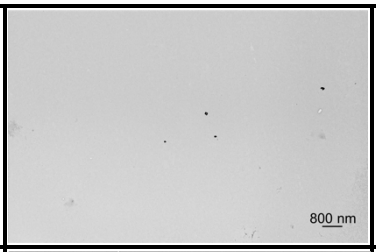	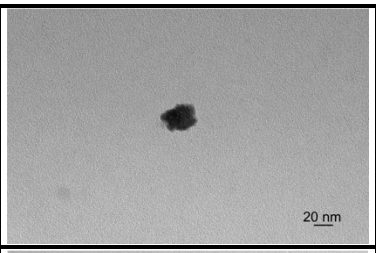	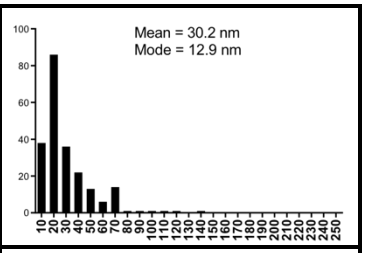
Nd	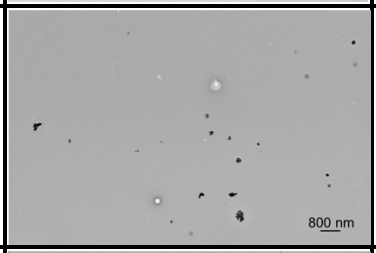	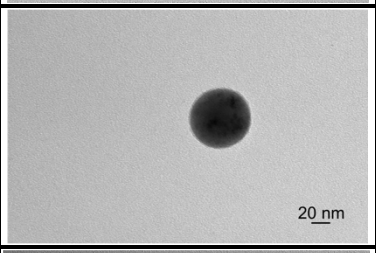	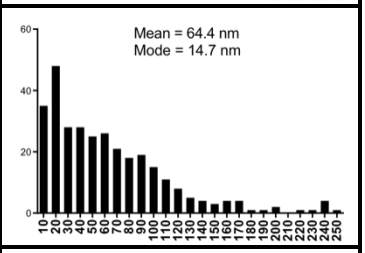
Sm	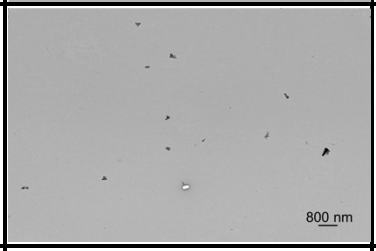	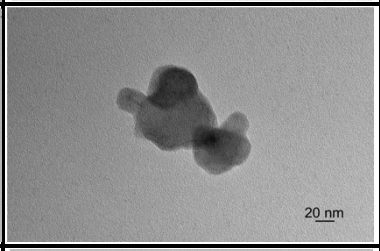	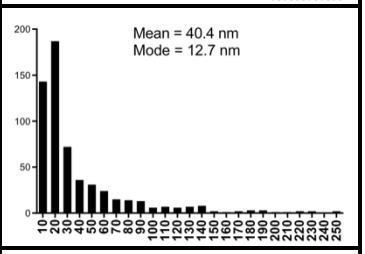
Eu	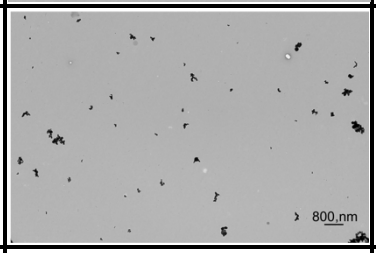	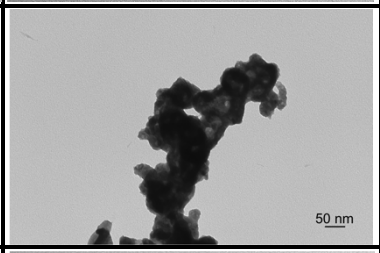	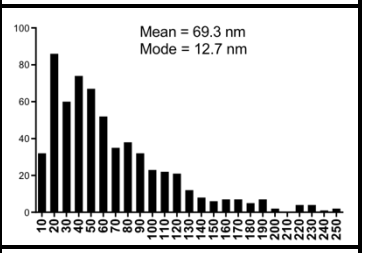
Gd	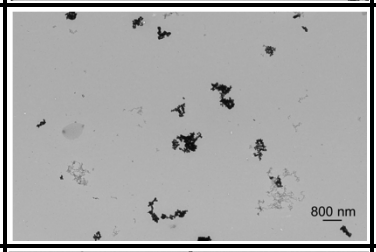	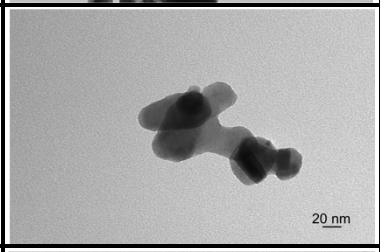	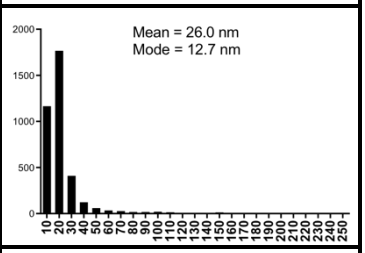
Tb	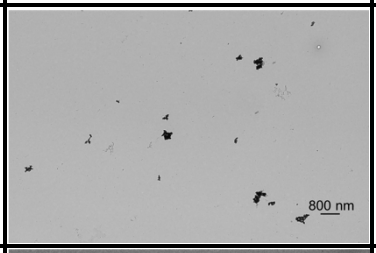	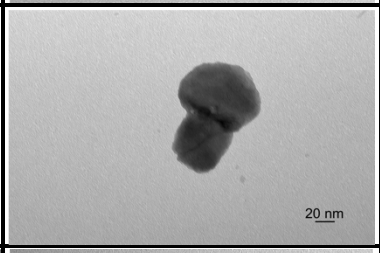	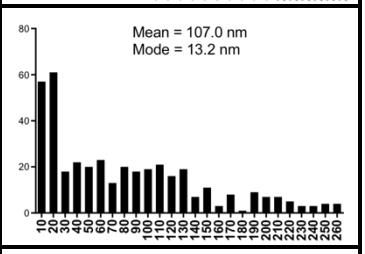
Dy	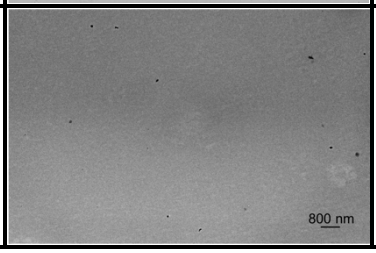	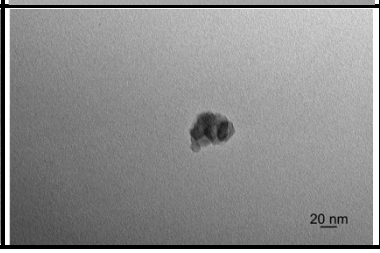	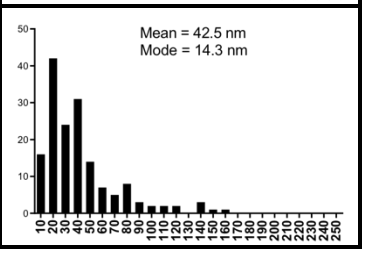

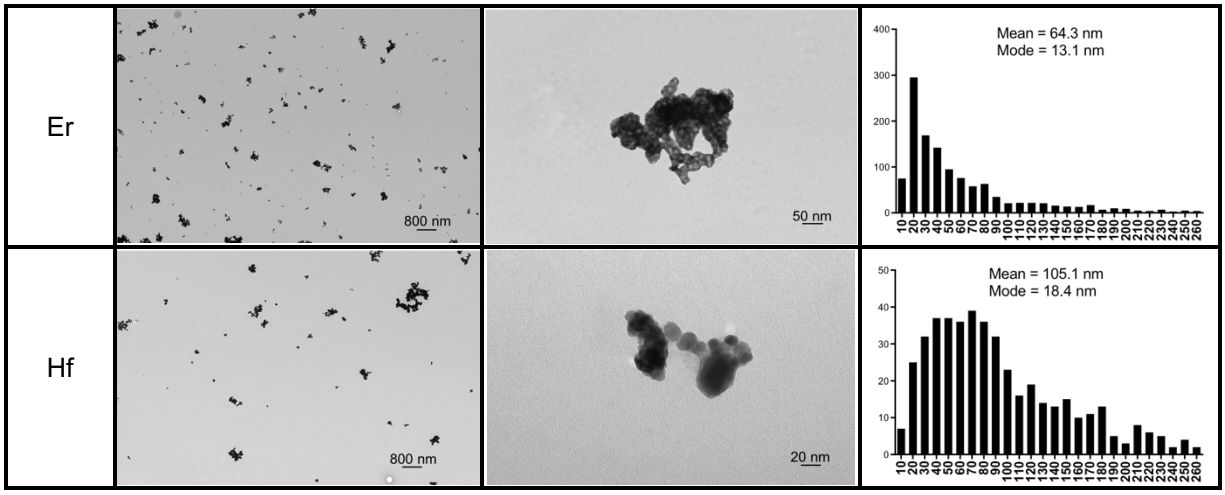

Supp Figure 4.1: NP TEM images (low and high magnification) and size histograms.

The remaining supplementary figures can be found in https://link.springer.com/article/10.1186/s12645-019-0057-9#Sec23 supplementary information.

4.3 Spearman correlation analysis

4.3.1 Results

A Spearman correlation analysis was conducted among $HO^{\cdot}$, O_2^{-} and $^1O_2$ and the correlation coefficient (r_s) calculated. Cohen´s standard was used to evaluate the strength of the relationships, where coefficients between 0.10 and 0.29 represent a small effect size, coefficients between 0.30 and 0.49 represent a moderate effect size, and coefficients above 0.50 indicate a large effect size (Cohen, 1988). Figure 4.7 presents the scatterplots of the correlations for all the NPs studied. A regression line has been added to assist the interpretation.

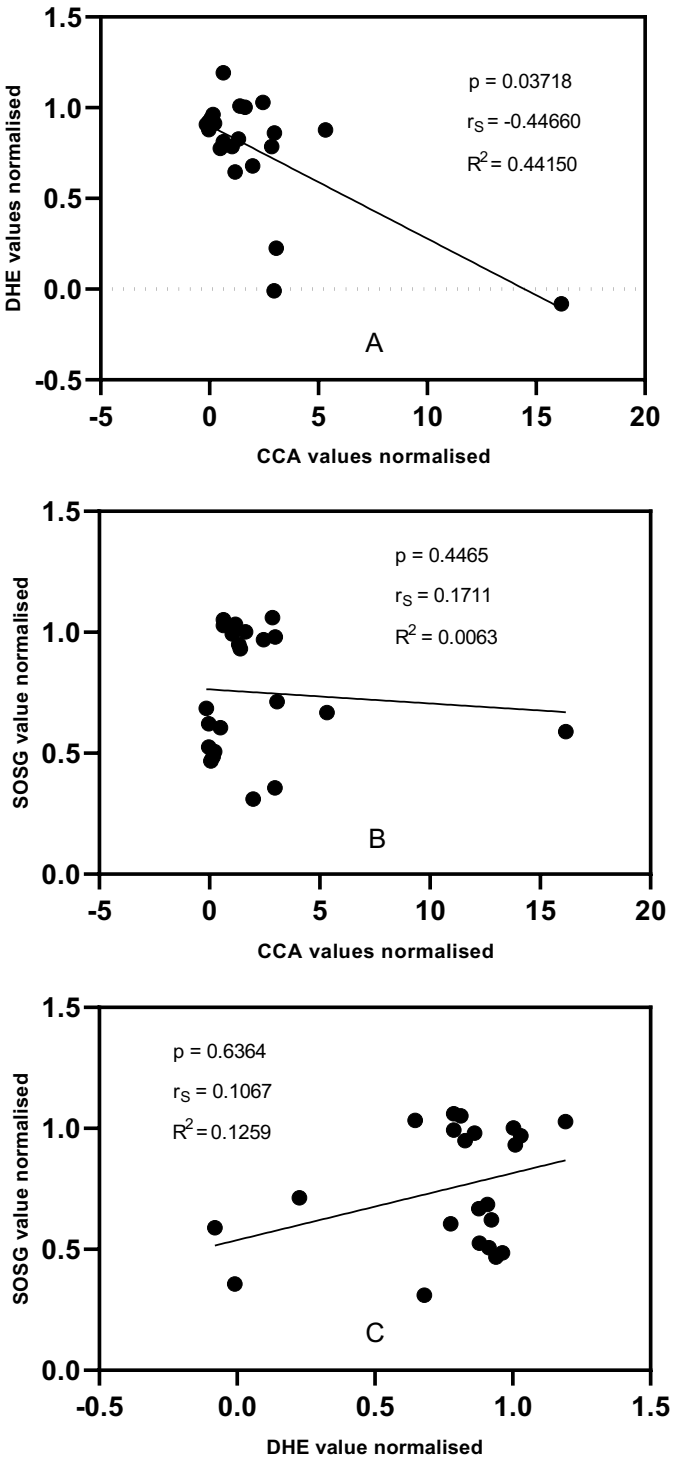

Figure 4.7: Scatterplots between each variable for all the NPs with the regression line. R^2, r_S and p values were added. A – scatterplot between $O_2^{\cdot-}$ and $HO^{\cdot}$; B - scatterplot between $^1O_2$ and $HO^{\cdot}$; C - scatterplot between $^1O_2$ and $O_2^{\cdot-}$.

A significant negative correlation was observed between $O_2^{\cdot-}$ (DHE) and $HO^{\cdot}$ (CCA) (r_S = -0.4466, p = 0.03718), as shown in Figure 4.7A. Positive but non-significant correlations were observed between $^1O_2$ (SOSG) and $HO^{\cdot}$ (CCA) (r_S = 0.1711, p = 0.4465), and between $^1O_2$ (SOSG) and $O_2^{\cdot-}$ (DHE) (r_S = 0.1067, p = 0.6364), as shown in Figures 4.7 B and C, respectively.

Considering only the NPs of period 4 of the periodic table: Sc, Ti, V, Cr, Mn, Fe, Co, Ni, Cu, and Zn, Spearman correlation analysis was again conducted among $HO^{\cdot}$, $O_2^{\cdot-}$ and $^1O_2$ (Figure 4.8).

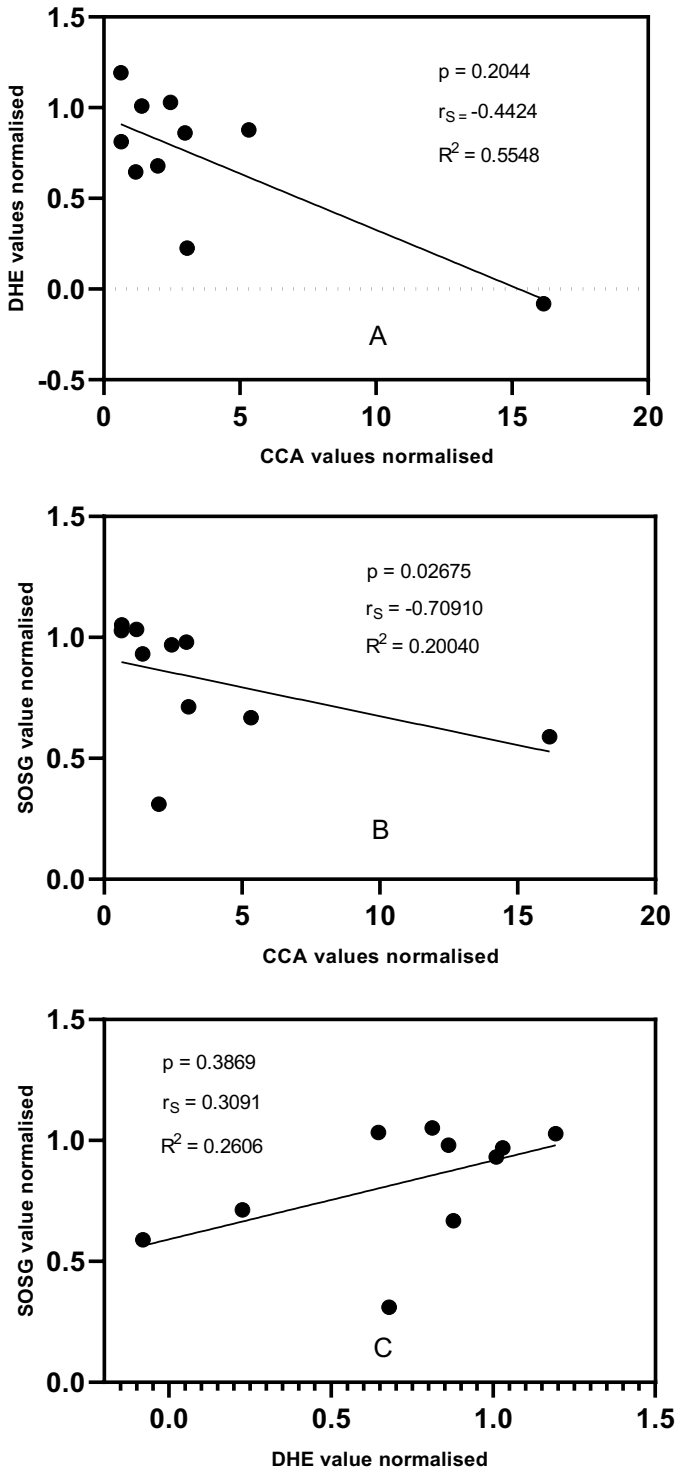

Figure 4.8: Scatterplots between each variable for the NPs of period 4 of the periodic table with the regression line. R^2, r_S and p values were added. A – scatterplot between $O_2^{\cdot-}$ and $HO^{\cdot}$; B - scatterplot between $^1O_2$ and $HO^{\cdot}$; C - scatterplot between $^1O_2$ and $O_2^{\cdot-}$.

In this case, a significant negative correlation was observed between $^1O_2$ and HO· (r_S = -0.70910, p = 0.02675), as shown in Figure 4.8B. A negative correlation was observed between O_2^- and HO· (r_S = -0.4424, p = 0.2044), but it was not significant with p > 0.05 (Figure 4.8A). On the other hand, a positive correlation was obtained between $^1O_2$ and O_2^- (r_S = 0.3091, p = 0.3869) (Figure 4.8C).

For the lanthanides such as, Nd, Sm, Eu, Gd, Tb, Dy, and Er, Spearman correlation analysis was again conducted among HO·, O_2^- and $^1O_2$. Figure 4.9 presents the scatterplots of the correlations that consider only the lanthanide type NPs. A regression line has been added to assist the interpretation.

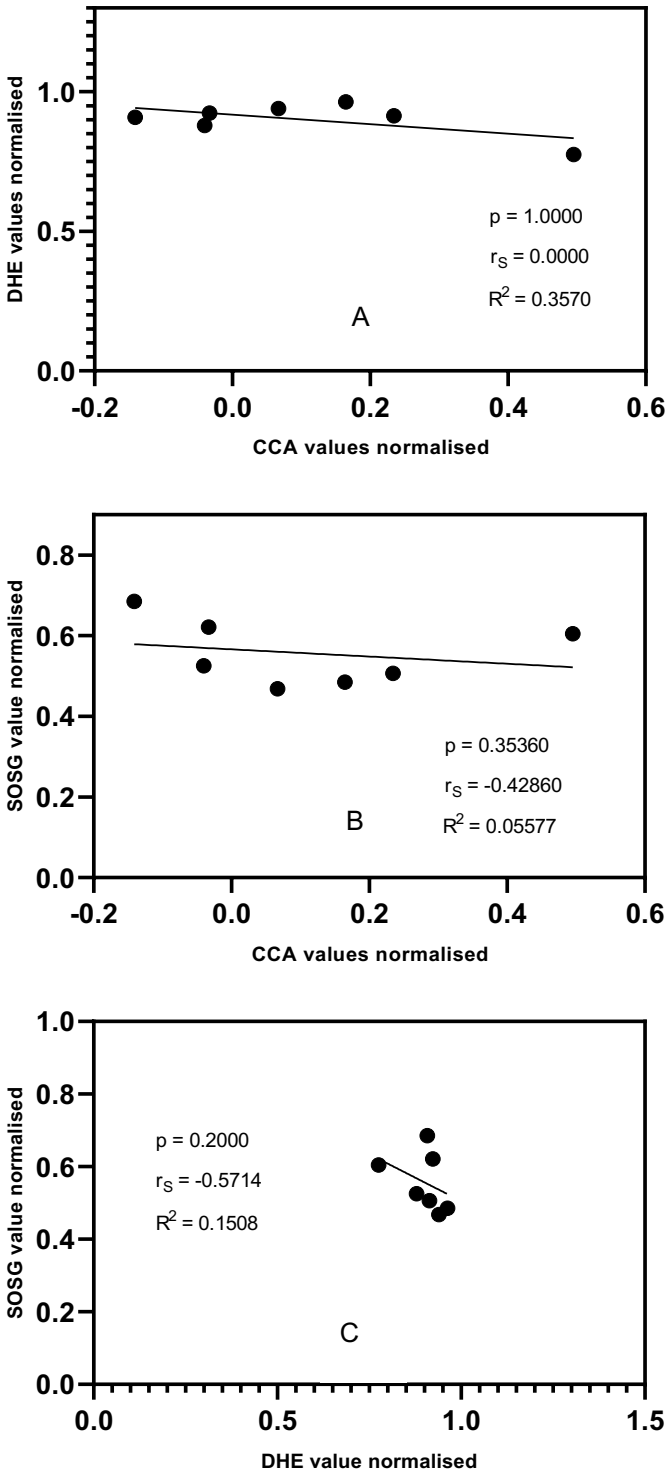

Figure 4.9: Scatterplots between each variable for the lanthanide NPs with the regression line. R^2, r_S and p values were added. A – scatterplot between $O_2^{\cdot-}$ and $HO^{\cdot}$; B - scatterplot between $^1O_2$ and $HO^{\cdot}$; C - scatterplot between $^1O_2$ and $O_2^{\cdot-}$.

No significant results were found for lanthanides correlation between each variable, with all p values above 0.05, as shown in Figure 4.9. There is no correlation between $O_2^{\cdot-}$ and $HO^{\cdot}$ (r_S = 0.0) for lanthanides (Figure 4.9A). For the remaining pairs, such as $^1O_2$ and $HO^{\cdot}$, and $O_2^{\cdot-}$ and $^1O_2$ (Figures 4.9 B and C, respectively), Spearman correlation was negative and indicates a moderate effect size for $^1O_2$ and $HO^{\cdot}$ (r_S = -0.42860), and a large effect size for $O_2^{\cdot-}$ and $^1O_2$ (r_S = -0.5714).

4.3.2 Discussion

Except for lanthanides (Figure 4.9 A and B), in general as hydroxyl radical production increases, both superoxide and singlet oxygen tend to decrease, and as superoxide increases, singlet oxygen increases as well (Figures 4.7C and 4.8C). It is possible to assume that reactions such as, for example:

$$^1O_2 + A \leftrightarrow HO^{\cdot} + B$$

$$O_2^{\cdot-} + C \leftrightarrow HO^{\cdot} + D$$

$$O_2^{\cdot-} + {}^1O_2 + E \leftrightarrow HO^{\cdot} + F$$

, with A, B, C, D, E and F, as unknown species, might be happening in the presence of some of NPs studied, with the exception of the lanthanide ones.

These results are in agreement with the reported Haber-Weiss reaction, which is considered the main mechanism by which the highly reactive radical is generated in the presence of metal oxide NPs (Hauser et al, 2016):

$$\text{Haber-Weiss reaction: } O_2^{\cdot-} + H_2O_2 \rightarrow O_2 + HO^- + HO^{\cdot}$$

In the case of singlet oxygen, different reactions have been reported in the presence of catalytic surfaces, such as (Hirakawa, 2018):

$$O_2^{\cdot-} + h^+ \rightarrow {}^1O_2 \qquad \text{reaction 4.1}$$

$$O_2^{\cdot-} + HO^{\cdot} \rightarrow {}^1O_2 + OH^- \qquad \text{reaction 4.2}$$

$$O_2^{\cdot-} + HO_2 + H^+ \rightarrow {}^1O_2 + H_2O_2 \qquad \text{reaction 4.3}$$

, where the photogenerated h^+ in the valence band of the catalyst, such as for example, TiO_2, and $HO^{\cdot}$, can act as the oxidants to produce $^1O_2$. Also, perhydroxyl radical generated from $O_2^{\cdot-}$ and H^+, also produces $^1O_2$.

Reaction 4.1 would mean that as superoxide decreases, singlet oxygen production would increase, which is not consistent with the Spearman correlation analysis. In addition, the previous hole scavenger results of some NPs such as, Fe_3O_4, CoO, NiO and ZnO, showed increases in superoxide radical

generation in the presence of formic acid (Figure 4.5B). There are two possible routes for the hole scavenger results: the hole scavenger is increasing the lifetime of the electrons and promoting superoxide formation at the NP surface, or the hole scavenger does not allow reaction 4.1 to happen, and so superoxide is not being consumed through the reaction with holes to generate singlet oxygen. Since Spearman correlation analysis found that as superoxide increases singlet oxygen increases, it is more likely that the hole scavenger experiment is actually testing the route of superoxide formation at the NP surface due to the interaction of oxygen with the electrons from the e^-/h^+ pairs.

Reaction 4.2 although it would mean that as superoxide decreases, singlet oxygen production would increase, which again is not consistent with the Spearman correlation analysis, it also means that as hydroxyl radical decreases, singlet oxygen increases which is consistent with the correlation results (Figures 4.7B and 4.8B). In this case, since through reaction 4.2 hydroxide ion (OH^-) is also formed, this species would have to be somehow present in a reaction that would generate superoxide radicals, due to the findings of the correlation analysis that as superoxide increases, singlet oxygen increases (Figures 4.7C and 4.8C). For example, or the Haber-Weiss reaction, where both hydroxyl radicals and hydroxide ions, in the presence of oxygen, form both hydrogen peroxide and superoxide, or the electrochemical reduction of O_2 (Hayyan et al., 2016):

$$2O_2^- + H_2O \rightarrow O_2 + HO_2 + OH^-$$

Due to the fact that O_2^- and its protonated form, HO_2, are in equilibrium in an aqueous solution (Rose, 2012):

$$O_2^- + H_2O \leftrightarrow O_2 + HO_2 + OH^-$$

, and that O_2^- dominates the equilibrium in solutions whose pH is above the $pK_a = 4.8$ (Bielski et al., 1985), in the nanoparticles solutions studied with a pH=7.4, superoxide is the predominant species. This means that the hydroxide ions produced in reaction 4.2, will produce superoxide through the electrochemical reduction of O_2. If this is the case, as singlet oxygen production increases through reaction 4.2, superoxide will increase through the electrochemical reduction of O_2, which is in accordance with the Spearman correlation results.

Reaction 4.3 leads to the conclusion that as superoxide decreases, singlet oxygen production would increase, which is not consistent with the Spearman correlation analysis. Once again, if there is another possible route for superoxide formation through hydrogen peroxide (the other product formed from reaction 4.3) then as singlet oxygen increases superoxide would increase as well, which will be consistent with Spearman correlation analysis. For example, one of the main reactions of oxidative stress induced by manganese is the superoxide dismutase (Aust et al., 1985):

$$2\ O_2^- + 2H^+ \rightarrow H_2O_2 + O_2$$

, where in this case superoxide leads to hydrogen peroxide production in the presence of oxygen.

5 Conclusions and Future Directions

RT is currently limited by the dose of X-rays that can be safely given to patients, since the dose of X-rays that will kill tumour tissue is similar to the dose that will kill surrounding healthy tissues. This thesis aimed to provide a further understanding of the different type of metal oxide NP radiosensitisers by studying their compatibility with cancer cells, their interaction with DNA and the type and amount of radicals formed during their interaction with X-rays. Other studies have looked at individual metal oxides, but differences in experimental designs made it very difficult to compare results.

First studies in the role of metal NPs in cancer treatment showed significant radiosensitisation *in vivo* (Hainfeld et al., 2008), while Monte Carlo simulations suggested that the observed radiosensitisation could not be fully explained by the increase in physical dose (Butterworth et al., 2012). Although the parameters that influence NP radiosensitisation are still not fully understood, it is believe that is the combination of physical and biological effects that is responsible for the radiosensitisation induced by the NPs (King et al., 2017). Different pathways have been proposed for the production of hydroxyl radicals in the presence of radiation and NPs. Taking into account three different pathways for hydroxyl radicals production a study using 7-hydroxycoumarin showed that the dominant mechanism for $HO^{\cdot}$ production is through the interaction of radiolysis products with water-NP interface (Sicard-Roselli et al., 2014). The link between the physical process, where the energy absorption by the NP, the chemical process, where radical production occurs, and the biological process, where biological interactions lead to cell death, is fundamental for the understanding of the role of the NPs in the interaction of radiation with cells. Indirect measurements reported a radical production induced by NPs four-times higher than normal radiolysis in the absence of oxygen and it was suggested that this overproduction arises from surface reactions or catalysis at NP-solvent interface (Baldacchino et al., 2019). For example, a study adapted to quantify the yields of solvated electrons and hydroxyl radicals produced in water by gold NPs submitted to keV and MeV ionising radiation proposed a key role for interfacial water around NPs for radical production (Gilles et al., 2018). Combining NPs into the process of water radiolysis does not always lead to an enhancement of radiosensitisation unless certain conditions are met. To optimise the whole system (NP+radiation+water) the knowledge of the individual enhancements given by the physical, chemical and biological processes is required since the highest enhancement will most likely be given when the highest individual enhancements are properly combined (Guo, 2019). The work presented in this thesis demonstrates the importance of ROS species created by metal oxide NPs in the process of cancer cell death.

The introduction of NPs into the RT treatment will require optimisation within treatment planning algorithms, such as accurate characterisation of NP interaction with the X-ray spectrum of the irradiation field as a function of NP material, size and concentration (Schuemann et al, 2016).

The main benefit of using NPs during RT treatment is the potential dose enhancement that results from the interaction of the MV treatment field with the NPs. Controlling NP site uptake, it will be possible to increase the dose to the tumour whilst maintaining or reducing the dose to the surrounding normal tissue. This approach is particularly important for SABR treatments since this type of RT treatment uses larger doses per treatment compared to the standard RT treatment. In this case a single geometric miss can result in a reduction in tumour control and/or an increase in toxicity effects. SABR is moving towards

the use of FF free fields since this approach results in significantly higher dose rates (R. B. King et al., 2013). *In vitro* studies suggested that the combination of FF free fields with NPs will lead to a further increase in dose deposition because of the increased proportion of lower energy photons, capable of inducing photocatalyst-like changes in the NPs (Detappe et al., 2016).

This work provided a fair comparison between the different types of NP metal oxides because important parameters for the inclusion of NPs in the field of RT were tested under the same conditions. Here evidence of ROS production by the different types of metal oxide NPs and of their behavior under the biological environment either by testing their interactions with plasmid DNA and with cancer cells under realistic tumour hypoxia conditions is provided. Once again, ROS outputs do not fit with the standard physical theory of radiosensitisation which is consistent with other recent work on nano-radiocatalysis (Guo, 2019). Furthermore, this thesis also showed evidence of NPs that most likely only work under the biological process providing no evidence of relevant ROS production but at the same time relevant interactions with plasmic DNA and cancer cells, as shown by CuO NPs.

The main limitations of this study include diameter and agglomeration state variability between the different type of NPs. Also, irradiation times after probe and NP interaction might play an important role. NP quenching is dependent on the interaction time with probe. Although consistency regarding the time between probe injection into the sample and scheduled irradiation time was maintained constant throughout the experiments it was not possible to control the hospital irradiation delay.

Future directions include studying the behaviour of these NPs in other cell lines, since as explained before, it is known that the radiosensitisation results depend on the type of cell line used. Furthermore, different types of coating should be tested to improve cellular uptake and toxicity and also for better radiosensitisation, since catalytic ability might be compromised by the type of coating used as shown by different studies (Gilles et al., 2014; Grellet et al., 2017). Understanding other principles than the physical ones that might be responsible for the radiosensitisation observed will be a very important step for the knowledge of the role of the NPs in the world of cancer therapy.

The future of NP radiosensitisers will be connected to the mixtures of high-Z elements with catalytic metal oxides, where the photoelectric effect of the high Z element will add secondary electrons into the catalyst allowing the production of more ROS. Work has already been made in this direction such as Bi_2WO_6 catalysts (Sahu & Cates, 2017), lanthanide-doped TiO_2 (Townley et al., 2012) and lanthanide-doped ZnO NPs (Ghaemi et al., 2016), ZnO-SiO_2 nanocomposites (Generalov et al., 2015) and Au-Bi_2S_3 heterostructures (Wang et al., 2019).

The two NPs radiosensitisers currently on the market, NBTXR3 and AGuIX, are still in clinical trial. The study of 50 nm hafnium-oxide (HfO_2) NPs (NBTXR3) in patients with locally advanced soft-tissue sarcoma showed that a significantly higher proportion of patients (twice as many) given NBTXR3 plus RT achieved a pathological complete response compared with patients who received RT alone (Bonvalot et al., 2019). This study lacks an appropriate control group, i.e. injection of solution without NBTXR3, since it is not possible to associate the observed results to the NPs effects without a control group that excludes the effects due to the intratumoral injection process where a difference of 10% of

tumoral volume is seen. Once again, the real mode of action of these NPs is still unclear and since evidence supports chemical and biological of these NPs during irradiation a potential toxicity due to long-term systemic persistency is still a possibility (Vilotte et al., 2019). AGuIX NPs were tested in multiple brain metastases in combination with whole brain RT (10 × 3 Gy over 3 weeks max) and showed a strong local radioenhancing effect (Lux et al., 2019). A limitation of this study was the lower number of patients used, around 15 to18 patients, (Verry et al., 2019). An important result for AGuIX NPs revealed the efficacy of the EPR effect inducing accumulation and more importantly retention of the ultrasmall (< 5 nm) NPs at the tumour sites. Nevertheless, this passive targeting strategy still has to be confirmed in human due to the complex heterogeneity of the tumour types and environments. The safety related to fast renal clearance coupled to the non-toxicity in the absence of radiation allows the use of these NPs into more clinical trials (Bort et al., 2020). Another clinical trial (NanoCOL clinical trial, NCT03308604) aimed to treat advanced cervical cancer through RT and brachytherapy is ongoing. Although these NPs are very strong candidates in this field a lot of work still needs to be done and parallel NPs should be tested due to the complexity of the different types of tumours. The more probable picture in the future will be the use of different radiosensitisers to improve the efficacy of RT in the treatment of the different types of tumours.

Although photon beam therapy is still the most used RT beam, other types of beams are emerging such as proton beams. For this reason, translating the NP studies into the different types of beams will be a very useful tool for the future of RT. A study already demonstrated the interaction of AGuIX NPs with a 150 MeV proton beam and concluded that once again addition of metal-based NPs is a promising strategy not only to increase cell killing action of fast protons, but also to improve tumour targeting (Schlathölter et al., 2016).

The work presented in this thesis showed that the pure physical aspect does not explain the process of radiosensitisation. For instance, gadolinium in the form of dendrimer (AGuIX) seems to be a strong candidate as a radiosensitiser in the RT treatment, but the results in this thesis showed that based only on physical principles, gadolinium is a poor radiosensitiser. This showed that research on the different mechanisms of radiosensitisation will help the introduction of the NPs in the field of RT in a way that we will be able to understand and control the early and late stage effects of these radiosensitisers when inside the patient. Furthermore, my work tested metal oxide NPs that have never been considered for this field and now become more interesting. Clearly, processes such as catalysis, seem to be a major player in radiosensitisation and my work opens a whole new field of investigations to try many different compounds that were not previously considered for RT on the basis of a predicted poor photoelectric effect.

6 Bibliography

Abdelhamid, M. A. S., Fábián, L., Macdonald, C. J., Cheesman, M. R., Gates, A. J., & Waller, Z. A. E. (2018). Redox-dependent control of i-Motif DNA structure using copper cations. *Nucleic Acids Research*, *46*(12), 5886–5893. https://doi.org/10.1093/nar/gky390

Abou-Zeid, S. M., El-Bialy, B. E., El-Borai, N. B., AbuBakr, H. O., & Elhadary, A. M. A. (2018). Radioprotective effect of Date syrup on radiation- induced damage in Rats. *Scientific Reports*, *8*(1), 1–10. https://doi.org/10.1038/s41598-018-25586-3

Adams, G. E., Asquith, J. C., Dewey, D. L., Foster, J. L., Michael, B. D., & Willson, R. L. (1971). Electron Affinic Sensitization. *International Journal of Radiation Biology and Related Studies in Physics, Chemistry and Medicine*, *19*(6), 575–585. https://doi.org/10.1080/09553007114550751

Algethami, M. (2015). Radiation Dose Enhancement Using Bi2S3 Nanoparticles in Cultured Mouse PC3 Prostate and B16 Melanoma Cells. *NanoWorld Journal*, *1*(3), 99–104. https://doi.org/10.17756/nwj.2015-013

Alimoradi, H., Matikonda, S. S., Gamble, A. B., Giles, G. I., & Griesh, K. (2017). Redox activated polymeric nanoparticles in tumor therapy. In *Nanostructures for Drug Delivery*. Elsevier Inc. https://doi.org/10.1016/b978-0-323-46143-6.00010-5

Alizadeh, E., Sanz, A. G., García, G., & Sanche, L. (2013). Radiation damage to DNA: The indirect effect of low-energy electrons. *Journal of Physical Chemistry Letters*, *4*(5), 820–825. https://doi.org/10.1021/jz4000998

Alkilany, A. M., & Murphy, C. J. (2010). Toxicity and cellular uptake of gold nanoparticles: What we have learned so far? *Journal of Nanoparticle Research*, *12*(7), 2313–2333. https://doi.org/10.1007/s11051-010-9911-8

Altomare, A., Corriero, N., Cuocci, C., Falcicchio, A., Moliterni, A., & Rizzi, R. (2015). QUALX2.0: A qualitative phase analysis software using the freely available database POW-COD. *Journal of Applied Crystallography*. https://doi.org/10.1107/S1600576715002319

Aspatwar, A., Becker, H. M., Parvathaneni, N. K., Hammaren, M., Svorjova, A., Barker, H., Supuran, C. T., Dubois, L., Lambin, P., Parikka, M., Parkkila, S., & Winum, J. Y. (2018). Nitroimidazole-based inhibitors DTP338 and DTP348 are safe for zebrafish embryos and efficiently inhibit the activity of human CA IX in Xenopus oocytes. *Journal of Enzyme Inhibition and Medicinal Chemistry*, *33*(1), 1064–1073. https://doi.org/10.1080/14756366.2018.1482285

Atha, D. H., Wang, H., Petersen, E. J., Cleveland, D., Holbrook, R. D., Jaruga, P., Dizdaroglu, M., Xing, B., & Nelson, B. C. (2012). Copper Oxide Nanoparticle Mediated DNA Damage in Terrestrial Plant Models. *Environmental Science & Technology*, *46*(3), 1819–1827. https://doi.org/10.1021/es202660k

Attia, M. F., Anton, N., Wallyn, J., Omran, Z., & Vandamme, T. F. (2019). An overview of active and passive targeting strategies to improve the nanocarriers efficiency to tumour sites. *Journal of Pharmacy and Pharmacology*, *71*(8), 1185–1198. https://doi.org/10.1111/jphp.13098

Aust, S. D., Morehouse, L. A., & Thomas, C. E. (1985). Role of metals in oxygen radical reactions. *Journal of Free Radicals in Biology and Medicine*, *1*(1), 3–25. https://doi.org/10.1016/0748-5514(85)90025-X

Azzam, E. I., Jay-Gerin, J. P., & Pain, D. (2012). Ionizing radiation-induced metabolic oxidative stress and prolonged cell injury. In *Cancer Letters*. https://doi.org/10.1016/j.canlet.2011.12.012

Baker, C. H. (2013). Harnessing cerium oxide nanoparticles to protect normal tissue from radiation damage. *Translational Cancer Research*, *2*(4), 343–358. https://doi.org/10.3978/j.issn.2218-676X.2013.08.15

Baldacchino, G., Brun, E., Denden, I., Bouhadoun, S., Roux, R., Khodja, H., & Sicard-Roselli, C. (2019). Importance of radiolytic reactions during high-LET irradiation modalities: LET effect, role of O2 and radiosensitization by nanoparticles. *Cancer Nanotechnology*, *10*(1), 1–21. https://doi.org/10.1186/s12645-019-0047-y

Barrow, M., Taylor, A., Murray, P., Rosseinsky, M. J., & Adams, D. J. (2015). Design considerations for the synthesis of polymer coated iron oxide nanoparticles for stem cell labelling and tracking using

MRI. *Chemical Society Reviews*, *44*(19), 6733–6748. https://doi.org/10.1039/c5cs00331h

Baskar, R., Dai, J., Wenlong, N., Yeo, R., & Yeoh, K. W. (2014). Biological response of cancer cells to radiation treatment. *Frontiers in Molecular Biosciences*, *1*(NOV), 1–9. https://doi.org/10.3389/fmolb.2014.00024

Bertrand, N., Grenier, P., Mahmoudi, M., Lima, E. M., Appel, E. A., Dormont, F., Lim, J. M., Karnik, R., Langer, R., & Farokhzad, O. C. (2017). Mechanistic understanding of in vivo protein corona formation on polymeric nanoparticles and impact on pharmacokinetics. *Nature Communications*, *8*(1). https://doi.org/10.1038/s41467-017-00600-w

Biaglow, J. E. (1981). The effects of ionizing radiation on mammalian cells. *Journal of Chemical Education*, *58*(2), 144–156. https://doi.org/10.1021/ed058p144

Bielski, B. H. J., Cabelli, D. E., Arudi, R. L., & Ross, A. B. (1985). Reactivity of HO2/O−2 Radicals in Aqueous Solution. *Journal of Physical and Chemical Reference Data*, *14*(4), 1041–1100. https://doi.org/10.1063/1.555739

Blatnik, J., Luebke, L., Simonet, S., Nelson, M., Price, R., Leek, R., Zeng, L., Wu, A., & Brown, E. (2012). Dye surface coating enables visible light activation of TiO 2 nanoparticles leading to degradation of neighboring biological structures. *Microscopy and Microanalysis*, *18*(1), 134–142. https://doi.org/10.1017/S1431927611012414

Bligaard, T., Nørskov, J. K., Dahl, S., Matthiesen, J., Christensen, C. H., & Sehested, J. (2004). The Brønsted-Evans-Polanyi relation and the volcano curve in heterogeneous catalysis. *Journal of Catalysis*, *224*(1), 206–217. https://doi.org/10.1016/j.jcat.2004.02.034

Bogdan, J., Pławińska-Czarnak, J., & Zarzyńska, J. (2017). Nanoparticles of Titanium and Zinc Oxides as Novel Agents in Tumor Treatment: a Review. *Nanoscale Research Letters*, *12*(1). https://doi.org/10.1186/s11671-017-2007-y

Bonvalot, S., Rutkowski, P. L., Thariat, J., Carrère, S., Ducassou, A., Sunyach, M. P., Agoston, P., Hong, A., Mervoyer, A., Rastrelli, M., Moreno, V., Li, R. K., Tiangco, B., Herraez, A. C., Gronchi, A., Mangel, L., Sy-Ortin, T., Hohenberger, P., de Baère, T., … Papai, Z. (2019). NBTXR3, a first-in-class radioenhancer hafnium oxide nanoparticle, plus radiotherapy versus radiotherapy alone in patients with locally advanced soft-tissue sarcoma (Act.In.Sarc): a multicentre, phase 2–3, randomised, controlled trial. *The Lancet Oncology*, *20*(8), 1148–1159. https://doi.org/10.1016/S1470-2045(19)30326-2

Boonstra, J., & Post, J. A. (2004). Molecular events associated with reactive oxygen species and cell cycle progression in mammalian cells. *Gene*, *337*(SUPPL.), 1–13. https://doi.org/10.1016/j.gene.2004.04.032

Bort, G., Lux, F., Dufort, S., Crémillieux, Y., Verry, C., & Tillement, O. (2020). EPR-mediated tumor targeting using ultrasmall-hybrid nanoparticles: From animal to human with theranostic AGuIX nanoparticles. *Theranostics*, *10*(3), 1319–1331. https://doi.org/10.7150/thno.37543

Brown, P. E. (1967). Mechanism of action of aminothiol radioprotectors. *Nature*, *213*(5074), 363–364. https://doi.org/10.1038/213363a0

Butterworth, K. T., McMahon, S. J., Currell, F. J., & Prise, K. M. (2012). Physical basis and biological mechanisms of gold nanoparticle radiosensitization. *Nanoscale*, *4*(16), 4830–4838. https://doi.org/10.1039/c2nr31227a

Calatayud, M. P., Sanz, B., Raffa, V., Riggio, C., Ibarra, M. R., & Goya, G. F. (2014). The effect of surface charge of functionalized Fe3O4 nanoparticles on protein adsorption and cell uptake. *Biomaterials*, *35*(24), 6389–6399. https://doi.org/10.1016/j.biomaterials.2014.04.009

Candelaria, M., Garcia-Arias, A., Cetina, L., & Dueñas-Gonzalez, A. (2006). Radiosensitizers in cervical cancer. Cisplatin and beyond. *Radiation Oncology*, *1*(1), 1–17. https://doi.org/10.1186/1748-717X-1-15

Carrasco-Flores, E. A., & LaVerne, J. A. (2007). Surface species produced in the radiolysis of zirconia nanoparticles. *The Journal of Chemical Physics*, *127*(23), 234703. https://doi.org/10.1063/1.2806164

Cedervall, T., Lynch, I., Lindman, S., Berggård, T., Thulin, E., Nilsson, H., Dawson, K. A., & Linse, S. (2007). Understanding the nanoparticle-protein corona using methods to quntify exchange rates and affinities of proteins for nanoparticles. *Proceedings of the National Academy of Sciences of the United States of America*, *104*(7), 2050–2055. https://doi.org/10.1073/pnas.0608582104

Cervantes-Cervantes, M. P., Calderón-Salinas, J. V., Albores, A., & Muñoz-Sánchez, J. L. (2005). Copper increases the damage to DNA and proteins caused by reactive oxygen species. *Biological Trace Element Research*, *103*(3), 229–248. https://doi.org/10.1385/BTER:103:3:229

Chelnokov, E., Cuba, V., Simeone, D., Guigner, J. M., Schmidhammer, U., Mostafavi, M., & Le Caër, S. (2014). Electron transfer at oxide/water interfaces induced by ionizing radiation. *Journal of Physical Chemistry C*, *118*(15), 7865–7873. https://doi.org/10.1021/jp501396a

Chen, E. I., Hewel, J., Krueger, J. S., Tiraby, C., Weber, M. R., Kralli, A., Becker, K., Yates, J. R., & Felding-Habermann, B. (2007). Adaptation of energy metabolism in breast cancer brain metastases. *Cancer Research*, *67*(4), 1472–1486. https://doi.org/10.1158/0008-5472.CAN-06-3137

Cherry, S. R., Sorenson, J., Phelps, M. E., & Methé, B. M. (2004). Physics in Nuclear Medicine. In *Medical Physics* (Vol. 31). https://doi.org/10.1118/1.1776595

Chithrani, D. B., Jelveh, S., Jalali, F., van Prooijen, M., Allen, C., Bristow, R. G., Hill, R. P., & Jaffray, D. A. (2010). Gold Nanoparticles as Radiation Sensitizers in Cancer Therapy. *Radiation Research*, *173*(6), 719. https://doi.org/10.1667/rr1984.1

Cho, S. H. (2005). Estimation of tumour dose enhancement due to gold nanoparticles during typical radiation treatments: A preliminary Monte Carlo study. *Physics in Medicine and Biology*, *50*(15). https://doi.org/10.1088/0031-9155/50/15/N01

Choi, S. W., Kim, W. S., & Kim, J. H. (2003). Surface modification of functional nanoparticles for controlled drug delivery. *Journal of Dispersion Science and Technology*, *24*(3–4), 475–487. https://doi.org/10.1081/DIS-120021803

Chu, S.-H., Karri, S., Ma, Y.-B., Feng, D.-F., & Li, Z.-Q. (2013). In vitro and in vivo radiosensitization induced by hydroxyapatite nanoparticles. *Neuro-Oncology*, *15*(7), 880–890. https://doi.org/10.1093/neuonc/not030

Chusuei, C. C., Wu, C. H., Mallavarapu, S., Hou, F. Y. S., Hsu, C. M., Winiarz, J. G., Aronstam, R. S., & Huang, Y. W. (2013). Cytotoxicity in the age of nano: The role of fourth period transition metal oxide nanoparticle physicochemical properties. *Chemico-Biological Interactions*, *206*(2), 319–326. https://doi.org/10.1016/j.cbi.2013.09.020

Cohen, J. (1988). Statistical Power Analysis for the Behavioral Sciences. *Lawrence Erlbaum Associates*. ISBN 0-8058-0283-5

Curtis, K. A., Miller, D., Millard, P., Basu, S., Horkay, F., & Chandran, P. L. (2016). Unusual salt and pH induced changes in polyethylenimine solutions. *PLoS ONE*, *11*(9), 1–20. https://doi.org/10.1371/journal.pone.0158147

Dai, Y., Xu, C., Sun, X., & Chen, X. (2017). Nanoparticle design strategies for enhanced anticancer therapy by exploiting the tumour microenvironment. *Chemical Society Reviews*, *46*(12), 3830–3852. https://doi.org/10.1039/c6cs00592f

Dahlmann, H., Vaidyanathan, V., Sturla, S., (2009) Investigating the Biochemical Impact of DNA Damage with Structure-Based Probes: Abasic Sites, Photodimers, Alkylation Adducts, and Oxidative Lesions. *Biochemistry.* 48(40): 9347–9359. https://doi:10.1021/bi901059k.

Degen, A., & Kosec, M. (2000). Effect of pH and impurities on the surface charge of zinc oxide in aqueous solution. *Journal of the European Ceramic Society*, *20*(6), 667–673. https://doi.org/10.1016/S0955-2219(99)00203-4

Desouky, O., Ding, N., & Zhou, G. (2015). Targeted and non-targeted effects of ionizing radiation. *Journal of Radiation Research and Applied Sciences*, *8*(2), 247–254. https://doi.org/10.1016/j.jrras.2015.03.003

Detappe, A., Kunjachan, S., Drané, P., Kotb, S., Myronakis, M., Biancur, D. E., Ireland, T., Wagar, M., Lux, F., Tillement, O., & Berbeco, R. (2016). Key clinical beam parameters for nanoparticle-mediated radiation dose amplification. *Scientific Reports*, *6*(September), 1–8. https://doi.org/10.1038/srep34040

Drescher, M., Hentschel, M., Kienberger, R., Uiberacker, M., Yakovlev, V., Scrinzi, A., Westerwalbesloh, T., Kleineberg, U., Heinzmann, U., & Krausz, F. (2002). Time-resolved atomic inner-shell spectroscopy. *Nature*, *419*(6909), 803–807. https://doi.org/10.1038/nature01143

Du, G., & Espenson, J. H. (2005). Oxidation of vanadium(III) by hydrogen peroxide and the oxomonoperoxo vanadium(V) ion in acidic aqueous solutions: A kinetics and simulation study. *Inorganic Chemistry*, *44*(15), 5514–5522. https://doi.org/10.1021/ic050502j

Du, J., Zhu, W., Yang, L., Wu, C., Lin, B., Wu, J., Jin, R., Shen, T., & Ai, H. (2016). Reduction of polyethylenimine-coated iron oxide nanoparticles induced autophagy and cytotoxicity by lactosylation. *Regenerative Biomaterials*, *3*(4), 223–229. https://doi.org/10.1093/RB/RBW023

Eghtedari, M., Liopo, a., Copland, J., Oraevsky, A., & Motamedi, M. (2009). Engineering of hetero-functional gold nanorods for the in-vivo molecular targeting of breast cancer cells. *Nano Lett*. 9(1): 287–291. https://doi.org/10.1021/nl802915q.

Fan, W., Bu, W., Shen, B., He, Q., Cui, Z., Liu, Y., Zheng, X., Zhao, K., & Shi, J. (2015). Intelligent MnO2 Nanosheets Anchored with Upconversion Nanoprobes for Concurrent pH-/H2O2-Responsive UCL Imaging and Oxygen-Elevated Synergetic Therapy. *Advanced Materials*, *27*(28), 4155–4161. https://doi.org/10.1002/adma.201405141

Farhood, B., Goradel, N. H., Mortezaee, K., Khanlarkhani, N., Salehi, E., Nashtaei, M. S., Mirtavoos-mahyari, H., Motevaseli, E., Shabeeb, D., Musa, A. E., & Najafi, M. (2019). Melatonin as an adjuvant in radiotherapy for radioprotection and radiosensitization. *Clinical and Translational Oncology*, *21*(3), 268–279. https://doi.org/10.1007/s12094-018-1934-0

Featherstone, C., & Jackson, S. P. (n.d.). *DNA double-strand break repair*. 759–761.

Fokas, E., Prevo, R., Pollard, J. R., Reaper, P. M., Charlton, P. A., Cornelissen, B., Vallis, K. A., Hammond, E. M., Olcina, M. M., Gillies McKenna, W., Musche, R. J., & Brunner, T. B. (2012). Targeting ATR in vivo using the novel inhibitor VE-822 results in selective sensitization of pancreatic tumors to radiation. *Cell Death and Disease*, *3*(12), e441-10. https://doi.org/10.1038/cddis.2012.181

Frick, R., Müller-Edenborn, B., Schlicker, A., Rothen-Rutishauser, B., Raemy, D. O., Günther, D., Hattendorf, B., Stark, W., & Beck-Schimmer, B. (2011). Comparison of manganese oxide nanoparticles and manganese sulfate with regard to oxidative stress, uptake and apoptosis in alveolar epithelial cells. *Toxicology Letters*, *205*(2), 163–172. https://doi.org/10.1016/j.toxlet.2011.05.1037

Fruehauf, J. P., & Meyskens, F. L. (2007). Reactive oxygen species: A breath of life or death? *Clinical Cancer Research*, *13*(3), 789–794. https://doi.org/10.1158/1078-0432.CCR-06-2082

Fujishima, A., & Zhang, X. (2006). Titanium dioxide photocatalysis: present situation and future approaches. *Comptes Rendus Chimie*, *9*(5–6), 750–760. https://doi.org/10.1016/j.crci.2005.02.055

Gara, P. M. D., Garabano, N. I., Portoles, M. J. L., Moreno, M. S., Dodat, D., Casas, O. R., Gonzalez, M. C., & Kotler, M. L. (2012). ROS enhancement by silicon nanoparticles in X-ray irradiated aqueous suspensions and in glioma C6 cells. *Journal of Nanoparticle Research*, *14*(3). https://doi.org/10.1007/s11051-012-0741-8

Gatenby, R. A., & Gillies, R. J. (2004). Why do cancers have high aerobic glycolysis? *Nature Reviews Cancer*, *4*(11), 891–899. https://doi.org/10.1038/nrc1478

Generalov, R., Kuan, W. B., Chen, W., Kristensen, S., & Juzenas, P. (2015). Radiosensitizing effect of zinc oxide and silica nanocomposites on cancer cells. *Colloids and Surfaces B: Biointerfaces*, *129*, 79–86. https://doi.org/10.1016/j.colsurfb.2015.03.026

Gérard, M., Corroyer-Dulmont, A., Lesueur, P., Collet, S., Chérel, M., Bourgeois, M., Stefan, D., Limkin,

E. J., Perrio, C., Guillamo, J.-S., Dubray, B., Bernaudin, M., Thariat, J., & Valable, S. (2019). Hypoxia Imaging and Adaptive Radiotherapy: A State-of-the-Art Approach in the Management of Glioma. *Frontiers in Medicine*, *6*(June). https://doi.org/10.3389/fmed.2019.00117

Ghaemi, B., Mashinchian, O., Mousavi, T., Karimi, R., Kharrazi, S., & Amani, A. (2016). Harnessing the Cancer Radiation Therapy by Lanthanide-Doped Zinc Oxide Based Theranostic Nanoparticles. *ACS Applied Materials and Interfaces*, *8*(5), 3123–3134. https://doi.org/10.1021/acsami.5b10056

Ghita, M., McMahon, S. J., Taggart, L. E., Butterworth, K. T., Schettino, G., & Prise, K. M. (2017). A mechanistic study of gold nanoparticle radiosensitisation using targeted microbeam irradiation. *Scientific Reports*, *7*(November 2016), 1–12. https://doi.org/10.1038/srep44752

Gilbert, D. L. (1963). The Role of Pro-Oxidants and Antioxidants in Oxygen Toxicity. *Radiation Research Supplement*, *3*(1963), 44. https://doi.org/10.2307/3583674

Gilbert, D. L., Gerschman, R., Ruhm, K. B., & Price, W. E. (1958). The production of hydrogen peroxide by high oxygen pressures. *The Journal of General Physiology*, *41*(5), 989–1003. https://doi.org/10.1085/jgp.41.5.989

Gill, M. R., & Vallis, K. A. (2019). Transition metal compounds as cancer radiosensitizers. *Chemical Society Reviews*, *48*(2), 540–557. https://doi.org/10.1039/c8cs00641e

Gilles, M., Brun, E., & Sicard-Roselli, C. (2014). Gold nanoparticles functionalization notably decreases radiosensitization through hydroxyl radical production under ionizing radiation. *Colloids and Surfaces B: Biointerfaces*. https://doi.org/10.1016/j.colsurfb.2014.10.028

Gilles, M., Brun, E., & Sicard-Roselli, C. (2018). Quantification of hydroxyl radicals and solvated electrons produced by irradiated gold nanoparticles suggests a crucial role of interfacial water. *Journal of Colloid and Interface Science*, *525*, 31–38. https://doi.org/10.1016/j.jcis.2018.04.017

Godbey, W. T., Wu, K. K., Hirasaki, G. J., & Mikos, A. G. (1999). Improved packing of poly(ethylenimine)/DNA complexes increases transfection efficiency. *Gene Therapy*, *6*(8), 1380–1388. https://doi.org/10.1038/sj.gt.3300976

Godbey, W. T., Wu, K. K., & Mikos, A. G. (1999). Poly(ethylenimine) and its role in gene delivery. *Journal of Controlled Release*, *60*(2–3), 149–160. https://doi.org/10.1016/S0168-3659(99)00090-5

Grdina, D. J., Murley, J. S., & Kataoka, Y. (2002). Radioprotectants: Current status and new directions. *Oncology*, *63*(SUPPL. 2), 2–10. https://doi.org/10.1159/000067146

Grellet, S., Tzelepi, K., Roskamp, M., Williams, P., Sharif, A., Slade-Carter, R., Goldie, P., Whilde, N., Smialek, M. A., Mason, N. J., & Golding, J. P. (2017). Cancer-selective, single agent chemoradiosensitising gold nanoparticles. *PLoS ONE*, *12*(7), 1–21. https://doi.org/10.1371/journal.pone.0181103

Guo, T. (2019). Physical, chemical and biological enhancement in X-ray nanochemistry. *Physical Chemistry Chemical Physics*, *21*(29), 15917–15931. https://doi.org/10.1039/c9cp03024g

Hainfeld, J. F., Dilmanian, F. A., Slatkin, D. N., & Smilowitz, H. M. (2008). Radiotherapy enhancement with gold nanoparticles. *Journal of Pharmacy and Pharmacology*, *60*(8), 977–985. https://doi.org/10.1211/jpp.60.8.0005

Hainfeld, J. F., Slatkin, D. N., & Smilowitz, H. M. (2004). The use of gold nanoparticles to enhance radiotherapy in mice. *Physics in Medicine and Biology*, *49*(18). https://doi.org/10.1088/0031-9155/49/18/N03

Hall, S., Rudrawar, S., Zunk, M., Bernaitis, N., Arora, D., McDermott, C. M., & Anoopkumar-Dukie, S. (2016). Protection against radiotherapy-induced toxicity. *Antioxidants*, *5*(3). https://doi.org/10.3390/antiox5030022

Hanley, C., Thurber, A., Hanna, C., Punnoose, A., Zhang, J., & Wingett, D. G. (2009). The influences of cell Type and ZnO nanoparticle size on immune cell cytotoxicity and cytokine induction. *Nanoscale Research Letters*, *4*(12), 1409–1420. https://doi.org/10.1007/s11671-009-9413-8

Haruta, M., Kobayashi, T., Sano, H., & Yamada, N. (1987). Novel Gold Catalysts for the Oxidation of Carbon Monoxide at a Temperature far Below 0 °C. *Chemistry Letters*, *16*(2), 405–408. https://doi.org/10.1246/cl.1987.405

Haume, K., Rosa, S., Grellet, S., Śmiałek, M. A., Butterworth, K. T., Solov'yov, A. V., Prise, K. M., Golding, J., & Mason, N. J. (2016). Gold nanoparticles for cancer radiotherapy: a review. *Cancer Nanotechnology*, *7*(1). https://doi.org/10.1186/s12645-016-0021-x

Hauser, A., Mitov, M., Daley, E., McGarry, R., Anderson, K., & Hilt, J. (2016) Targeted iron oxide nanoparticles for the enhancement of radiation therapy. *Biomaterials.* https://doi.org/10.1016/j.biomaterials.2016.07.032.

Hayyan, M., Hashim, M. A., & Alnashef, I. M. (2016). Superoxide Ion: Generation and Chemical Implications. *Chemical Reviews*, *116*(5), 3029–3085. https://doi.org/10.1021/acs.chemrev.5b00407

He, W., Zhou, Y. T., Wamer, W. G., Hu, X., Wu, X., Zheng, Z., Boudreau, M. D., & Yin, J. J. (2013). Intrinsic catalytic activity of Au nanoparticles with respect to hydrogen peroxide decomposition and superoxide scavenging. *Biomaterials*, *34*(3), 765–773. https://doi.org/10.1016/j.biomaterials.2012.10.010

Hejmadi, M. (2010). Introduction to cancer biology. *Bookboon*. ISBN 978-87-7681-478-6

Henderson, L. M., & Chappell, J. B. (1993). Dihydrorhodamine 123: a fluorescent probe for superoxide generation? *European Journal of Biochemistry*, *217*(3), 973–980. https://doi.org/10.1111/j.1432-1033.1993.tb18328.x

Henk, J. M. (1986). Late results of a trial of hyperbaric oxygen and radiotherapy in head and neck cancer: A rationale for hypoxic cell sensitizers? *International Journal of Radiation Oncology, Biology, Physics*, *12*(8), 1339–1341. https://doi.org/10.1016/0360-3016(86)90167-7

Hermes-Lima, M., Moreira, D. C., Rivera-Ingraham, G. A., Giraud-Billoud, M., Genaro-Mattos, T. C., & Campos, É. G. (2015). Preparation for oxidative stress under hypoxia and metabolic depression: Revisiting the proposal two decades later. *Free Radical Biology and Medicine*, *89*, 1122–1143. https://doi.org/10.1016/j.freeradbiomed.2015.07.156

Hill, R., Healy, B., Holloway, L., Kuncic, Z., Thwaites, D., & Baldock, C. (2014). Advances in kilovoltage x-ray beam dosimetry. *Physics in Medicine and Biology*, *59*(6). https://doi.org/10.1088/0031-9155/59/6/R183

Hirakawa, K. (2018). Biomolecules Oxidation by Hydrogen Peroxide and Singlet Oxygen. *Reactive Oxygen Species (ROS) in Living Cells*. https://doi.org/10.5772/intechopen.71465

Horie, M., Fujita, K., Kato, H., Endoh, S., Nishio, K., Komaba, L. K., Nakamura, A., Miyauchi, A., Kinugasa, S., Hagihara, Y., Niki, E., Yoshida, Y., & Iwahashi, H. (2012). Association of the physical and chemical properties and the cytotoxicity of metal oxide nanoparticles: Metal ion release, adsorption ability and specific surface area. *Metallomics*, *4*(4), 350–360. https://doi.org/10.1039/c2mt20016c

Horsman, M. R., & Overgaard, J. (2016). The impact of hypoxia and its modification of the outcome of radiotherapy. *Journal of Radiation Research*, *57*(March), i90–i98. https://doi.org/10.1093/jrr/rrw007

Hosoya, N., & Miyagawa, K. (2014). Targeting DNA damage response in cancer therapy. *Cancer Science*, *105*(4), 370–388. https://doi.org/10.1111/cas.12366

Huang, X., & El-Sayed, M. A. (2010). Gold nanoparticles: Optical properties and implementations in cancer diagnosis and photothermal therapy. *Journal of Advanced Research*, *1*(1), 13–28. https://doi.org/10.1016/j.jare.2010.02.002

Huang, Y.-W., Cambre, M., & Lee, H.-J. (2017). The Toxicity of Nanoparticles Depends on Multiple Molecular and Physicochemical Mechanisms. *International Journal of Molecular Sciences*, *18*(12). https://doi.org/10.3390/ijms18122702

Hvolbæk, B., Janssens, T. V. W., Clausen, B. S., Falsig, H., Christensen, C. H., & Nørskov, J. K. (2007).

Catalytic activity of Au nanoparticles. *Nano Today*, *2*(4), 14–18. https://doi.org/10.1016/S1748-0132(07)70113-5

Hwang, C., Kim, J. M., & Kim, J. (2017). Influence of concentration, nanoparticle size, beam energy, and material on dose enhancement in radiation therapy. *Journal of Radiation Research*, *58*(4), 405–411. https://doi.org/10.1093/jrr/rrx009

Ivanković, S., Musić, S., Gotić, M., & Ljubešić, N. (2006). Cytotoxicity of nanosize V2O5 particles to selected fibroblast and tumor cells. *Toxicology in Vitro*, *20*(3), 286–294. https://doi.org/10.1016/j.tiv.2005.08.011

Ivask, A., Titma, T., Visnapuu, M., Vija, H., Kakinen, A., Sihtmae, M., Pokhrel, S., Madler, L., Heinlaan, M., Kisand, V., Shimmo, R., & Kahru, A. (2015). Toxicity of 11 Metal Oxide Nanoparticles to Three Mammalian Cell Types *In V.itro*. *Current Topics in Medicinal Chemistry*, *15*(18), 1914–1929. https://doi.org/10.2174/1568026615666150506150109

Jain, S., Coulter, J. A., Butterworth, K. T., Hounsell, A. R., McMahon, S. J., Hyland, W. B., Muir, M. F., Dickson, G. R., Prise, K. M., Currell, F. J., Hirst, D. G., & O'Sullivan, J. M. (2014). Gold nanoparticle cellular uptake, toxicity and radiosensitisation in hypoxic conditions. *Radiotherapy and Oncology*, *110*(2), 342–347. https://doi.org/10.1016/j.radonc.2013.12.013

Jain, S., Coulter, J. A., Hounsell, A. R., Butterworth, K. T., McMahon, S. J., Hyland, W. B., Muir, M. F., Dickson, G. R., Prise, K. M., Currell, F. J., O'Sullivan, J. M., & Hirst, D. G. (2011). Cell-Specific Radiosensitization by gold nanoparticles at megavoltage radiation energies. *International Journal of Radiation Oncology Biology Physics*, *79*(2), 531–539. https://doi.org/10.1016/j.ijrobp.2010.08.044

Jayakumar, S., Kunwar, A., Sandur, S. K., Pandey, B. N., & Chaubey, R. C. (2014). Differential response of DU145 and PC3 prostate cancer cells to ionizing radiation: Role of reactive oxygen species, GSH and Nrf2 in radiosensitivity. *Biochimica et Biophysica Acta - General Subjects*, *1840*(1), 485–494. https://doi.org/10.1016/j.bbagen.2013.10.006

Jeggo, P. A., & Löbrich, M. (2007). DNA double-strand breaks: Their cellular and clinical impact? *Oncogene*, *26*(56), 7717–7719. https://doi.org/10.1038/sj.onc.1210868

Jiang, J., Pi, J., & Cai, J. (2018). The Advancing of Zinc Oxide Nanoparticles for Biomedical Applications. *Bioinorganic Chemistry and Applications*, *2018*. https://doi.org/10.1155/2018/1062562

Jiang, Y. W., Gao, G., Jia, H. R., Zhang, X., Zhao, J., Ma, N., Liu, J. B., Liu, P., & Wu, F. G. (2019). Copper Oxide Nanoparticles Induce Enhanced Radiosensitizing Effect via Destructive Autophagy [Research-article]. *ACS Biomaterials Science and Engineering*, *5*(3), 1569–1579. https://doi.org/10.1021/acsbiomaterials.8b01181

Kennedy, K., Teicher, B., Rockwell, S., & Sartorelli, A. (1980). The hypoxic tumor cell: A Target for selective cancer chemotherapy. *Biochemical Pharmacology*. https://doi.org/10.1016/0006-2952(80)90235-X

Khoei, S., Mahdavi, S. R., Fakhimikabir, H., Shakeri-Zadeh, A., & Hashemian, A. (2014). The role of iron oxide nanoparticles in the radiosensitization of human prostate carcinoma cell line DU145 at megavoltage radiation energies. *International Journal of Radiation Biology*, *90*(5), 351–356. https://doi.org/10.3109/09553002.2014.888104

King, C., Diaz, H. B., McNeely, S., Barnard, D., Dempsey, J., Blosser, W., Beckmann, R., Barda, D., & Marshall, M. S. (2015). LY2606368 causes replication catastrophe and antitumor effects through CHK1-dependent mechanisms. *Molecular Cancer Therapeutics*, *14*(9), 2004–2013. https://doi.org/10.1158/1535-7163.MCT-14-1037

King, R. B., Hyland, W. B., Cole, A. J., Butterworth, K. T., McMahon, S. J., Redmond, K. M., Trainer, C., Prise, K. M., McGarry, C. K., & Hounsell, A. R. (2013). An in vitro study of the radiobiological effects of flattening filter free radiotherapy treatments. *Physics in Medicine and Biology*, *58*(5). https://doi.org/10.1088/0031-9155/58/5/N83

King, Raymond B., McMahon, S. J., Hyland, W. B., Jain, S., Butterworth, K. T., Prise, K. M., Hounsell,

A. R., & McGarry, C. K. (2017). An overview of current practice in external beam radiation oncology with consideration to potential benefits and challenges for nanotechnology. *Cancer Nanotechnology*, *8*(1). https://doi.org/10.1186/s12645-017-0027-z

Kinouchi, M., Izumi, S., Nakashiro, K. ichi, Haruyama, Y., Kobashi, G., Uchida, D., Hasegawa, T., & Kawamata, H. (2018). Determination of the origin of oral squamous cell carcinoma by microarray analysis: Squamous epithelium or minor salivary gland? *International Journal of Cancer*, *143*(10), 2551–2560. https://doi.org/10.1002/ijc.31811

Klein, S., Sommer, A., Distel, L. V. R., Neuhuber, W., & Kryschi, C. (2012). Superparamagnetic iron oxide nanoparticles as radiosensitizer via enhanced reactive oxygen species formation. *Biochemical and Biophysical Research Communications*, *425*(2), 393–397. https://doi.org/10.1016/j.bbrc.2012.07.108

Kljuev, V. V. (2001). NDT Techniques: Radiographic. *Encyclopedia of Materials: Science and Technology*, *mm*, 6029–6032. https://doi.org/10.1016/b0-08-043152-6/01063-9

Konefał, A., Bakoniak, M., Orlef, A., Maniakowski, Z., & Szewczuk, M. (2015). Energy spectra in water for the 6 MV X-ray therapeutic beam generated by Clinac-2300 linac. *Radiation Measurements*, *72*, 12–22. https://doi.org/10.1016/j.radmeas.2014.11.008

Kralj, S., Rojnik, M., Romih, R., Jagodic, M., Kos, J., & Makovec, D. (2012). Effect of surface charge on the cellular uptake of fluorescent magnetic nanoparticles. *Journal of Nanoparticle Research*, *14*(10). https://doi.org/10.1007/s11051-012-1151-7

Kuncic, Z., & Lacombe, S. (2018). Nanoparticle radio-enhancement: Principles, progress and application to cancer treatment. *Physics in Medicine and Biology*, *63*(2). https://doi.org/10.1088/1361-6560/aa99ce

Kuntić, V. S., Stanković, M. B., Vujić, Z. B., Brborić, J. S., & Uskoković-Marković, S. M. (2013). Radioprotectors - The evergreen topic. *Chemistry and Biodiversity*, *10*(10), 1791–1803. https://doi.org/10.1002/cbdv.201300054

Kwatra, D., Venugopal, A., Anant, S. (2013). Nanoparticles in radiation therapy: a summary of various approaches to enhance radiosensitization in cancer. *Translational Cancer Research*. https://doi.org/10.3978/j.issn.2218-676X.2013.08.06.

Le Caër. (2011). *Water Radiolysis: Influence of Oxide Surfaces on H 2 Production under Ionizing Radiation*. *3*, 235–253. https://doi.org/10.3390/w3010235

Lee, K. M., Lai, C. W., Ngai, K. S., & Juan, J. C. (2016). Recent developments of zinc oxide based photocatalyst in water treatment technology: A review. *Water Research*, *88*, 428–448. https://doi.org/10.1016/j.watres.2015.09.045

Li, J., Jiang, M., Zhou, H., Jin, P., Cheung, K. M. C., Chu, P. K., & Yeung, K. W. K. (2019). Vanadium Dioxide Nanocoating Induces Tumor Cell Death through Mitochondrial Electron Transport Chain Interruption. *Global Challenges*, *3*(3), 1800058. https://doi.org/10.1002/gch2.201800058

Liao, H., & Hafner, J. H. (2005). Gold nanorod bioconjugates Supplementary Information. *Chemistry of Materials*, *17*(18), 50935.

Liberti, M. V, & Locasale, J. W. (2016). The Warburg Effect: How Does it Benefit Cancer Cells? (vol 41, pg 211, 2016). *Trends in Biochemical Sciences*, *41*(3, SI), 287. https://doi.org/10.1016/j.tibs.2016.01.004

Liu, G., Wang, Z., Lu, J., Xia, C., Gao, F., Gong, Q., Song, B., Zhao, X., Shuai, X., Chen, X., Ai, H., & Gu, Z. (2011). Low molecular weight alkyl-polycation wrapped magnetite nanoparticle clusters as MRI probes for stem cell labeling and in vivo imaging. *Biomaterials*, *32*(2), 528–537. https://doi.org/10.1016/j.biomaterials.2010.08.099

Liu, P., Jin, H., Guo, Z., Ma, J., Zhao, J., Li, D., Wu, H., & Gu, N. (2016). Silver nanoparticles outperform gold nanoparticles in radiosensitizing U251 cells in vitro and in an intracranial mouse model of glioma. *International Journal of Nanomedicine*, *11*, 5003–5014. https://doi.org/10.2147/IJN.S115473

Liu, R. (2013). Adsorption and dissociation of H2O on Au(111) surface: A DFT study. *Computational and Theoretical Chemistry*, *1019*(1), 141–145. https://doi.org/10.1016/j.comptc.2013.07.009

Liu, Y., Zhang, P., Li, F., Jin, X., Li, J., Chen, W., & Li, Q. (2018). Metal-based NanoEnhancers for future radiotherapy: Radiosensitizing and synergistic effects on tumor cells. *Theranostics*, *8*(7), 1824–1849. https://doi.org/10.7150/thno.22172

Louit, G., Hanedanian, M., Taran, F., Coffigny, H., Renault, J. P., & Pin, S. (2009). Determination of hydroxyl rate constants by a high-throughput fluorimetric assay: Towards a unified reactivity scale for antioxidants. *Analyst*, *134*(2), 250–255. https://doi.org/10.1039/b813871k

Lousada, C. M., Johansson, A. J., Brinck, T., & Jonsson, M. (2013). Reactivity of metal oxide clusters with hydrogen peroxide and water - A DFT study evaluating the performance of different exchange-correlation functionals. *Physical Chemistry Chemical Physics*, *15*(15), 5539–5552. https://doi.org/10.1039/c3cp44559c

Luchette, M., Korideck, H., Makrigiorgos, M., Tillement, O., & Berbeco, R. (2014). Radiation dose enhancement of gadolinium-based AGuIX nanoparticles on HeLa cells. *Nanomedicine: Nanotechnology, Biology and Medicine*, *10*(8), 1751–1755. https://doi.org/10.1016/j.nano.2014.06.004

Lux, F., Tran, V. L., Thomas, E., & Dufort, S. (2019). *AGuIX ® from bench to bedside — Transfer of an ultrasmall theranostic gadolinium-based nanoparticle to clinical medicine*. *July 2018*, 1–19.

Lux, F., Tran, V. L., Thomas, E., Dufort, S., Rossetti, F., Martini, M., Truillet, C., Doussineau, T., Bort, G., Denat, F., Boschetti, F., Angelovski, G., Detappe, A., Crémillieux, Y., Mignet, N., Doan, B.-T., Larrat, B., Meriaux, S., Barbier, E., … Tillement, O. (2018). AGuIX ® from bench to bedside—Transfer of an ultrasmall theranostic gadolinium-based nanoparticle to clinical medicine . *The British Journal of Radiology*. https://doi.org/10.1259/bjr.20180365

Ma, N., Wu, F. G., Zhang, X., Jiang, Y. W., Jia, H. R., Wang, H. Y., Li, Y. H., Liu, P., Gu, N., & Chen, Z. (2017). Shape-Dependent Radiosensitization Effect of Gold Nanostructures in Cancer Radiotherapy: Comparison of Gold Nanoparticles, Nanospikes, and Nanorods. *ACS Applied Materials and Interfaces*, *9*(15), 13037–13048. https://doi.org/10.1021/acsami.7b01112

Maggiorella, L., Barouch, G., Devaux, C., Pottier, A., Deutsch, E., Bourhis, J., Borghi, E., & Levy, L. (2012). Nanoscale radiotherapy with hafnium oxide nanoparticles. *Future Oncology*, *8*(9), 1167–1181. https://doi.org/10.2217/fon.12.96

Manevich, Y., Held, K. D., & Biaglow, J. E. (1997). Coumarin-3-Carboxylic Acid as a Detector for Hydroxyl Radicals Generated Chemically and by Gamma Radiation. *Radiation Research*, *148*(6), 580. https://doi.org/10.2307/3579734

Manke, A., Wang, L., & Rojanasakul, Y. (2013). Mechanisms of nanoparticle-induced oxidative stress and toxicity. *BioMed Research International*, *2013*. https://doi.org/10.1155/2013/942916

Marill, J., Anesary, N. M., Zhang, P., Vivet, S., Borghi, E., Levy, L., & Pottier, A. (2014). Hafnium oxide nanoparticles: Toward an in vitro predictive biological effect? *Radiation Oncology*, *9*(1), 1–11. https://doi.org/10.1186/1748-717X-9-150

Marill, J., Anesary, N., Zhang, P., Vivet, S., Borghi, E., Levy, L., Pottier, A., Hall, E., Giaccia, A., Maggiorella, L., Barouch, G., Devaux, C., Pottier, A., Deutsch, E., Bourhis, J., Borghi, E., Levy, L., Kong, T., Zeng, J., … Barendsen, G. (2014). Hafnium oxide nanoparticles: toward an in vitro predictive biological effect? *Radiation Oncology*, *9*(1), 150. https://doi.org/10.1186/1748-717X-9-150

Matsubara, J. (1988). Metallothionein induction: A measure of radioprotective action. *Health Physics Society*. http://dx.doi.org/

McKeown, S. R. (2014). Defining normoxia, physoxia and hypoxia in tumours - Implications for treatment response. *British Journal of Radiology*, *87*(1035), 1–12. https://doi.org/10.1259/bjr.20130676

McMahon, S. J., McNamara, A. L., Schuemann, J., Prise, K. M., & Paganetti, H. (2017). Mitochondria as a target for radiosensitisation by gold nanoparticles. *Journal of Physics: Conference Series*,

777(1). https://doi.org/10.1088/1742-6596/777/1/012008

McMahon, Stephen J., Hyland, W. B., Muir, M. F., Coulter, J. A., Jain, S., Butterworth, K. T., Schettino, G., Dickson, G. R., Hounsell, A. R., O'Sullivan, J. M., Prise, K. M., Hirst, D. G., & Currell, F. J. (2011). Nanodosimetric effects of gold nanoparticles in megavoltage radiation therapy. *Radiotherapy and Oncology*. https://doi.org/10.1016/j.radonc.2011.08.026

McMahon, Stephen J., Paganetti, H., & Prise, K. M. (2016). Optimising element choice for nanoparticle radiosensitisers. *Nanoscale*, *8*(1), 581–589. https://doi.org/10.1039/c5nr07089a

McNamara, A., Kam, W., Scales, N., McMahon, S., Bennett, J., Byrne, H., Schuemann, J., Paganetti, H., Banati, R., & Kuncic, Z. (2016). Dose enhancement effects to the nucleus and mitochondria from gold nanoparticles in the cytosol. *Phys Med Biol*. http://dx.doi.org/ 10.1088/0031-9155/61/16/5993

McQuaid, H. N., Muir, M. F., Taggart, L. E., McMahon, S. J., Coulter, J. A., Hyland, W. B., Jain, S., Butterworth, K. T., Schettino, G., Prise, K. M., Hirst, D. G., Botchway, S. W., & Currell, F. J. (2016). Imaging and radiation effects of gold nanoparticles in tumour cells. *Scientific Reports*, *6*(May 2015), 1–10. https://doi.org/10.1038/srep19442

Mesbahi, A. (2010). A review on gold nanoparticles radiosensitization effect in radiation therapy of cancer. In *Reports of Practical Oncology and Radiotherapy*. https://doi.org/10.1016/j.rpor.2010.09.001

Michi, Y., Morita, I., Amagasa, T., & Murota, S. (2000). Human oral squamous cell carcinoma cell lines promote angiogenesis via expression of vascular endothelial growth factor and upregulation of KDR/flk-1 expression in endothelial cells. *Oral Oncology*, *36*(1), 81–88. https://doi.org/10.1016/S1368-8375(99)00059-7

Miguel, C., & Patrício, L. (2013). *Reactions of aqueous radiolysis products with oxide surfaces : An experimental and DFT study* (Issue April).

Mirjolet, C., Papa, A. L., Créhange, G., Raguin, O., Seignez, C., Paul, C., Truc, G., Maingon, P., & Millot, N. (2013). The radiosensitization effect of titanate nanotubes as a new tool in radiation therapy for glioblastoma: A proof-of-concept. *Radiotherapy and Oncology*, *108*(1), 136–142. https://doi.org/10.1016/j.radonc.2013.04.004

Mitra, S., Nguyen, L. N., Akter, M., Park, G., Choi, E. H., & Kaushik, N. K. (2019). Impact of ROS generated by chemical, physical, and plasma techniques on cancer attenuation. *Cancers*, *11*(7), 1–31. https://doi.org/10.3390/cancers11071030

Mitsui, Y., & Schneider, E. L. (1976). *Relationship Between Cell Replication and Volume in*. *I*, 45–56.

Mladenov, E., Iliakis, G. (2011). The Pathways of Double-Strand Break Repair, DNA Repair - On the Pathways to Fixing DNA Damage and Errors. *InTech*. ISBN: 978-953-307-649-2. Available from: http://www.intechopen.com/books/dna-repair-on-the-pathways-to-fixing-dna-damage-and-errors/the-pathways-of-double-strand-break-repair

Morrison, R. A., Rybak-Smith, M. J., Thompson, J. M., Thiebaut, B., Hill, M. A., & Townley, H. E. (2017). Efficacy of radiosensitizing doped titania nanoparticles under hypoxia and preparation of an embolic microparticle. *International Journal of Nanomedicine*, *12*, 3851–3863. https://doi.org/10.2147/IJN.S127341

Muhammad, M. A., Rashid, R. A., Lazim, R. M., Dollah, N., Razak, K. A., & Rahman, W. N. (2018). Evaluation of radiosensitization effects by platinum nanodendrites for 6 MV photon beam radiotherapy. *Radiation Physics and Chemistry*, *150*(April), 40–45. https://doi.org/10.1016/j.radphyschem.2018.04.018

Muz, B., de la Puente, P., Azab, F., & Azab, A. K. (2015). The role of hypoxia in cancer progression, angiogenesis, metastasis, and resistance to therapy. *Hypoxia*, 83. https://doi.org/10.2147/hp.s93413

Nair, C. K. K., Parida, D. K., & Nomura, T. (2001). Radioprotectors in Radiotherapy. *Journal of Radiation Research*, *42*(1), 21–37. https://doi.org/10.1269/jrr.42.21

Nakayama, M., Sasaki, R., Ogino, C., Tanaka, T., Morita, K., Umetsu, M., Ohara, S., Tan, Z., Nishimura, Y., Akasaka, H., Sato, K., Numako, C., Takami, S., & Kondo, A. (2016). Titanium peroxide nanoparticles enhanced cytotoxic effects of X-ray irradiation against pancreatic cancer model through reactive oxygen species generation in vitro and in vivo. *Radiation Oncology*, *11*(1), 1–11. https://doi.org/10.1186/s13014-016-0666-y

Nazarewicz, R., Bikineyeva, A., & Dikalov, S. (2013). Rapid and specific measurements of superoxide using fluorescence spectroscopy. *J Biomol Screen*, 18(4): 498–503. https://doi.org/10.1177/1087057112468765.

Nel, A., Xia, T., Mädler, L., & Li, N. (2006). Toxic potential of materials at the nanolevel. *Science*, *311*(5761), 622–627. https://doi.org/10.1126/science.1114397

Neshatian, M., Chung, S., Yohan, D., Yang, C., & Chithrani, D. B. (2014). Determining the Size Dependence of Colloidal Gold Nanoparticle Uptake in a Tumor-like Interface (Hypoxic). *Colloids and Interface Science Communications*, *1*, 57–61. https://doi.org/10.1016/j.colcom.2014.07.004

Nickoloff, J. A. (2015). Photon, light ion, and heavy ion cancer radiotherapy: Paths from physics and biology to clinical practice. *Annals of Translational Medicine*, *3*(21), 1–6. https://doi.org/10.3978/j.issn.2305-5839.2015.12.18

Nosaka, Y., Nishikawa, M., & Nosaka, A. Y. (2014). Spectroscopic investigation of the mechanism of photocatalysis. *Molecules*, *19*(11), 18248–18267. https://doi.org/10.3390/molecules191118248

Oberdörster, G., Oberdörster, E., & Oberdörster, J. (2005). Nanotoxicology: An emerging discipline evolving from studies of ultrafine particles. *Environmental Health Perspectives*, *113*(7), 823–839. https://doi.org/10.1289/ehp.7339

Oh, J. Y., Kim, H. S., Palanikumar, L., Go, E. M., Jana, B., Park, S. A., Kim, H. Y., Kim, K., Seo, J. K., Kwak, S. K., Kim, C., Kang, S., & Ryu, J. H. (2018). Cloaking nanoparticles with protein corona shield for targeted drug delivery. *Nature Communications*, *9*(1), 1–9. https://doi.org/10.1038/s41467-018-06979-4

Omidi, Y., & Kafil, V. (2011). Cytotoxic Impacts of Linear and Branched Polyethylenimine Nanostructures in A431 Cells. *BioImpacts*, *1*(1), 23–30. http://bi.tbzmed.ac.ir/

Overgaard, J. (2007). Hypoxic radiosensitization: Adored and ignored. *Journal of Clinical Oncology*, *25*(26), 4066–4074. https://doi.org/10.1200/JCO.2007.12.7878

Parveen, I. (2001). Novel hypoxia-selective prodrugs of radiosensitisers and chemosensitisers. *PhD thesis from University of Bath*. Available from: https://researchportal.bath.ac.uk/en/studentTheses/novel-hypoxia-selective-prodrugs-of-radiosensitisers-and-chemosen

Paterson, I. C. M. (1981). Radiosensitisers. *British Medical Journal*, *282*(6257), 69–70. https://doi.org/10.1136/bmj.282.6257.69-b

Petković, J., Küzma, T., Rade, K., Novak, S., & Filipič, M. (2011). Pre-irradiation of anatase TiO 2 particles with UV enhances their cytotoxic and genotoxic potential in human hepatoma HepG2 cells. *Journal of Hazardous Materials*, *196*, 145–152. https://doi.org/10.1016/j.jhazmat.2011.09.004

Petri-Fink, A., Steitz, B., Finka, A., Salaklang, J., & Hofmann, H. (2008). Effect of cell media on polymer coated superparamagnetic iron oxide nanoparticles (SPIONs): Colloidal stability, cytotoxicity, and cellular uptake studies. *European Journal of Pharmaceutics and Biopharmaceutics*, *68*(1), 129–137. https://doi.org/10.1016/j.ejpb.2007.02.024

Petrik, N. G., A. B. Alexandrov, A. I., & Vall. (2001). *Interfacial Energy Transfer during Gamma Radiolysis of Water on the Surface of ZrO2 and Some Other Oxides*. https://doi.org/10.1021/JP004440O

Pissuwan, D., Niidome, T., & Cortie, M. B. (2011). The forthcoming applications of gold nanoparticles in drug and gene delivery systems. *Journal of Controlled Release*, *149*(1), 65–71. https://doi.org/10.1016/j.jconrel.2009.12.006

Podgorsak, E. (2005). Radiation Oncology Physics: A Handbool for Teacher and Students. *International Atomic Energy Agency*. ISBN 92–0–107304–6.

Pottier, A., Borghi, E., & Levy, L. (2014). New use of metals as nanosized radioenhancers. *Anticancer Research*, *34*(1), 443–453.

Puangpetch, T., Chavadej, S., & Sreethawong, T. (2011). Hydrogen production over Au-loaded mesoporous-assembled SrTiO3 nanocrystal photocatalyst: Effects of molecular structure and chemical properties of hole scavengers. *Energy Conversion and Management*, *52*(5), 2256–2261. https://doi.org/10.1016/J.ENCONMAN.2010.12.026

Purdy, J. A. (2001). Intensity-modulated radiotherapy: Current status and issues of interest. *International Journal of Radiation Oncology Biology Physics*, *51*(4), 880–914. https://doi.org/10.1016/S0360-3016(01)01749-7

Purdy, James A. (2008). Dose to normal tissues outside the radiation therapy patient's treated volume: A review of different radiation therapy techniques. *Health Physics*, *95*(5), 666–676. https://doi.org/10.1097/01.HP.0000326342.47348.06

Rahman, W. N., Corde, S., Yagi, N., Abdul Aziz, S. A., Annabell, N., & Geso, M. (2014). Optimal energy for cell radiosensitivity enhancement by gold nanoparticles using synchrotron-based monoenergetic photon beams. *International Journal of Nanomedicine*, *9*(1), 2459–2467. https://doi.org/10.2147/IJN.S59471

Rasmussen, J. W., Martinez, E., Louka, P., & Wingett, D. G. (2010). Zinc oxide nanoparticles for selective destruction of tumor cells and potential for drug delivery applications. *Expert Opinion on Drug Delivery*, *7*(9), 1063–1077. https://doi.org/10.1517/17425247.2010.502560

Ray, C., & Pal, T. (2017). Recent advances of metal-metal oxide nanocomposites and their tailored nanostructures in numerous catalytic applications. *Journal of Materials Chemistry A*, *5*(20), 9465–9487. https://doi.org/10.1039/c7ta02116j

Rehman, J. ur, Zahra, Ahmad, N., Khalid, M., Noor ul Huda Khan Asghar, H. M., Gilani, Z. A., Ullah, I., Nasar, G., Akhtar, M. M., & Usmani, M. N. (2018). Intensity modulated radiation therapy: A review of current practice and future outlooks. *Journal of Radiation Research and Applied Sciences*, *11*(4), 361–367. https://doi.org/10.1016/j.jrras.2018.07.006

Reinhardt, K., Kern, W. (2008). Handbook of Silicon Wafer Cleaning Technology. *William Andrew*. ISBN 978-0-8155-1554-8 (978-0-8155) Reinhardt & Kern, 2008

Retif, P., Pinel, S., Toussaint, M., Frochot, C., Chouikrat, R., Bastogne, T., & Barberi-Heyob, M. (2015). Nanoparticles for radiation therapy enhancement: The key parameters. *Theranostics*, *5*(9), 1030–1044. https://doi.org/10.7150/thno.11642

Revia, R. A., & Zhang, M. (2016). Magnetite nanoparticles for cancer diagnosis, treatment, and treatment monitoring: Recent advances. *Materials Today*, *19*(3), 157–168. https://doi.org/10.1016/j.mattod.2015.08.022

Richmond, R., Halliwell, B., Chauhan, J., & Darbre, A. (1981). Superoxide-dependent formation of hydroxyl radicals: Detection of hydroxyl radicals by the hydroxylation of aromatic compounds. *Analytical Biochemistry*, *118*(2), 328–335. https://doi.org/10.1016/0003-2697(81)90590-X

Rim, K. T., Koo, K. H., & Park, J. S. (2013). Toxicological evaluations of rare earths and their health impacts to workers: A literature review. *Safety and Health at Work*, *4*(1), 12–26. https://doi.org/10.5491/SHAW.2013.4.1.12

Robar, J. L., & Clark, B. G. (1999). The use of radiographic film for linear accelerator stereotactic radiosurgical dosimetry. *Medical Physics*, *26*(10), 2144–2150. https://doi.org/10.1118/1.598730

Robar, James L., Riccio, S. A., & Martin, M. A. (2002). Tumour dose enhancement using modified megavoltage photon beams and contrast media. *Physics in Medicine and Biology*, *47*(14), 2433–2449. https://doi.org/10.1088/0031-9155/47/14/305

Rockwell, S., Dobrucki, I., Kim, E., Marrison, S., & Vu, V. (2009). Hypoxia and Radiation Therapy: Past History, Ongoing Research, and Future Promise. *Current Molecular Medicine*, *9*(4), 442–458.

https://doi.org/10.2174/156652409788167087

Rodnyi, P. A. (1997). *Physical processes in inorganic scintillators*. CRC Press.

Roeske, J. C., Nuñez, L., Hoggarth, M., Labay, E., & Weichselbaum, R. R. (2007). Characterization of the theorectical radiation dose enhancement from nanoparticles. *Technology in Cancer Research and Treatment*, *6*(5), 395–401. https://doi.org/10.1177/153303460700600504

Rosa, S., Connolly, C., Schettino, G., Butterworth, K. T., & Prise, K. M. (2017). Biological mechanisms of gold nanoparticle radiosensitization. *Cancer Nanotechnology*, *8*(1). https://doi.org/10.1186/s12645-017-0026-0

Rose, A. L. (2012). The influence of extracellular superoxide on iron redox chemistry and bioavailability to aquatic microorganisms. *Frontiers in Microbiology*, *3*(APR), 1–21. https://doi.org/10.3389/fmicb.2012.00124

Roth, O., Hiroki, A., & LaVerne, J. A. (2011). Effect of Al_2O_3 Nanoparticles on Radiolytic H_2O_2 Production in Water. *The Journal of Physical Chemistry C*, *115*(16), 8144–8149. https://doi.org/10.1021/jp111918v

Saenko, Y., Cieslar-Pobuda, A., Skonieczna, M., & Rzeszowska-Wolny, J. (2013). Changes of Reactive Oxygen and Nitrogen Species and Mitochondrial Functioning in Human K562 and HL60 Cells Exposed to Ionizing Radiation. *Radiation Research*, *180*(4), 360–366. https://doi.org/10.1667/rr3247.1

Sahu, S. P., & Cates, E. L. (2017). X-ray Radiocatalytic Activity and Mechanisms of Bismuth Complex Oxides. *Journal of Physical Chemistry C*, *121*(19), 10538–10545. https://doi.org/10.1021/acs.jpcc.7b00776

Saito, I., Matsuura, T., & Inoue, K. (1983). Formation of Superoxide Ion via One-Electron Transfer from Electron Donors to Singlet Oxygen. *Journal of the American Chemical Society*. https://doi.org/10.1021/ja00348a040

Sakulkhu, U., Mahmoudi, M., Maurizi, L., Coullerez, G., Hofmann-Amtenbrink, M., Vries, M., Motazacker, M., Rezaee, F., & Hofmann, H. (2015). Significance of surface charge and shell material of superparamagnetic iron oxide nanoparticle (SPION) based core/shell nanoparticles on the composition of the protein corona. *Biomaterials Science*, *3*(2), 265–278. https://doi.org/10.1039/c4bm00264d

Sakulkhu, U., Mahmoudi, M., Maurizi, L., Salaklang, J., & Hofmann, H. (2014). Protein corona composition of superparamagnetic iron oxide nanoparticles with various physico-Chemical properties and coatings. *Scientific Reports*, *4*, 1–9. https://doi.org/10.1038/srep05020

Sakulkhu, U., Maurizi, L., Mahmoudi, M., Motazacker, M., Vries, M., Gramoun, A., Ollivier Beuzelin, M. G., Vallée, J. P., Rezaee, F., & Hofmann, H. (2014). Ex situ evaluation of the composition of protein corona of intravenously injected superparamagnetic nanoparticles in rats. *Nanoscale*, *6*(19), 11439–11450. https://doi.org/10.1039/c4nr02793k

Schlathölter, T., Eustache, P., Porcel, E., Salado, D., Stefancikova, L., Tillement, O., Lux, F., Mowat, P., Biegun, A. K., Van Goethem, M. J., Remita, H., & Lacombe, S. (2016). Improving proton therapy by metal-containing nanoparticles: Nanoscale insights. *International Journal of Nanomedicine*, *11*(April), 1549–1556. https://doi.org/10.2147/IJN.S99410

Schuemann, J., Berbeco, R., Chithrani, B., Cho, S., Kumar, R., McMahon, S., Sridhar, S., & Krishnan S. (2016). Roadmap to clinical use of gold nanoparticles for radiosensitization. *Int J Radiat Oncol Biol Phys*, 94(1): 189–205. https://doi.org/10.1016/j.ijrobp.2015.09.032.

Schuemann, J., McNamara, A. L., Warmenhoven, J. W., Henthorn, N. T., Kirkby, K. J., Merchant, M. J., Ingram, S., Paganetti, H., Held, K. D., Ramos-Mendez, J., Faddegon, B., Perl, J., Goodhead, D. T., Plante, I., Rabus, H., Nettelbeck, H., Friedland, W., Kundrát, P., Ottolenghi, A., … McMahon, S. J. (2018). A New Standard DNA Damage (SDD) Data Format. *Radiation Research*, *191*(1), 76. https://doi.org/10.1667/rr15209.1

Sen, T., Della Corte, C. M., Milutinovic, S., Cardnell, R. J., Diao, L., Ramkumar, K., Gay, C. M., Stewart, C. A., Fan, Y., Shen, L., Hansen, R. J., Strouse, B., Hedrick, M. P., Hassig, C. A., Heymach, J. V.,

Wang, J., & Byers, L. A. (2019). Combination Treatment of the Oral CHK1 Inhibitor, SRA737, and Low-Dose Gemcitabine Enhances the Effect of Programmed Death Ligand 1 Blockade by Modulating the Immune Microenvironment in SCLC. *Journal of Thoracic Oncology*, *14*(12), 2152–2163. https://doi.org/10.1016/j.jtho.2019.08.009

Senapati, V. A., Jain, A. K., Gupta, G. S., Pandey, A. K., & Dhawan, A. (2015). Chromium oxide nanoparticle-induced genotoxicity and p53-dependent apoptosis in human lung alveolar cells. *Journal of Applied Toxicology*, *35*(10), 1179–1188. https://doi.org/10.1002/jat.3174

Sicard-Roselli, C., Brun, E., Gilles, M., Baldacchino, G., Kelsey, C., McQuaid, H., Polin, C., Wardlow, N., & Currell, F. (2014). A new mechanism for hydroxyl radical production in irradiated nanoparticle solutions. *Small*, *10*(16), 3338–3346. https://doi.org/10.1002/smll.201400110

Sies, H. (1985). Oxidative Stress: Introductory Remarks. In *Oxidative Stress*. PERGAMON PRESS INC. https://doi.org/10.1016/b978-0-12-642760-8.50005-3

Storm, G., Belliot, S. O., Daemen, T., & Lasic, D. D. (1995). Surface modification of nanoparticles to oppose uptake by the mononuclear phagocyte system. *Advanced Drug Delivery Reviews*, *17*(1), 31–48. https://doi.org/10.1016/0169-409X(95)00039-A

Sukhanova, A., Bozrova, S., Sokolov, P., Berestovoy, M., Karaulov, A., & Nabiev, I. (2018). Dependence of Nanoparticle Toxicity on Their Physical and Chemical Properties. *Nanoscale Research Letters*, *13*. https://doi.org/10.1186/s11671-018-2457-x

Taggart, L. E., McMahon, S. J., Butterworth, K. T., Currell, F. J., Schettino, G., & Prise, K. M. (2016). Protein disulphide isomerase as a target for nanoparticle-mediated sensitisation of cancer cells to radiation. *Nanotechnology*, *27*(21). https://doi.org/10.1088/0957-4484/27/21/215101

Takahashi, H., Niidome, T., Kawano, T., Yamada, S., & Niidome, Y. (2008). Surface modification of gold nanorods using layer-by-layer technique for cellular uptake. *Journal of Nanoparticle Research*, *10*(1), 221–228. https://doi.org/10.1007/s11051-007-9227-5

Tan, T., Beydoun, D., & Amal, R. (2003). Effects of organic hole scavengers on the photocatalytic reduction of selenium anions. *Journal of Photochemistry and Photobiology A: Chemistry*, *159*(3), 273–280. https://doi.org/10.1016/S1010-6030(03)00171-0

Thariat, J., Hannoun-Levi, J. M., Sun Myint, A., Vuong, T., & Gérard, J. P. (2013). Past, present, and future of radiotherapy for the benefit of patients. *Nature Reviews Clinical Oncology*, *10*(1), 52–60. https://doi.org/10.1038/nrclinonc.2012.203

Tiligada, E. (2006). Chemotherapy: Induction of stress responses. *Endocrine-Related Cancer*, *13*(SUPPL. 1), 115–124. https://doi.org/10.1677/erc.1.01272

To, T. L., Fadul, M. J., & Shu, X. (2014). Singlet oxygen triplet energy transfer-based imaging technology for mapping protein-protein proximity in intact cells. *Nature Communications*, *5*(May), 1–9. https://doi.org/10.1038/ncomms5072

Townley, H. E., Kim, J., & Dobson, P. J. (2012). In vivo demonstration of enhanced radiotherapy using rare earth doped titania nanoparticles. *Nanoscale*, *4*(16), 5043–5050. https://doi.org/10.1039/c2nr30769c

Townley, H. E., Rapa, E., Wakefield, G., Dobson, P. J., Xu, M., Huang, N., Xiao, Z., Lu, Z., Vrouenraets, M. B., Visser, G. W. M., Snow, G. B., Dongen, G. A. M. S. van, Tamura, K., Ohko, Y., Kawamura, H., Yoshikawa, H., Tatsuma, T., Fujishima, A., Al., E., … Lesser, M. P. (2012). Nanoparticle augmented radiation treatment decreases cancer cell proliferation. *Nanomedicine : Nanotechnology, Biology, and Medicine*, *8*(4), 526–536. https://doi.org/10.1016/j.nano.2011.08.003

Toyokuni, S., Okamoto, K., Yodoi, J., & Hiai, H. (1995). Persistent oxidative stress in cancer. *FEBS Letters*, *358*(1), 1–3. https://doi.org/10.1016/0014-5793(94)01368-B

Trachootham, D., Alexandre, J., & Huang, P. (2009). Targeting cancer cells by ROS-mediated mechanisms: A radical therapeutic approach? *Nature Reviews Drug Discovery*, *8*(7), 579–591. https://doi.org/10.1038/nrd2803

Tzelepi, K., Espinosa Garcia, C., Williams, P., & Golding, J. (2019). Galactose:PEGamine coated gold nanoparticles adhere to filopodia and cause extrinsic apoptosis. *Nanoscale Advances*, *1*(2), 807–816. https://doi.org/10.1039/C8NA00270C

VanWinkle, B., de Mesy Bentley, K., Malecki, J., Gunter, K., Evans, I., Elder, A., Finkelstein, J., Oberdorster, G., & Gunter, T. (2009). Nanoparticle (NP) uptake by type I alveolar epithelial cells and their oxidant stress response. *Nanotoxicology*, *3*(4), 1–12. https://doi.org/10.1080/17435390903121949

Varanda, E., Tavares, D. (1998). Radioprotection: mechanisms and radioprotective agents including honeybee venom. *Journal of Venomous Animals and Toxins*. http://dx.doi.org/10.1590/S0104-79301998000100002

Verhagen, C. V. M., De Haan, R., Hageman, F., Oostendorp, T. P. D., Carli, A. L. E., O'Connor, M. J., Jonkers, J., Verheij, M., Van Den Brekel, M. W., & Vens, C. (2015). Extent of radiosensitization by the PARP inhibitor olaparib depends on its dose, the radiation dose and the integrity of the homologous recombination pathway of tumor cells. *Radiotherapy and Oncology*, *116*(3), 358–365. https://doi.org/10.1016/j.radonc.2015.03.028

Verry, C., Sancey, L., Dufort, S., Le Duc, G., Mendoza, C., Lux, F., Grand, S., Arnaud, J., Quesada, J. L., Villa, J., Tillement, O., & Balosso, J. (2019). Treatment of multiple brain metastases using gadolinium nanoparticles and radiotherapy: NANO-RAD, a phase I study protocol. *BMJ Open*, *9*(2), 1–6. https://doi.org/10.1136/bmjopen-2018-023591

Vilotte, F., Jumeau, R., & Bourhis, J. (2019). High Z nanoparticles and radiotherapy: a critical view. *The Lancet Oncology*, *20*(10), e557. https://doi.org/10.1016/S1470-2045(19)30579-0

Voinov, M. A., Pagán, J. O. S., Morrison, E., Smirnova, T. I., & Smirnov, A. I. (2011). Surface-mediated production of hydroxyl radicals as a mechanism of iron oxide nanoparticle biotoxicity. *Journal of the American Chemical Society*, *133*(1), 35–41. https://doi.org/10.1021/ja104683w

Wang, H., Mu, X., He, H., & Zhang, X. D. (2018). Cancer Radiosensitizers. *Trends in Pharmacological Sciences*, *39*(1), 24–48. https://doi.org/10.1016/j.tips.2017.11.003

Wang, J. song, Wang, H. juan, & Qian, H. li. (2018). Biological effects of radiation on cancer cells. *Military Medical Research*, *5*(1), 1–10. https://doi.org/10.1186/s40779-018-0167-4

Wang, X., Zhang, C., Du, J., Dong, X., Jian, S., Yan, L., Gu, Z., & Zhao, Y. (2019). Enhanced Generation of Non-Oxygen Dependent Free Radicals by Schottky-type Heterostructures of Au-Bi2S3 Nanoparticles via X-ray-Induced Catalytic Reaction for Radiosensitization [Research-article]. *ACS Nano*, *13*(5), 5947–5958. https://doi.org/10.1021/acsnano.9b01818

Wardman, P. (2007). Chemical Radiosensitizers for Use in Radiotherapy. *Clinical Oncology*, *19*(6), 397–417. https://doi.org/10.1016/j.clon.2007.03.010

Weiss, J., Landauer, M. (2006). Radioprotection by Antioxidants. *The New York Academy of Sciences.* https://doi.org/10.1111/j.1749-6632.2000.tb06175.x

Weiss, J. F., & Landauer, M. R. (2009). History and development of radiation-protective agents. *International Journal of Radiation Biology*, *85*(7), 539–573. https://doi.org/10.1080/09553000902985144

Wong, C. C., & Chu, W. (2003). The hydrogen peroxide-assisted photocatalytic degradation of alachlor in TiO2 suspensions. *Environmental Science and Technology*, *37*(10), 2310–2316. https://doi.org/10.1021/es020898n

Wu, M., Hou, P., Dong, L., Cai, L., Chen, Z., Zhao, M., & Li, J. (2019). Manganese dioxide nanosheets: From preparation to biomedical applications. *International Journal of Nanomedicine*, *14*, 4781–4800. https://doi.org/10.2147/IJN.S207666

Wu, W. S. (2006). The signaling mechanism of ROS in tumor progression. *Cancer and Metastasis Reviews*, *25*(4), 695–705. https://doi.org/10.1007/s10555-006-9037-8

Xi, W. S., Tang, H., Liu, Y. Y., Liu, C. Y., Gao, Y., Cao, A., Liu, Y., Chen, Z., & Wang, H. (2019). Cytotoxicity of vanadium oxide nanoparticles and titanium dioxide-coated vanadium oxide

nanoparticles to human lung cells. *Journal of Applied Toxicology*, *October*, 1–11. https://doi.org/10.1002/jat.3926

Zhang, Chen, Zhao, K., Bu, W., Ni, D., Liu, Y., Feng, J., & Shi, J. (2015). Marriage of scintillator and semiconductor for synchronous radiotherapy and deep photodynamic therapy with diminished oxygen dependence. *Angewandte Chemie - International Edition*, *54*(6), 1770–1774. https://doi.org/10.1002/anie.201408472

Zhang, Chenyang, Yan, L., Gu, Z., & Zhao, Y. (2019). Strategies based on metal-based nanoparticles for hypoxic-tumor radiotherapy. *Chemical Science*, *10*(29), 6932–6943. https://doi.org/10.1039/c9sc02107h

Zhang, Chenyang, Yan, L., Wang, X., Dong, X., Zhou, R., Gu, Z., & Zhao, Y. (2019). Tumor Microenvironment-Responsive Cu 2 (OH)PO 4 Nanocrystals for Selective and Controllable Radiosentization via the X-ray-Triggered Fenton-like Reaction. *Nano Letters*, *19*(3), 1749–1757. https://doi.org/10.1021/acs.nanolett.8b04763

Zhang, D., Zhou, T., He, F., Rong, Y., Lee, S. H., Wu, S., & Zuo, L. (2016). Reactive oxygen species formation and bystander effects in gradient irradiation on human breast cancer cells. *Oncotarget*, *7*(27), 41622–41636. https://doi.org/10.18632/oncotarget.9517

Zhang , H., Ji, Z., Xia, T., Meng, H., Low-Kam, C., Liu, R., Pokhrel, S., Lin, S., Wang, X., Liao, Y., Wang, M., Li, L., Rallo, R., Damoiseaux, R., Telesca, D., Mädler, L., Cohen, Y., Zink, J., & Nel, A. (2012) Use of Metal Oxide Nanoparticle Band Gap to Develop a Predictive Paradigm for Oxidative Stress and Acute Pulmonary Inflammation. *ACS Nano*. 6(5): 4349–4368. https://doi.org/10.1021/nn3010087.

Zhao, H., Kalivendi, S., Zhang, H., Joseph, J., Nithipatikom, K., Vásquez-Vivar, J., & Kalyanaraman, B. (2003). Superoxide reacts with hydroethidine but forms a fluorescent product that is distinctly different from ethidium: potential implications in intracellular fluorescence detection of superoxide. *Free Radical Biology and Medicine*, *34*(11), 1359–1368. https://doi.org/10.1016/S0891-5849(03)00142-4

Zhao, N., Yang, Z., Li, B., Meng, J., Shi, Z., Li, P., & Fu, S. (2016). RGD-conjugated mesoporous silica-encapsulated gold nanorods enhance the sensitization of triplenegative breast cancer to megavoltage radiation therapy. *International Journal of Nanomedicine*, *11*, 5595–5610. https://doi.org/10.2147/IJN.S104034

Zhu, W., Dong, Z., Fu, T., Liu, J., Chen, Q., Li, Y., Zhu, R., Xu, L., & Liu, Z. (2016). Modulation of Hypoxia in Solid Tumor Microenvironment with MnO2 Nanoparticles to Enhance Photodynamic Therapy. *Advanced Functional Materials*, *26*(30), 5490–5498. https://doi.org/10.1002/adfm.201600676

Zobel, M. (2016). Observing structural reorientations at solvent-nanoparticle interfaces by X-ray diffraction - Putting water in the spotlight. *Acta Crystallographica Section A: Foundations and Advances*, *72*(6), 621–631. https://doi.org/10.1107/S2053273316013516

Zobel, M., Neder, R. B., & Kimber, S. A. J. (2015). Universal solvent restructuring induced by colloidal nanoparticles. *Science*, *347*(6219), 292–294. https://doi.org/10.1126/science.1261412

Zucker, R. M., Ortenzio, J., Degn, L. L., Lerner, J. M., & Boyes, W. K. (2019). Biophysical comparison of four silver nanoparticles coatings using microscopy, hyperspectral imaging and flow cytometry. *PLoS ONE*, *14*(7), 1–24. https://doi.org/10.1371/journal.pone.0219078